

Analysis and Numerics of Novel Shape Optimization Methods for the Bernoulli Problem

Julius Fergy Tiongson-RABAGO

ベルヌイ問題に対する新しい形状最適化 問題の解析と数値計算

ジュリアス ファーザー ティオンソン ラバゴ

PHD THESIS

Analysis and Numerics of Novel Shape Optimization Methods for the Bernoulli Problem

Author:
Julius Fergy Tiongson-RABAGO

Supervisor:
Hideyuki AZEGAMI



Graduate School of Informatics
NAGOYA UNIVERSITY

A thesis submitted in fulfillment of the
requirements for the degree of
DOCTOR IN PHILOSOPHY

JULY 2020

ABSTRACT

Shape optimization methods are well-established tools for solving free boundary problems. A prototype problem of free boundary problems is the so-called Bernoulli problem. In the literature, several shape optimization reformulation of the problem have been offered and intensively studied. Although these existing formulations already provide excellent numerical results, much improvement can be done as we will showcase in this thesis. Therefore, one of the main objectives of this study is to introduced new shape optimization formulations of the Bernoulli problems. In comparison with the classical settings, it will be shown that the new formulations are more attractive, not only in the theoretical point of view, but also in terms of numerical aspects. In this respect, we design a state-of-the-art gradient-based iterative scheme for the numerical realization of the proposed shape optimization problems. Several numerical experiments are carried out to demonstrate the performance and efficacy as well as the stability of the proposed methods. The results are compared with those obtained from classical formulations.

ACKNOWLEDGMENTS AND DEDICATION

Acknowledgments

I would like to take this opportunity to express my sincere gratitude to my supervisor Prof. Hideyuki Azegami. His continuous support, guidance, and inspiration throughout the years of my PhD have made this work possible. I am deeply indebted to him for placing his trust in my abilities and for the many great discussions which help me improve my mathematical understanding of shape optimization methods.

I would also like to thank Prof. Masahiro Ohka and Prof. Takashi Watanabe for serving as my thesis examiners. Without their passionate participation and input, the evaluation survey of my research project could not have been successfully conducted.

I also would like thank my mentor and previous supervisor Prof. Jerico B. Bacani for introducing me into the field of shape optimization. I am always thankful to him for his warm and friendly advice, for the sharp and unconventional thoughts he has shared with me, not necessarily related to mathematics, which made me not only a better student but also a better person.

Also, I would like to greatly acknowledge the Japanese Ministry of Education, Culture, Sports, Science and Technology for scholarship support during my doctoral study.

Dedication

Finally, I would like to express my very profound gratitude to my family and friends.

To my father, Ferdinand, and my mother, Gloria, who have loved and supported me my entire life.

My siblings, Joy and Nica, deserve my wholehearted thanks as well.

All my friends wherever they are, especially my friends in Nagoya, for all the laughs and good memories.

To my lovely wife Kristine, my heartfelt gratitude for her support, encouragement, quiet patience, unwavering and unconditional love. I love you so much my dearest! Thank you!

A special gratitude and love goes to my lovely son, Caius. Your sweet smile serves as my most precious inspiration. *Mahal na mahal ka ni tatay, anak!*

And above all, I praise God, the almighty for providing me this opportunity and granting me the capability to proceed successfully.

Maraming salamat po sa inyong lahat!

Julius Fergy Tiongson-Rabago
Nagoya University
2020 July 31

AUTHOR'S DECLARATION

I hereby declare that except where specific reference is made to the work of others, the contents of this thesis are original and have not been submitted in whole or in part for consideration for any other degree or qualification in this, or any other university. This thesis is my own work and contains nothing which is the outcome of work done in collaboration with others, except as specified in the text and Acknowledgements.

Julius Fergy Tiongson-RABAGO
Nagoya, 2020 July 31

TABLE OF CONTENTS

	Page
List of Figures	ix
List of Tables	xiii
Preface	xviii
1 Introduction	1
1.1 An Overview of Shape Optimization	2
1.2 Notations, Abbreviations and Functions Spaces	5
1.2.1 Notations and Abbreviations	5
1.2.2 Continuous Functions	6
1.2.3 Lebesgue and Sobolev Spaces	8
1.2.4 Continuous Functions on Manifolds	9
1.2.5 Lebesgue and Sobolev Spaces on Manifolds	10
1.3 The Bernoulli Free Boundary Problem	11
1.3.1 Classical Shape Optimization Formulations of the Bernoulli Problem	13
1.3.2 New Shape Optimization Formulations of the Bernoulli Problem	15
1.4 Existence of an Optimal Solution to Shape Problems	19
1.4.1 Abstract Setting of Optimal Shape Problem subject to PDE Constraints	20
1.4.2 Existence of Optimal Solution to the Proposed Shape Problems	21
2 Shape Sensitivity Analyses	33
2.1 Tools for Shape Optimization	34
2.1.1 Two Methods for Domain Perturbation	34
2.1.2 Some Properties of the Perturbation of the Identity Operator	36
2.1.3 Some Identities from Tangential Calculus	39
2.1.4 Material and Shape Derivatives	40
2.2 Shape Derivative of J_1	45
2.2.1 The Minimax Formulation	45
2.2.2 The Shape Gradient of J_1	49

TABLE OF CONTENTS

2.3	Shape Derivative of J_2	55
2.3.1	The Shape Gradient of J_2	56
2.3.2	The Shape Hessian of J_2	59
2.4	Shape Derivative of J_3	63
2.4.1	The Shape Gradient of J_3	63
2.4.2	The Shape Hessian of J_3	66
2.4.3	The Shape Derivative of the Adjoint State	68
2.4.4	Symmetry of the Shape Hessian of J_3 at a Critical Shape	72
2.5	Coercivity Estimates for the Shape Hessians at the Optimal Solution	76
3	Numerical Analyses	79
3.1	Numerical Algorithm	80
3.1.1	The Sobolev Gradient Method	80
3.1.2	Step Size for the First-Order Method	81
3.1.3	The Boundary Variation Algorithm	83
3.1.4	Stopping Criteria	83
3.1.5	The Sobolev Newton Method	85
3.1.6	Step Size for the Second-Order Method	86
3.2	Numerical Examples	88
3.2.1	Examples for the First Proposed Shape Problem	90
3.2.2	Examples for the Second Proposed Shape Problem	108
3.2.3	Examples for the Third Proposed Shape Problem	120
4	Conclusion	139
A	Appendix	143
A.1	Embedding Theorems	143
A.2	Gâteaux Semiderivatives	144
	Bibliography	147

LIST OF FIGURES

FIGURE	Page
1.1 A $C^{1,1}$ -domain Ω with ψ_y a diffeomorphic map from \mathcal{N}_y to $\mathcal{B}(\mathbf{0}, 1)$	9
1.2 The domain Ω for the exterior (left) and interior (right) Bernoulli FBP	13
2.1 The action of T_t on a $C^{1,1}$ -domain	37
2.2 At first order, a <i>tangential vector field</i> \mathbf{V} (i.e., $\mathbf{V} \cdot \mathbf{n} = 0$) only results in a convection of the shape Ω , and it is expected that $dJ(\Omega)[\mathbf{V}] = 0$	43
3.1 Histories of mean radii (plot a) and descent step sizes (plot b) when $\mathcal{X} = H^1(\Omega_k), H_{\Gamma,0}^1(\Omega_k), L^2(\Sigma_k)$ in (3.3) with $\alpha = 0.01$ using the proposed formulation, running the algorithm for 300 seconds	91
3.2 Histories of mean radii (plot a) and their corresponding histories of standard deviations (plot b) when $\mathcal{X} = H^1(\Omega_k), H_{\Gamma,0}^1(\Omega_k), L^2(\Sigma_k)$ in (3.3) with $\alpha = 0.01$ using the classical Neumann-data tracking approach after 300 seconds of run time	92
3.3 Order of convergences of the algorithm when applying the proposed formulation (plots a and b) and when using the Neumann-data tracking approach (plots c and d) with $\alpha = 0.01$, employing the stopping condition (3.6) with $\text{Tol} = 10^{-5}$ and 10^{-3} for the first and second approach, respectively	95
3.4 Histories of Hausdorff distances using the proposed formulation with $\mathcal{X} = L^2(\Sigma_k)$ (plot a) and when applying the Neumann-data tracking approach with $\mathcal{X} = H^1(\Omega_k)$ for some values of α	96
3.5 The optimal free (or exterior) boundaries Σ^* using the proposed formulation	98
3.6 Optimal free (or exterior) boundaries obtained through the proposed formulation for Example 3.2.1.2 (the case where $\Gamma = \partial S$) when $\lambda = -1$ (plot a) and when $\lambda = -8$ (plot b)	99
3.7 Evolutions of the free boundary for the case $\lambda = -10$ when the proposed formulation is employed with $\alpha = 0.10$ (plot a) and when the Neumann-data tracking approach is applied with $\alpha = 0.10, 0.01$ (plots b , and c , respectively); d : direct comparison between the optimal free boundaries obtained through the proposed and the classical Neumann-data tracking approach when $\alpha = 0.10$	99
3.8 Convergence history of the cost function for Example 3.2.1.2 when $\lambda = -10$, applying the Neumann-data tracking approach with $\alpha = 0.10$	100

3.9 Evolutions of the free boundary for Example 3.2.1.3 when the proposed formulation is employed (plot **a**) and when the Neumann-data tracking approach is applied (plot **b**) where $\alpha = 0.10$ in both cases; **c**: direct comparison between the optimal free boundaries obtained through the proposed and the classical Neumann-data tracking approach when $\alpha = 0.10$; **d**: histories of cost values (*upper plot*) and Hausdorff distances (*lower plot*) obtained through the Neumann-data tracking approach corresponding to plot **b** 101

3.10 Evolutions of the free boundary corresponding to Example 3.2.1.4 when the proposed formulation is employed with $\alpha = 0.10, 0.25, 0.50$ (plots **a**, **c**, and **e**, respectively) and when the Neumann-data tracking approach is applied with $\alpha = 0.001, 0.010, 0.100$ (plots **b**, **d**, and **f**, respectively) 103

3.11 **a**: Convergence histories of the cost function for both the proposed and classical formulations with different values of α ; the histories of Hausdorff distances between Σ_k and the final computed free boundary Σ_M obtained through the proposed formulation, for each $\alpha = 0.10, 0.25, 0.50$ (plot **b**), and via the Neumann-data tracking approach, for each $\alpha = 0.001, 0.010, 0.100$ (plot **c**); **d**: direct comparison between the optimal free boundaries obtained through the proposed and the classical Neumann-data tracking approach . . . 104

3.12 Histories of mean radii (plot **a**) and Hausdorff distances (plot **b**) obtained through the application of the proposed formulation after running the algorithm for 60 seconds . . . 106

3.13 Evolutions of the free boundary for Example 3.2.1.6 when the proposed formulation is employed (plot **a**) and when the Neumann-data tracking approach is applied (plot **b**); **c**: direct comparison between the optimal free boundaries obtained through the proposed and the classical Neumann-data tracking approach; **d**: convergence history of the function (*upper plot*) and history of Hausdorff distances (*lower plot*) obtained through the Neumann-data tracking approach corresponding to plot **b** 107

3.14 Initial (*left*) and final (*right*) free boundaries for Example 3.2.2.1 with $\alpha = 0.1$ in (3.3) . . . 109

3.15 (a)-(b): Respective histories of cost values and Hausdorff distances via first-order method with $\alpha = 0.1$ in (3.3) and varying initial free boundary $\Sigma_0^i, i = 1, 2, 3$; (c)-(d): respective histories of cost values and Hausdorff distances via second-order method with $\alpha = 0.1$ in (3.3) and different initial free boundary $\Sigma_0^i, i = 1, 2, 3$ 110

3.16 *Forest-green solid lines*: Optimal free boundaries for Example 3.2.2.2 when $\lambda = -10, -9, \dots, -1$ (the outermost boundary corresponds to $\lambda = -1$ and the innermost boundary to $\lambda = -10$); *dashed-dot orange line*: initial guess for the free boundary 112

3.17 Results of Example 3.2.2.2 for $\lambda = -9$ when $\text{Tol} = 10^{-6}$ in the stopping condition (3.6) and $\alpha = 0.99$ in (3.3) 113

3.18 (a): Histories of descent step sizes for the proposed and classical formulations (with almost equal initial step size t_0 for the two formulations); (b): optimal free boundaries obtained when $\lambda = -9, -4, -1$ in Example 3.2.2.2 using the proposed and classical formulations with $\text{Tol} = 10^{-4}$ in the stopping condition (3.6) 115

3.19	(a)-(b): histories of free boundaries obtained through the proposed formulation with initial guess Σ_0^1 and Σ_0^3 , respectively, where $\text{Tol} = 10^{-6}$ in (3.6); (c)-(d): Histories of free boundaries obtained via the classical Kohn-Vogelius formulation with initial guess Σ_0^1 and Σ_0^3 , respectively, where $\text{Tol} = 10^{-4}$ in (3.6)	117
3.20	(a)-(b): corresponding histories of curvatures of the free boundaries obtained through the proposed formulation with initial guess Σ_0^1 and Σ_0^3 , respectively, shown in Figure 3.19a–3.19b; (c)-(d): Corresponding histories of curvatures of the free boundaries obtained via the classical Kohn-Vogelius formulation with initial guess Σ_0^1 and Σ_0^3 , respectively, shown in Figure 3.19c–3.19d	118
3.22	Results of Example 3.2.2.3 when $\lambda = -10, -4, -1$ for both of the proposed and classical formulations	122
3.23	(a)-(b): histories of free boundaries obtained through the proposed formulation with initial guess $C(\mathbf{0}, 0.6)$ and Σ_0^{ell} , respectively, where $\text{Tol} = 10^{-6}$ in (3.6); (c)-(d): histories of free boundaries obtained via the classical Kohn-Vogelius formulation with initial guess $C(\mathbf{0}, 0.6)$ and Σ_0^{ell} , respectively, where $\text{Tol} = 10^{-4}$ in (3.6)	123
3.24	(a)-(b): Corresponding histories of curvatures of the free boundaries obtained through the proposed formulation with initial guess Σ_0^1 and Σ_0^3 shown in Figure 3.23a–3.23b, respectively; (c)-(d): corresponding histories of curvatures of the free boundaries obtained via the classical Kohn-Vogelius formulation with initial guess Σ_0^1 and Σ_0^3 shown in Figure 3.23c–3.23d, respectively	124
3.25	Variation of the cost functionals $J_D, J_N, J_{KV}, J_1, J_2,$ and J_3 with respect to ρ	126
3.26	Histories of (a) mean radii, (b) error values and (c) cost values of Example 3.2.3.1 for values of $\alpha = 0.1, 0.3, 0.5$ (<i>left, middle</i> and <i>right</i> plots, respectively) using the gradient based algorithms A.1, B.1, and C.1	127
3.27	Histories of mean radii (<i>left plot</i>), error values (<i>mid plot</i>) and cost values (<i>right plot</i>) for Example 3.2.3.1 using the second-order shape optimization algorithms A.2, B.2 and C.2	128
3.28	Computational results of Example 3.2.3.2 using algorithms A.1, B.1, A.2 and B.2	129
3.29	Computational results of Example 3.2.3.3 using algorithms A.1, B.1, A.2 and B.2	131
3.30	Computational results of Example 3.2.3.4 using algorithms B.1, C.1, B.2 and C.2	133
3.31	Computational results of Example 3.2.3.4 using Algorithm B.2 and Algorithm C.2 with the full Newton step (i.e., $\tilde{\alpha} = 1.$)	135
3.32	Direct comparison of the free boundaries corresponding to Figure 3.31	136
3.33	Computational results of Example 3.2.3.4 using Algorithm B.2 and Algorithm C.2 with the scaled full Newton step (i.e., $\tilde{\alpha} = 0.2$)	137

LIST OF TABLES

TABLE	Page
3.1 Summary of results of the computational experiments when $\mathcal{X} = H^1(\Omega_k), H_{\Gamma,0}^1(\Omega_k), L^2(\Sigma_k)$ in (3.3) with $\alpha = 0.01$ using the proposed formulation	92
3.2 Summary of results of the computational experiments when $\mathcal{X} = H^1(\Omega_k), H_{\Gamma,0}^1(\Omega_k), L^2(\Sigma_k)$ in (3.3) with $\alpha = 0.01$ using the Neumann-data tracking approach	93
3.3 Summary of results of the computational experiments corresponding to Figure 3.4	96
3.4 Summary of computational results corresponding to the optimal free boundaries shown in Figure 3.5	98
3.5 Summary of computational results corresponding to Example 3.2.1.4	104
3.6 Summary of computational results corresponding to Example 3.2.1.5 using the proposed formulation terminated with the stopping rule (3.6) with $\text{Tol} = 10^{-4}$	106
3.7 Summary of computational results corresponding to Example 3.2.1.6	107
3.8 Convergence test toward exact solution using the proposed formulation via the modified H^1 -gradient method with initial free boundaries $\Sigma_0^i, i = 1, 2, 3$, and $\alpha = 0.10, 0.50, 0.99$ in (3.3)	108
3.9 Convergence test toward exact solution using the proposed formulation via the modified H^1 -Newton method with $\alpha = 0.1$ and different initial free boundary $\Sigma_0^i, i = 1, 2, 3$	109
3.10 Summary of computational results for an L-shaped fixed boundary $\Gamma = \partial S$ with $\lambda = -10, -9, \dots, -1$ where $\alpha = 0.99$ in (3.3) and $\text{Tol} = 10^{-6}$ in the stopping condition (3.6)	111
3.11 Computational results obtained via the classical formulation with $\text{Tol} = 10^{-6}$ in the stopping condition (3.6) for an L-shaped fixed boundary $\Gamma = \partial S$ when $\lambda = -9, -4, -1$ for different values of α in (3.3)	114
3.12 Comparison of computational results obtained through the proposed and classical formulations with $\text{Tol} = 10^{-4}$ in (3.6) for an L-shaped fixed boundary $\Gamma = \partial S$ when $\lambda = -9, -4, -1$ with almost the same initial step size t_0 for both formulations	114
3.13 Comparison of computational results obtained through the proposed and classical formulations for an L-shaped fixed boundary $\Gamma = \partial S$ when $\lambda = -10$ with almost the same initial step size t_0 for both formulations	116

3.14 Computational results obtained through the classical formulation with $\text{Tol} = 10^{-4}$ in (3.6) for an L-shaped fixed boundary $\Gamma = \partial S$ for $\lambda = -10, -8, -7, -6, -5, -3, -2$ with almost the same initial step size t_0 with respect to that of the proposed formulation shown in Table 3.10 118

3.15 Means and standard deviations (std) of the number of iterations, computing time and computing time per iteration for the proposed formulation with $\text{Tol} = 10^{-6}$ and classical formulation with $\text{Tol} = 10^{-4}$ in (3.6) 119

3.16 Summary of computational results of Example 3.2.2.3 for $\lambda = -10, -9, \dots, -1$ where the highlighted rows correspond to the results due to the proposed formulation 121

3.17 Means and standard deviations (std) of the number of iterations, computing time and computing time per iteration of the computational results shown in Table 3.16 121

The research described in this work has been carried out under the supervision of Hideyuki Azegami at Azegami Laboratory under the Department of Complex Systems Science. The investigation primarily focuses on the analysis and numerical studies of new shape optimization methods for solving free boundary problems, including shape identification problems, which was made possible through a Japanese Government (*Monbukagakusho*) scholarship.

Overview of the thesis

This thesis pays particular attention to state-of-the-art numerical techniques for solving free boundary problems in the framework of shape optimization. Therefore, this work considers the prototype problem of free boundary problems known as the Bernoulli problem (also called as Alt-Caffarelli problem in some literature). In this respect, new shape optimization reformulations of the Bernoulli problem are proposed as improvements to existing classical and standard formulations.

The objectives of this thesis

The main contribution of this research work is two-fold:

- First, we present three reformulations of the Bernoulli problem into shape optimization settings that have not been examined yet in the literature. The main point of departure for the first two formulations is the introduction of a new state problem associated with a classical boundary-data-tracking cost functional minimization approach and a standard energy-like error objective functional minimization problem. The third proposed formulation, on the other hand, consists of a new objective functional which basically tracks the L^2 mismatch at the *free* boundary between the computed Dirichlet boundary data of two auxiliary state problems. As a customary problem, the existence of optimal shape solutions to these shape problems is established through a C^1 -diffeomorphism of a uniform tubular neighborhood of the free boundary under a C^1 -regularity assumption on the unknown free boundary.
- Second, we offer a Lagrangian-like approach based on finite element methods to numerically solve various concrete numerical examples of the proposed shape optimization formulations of the Bernoulli problem. This is in contrast to the fixed-point approach, the level-set method, or the boundary element method which are commonly used numerical techniques in the

literature for solving the Bernoulli problem in the context of shape optimization. Towards this end, we design a novel gradient-based optimization procedure exploiting both the gradient and Hessian informations to numerically solve the new shape optimization problems. The novelty of our proposed iterative scheme lies in the practical application of the so-called Sobolev Newton method and in the use of appropriate formula for the step size of the algorithm. We point out that in the standard H^1 Newton method, the exact expression for the (shape) Hessian is used to regularized the descent vector. Here, however, we will only use the Hessian information at the solution of the free boundary problem in preconditioning the said vector. Because the selection of the step size is critical for the efficiency of the algorithm, we will couple our proposed first- and second-order gradient-based methods with a natural choice for the step size formula. We emphasize that the choice for the step size, especially in the case of the second-order method, is new to this work.

The structure of this thesis

The plan of the thesis is as follows:

Chapter 1 The first chapter gives a brief introduction to shape optimization and reviews the notion of free boundary problems. Essential notations, abbreviations, and necessary function spaces used throughout the thesis are gathered and introduced here. The class of Bernoulli problems, considered as prototype of free boundary problems, is then discussed. Its various shape optimization formulations in the classical setting are recalled and new formulations are presented. In this respect, different methods available to derive the so-called shape derivative of cost functions are reviewed. A short exposition of the theory about optimal shape problems in an abstract setting is also provided. The chapter ends by addressing the existence of optimal shape solutions for the new shape optimization formulations of the (exterior) Bernoulli problem.

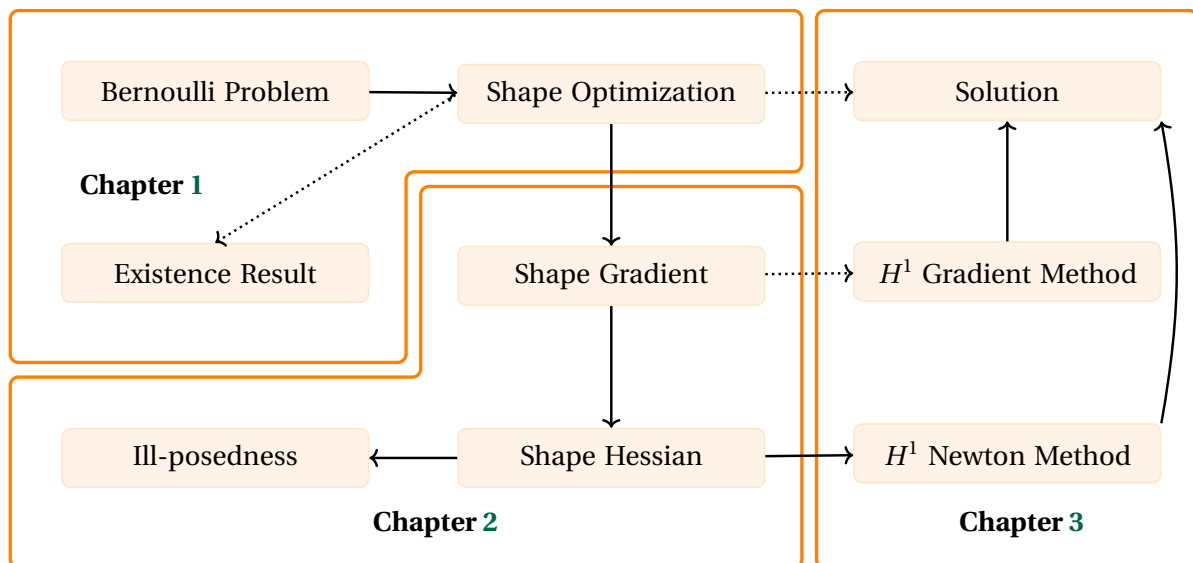
Chapter 2 The second chapter provides the essentials and tools for shape optimization problems. An overview of the development of shape calculus through the notion of the velocity (or speed) method and of the perturbation of the identity operator method are discussed. Some properties of the operator of the latter method are also presented. Moreover, several useful identities from tangential calculus are given. Formal definitions of material and shape derivatives of the states, as well as the definition of Eulerian shape derivatives, are also provided, including a fundamental result in shape optimization known as Hadamard-Zolésio structure theorem. The chapter then examines the sensitivity of the cost functionals with respect to domain variations. In this regard, the concept of shape derivatives via minimax differentiability of a Lagrangian due to Delfour and Zolésio is revisited and then applied to derive the first-order Eulerian shape derivative (or *shape gradient*) of the L^2 tracking functional. On the other hand, the chain-rule approach, also known as the material derivative method, is used to calculate the Eulerian shape derivatives (up to the second-order) of an energy-gap-type functional and a

new boundary objective functional. The computed shape derivatives of the shape functionals are characterized in accordance with the structure theorem.

Chapter 3 The third chapter deals with the numerical treatment of the proposed shape optimization formulations of the Bernoulli problem. It is demonstrated here how the computed first- and second-order shape derivatives of the cost functions can be used to devise an efficient boundary variation algorithm to solve concrete numerical examples of the shape optimization problems. The novel part of the optimization procedure put forward in the chapter is the utilization of the *shape Hessian* (i.e., the second-order Eulerian shape derivative) information at the solution of the Bernoulli free boundary problem, instead of using the exact boundary integral form of the expression, coupled with an original Newton step-size formula. Various numerical experiments are conducted to evaluate the efficiency of the proposed methods. Numerical results are compared with those obtained from classical formulations.

The final chapter, **Chapter 4**, gives the conclusion of this thesis. Some recommendations for future works related to the present investigation are also given.



The main contents of each chapter of the thesis can also be visualized in the diagram below.



Publications related to the thesis

The main results of this thesis are derived from the following papers:

- [99] J. F. T. Rabago and H. Azegami, *A second-order shape optimization algorithm for solving the exterior Bernoulli free boundary problem using a new boundary cost functional*, Computational Optimization and Application, 77(1):251–305 [doi](#)

- [98] J. F. T. Rabago and H. Azegami, *A new energy-gap cost functional approach for the exterior Bernoulli free boundary problem*, *Evolution Equations & Control Theory*, 8(4):785–824 
- [97] J. F. T. Rabago and H. Azegami, *An improved shape optimization formulation of the Bernoulli problem by tracking the Neumann data*, *Journal of Engineering Mathematics*, 117(1):1–29 

Communications related to the thesis

The results issued in this research work and other related findings were first presented through oral communications in the following scientific meetings:

- [2019 Dec 17–20] **On a Shape Optimization Approach to the Quadrature Surface Free Boundary Problem**, Mini-symposium on “Optimization Methods and Applications,” *The 7th Asia-Pacific Congress on Computational Mechanics (APCOM 2019)*, TICC, Taipei, Taiwan (with H. Azegami)
- [2019 Sep 9–11] **Shape Optimization Methods for Free Boundary Problems**, *Theoretical and Numerical Research on Iterative Methods for Free Boundary Problems*, RIMS, Kyoto University, Kyoto, Japan
- [2019 Jul 15–19] **A Newton Method in Sobolev Space for Solving Free Boundary Problems**, *9th International Congress on Industrial and Applied Mathematics (ICIAM 2019)*, Campus de Blasco Ibáñez, Universitat de València, València, Spain (with H. Azegami)
- [2019 Mar 3–4] **A New Energy-Gap Cost Functional Approach for the Exterior Bernoulli Free Boundary Problem**, *The Japan Society of Industrial and Applied Mathematics (JSIAM) 2019 Spring Meeting*, Tsukuba University, Ibaraki, Japan (with H. Azegami)
- [2018 Nov 27–30] **A Novel Shape Optimization Formulation of the Exterior Bernoulli Free Boundary Problem**, *The Computational Techniques and Applications Conference (CTAC) 2018*, Newcastle City Hall, Newcastle, NSW, Australia (with H. Azegami)
- [2018 Nov 5–9] **An Efficient Second-Order Method for the Numerical Resolution of the Exterior Bernoulli Problem via Partial Gradient**, *The 6th Asian Conference on Nonlinear Analysis and Optimization (NAO-Asia 2018)*, Okinawa Institute of Science and Technology Graduate University, Onna, Okinawa, Japan (with H. Azegami)
- [2018 Sep 3–5] **An Improved Shape Optimization Formulation of the Bernoulli Problem by Tracking the Neumann Data**, *The Japan Society of Industrial and Applied Mathematics (JSIAM) 2018 Annual Meeting*, Nagoya University, Nagoya, Aichi, Japan (with H. Azegami)

INTRODUCTION

Contents

	Page
1.1 An Overview of Shape Optimization	2
1.2 Notations, Abbreviations and Functions Spaces	5
1.2.1 Notations and Abbreviations	5
1.2.2 Continuous Functions	6
1.2.3 Lebesgue and Sobolev Spaces	8
1.2.4 Continuous Functions on Manifolds	9
1.2.5 Lebesgue and Sobolev Spaces on Manifolds	10
1.3 The Bernoulli Free Boundary Problem	11
1.3.1 Classical Shape Optimization Formulations of the Bernoulli Problem	13
1.3.2 New Shape Optimization Formulations of the Bernoulli Problem	15
1.4 Existence of an Optimal Solution to Shape Problems	19
1.4.1 Abstract Setting of Optimal Shape Problem subject to PDE Constraints	20
1.4.2 Existence of Optimal Solution to the Proposed Shape Problems	21

In this chapter, an overview of the ideas and principles of shape optimization are discussed as one can find in introductory texts about the subject (see, e.g., [43, 73, 106]). A separate chapter is provided for the essentials and tools in shape optimization.

1.1 An Overview of Shape Optimization

One of the main purpose of *shape optimization* is to provide a common and systematic framework for optimizing structures described by various possible physical or mechanical models. A typical problem is to modify an object's shape in such a way that the result is optimal with respect to a certain specification. This specification is usually some sort of an *objective functional* which then has to be minimized or maximized. Usually, the functional being solved depends on the solution of a given partial differential equation (PDE) defined on an unknown domain. One of the classical shape optimization problem is the so-called isoperimetric problem or more popularly known as Dido's problem in modern *calculus of variations*. The problem seeks to find, among all admissible domains with a given perimeter (this explains the term "isoperimetric"), the one whose Lebesgue measure is as large as possible. Equivalently, one could minimize the perimeter of a set among all admissible domains whose Lebesgue measure is specified [23]. A variant of this problem wherein a part of the boundary is fixed is often associated with Queen Dido as she dealt with, possibly, one of the first kind of an isoperimetric problem.

In recent years, the study of shape optimization has become increasingly popular in the academics and in industry, partly because many problems from real world applications can be recasted into shape optimization problems. In fact, the topic is quite indispensable in the design and construction of industrial structures such as drag reduction of cars, boats, aircrafts and spacecrafts [106].

In general, a shape optimization problem consists of two main ingredients: an *objective function* (and sometimes called a *shape function* or a *cost function*) $J(\Omega, u)$ with arguments $\Omega \subset \mathbb{R}^d$ and u , where the state variable $u := u(\Omega)$ satisfies an equality constraint $e(\Omega, u) = 0$. The goal then is to minimize the cost function $J : \mathcal{O}_{\text{ad}} \rightarrow \mathbb{R}$ over some admissible subset \mathcal{O}_{ad} of the larger collection of sets or shapes $\{\Omega : \Omega \subset \mathbb{R}^d\}$. In an abstract formulation, a typical problem can be stated as follows

$$(1.1) \quad \begin{aligned} & \text{minimize } J(\Omega, u) \text{ over } (\Omega, u) \in \mathcal{O}_{\text{ad}} \times \mathcal{X}(\Omega) \\ & \text{subject to } u = u(\Omega) \text{ solves } e(\Omega, u) = 0, \end{aligned}$$

where \mathcal{X} is usually a function space. The constraint $e(\Omega, u) = 0$ could be a PDE or systems of PDEs such as the Poisson equation with a Dirichlet condition. A specific \mathcal{O}_{ad} could be the set of all open subsets of a set $U \subset \mathbb{R}^d$.

Apart from its numerous applications in engineering and applied sciences, an interesting characteristic of shape optimization is that it involves different areas of mathematics, such as *differential geometry, partial differential equations, real and complex analysis, and topology*. However, the major difficulty with the study of the subject is the lack of a vector space structure for the set of sets $\{\Omega : \Omega \subset \mathbb{R}^d\}$. Therefore, one cannot actually apply the standard tools from real analysis such as the Fréchet or the Gâteaux derivative to examine (1.1). A workaround for this problem is to identify sets with functions; thereby giving the space of these functions a *Lie group* or *manifold structure* as detailed below; cf. [43].

In order to investigate the behavior of shape functions with respect to variations of domains, the concept of *shape calculus* was developed. The study of shape optimization then began in the 1970s where the first results involved *shape derivatives*, the *shape gradient*, and the associated *shape differential equation* that provides existence results for asymptotic evolution of a shape gradient flow [61]. In his 1973 seminal work [113] on shape optimization, Zolésio adopted the idea of *velocity method*, and in the 1980s, the subject of *shape sensitivity analysis*, which was first applied by Hadamard in [63] in his study of elastic plates, was then intensively studied by Sokołowski and Zolésio. A formal discussion of the mathematical methods used in shape sensitivity analysis, especially the notion of *material derivative*, is issued in [106].

Basically, in general, two types of domain perturbations are considered: the first strategy is known as the *method of perturbation of the identity operator*, and the second one is called the *velocity* or *speed method*. The latter method, which is based on the deformation generated by the flow of a velocity field, is more general than the former approach. However, it may be shown that the two methods of deforming a domain are actually equivalent [43, 106], and that using one or the other is rather a matter of preference. Therefore, in this thesis, the results with respect to shape sensitivity analyses will be given using the method of perturbation of the identity operator, but, of course, the speed method can also be applied.

Consider a shape function $J : \mathcal{O}_{\text{ad}} \rightarrow \mathbb{R}$ defined on some admissible set \mathcal{O}_{ad} and a set Ω contained in a larger set U . Then, the *reference* domain Ω is perturbed by an appropriate family of *diffeomorphisms* $T_t : \bar{U} \rightarrow \bar{U}$, $t \geq 0$, with $T_0 = I$ where I denotes the identity operator. The diffeomorphisms generates a family of perturbed domains $\Omega_t := T_t(\Omega)$, for $t \geq 0$, and one may define T_t as the flow of a vector field $\mathbf{V} : \bar{U} \rightarrow \mathbb{R}^d$. Here, of course, $\Omega = \Omega_0$ by convention. The *Eulerian semi-derivative* (if it exists) is then defined as the limit

$$dJ(\Omega)[\mathbf{V}] := \lim_{t \searrow 0} \frac{J(\Omega_t) - J(\Omega)}{t}.$$

The map $\mathbf{V} \rightarrow dJ(\Omega)[\mathbf{V}]$ is said to be *shape differentiable* if it is linear and continuous. In this case, the expression $dJ(\Omega)[\mathbf{V}]$ is called the *shape derivative* of J at Ω in the direction of the vector field \mathbf{V} . The well-known “structure theorem” of shape optimization states that under certain assumptions on the domain Ω and on the state variable u , the shape derivative is a distribution acting on the normal part $\mathbf{V} \cdot \mathbf{n}$ of the perturbation field \mathbf{V} on the boundary $\partial\Omega$. In most cases, when the boundary possesses enough regularity, the shape derivative dJ may be written in boundary integral form

$$(1.2) \quad dJ(\Omega)[\mathbf{V}] = \int_{\partial\Omega} g(\Omega) \mathbf{n} \cdot \mathbf{V} \, d\sigma,$$

where $g(\Omega) : \partial\Omega \rightarrow \mathbb{R}$ is usually the restriction of a function defined in a neighborhood of $\partial\Omega$. The boundary integral (1.2) is viewed as the canonical form of shape derivative of shape functionals in shape optimization literature (see Theorem 2.1.7).

For *state constrained* shape optimization problems, where the state is a solution to a system of PDEs, the shape differentiability may be difficult to prove depending on the state system. Nevertheless, several methods are available in the literature to derive the shape derivative of a given

cost functional and one procedure is as follows One may express the cost function $g(z)$ (z being an element of a topological vector space) of PDE constrained shape optimization problems as a minimax of a Lagrangian function \mathcal{L} taken over vector spaces \mathcal{X} and \mathcal{Y} , i.e.,

$$g(z) = \min_{x \in \mathcal{X}} \max_{y \in \mathcal{Y}} \mathcal{L}(z, x, y).$$

The shape differentiability problem of the cost function is then transported to the differentiability of the minimax. In this regard, a theorem due to Correa and Seeger [33] provides a direct result on the differentiability of $g(z)$, where $z \in \mathcal{Z}$, \mathcal{Z} a locally convex space, and $(x, y) \in \mathcal{X} \times \mathcal{Y}$, where \mathcal{X} and \mathcal{Y} are two Hausdorff topological spaces. Because spaces of shapes or domains are not locally convex spaces, Delfour and Zolésio [38] reformulated the hypotheses of the said theorem to make them readily applicable to the computation of the shape derivative.

Another approach which may be used to derive the shape differentiability is the so-called *chain rule approach*. In this method, the material derivative which can be interpreted as the derivative of the state with respect to the domain is introduced to derive the shape differentiability. This derivative only appears in an intermediate step and is not actually present in the final expression for the shape derivative of the cost functional. The term material derivative originates from continuum mechanics where it describes the time rate of change of some physical quantity, such as the mass, for a material element subjected to a time dependent velocity field. From the optimal control point of view this is nothing but the derivative of the control-solution operator, where the control is the domain and the solution is some function solving a PDE. Here, it is worth to mention that the minimax formulation mentioned previously actually has an advantage over the chain rule approach because the former provides the shape derivative of cost functionals bypasses the computation of the expressions for the shape and material derivative of the states though the introduction of appropriate adjoint variables.

Other methods which may be used to prove the existence of the shape derivative of a given cost functional are the following:

- Another formal approach which is often used to derive the boundary expression is due to C ea [29]. This method, now popularly known as *C ea's Lagrange method*, uses the same Lagrangian as in the minimax formulation. However, it requires that the shape derivatives of the state and the adjoint equation exist and belong to the solution space of the PDE. In addition, the method has to be used with caution because it may yield the wrong formula, and there are some instances where the method actually fails [94].
- In a quite recent paper [79], Ito, Kunisch and Peichl proposed a rigorous approach, now known as the *rearrangement method*, to derive the shape derivative of a cost functional. This method allows to prove the shape differentiability under the assumption that the domain-solution operator is H older continuous with an exponent bigger than 1/2 and admits a second-order expansion with respect to the unknown. Moreover, the method does not need the state or the cost to be convex but requires a first-order expansion of the PDE and cost function with respect to the unknown such that the remainder vanishes with order two.

- In [108], Sturm proposed an improvement of the minimax formulation. This new method does not require a saddle point assumption when the function \mathcal{L} is a Lagrangian (i.e., a sum of a utility function and a linear penalization of the state equation), and the novelty of the approach is to replace the usual adjoint state equation by an averaged adjoint state equation. For problems where the function is a Lagrangian, this result allows one to carry out shape sensitivity analyses for a very broad class of shape optimization problems involving linear, semi-linear and even quasi-linear PDEs. Finally, we mention that there is an interesting *penalization method* introduced in [39].

In this thesis, we will use the minimax formulation as well as the chain rule approach to prove the shape differentiability of the cost functions that will be introduced in subsection 1.3.2. The cost functions that will be examined here actually serve as criteria for the shape optimization reformulations of the *Bernoulli free boundary problem* which is the main topic of this thesis. Before we concentrate on the Bernoulli problem itself (see Section 1.3), we first introduce the necessary function spaces that will be used in our discussion.

1.2 Notations, Abbreviations and Functions Spaces

In this section, we will introduce and give a rough discussion of the function spaces necessary for the weak formulation of elliptic boundary value problems and for the boundary transformations used in the investigation of the shape optimization problems issued in this thesis. The notations, definitions, and results stated in this section can be found mostly in Chapter 2 of [43]. For further discussions of the topics, see, for instance, [4, Chapter 2–4], [95, Chapters 3 and 4] and [102, Chapter 2].

We first list below all symbols, abbreviations and notations that are frequently used in the thesis. These are, of course, standard and will also be recalled occasionally in the subsequent parts of the thesis for the readers convenience.

1.2.1 Notations and Abbreviations

$\mathbb{R}, \mathbb{N}, \mathbb{N}_0$	real numbers, natural numbers, non-negative integers
d	dimension of a space
\mathbb{R}^d	d - times product of \mathbb{R}
BVP(s)	boundary value problem(s)
PDE(s)	partial differential equation(s)
Ω	a bounded, open connected subset of \mathbb{R}^2 of class $C^{k,l}$
$\partial\Omega$	boundary of Ω
$\bar{\Omega}$	closure of Ω , i.e. $\bar{\Omega} = \Omega \cup \partial\Omega$
U	a $C^{k,l}$ domain in \mathbb{R}^d , hold-all or universal domain
$\det A$	determinant of a matrix A

$A^{-1}, A^\top, A^{-\top}$	inverse, transpose and inverse traspose of a matrix A
T_t	perturbation of the identity operator
DT_t	Jacobian of the transformation T_t
I	identity operator
H, H'	Hilbert space, dual of the Hilbert space H
$\ \cdot\ _H$	norm in space H
\mathbf{n}	the outward unit normal vector, $\mathbf{n} := (n_1, n_2)$ in \mathbb{R}^2
$\boldsymbol{\tau}$	the unit tangent vector
$\nabla\varphi$	gradient of a scalar function φ
$\nabla\varphi \cdot \mathbf{n}$	the normal derivative a scalar function φ ; also expressed here as $\partial_{\mathbf{n}}\varphi$
$\nabla_{\Sigma}\varphi$	tangential gradient of a scalar function φ
$\mathbf{V}, \hat{\mathbf{V}}$	autonomous (time-independent), non-autonomous (time-dependent) velocity field
$D\mathbf{V}$	Jacobian of a vector field \mathbf{V}
$\operatorname{div}_{\Sigma}\mathbf{V}$	tangential divergence of a vector field \mathbf{V}

Also, for our convenience, we will use the notation “ \lesssim ” throughout the thesis. This means that if $P \lesssim Q$, then there exists some constant $c > 0$ such that $P \leq cQ$. Obviously, $Q \gtrsim P$ is defined as $P \lesssim Q$. Meanwhile, the notation “ $P \sim Q$ ” means that “ $P \lesssim Q$ and $P \gtrsim Q$.”

1.2.2 Continuous Functions

Let $U \subset \mathbb{R}^d$ be an (open) bounded domain. We denote by $C(U) := C^0(U)$ the set of functions $\varphi : U \rightarrow \mathbb{R}$ continuous in U . By $C^k(U)$, with $k \in \mathbb{N}_0$, we denote the space of k -times continuously differentiable functions in U ; that is,

$$C^k(U) := \{\varphi \in C(U) : D^{\alpha}\varphi \in C(U) \text{ for all } \alpha, |\alpha| \leq k\},$$

where α is multi-index: $\alpha := [\alpha_1, \alpha_2, \dots, \alpha_d] \in [\mathbb{N}_0]^d$, of length $|\alpha| := \alpha_1 + \alpha_2 + \dots + \alpha_d$, and the partial derivative operator D^{α} is defined as

$$D^{\alpha}\varphi := \frac{\partial^{|\alpha|}}{\partial x_1^{\alpha_1} \partial x_2^{\alpha_2} \dots \partial x_d^{\alpha_d}} \varphi, \quad \frac{\partial^0}{\partial x_i^0} \varphi := \varphi.$$

For $k \in \mathbb{N}_0$, the set of k -times continuously differentiable functions with compact support in U is denoted as

$$C_0^k(U) := \{\varphi \in C^k(U) : \operatorname{supp} \varphi := \overline{\{x \in U : \varphi(x) \neq 0\}} \subset U \text{ is compact}\}.$$

Accordingly, we define $C^{\infty}(U) := \bigcap_{k \in \mathbb{N}} C^k(U)$, $C_0^{\infty}(U) := \bigcap_{k \in \mathbb{N}} C_0^k(U)$, and denote $\mathcal{D}^k(U)$ as the space of C^k functions from U to \mathbb{R}^d with compact support contained in \mathbb{R}^d .

Definition 1.2.1. We say that a function φ is called uniformly continuous on a set $U \subset \mathbb{R}^d$, and denote $\varphi \in C(U)$, if for every $\varepsilon > 0$ there exists $\delta > 0$ such that for all points $x, y \in U$ satisfying $|x - y| < \delta$ it holds that $|\varphi(x) - \varphi(y)| < \varepsilon$.

By $C(\bar{U}) := C^0(\bar{U})$ we understand functions bounded and uniformly continuous in U , and are continuously extensible to its boundary $\partial\Omega$. For $k \in \mathbb{N}_0$, we also introduce the complete (i.e. Banach) spaces

$$C^k(\bar{U}) := \left\{ \varphi \in C(\bar{U}) : D^\alpha \varphi \in C(\bar{U}) \text{ for all } \alpha, |\alpha| \leq k \right\},$$

equipped with the norm

$$\|\varphi\|_{C^k(\bar{U})} := \sum_{|\alpha| \leq k} \max_{x \in \bar{U}} |D^\alpha \varphi(x)|.$$

Here, we identify $D^\alpha \varphi$ with its extension to \bar{U} . In accordance with this definition, we denote $C^\infty(\bar{U}) := \bigcap_{k \in \mathbb{N}} C^k(\bar{U})$ and $C_0^\infty(\bar{U}) := \bigcap_{k \in \mathbb{N}} C_0^k(\bar{U})$.

Definition 1.2.2. We have the following definitions.

Equicontinuous A set $K \subset C(\bar{U})$ is called equicontinuous if the parameter $\delta := \delta(\varepsilon)$ in Definition 1.2.1 can be chosen independently of $\varphi \in K$.

Relative Compactness Let \mathcal{X} denote a metric space. The set $\mathcal{Y} \subset \mathcal{X}$ is relatively compact in \mathcal{X} if for every sequence $\{y_n\} \subset \mathcal{Y}$ there exists a subsequence $\{y_{n_k}\}$ and an element $y \in \mathcal{X}$ such that $y_{n_k} \rightarrow y$ in \mathcal{X} .

We have the following classical compactness theorem (see, e.g., [43, Theorem 2.4, p. 65]).

Theorem 1.2.1 (Arzelà-Ascoli). A set $K \subset C(U)$ is relatively compact if and only if it is bounded and equicontinuous.

For the proof of this standard result, we refer the readers, for example, to [95].

Using an inductive argument, it can also be shown that a set $K \subset C^k(\bar{U})$ is relatively compact if and only if it is bounded in $C^k(\bar{U})$ and the sets $K^s := \{D^\alpha \varphi : \varphi \in K, |\alpha| = s\}$ are equicontinuous for all $s \leq k$.

Lastly, we define the Banach space of Hölder continuous functions for $k \in \mathbb{N}_0, \mu \in (0, 1]$,

$$C^{k,\mu}(\bar{U}) := \left\{ \varphi \in C^k(\bar{U}) : [\varphi]_{\alpha,k} < \infty \text{ for all } \alpha, |\alpha| \leq k \right\},$$

with norm

$$\|\varphi\|_{C^{k,\mu}(\bar{U})} := \|\varphi\|_{C^k(\bar{U})} + \sum_{\alpha, |\alpha|=k} [\varphi]_{\alpha,k}, \quad [\varphi]_{\alpha,k} := \sup_{\substack{x,y \in \bar{U} \\ x \neq y}} \frac{|D^\alpha \varphi(x) - D^\alpha \varphi(y)|}{|x-y|^\mu}.$$

The set $C^{0,1}(\bar{U})$ is the space of Lipschitz continuous functions.

1.2.3 Lebesgue and Sobolev Spaces

For $1 \leq p \leq \infty$ we define the Lebesgue spaces

$$L^p(U) := \{\varphi \text{ is measurable on } \Omega : \|\varphi\|_{L^p(\Omega)} < \infty\}$$

with

$$\|\varphi\|_{L^p(U)} := \left(\int_U |\varphi(x)|^p dx \right)^{1/p}, \quad \|\varphi\|_{L^\infty(U)} := \operatorname{ess\,sup}_U |\varphi|.$$

Equipped with the respective norms, the spaces $L^p(U)$ and $L^\infty(U)$ are Banach spaces. In the special case, $p = 2$, the $L^2(U)$ space with the inner product

$$\langle \varphi, \psi \rangle_{L^2(U)} := \int_U \varphi(x) \psi(x) dx$$

inducing the $\|\cdot\|_{L^2(U)}$ norm, is a Hilbert space. Additionally, we define the space $L^1_{\text{loc}}(K)$ of functions $\varphi \in L^1(K)$ for any compact subset $K \subset U$.

Now, to define weak solutions to boundary value problems (BVPs), it is necessary to introduce the Sobolev spaces. On $C^\infty(\bar{U})$, $C^\infty_0(\bar{U})$ we define for $p \in [1, \infty)$ and $m \in \mathbb{N}$ the Sobolev norms

$$\|\varphi\|_{W^{m,p}(U)} := \left(\sum_{\alpha, |\alpha| \leq m} \|D^\alpha \varphi\|_{L^p(U)}^p \right)^{1/p}, \quad \|\varphi\|_{W^{m,\infty}(U)} := \max_{\alpha, |\alpha| \leq m} \|D^\alpha \varphi\|_{L^\infty(U)}.$$

The spaces $W^{m,p}(U)$ and $W^{m,p}_0(U)$ with $p \in [1, \infty) \cup \{\infty\}$ are the completions of $C^\infty(\bar{U})$ and $C^\infty_0(\bar{U})$ with respect to the norms $\|\cdot\|_{W^{m,p}(U)}$ and $\|\cdot\|_{W^{m,\infty}(U)}$, respectively (see also Appendix A).

For $p \in [1, \infty)$ and $m = k + s$ with $k \in \mathbb{N}_0$, $s \in (0, 1)$, the definition of $W^{m,p}(U)$ can be extended by considering the Sobolev–Slobodeckij norms

$$\|\varphi\|_{W^{m,p}(U)} := \left(\|\varphi\|_{W^{k,p}(U)} + |\varphi|_{m,p,U} \right)^{1/p},$$

with the semi-norm

$$|\varphi|_{m,p,U} := \left(\sum_{\alpha, |\alpha|=k} \int_U \int_U \frac{|D^\alpha \varphi(x) - D^\alpha \varphi(y)|^p}{\|x-y\|^{d+sp}} dy dx \right)^{1/p}.$$

For convenience, we denote the $L^2(U)$ based Hilbert spaces, for example, $H^m(U) := W^{m,2}(U)$, with the inner product $\langle \varphi, \psi \rangle_{H^m(U)} := \sum_{\alpha, |\alpha|=k} \langle D^\alpha \varphi, D^\alpha \psi \rangle_{L^2(U)}$ for $m \in \mathbb{N}$, and

$$\begin{aligned} \langle \varphi, \psi \rangle_{H^m(U)} &:= \sum_{\alpha, |\alpha| \leq k} \langle D^\alpha \varphi, D^\alpha \psi \rangle_{L^2(U)} \\ &+ \sum_{\alpha, |\alpha|=k} \int_U \int_U \frac{(D^\alpha \varphi(x) - D^\alpha \varphi(y))(D^\alpha \psi(x) - D^\alpha \psi(y))}{\|x-y\|^{2+sp}} dy dx, \end{aligned}$$

for $m = k + s$ with $k \in \mathbb{N}_0$ and $s \in (0, 1)$. The above inner products induce the norm $\|\cdot\|_{W^{m,2}(U)}$ for $m = k + s$ with $k \in \mathbb{N}_0$ and $s \in (0, 1)$ for $p = 2$. For further discussion of Lebesgue and Sobolev spaces, we refer the readers, for instance, to [4, Chapter 2 and 3] and [95, Chapter 2].

1.2.4 Continuous Functions on Manifolds

Here we are primarily interested in $C^{k,1}$ -domains, particularly in the case when $k \in \{1, 2\}$. These domains of interest are bounded and connected subsets of a bigger set U . This set U is also a bounded connected $C^{k,1}$ domain and is sometimes called the *universal* or the *hold-all domain* in the literature. The smoothness of these domains can be defined in the following sense. For a point $x = (x_1, x_2, \dots, x_n) \in \mathbb{R}^d$, let $\mathbf{x} = (x_1, x_2, \dots, x_{n-1}) \in \mathbb{R}^{d-1}$ so as to write $x = (\mathbf{x}, x_n)$. Consider the unit ball $\mathcal{B}_1 := \mathcal{B}(\mathbf{0}, 1)$ and its subsets

$$\mathcal{B}_1^+ := \{x \in \mathcal{B}_1 : x_n > 0\}, \quad \mathcal{B}_1^0 := \{x \in \mathcal{B}_1 : x_n = 0\}, \quad \mathcal{B}_1^- := \{x \in \mathcal{B}_1 : x_n < 0\}.$$

With these constructed set, a $C^{k,\mu}$ -domain is formally defined as follows (see, e.g., [43, Definition 3.1, p. 68]).

Definition 1.2.3. A domain $\Omega \subset \mathbb{R}^d$ with a non-empty boundary $\partial\Omega$ is called a $C^{k,\mu}$ -domain, where $0 \leq k, 0 < \mu \leq 1$, if for every $y \in \partial\Omega$ there exists a neighborhood \mathcal{N}_y of y and a $C^{k,\mu}$ diffeomorphic map $\psi_y : \mathcal{N}_y \rightarrow \mathcal{B}_1 := \mathcal{B}(\mathbf{0}, 1)$ such that

$$\psi_y(\mathcal{N}_y \cap \Omega) = \mathcal{B}_1^+, \quad \psi_y(\mathcal{N}_y \cap \partial\Omega) = \mathcal{B}_1^0, \quad \psi_y(\mathcal{N}_y \cap \Omega^c) = \mathcal{B}_1^-.$$

We illustrate the definition for a $C^{1,1}$ -domain Ω in two-dimensional space and the configuration of the diffeomorphic mapping ψ_y is shown in Figure 1.1. A $C^{0,\mu}$ domain is called an μ -Lipschitz

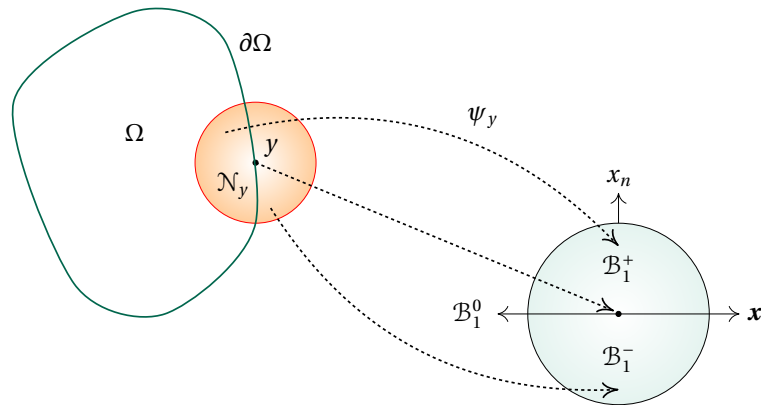


Figure 1.1: A $C^{1,1}$ -domain Ω with ψ_y a diffeomorphic map from \mathcal{N}_y to $\mathcal{B}(\mathbf{0}, 1)$

domain, and, in this case, the map ψ_y is Lipschitz-continuous with Lipschitz constant μ [31].

Remark 1.2.1. It can be shown that a domain $\Omega \subset \mathbb{R}^d$ is μ -Lipschitz if and only if it satisfies the so-called ε -cone property [30, Definition 1].

The ε -cone property of Lipschitz domains will be essential to our analysis regarding the *existence of optimal shape solution* to the shape optimization formulations of the Bernoulli problem that will be introduced in Section 1.3.2.

1.2.5 Lebesgue and Sobolev Spaces on Manifolds

The Lebesgue spaces on boundaries of domains $L^p(\partial U)$ can also be defined following the definition for continuous functions. However, we skip the details and simply provide some facts because we are only interested in the case $p = 2$. The space $L^2(\partial U)$ is a Hilbert space with the inner product

$$\langle \varphi, \psi \rangle_{L^2(\partial U)} := \int_{\partial U} \varphi(x) \psi(x) \, d\sigma$$

inducing the norm $\| \cdot \|_{L^2(\partial U)} := \left(\int_{\partial U} | \cdot |^2 \, d\sigma \right)^{1/2}$.

For $s \in (0, 1)$, the Sobolev–Slobodeckij norm is defined as

$$\| \varphi \|_{H^s(\partial U)} := \left(\| \varphi \|_{L^2(\partial U)} + | \varphi |_{s,2,\partial U} \right)^{1/2},$$

with the semi-norm

$$| \varphi |_{s,2,\partial U} := \left(\int_{\partial U} \int_{\partial U} \frac{|\varphi(x) - \varphi(y)|^2}{\|x - y\|^{d-1+2s}} \, d\sigma_x \, d\sigma_y \right)^{1/2},$$

where d is, of course, the dimension of U .

For $s < 0$, we introduce the dual space $H^s(\partial U) := [H^{-s}(\partial U)]^*$.

Theorem 1.2.2. For $k \in \mathbb{N}$, $\mu \in (0, 1]$, $0 \leq s \leq k$, and $C^{k-1,\mu}$ domain it holds

$$H^s(\partial U) \hookrightarrow L^2(\partial U) = [L^2(\partial U)] \hookrightarrow H^{-s}(\partial U).$$

In above theorem, both embeddings are continuous and dense. Moreover, the equality of $L^2(\partial U)$ and its dual is understood in Riesz' sense. In addition, the previous result actually refers to the so-called Gelfand triples. For details, see, for example, [102, Section 2.1.2.4, pp. 29–30].

Theorem 1.2.2 ensures that the inner product $\langle \cdot, \cdot \rangle_{L^2(\partial U)}$ can be continuously extended to the duality pairing on $H^{-s}(\partial U) \times H^s(\partial U)$; that is,

$$\langle \varphi, \psi \rangle_{L^2(\partial U)} := \langle \varphi, \psi \rangle_{H^{-s}(\partial U) \times H^s(\partial U)} = \lim_{n \rightarrow \infty} \int_{\partial U} \varphi_n(x) \psi(x) \, d\sigma$$

for a sequence $\{\varphi_n\} \subset L^2(\partial U)$, $\varphi_n \rightarrow \varphi$ in the standard dual norm of H^{-s} :

$$\|\varphi\|_{H^{-s}(\partial U)} := \sup_{\psi \in H^s(\partial U) \setminus \{0\}} \frac{\langle \varphi, \psi \rangle_{\partial U}}{\|\psi\|_{H^s(\partial U)}}.$$

For further details about Sobolev spaces on boundaries (or surfaces) and their embedding properties, we refer the readers, for example, to [102, Section 2.4 and 2.5].

Finally, we end this section with the definition of the *trace operator* (see, e.g., [87, p. 100] or [102, Section 2.6]) and a remark.

Proposition 1.2.1. Let $\Omega \subset \mathbb{R}^d$ denote a Lipschitz domain. Then, there exists a unique linear continuous mapping

$$\gamma : H^m(\Omega) \rightarrow H^{m-1/2}(\partial\Omega)$$

satisfying

- (i) $\gamma(\varphi) = \varphi|_{\partial\Omega}$, for any $\varphi \in C(\overline{\Omega}) \cap H^m(\Omega)$, and
- (ii) $\|\gamma(\varphi)\|_{H^{m-1/2}(\partial\Omega)} \lesssim \|\varphi\|_{H^m(\Omega)}$.

The function $\gamma^0(\varphi) = \varphi|_{\partial\Omega}$, $\gamma^0 := \gamma : H^1(\Omega) \rightarrow H^{1/2}(\partial\Omega)$ is called the (Dirichlet) trace of the function $\varphi \in H^1(\Omega)$. For the proof of the previous proposition, see, for example, [87, Theorem 3.37, p. 102].

Remark 1.2.2. Due to a result of Rademacher (see, e.g., [102, Theorem 2.7.1] or [112, Theorem 11A, p. 272]), for Lipschitz domain $\Omega \subset \mathbb{R}^d$, the unit outward normal vector \mathbf{n} can be defined almost everywhere on $\partial\Omega$ and $\mathbf{n} \in \mathbf{L}^\infty(\partial\Omega) := [L^\infty(\partial\Omega)]^d$. For $\varphi \in H^2(\Omega)$, we can define the normal derivative as

$$\gamma^1(\varphi) := \langle \boldsymbol{\gamma}^0(\nabla\varphi), \mathbf{n} \rangle \in L^2(\partial\Omega) = [L^2(\partial\Omega)]^* \hookrightarrow H^{-1/2}(\partial\Omega),$$

where the trace operator $\boldsymbol{\gamma}^0$ is, of course, understood as a component-wise application of γ^0 .

Throughout the thesis, instead of $\gamma(\varphi)$, we simply write $\varphi|_{\partial\Omega}$.

For further discussion about integer order Sobolev spaces on Lipschitz domains, we refer to the classical textbook by Calderón [25] or by Stein [107]. For the case of fractional order Sobolev spaces on Lipschitz domains, we refer to the book by McLean [87].

1.3 The Bernoulli Free Boundary Problem

Free boundary problems (FBPs) are usually PDEs which are to be solved for both unknown state function(s) and an unknown domain. The phrase “free boundary” is used because the boundary

of the domain or a part of it is not known in advance, and hence, *a priori*. Usually this terminology is used to indicate that the boundary is stationary and a steady state problem exists but it is also sometimes used to refer to the so-called *moving boundaries*. However, moving boundary problems typically refer to problems that vary with time. For various biological and physical phenomena modeled by FBP, one is referred to [26, 34, 57, 58, 110].

Now, in particular, if one is looking for a domain Ω on which a harmonic function u satisfies a linear homogenous Dirichlet condition and a nonhomogenous Neumann boundary condition, then one is solving the so-called *Bernoulli free boundary problem*. The problem is considered as the prototype of a stationary FBP and is called in some literature as the *Alt-Caffarelli problem* (see [5]). The name Bernoulli, as mentioned by Shargorodsky and Toland in [103, p. 1], was originally associated to problems in hydrodynamics. In fact, Bernoulli problems find their origin in the description of free surfaces for ideal fluids [59]. There are, however, numerous other applications leading to similar formulations. More precisely, the problem arises in the context of optimal design related to insulation minimizing the current or heat leakage [2, 55], or in galvanization, where the goal is to design an electrode layered with metal coating of constant thickness across a given object [34, 85]. The problem also appears in the context of electro chemistry and electro statics (see, e.g., [57]). For more industrial applications, see [54].

The Bernoulli problem is classified as *exterior* and *interior* [56]. In the exterior problem, a bounded and connected domain $\omega \subset \mathbb{R}^2$ with a *fixed boundary* $\Gamma := \partial\omega$ and a constant $\lambda < 0$ are known or given. The task is to find a bounded connected domain $D \subset \mathbb{R}^2$ with a *free boundary* $\Sigma := \partial D$, D contains the closure of ω , and an associated state function $u := u(\Omega)$, where $\Omega = D \setminus \bar{\omega}$, such that the following overdetermined system of partial differential equations (PDEs) is satisfied:

$$(1.3) \quad \begin{cases} -\Delta u = 0 & \text{in } \Omega, \\ u = 1 & \text{on } \Gamma, \\ u = 0 & \text{on } \Sigma, \\ \frac{\partial u}{\partial \mathbf{n}} = \lambda & \text{on } \Sigma. \end{cases}$$

In this formulation, \mathbf{n} denotes the outward unit normal vector to the free boundary Σ . For an illustration of the domain Ω and its boundaries, refer to Figure 1.2.

Instead of the Neumann condition on the free boundary, the authors in [17, 53] consider a condition of the gradient of the state function u which results to the exterior Bernoulli FBP:

$$(1.4) \quad -\Delta u = 0 \text{ in } \Omega, \quad u = 1 \text{ on } \Gamma, \quad u = 0 \quad \text{and} \quad |\nabla u| = \text{constant} (< 0) \text{ on } \Sigma.$$

The positivity of the Dirichlet data implies that $u > 0$ in Ω . Also, since $u = 0$ on Σ , all tangential derivatives of u along Σ are actually zero. Hence, the gradient has only component in the normal direction which eventually leads to the identity $|\nabla u| = -\nabla u \cdot \mathbf{n}$ on Σ (cf. [53]). This means that (1.4) can be simplified into (1.3). On the other hand, in the *interior Bernoulli problem*, the boundaries Γ

and Σ are reversed with $u = 0$ on Γ , and $u = 1$ and $\partial_{\mathbf{n}}u = \lambda$, where $\lambda > 0$, on Σ . More exactly, we have

$$(1.5) \quad -\Delta u = 0 \text{ in } \Omega, \quad u = 0 \text{ on } \Gamma, \quad u = 1 \text{ and } \frac{\partial u}{\partial \mathbf{n}} = \lambda \text{ on } \Sigma,$$

where \mathbf{n} is the interior unit normal to Σ (see right drawing in Figure 1.2). These aforementioned problems can be posed for the p -Laplacian [3] but here we mainly focus on problems (1.3) and (1.5). The existence of solutions to the Bernoulli problem can be established by means of sub and

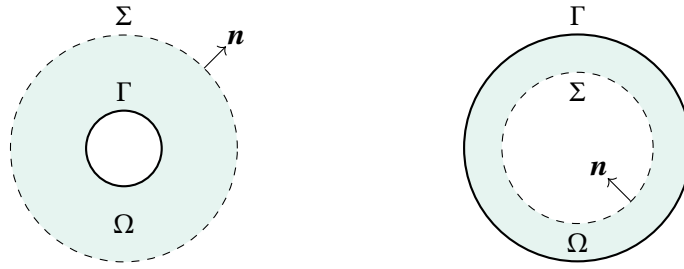


Figure 1.2: The domain Ω for the exterior (left) and interior (right) Bernoulli FBP

supersolutions [17] or through variational methods in the context of shape optimization [5]. The former approach uses the idea of conformal mapping and extremal length while the latter technique considers the problem of minimizing a certain cost functional over all elements of the solution space. There is also another more recent approach that was offered in [57] wherein the notion of capacity of a subdomain is introduced. The existence of solution is then proved via *Poincaré's variational formula* which was eventually utilized in minimizing the capacity among sets of equal volume.

Generally, the Bernoulli problem has *no unique solution*. In the case of exterior problem, it is known that the problem admits elliptic solution for any $\lambda < 0$ [57] and uniqueness can be guaranteed in the context of convex domains (see [57, Section 6.3] and [74]). In addition, the optimal free boundary in this case is actually $C^{2,\mu}$ regular (see [76, Theorem 1.1]). On the contrary, the interior case need not have a solution for every domain ω and for every positive constant $\lambda > 0$. Even so, at least one solution exists for the more general case of p -Laplacian when ω is a convex domain with smooth (at least C^1) boundary and λ is not less than the *Bernoulli constant* $\lambda^*(\Omega) > 0$ [75]. Moreover, uniqueness of solution holds for the interior case when $\lambda = \lambda^*(\Omega)$ [27].

1.3.1 Classical Shape Optimization Formulations of the Bernoulli Problem

Shape optimization is basically an area of study in the field of optimal control theory wherein the main objective, as we have mentioned already, is to determine an optimal shape that minimizes a particular cost functional subject to some given constraints. It is an infinite dimensional optimization where the variable is no longer a scalar, a vector or a function, but rather a geometric domain which makes the sensitivity analysis nontrivial. Methods of shape optimization can be applied to solve the Bernoulli FBP. We emphasize that, because the conditions imposed on the free boundary Σ is overdetermined, the problem is actually ill-posed. To circumvent this issue and solve the problem, one can actually

rewrite the FBP into a shape optimization setting which involves now a well-posed state equation (or set of well-posed state equations). This can be done in several ways. A common approach is to choose one of the boundary conditions on the free boundary to obtain a well-posed state equation, and then track the remaining boundary data in a least-squares sense. Such formulation has been carried-out in several previous investigations; see, for instance, [49, 50, 67, 78, 100, 101]. Alternatively, one can consider an energy-gap type cost function which consists of two auxiliary states; one that is a solution of pure Dirichlet problem and one that satisfies a mixed Dirichlet-Neumann problem (see, e.g., [1, 13–15, 51]). The objective function used in such a formulation is sometimes called the Kohn-Vogelius cost functional since Kohn and Vogelius [82] were among the first who used such a criterion in the context of inverse problems. Mathematically, in the case of the exterior problem, these aforementioned formulations are given as follows:

Dirichlet-data-tracking functional minimization approach [50, 78, 100]

$$(1.6) \quad \min_{\Omega} J_D(\Sigma) \equiv \min_{\Omega} \frac{1}{2} \|u_N\|_{L^2(\Sigma)}^2 \equiv \min_{\Omega} \frac{1}{2} \int_{\Sigma} u_N^2 \, d\sigma$$

where the state function $u_N := u_N(\Omega)$ is the solution to the mixed Dirichlet-Neumann problem

$$(1.7) \quad -\Delta u_N = 0 \text{ in } \Omega, \quad u_N = 1 \text{ on } \Gamma, \quad \partial_n u_N = \lambda \text{ on } \Sigma;$$

Neumann-data-tracking functional minimization approach [49, 67, 101]

$$(1.8) \quad \min_{\Omega} J_N(\Sigma) \equiv \min_{\Omega} \frac{1}{2} \left\| \frac{\partial u_D}{\partial \mathbf{n}} - \lambda \right\|_{L^2(\Sigma)}^2 \equiv \min_{\Omega} \frac{1}{2} \int_{\Sigma} \left(\frac{\partial u_D}{\partial \mathbf{n}} - \lambda \right)^2 \, d\sigma$$

where the state function $u_D := u_D(\Omega)$ is the solution to the pure Dirichlet problem

$$(1.9) \quad -\Delta u_D = 0 \text{ in } \Omega, \quad u_D = 1 \text{ on } \Gamma, \quad u_D = 0 \text{ on } \Sigma;$$

Energy-gap type cost functional minimization approach [1, 13–15, 51]

$$(1.10) \quad \min_{\Omega} J_{KV}(\Omega) \equiv \min_{\Omega} \frac{1}{2} \|u_N - u_D\|_{H^1(\Omega)}^2 \equiv \min_{\Omega} \frac{1}{2} \int_{\Omega} |\nabla(u_N - u_D)|^2 \, dx$$

where the state functions u_N and u_D satisfy systems (1.7) and (1.9), respectively.

Note that by Green's first identity $\frac{1}{2} \int_{\Omega} |\nabla(u_N - u_D)|^2 \, dx = - \int_{\Sigma} u_N (\partial_n u_D - \lambda) \, d\sigma$. Hence, minimizing the cost functional J_{KV} is equivalent to maximizing $\int_{\Sigma} u_N (\partial_n u_D - \lambda) \, d\sigma$ over all admissible domains Ω .

In addition to the above formulations, one may also consider minimizing the Dirichlet energy functional J_{DE} subject to the pure Dirichlet boundary value problem (1.9):

Dirichlet-energy cost functional minimization approach [48, 52, 109]

$$(1.11) \quad \min_{\Omega} J_{DE}(\Omega) \equiv \min_{\Omega} \frac{1}{2} \int_{\Omega} (\|\nabla u_D\|^2 + \lambda^2) \, dx$$

where the state function u_D is the solution to the BVP (1.9).

Finally, one may also opt to track, instead of the $L^2(\Sigma)$ -norm, the $H^{-1/2}(\Sigma)$ -norm of the Neumann data of the pure Dirichlet problem (1.9), and consider the shape optimization reformulation of (1.3) given as follows:

Minimization of the Neumann-data in $H^{-1/2}(\Sigma)$ -norm [68–70]

$$(1.12) \quad \min_{\Omega} J_{H^{-1/2}(\Sigma)} \equiv \min_{\Omega} \frac{1}{2} \left\| \frac{\partial u_D}{\partial \mathbf{n}} - \lambda \right\|_{H^{-1/2}(\Sigma)}^2.$$

where the state function u_D satisfy the BVP (1.7).

Obviously, the minimization problems (1.8) and (1.12) only differ in terms of the tracking norm. From the theoretical point of view, it seems that the latter formulation is more natural because for Lipschitz domain Ω , the solution u_D lives in the functional space $H^1(\Omega)$ and therefore the trace of u on $\partial\Omega$ is in $H^{-1/2}(\partial\Omega)$. However, this choice of the tracking norm leads to difficulties in the sensitivity analysis of the cost functional that is essential in the study of optimality conditions for the shape optimization problem [80]. Nevertheless, in [70], the authors were able to bypass this difficulty by applying a genetic algorithm in the optimization procedure which does not require shape sensitivity analysis. On the other, in the subject of finite element discretization of (1.3) the numerical realization of the standard dual $H^{-1/2}(\Sigma)$ -norm poses a non-trivial task primarily because the Neumann data is not easy to obtain. In [69], the same authors propose a *fictitious domain method* to solve the minimization problem (1.12). As a consequence of their proposed approach, the Neumann data is approximated via Lagrange multiplier method while enforcing the Dirichlet boundary conditions in (1.9). The norm computed with respect to $H^{-1/2}(\Sigma)$ is then realized as a volume $H^1(\Omega)$ -norm of a function that is a solution of a certain transmission problem. Meanwhile, it should be noted that higher regularity of the domain Ω (say Ω is a $C^{2,1}$ -domain) lifts the regularity of the state function u_D (cf. [14, Theorem 29]) as well as its Cauchy data which will then allow the consideration of the $L^2(\Sigma)$ -norm tracking of the Neumann data.

On the other hand, of course, similar formulations can be stated for the case of the interior problem. For example, one can consider the minimization problem

$$(1.13) \quad \min_{\Omega} J_N^{\text{int}}(\Sigma) \equiv \min_{\Omega} \frac{1}{2} \left\| \frac{\partial u_D^{\text{int}}}{\partial \mathbf{n}} - \lambda \right\|_{L^2(\Sigma)}^2.$$

where the state variable u_D^{int} satisfies the following PDE system

$$(1.14) \quad -\Delta u_D^{\text{int}} = 0 \text{ in } \Omega, \quad u_D^{\text{int}} = 0 \text{ on } \Gamma, \quad u_D^{\text{int}} = 1 \text{ on } \Sigma.$$

1.3.2 New Shape Optimization Formulations of the Bernoulli Problem

The shape optimization reformulations of the Bernoulli problem presented in the previous section already provide excellent results when combined with a numerical scheme to solve concrete numerical examples of the problem. However, further improvements of these existing shape optimization

formulations is still possible as we will show in this thesis. Therefore, one of our main objectives in this study is to introduce three novel reformulations of (1.3) into shape optimization settings which, to the best of our knowledge, have not been studied yet in any previous investigation.

The main point of departure for the new formulations is the modification of the state equation or one of the state constraint equations appearing in the shape optimization problems presented previously. More precisely, given a strictly positive real number β , we consider the following equivalent form of (1.3) with a Robin boundary condition:

$$(1.15) \quad -\Delta u_R = 0 \text{ in } \Omega, \quad u_R = 1 \text{ on } \Gamma, \quad \frac{\partial u}{\partial \mathbf{n}} + \beta u_R = \lambda \text{ on } \Sigma.$$

We will see in Chapter 2, especially in Section 2.2, and Section 3.2 that by utilizing the above problem we will be able to improve not only the theoretical feature, but also the numerical aspect of the shape optimization formulation presented in the previous sections. At this point, it is also noteworthy to mention that Tiihonen [109] already consider such a state constraint in a shape optimization reformulation of the exterior Bernoulli problem (1.3). In fact, instead of the mixed Dirichlet-Neumann problem (1.7), Tiihonen used the mixed Dirichlet-Robin problem (1.15) as the state constraint for the cost function $J_D(\Sigma)$ in his work in [109]. However, in this thesis, we will see that the use of such a state problem is more advantageous when utilized in the case of tracking the Neumann-data in L^2 sense (see Section 2.2).

Focusing on the exterior case, let us now introduce the new shape optimization reformulations of the Bernoulli problem which we will investigate in this thesis. After stating each of the proposed formulations, we will give a short motivation on why we proposed to examine the given shape optimization problems. The first reformulation is a simple modification of the classical Neumann-data-tracking approach. Instead of taking the pure Dirichlet problem (1.9) as the state system, we consider the mixed Dirichlet-Robin problem (1.15) as the new state equation. That is, we have the following minimization problem

Improved Neumann-data-tracking functional minimization approach

$$(1.16) \quad \min_{\Omega} J_1(\Sigma) \equiv \min_{\Omega} \frac{1}{2} \left\| \frac{\partial u_R}{\partial \mathbf{n}} - \lambda \right\|_{L^2(\Sigma)}^2 \equiv \min_{\Omega} \frac{1}{2} \int_{\Sigma} \left(\frac{\partial u_R}{\partial \mathbf{n}} - \lambda \right)^2 d\sigma$$

where the state function $u_R := u_R(\Omega)$ solves the Robin problem (1.15). Note that when (Ω, u_R) is the solution to (1.3), $J_1(\Sigma) = 0$ since $\frac{\partial u_R}{\partial \mathbf{n}} = \lambda$ on Σ . On the other hand, when $J_1(\Sigma) = 0$, we get from (1.15) the equation $-\beta u_R = \frac{\partial u_R}{\partial \mathbf{n}} - \lambda = 0$. Since $\beta > 0$, we obtain $u_R = 0$ on Σ , and hence the overdetermined system (1.3).

Motivation. The classical formulation of (1.3) in terms of tracking the Neumann-data in L^2 -sense was studied in [67]. In this aforementioned study, the authors computed the shape derivative of J_N through rearrangement method; thereby avoiding the computation of the material derivative of

the states but in turn requires the introduction of an appropriate adjoint state systems. The adjoint state of the classical formulation (1.8)–(1.9) of (1.3), however, only enjoys one regularity less than its corresponding state variable u_D . In fact, when the domain Ω is of class $C^{1,1}$, the state variable u_D is $H^2(\Omega)$ regular while its corresponding adjoint state is only in $H^1(\Omega)$. This motivates us to consider the minimization problem (1.16) subject to (1.15) since the Robin problem actually yields a more regular adjoint state than the Dirichlet problem. Later on in this thesis, we will see that this higher regularity of the adjoint state, coupled with a specific choice of the parameter β , provides *more stability* when used in an iterative scheme than in the case of using the classical Neumann-data-tracking formulation. We point out here that the proposed formulation (1.16) was also inspired by yet another shape optimization formulation of (1.3) due to [109]. In the said paper, Tiihonen studied the Dirichlet-data-tracking formulation of (1.3) but with state constraint given by (1.15). The main result issued in the paper is that the choice of β appearing in the Robin boundary condition can possibly influence the conditioning of the shape cost functional which is also the case in our new formulation.

Now, the second formulation is a modification of the Kohn-Vogelius cost functional minimization problem (1.10) subject to (1.7) and (1.9). To be precise, we simply replace the state constraint u_D with u_R which leads to the following formulation:

Modified Kohn-Vogelius cost functional minimization approach

$$(1.17) \quad \min_{\Omega} J_2(\Omega) \equiv \min_{\Omega} \frac{1}{2} \|u_R - u_N\|_{H^1(\Omega)}^2 \equiv \min_{\Omega} \frac{1}{2} \int_{\Omega} |\nabla(u_R - u_N)|^2 dx$$

where, of course, u_N and u_R are the respective solutions to the PDE systems (1.7) and (1.15).

Motivation. The main reason we consider such modification of the classical Kohn-Vogelius cost functional minimization approach roots from the fact that in most, if not all, shape optimization reformulation of the Bernoulli problem, one is required to solve at least two systems of PDEs in order to evaluate the gradient of the associated cost function (see, e.g., [14, Theorem 33] or [1, Theorem 2] for the case of J_{KV} , and also [51, Theorem 1] for the n -dimensional case of the problem). Contrary to the classical energy-gap type minimization formulation, we shall see in a subsequent chapter that, with the right choice of β and an additional assumption on u_R , the shape gradient of the cost function obtained from this new formulation depends only on the solution of the state system (1.7). As a consequence, the shape problem (1.17) stated previously is more attractive compared to that of the classical setting (1.8), especially in terms of numerical aspects of the formulation. We announce in advance that, in the numerical examples presented here, the above proposed formulation provides less computing time per iteration than the classical Kohn-Vogelius cost functional minimization approach. The two formulations, however, are comparable in terms of mean over-all computing time. In addition, it appears that the proposed formulation provides a somewhat more accurate approximation of the optimal solution than the classical Kohn-Vogelius approach. We support these claims with various numerical examples that are reported in the numerical part of the thesis.

Lastly, we state our third proposed shape optimization reformulation of (1.3). The minimization problem we give below is, to the best of our knowledge, has not been studied in any previous investigation. Therefore it is a new shape optimization reformulation of (1.3). Its cost functional is a boundary integral and involves two auxiliary states. More precisely, we have the following problem.

Dirichlet-data-gap cost functional minimization approach

$$(1.18) \quad \min_{\Sigma} J_3(\Sigma) \equiv \min_{\Omega} \frac{1}{2} \|u_R - u_N\|_{L^2(\Sigma)}^2 \equiv \min_{\Omega} \frac{1}{2} \int_{\Sigma} |u_R - u_N|^2 d\sigma$$

where, again, u_N and u_R satisfies the PDE systems (1.7) and (1.15).

Notice that the cost function basically measures the $L^2(\Sigma)$ distance between the Dirichlet-data of the solutions u_N and u_R of the PDE systems (1.7) and (1.15), respectively. For this reason, we call J_3 as the *Dirichlet-data-gap* cost functional.

It should be apparent that the above formulation is equivalent to the exterior Bernoulli problem (1.3) in the case of matching Dirichlet-data. Note that if (Ω, u) is a solution of (1.3), then $u_N = u_R = u$, and therefore, $J_3(\Sigma) = 0$. Conversely, if $J_3(\Sigma) = 0$, then $u_N = u_R$ on Σ . Hence, the equation $\partial_n(u_N - u_R) = \beta u_R = 0$ on Σ and the assumption $\beta > 0$ implies that $u_R = u_N = 0$ on Σ . Consequently, $u = u_N = u_R$ is a solution of problem (1.3).

It is worth remarking that, in the limiting case that β goes to infinity, the PDE system (1.15) transforms into the pure Dirichlet problem (1.9) (this means that $u_R = 0$ on Σ), leading us to recover from (1.18) the classical Dirichlet-data-tracking formulation of the FBP (1.3).

We complete our introduction of the above novel shape optimization reformulation of (1.3) by stating below our motivation behind the above problem.

Motivation. Our reason for considering the new cost functional $J_3(\Sigma)$ stems from the fact that minimizing $J_2(\Omega)$ subject to (1.7) and (1.15) over some set of admissible domains of Ω is, in some sense, equivalent to finding the optimal shape solution to the optimization problem (1.18) subject to the same state constraints. We explain this statement in more detail. Consider an open bounded domain $\Omega \subset \mathbb{R}^2$ with Lipschitz boundary $\partial\Omega$, and let Γ be a closed subset of $\partial\Omega$. Then, the inequality $\|w\|_{L^2(\partial\Omega)} \lesssim \|w\|_{H^1(\Omega)}$ obviously holds, for all $w \in H^1(\Omega)$. This inequality clearly exhibits the compact embedding of $H^1(\Omega)$ in $L^2(\partial\Omega)$ (see, e.g., [86, p. 159]) which is primarily a consequence of the well-known *trace theorem* (see, e.g., [87, Theorem 3.3.7, p. 102], [90, Theorem 5.5, p. 95]) coupled with the compact embedding of $H^{1/2}(\partial\Omega)$ in $L^2(\partial\Omega)$ (cf. [102, Theorem, 2.5.5, p. 61]). Moreover, because of the relation $\|w\|_{L^2(\Gamma)} \lesssim \|w\|_{H^1(\Omega)}$, we know that the set $H_{\Gamma,0}^1(\Omega) = \{w \in H^1(\Omega) : w = 0 \text{ on } \Gamma\}$ is strongly closed in $H^1(\Omega)$ and, in addition, a convex set. From [32, p. 54], for instance, we know that strongly closed convex sets are also weakly closed (see also [24, Lemma 3.1.15, p. 119]). Hence, the weak convergence $w_{n_k} \rightharpoonup w$ implies that w is in fact in the same set $H_{\Gamma,0}^1(\Omega)$. Furthermore, it may be shown (following, for example, the proof of [71, Lemma 2.19, p. 62]) that $\|w\|_{H^1(\Omega)} = \|\nabla w\|_{L^2(\Omega)} \gtrsim \|w\|_{H^1(\Omega)}$, for all $w \in H_{\Gamma,0}^1(\Omega)$. This bound shows that the $H^1(\Omega)$ -seminorm $|\cdot|_{H^1(\Omega)}$ is actually equivalent to the

$H^1(\Omega)$ -norm on $H_{\Gamma,0}^1(\Omega)$. Lastly, one can also verify, possibly by way of contradiction, that the norm

$$(1.19) \quad \|\cdot\|_{H_{\Gamma,0}^1(\Omega)} := \left(|\cdot|_{H^1(\Omega)}^2 + \|\cdot\|_{L^2(\Sigma)}^2 \right)^{1/2},$$

on the other hand, is equivalent to the usual Sobolev $H^1(\Omega)$ -norm. From these results, taking $w = u_N - u_R \in H_{\Gamma,0}^1(\Omega)$, we can easily deduce the following sequence of inequalities

$$\|u_N - u_R\|_{L^2(\Sigma)}^2 \lesssim |u_N - u_R|_{H^1(\Omega)}^2 + \|u_N - u_R\|_{L^2(\Omega)}^2 \lesssim |u_N - u_R|_{H^1(\Omega)}^2.$$

It should also be recognized that the above relation is a mere consequence of the inequality

$$\|u_N - u_R\|_{L^2(\Sigma)}^2 \lesssim \|u_N - u_R\|_{H^{1/2+\varepsilon}(\Omega)}^2$$

which holds true for any $\varepsilon > 0$ due to the trace theorem. This observation further gives us the motivation to consider the minimization (1.18) subject to (1.7) and (1.15) over some set of admissible domains (which we will specify later) for Ω to numerically solve the free boundary problem (1.3).

Before we end this section, we mention that the three formulations presented previously can also be applied in the case of the interior problem. For example, the corresponding formulation to (1.16) in the context of the interior problem can be stated as follows:

$$(1.20) \quad \min_{\Omega} J_1^{\text{int}}(\Sigma) \equiv \min_{\Omega} \frac{1}{2} \left\| \frac{\partial u_R^{\text{int}}}{\partial \mathbf{n}} - \lambda \right\|_{L^2(\Sigma)}^2,$$

where the state variable u_D^{int} satisfies the following PDE system

$$(1.21) \quad -\Delta u_D^{\text{int}} = 0 \text{ in } \Omega, \quad u_R^{\text{int}} = 0 \text{ on } \Gamma, \quad \frac{\partial u_R^{\text{int}}}{\partial \mathbf{n}} + \tilde{\beta} u_R^{\text{int}} = \lambda + \tilde{\beta} \text{ on } \Sigma,$$

and $\tilde{\beta}$ is, of course, a given non-negative positive number.

1.4 Existence of an Optimal Solution to Shape Problems

Our ultimate goal in this thesis is to solve concrete examples of the Bernoulli problem by performing novel iterative gradient-based optimization procedures. Because our formulations are new, it is customary to first show the existence of optimal solutions to our proposed shape problems. In this section, we will resolve the issue of existence of a solution to the optimization problems presented in the previous section by proving the continuity of solutions of the state problems with respect to the domain. In order to do this, we will use a result concerning uniform continuity of the trace operator with respect to a domain and a recent result regarding a uniform Poincaré inequality for variable domains. To begin with, let us first give a general idea in proving existence of an optimal solution to shape optimization problems. The discussion is borrowed from [71, Section 2.4, pp. 45–47].

1.4.1 Abstract Setting of Optimal Shape Problem subject to PDE Constraints

Since the object of optimization in shape optimization problems are the domain in which state problems are solved, then one needs to define convergence of sets through convergence of functions that describe the boundary of the domains. In the literature, the convergences of sets and of functions defined in variable domains can be described in many different ways and usually it depends on the type of state problems that are in consideration. Here, however, we shall not particularize any specific choice of these convergences in the abstract setting.

Let \mathcal{O}_{ad} be the set of admissible domains and $\tilde{\mathcal{O}}_{\text{ad}}$ be a larger set containing \mathcal{O}_{ad} . Consider a sequence $\{\Omega_n\} \subset \tilde{\mathcal{O}}_{\text{ad}}$. The notation $\Omega_n \xrightarrow{\tilde{\mathcal{O}}_{\text{ad}}} \Omega$ as $n \rightarrow \infty$ means $\{\Omega_n\}$ tends to Ω where the convergence is defined as $\Omega_{n_k} \xrightarrow{\tilde{\mathcal{O}}_{\text{ad}}} \Omega$, as $k \rightarrow \infty$ for any subsequence $\{\Omega_{n_k}\}$ of $\{\Omega_n\}$.

For each $\Omega \in \tilde{\mathcal{O}}_{\text{ad}}$, we associate a function space $\mathcal{X}(\Omega)$ of real functions defined in Ω . Then, we introduce convergence of functions form $\mathcal{X}(\Omega)$ for different $\Omega \in \mathcal{O}_{\text{ad}}$. So, if $\{y_n\}$ is a subsequence in $\mathcal{X}(\Omega)$, $\Omega_n \in \tilde{\mathcal{O}}_{\text{ad}}$, $y \in \mathcal{X}(\Omega)$, and $\Omega \in \tilde{\mathcal{O}}_{\text{ad}}$, the convergence of y_n to y is denoted by $y_n \rightsquigarrow y$ and again we suppose that for any subsequence $\{y_{n_k}\}$ of $\{y_n\}$ we have that $y_{n_k} \rightsquigarrow y$ as $k \rightarrow \infty$.

Now, for a domain Ω in $\tilde{\mathcal{O}}_{\text{ad}}$, we solve a state problem, say $e(\cdot) = 0$, whose solution is denoted by $u : \Omega \mapsto u(\Omega) \in \mathcal{X}(\Omega)$. In this respect, assume that $e(u(\Omega)) = 0$ admits a unique solution in $\mathcal{X}(\Omega)$ for $\Omega \in \tilde{\mathcal{O}}_{\text{ad}}$.

Lastly, we consider a shape functional $J : (\Omega, u(\Omega)) \mapsto J(\Omega, u(\Omega)) \in \mathbb{R}$, $\Omega \in \tilde{\mathcal{O}}_{\text{ad}}$, $u(\Omega) \in \mathcal{X}(\Omega)$ and define the graph

$$\mathfrak{G} := \{(\Omega, u(\Omega)) : \Omega \in \mathcal{O}_{\text{ad}}\}.$$

The abstract optimal shape problem is then given by

$$(1.22) \quad \begin{cases} \text{Find } (\Omega^*, u(\Omega^*)) \in \mathfrak{G} \text{ such that} \\ J(\Omega^*, u(\Omega^*)) \leq J(\Omega, u(\Omega)), \forall (\Omega, u(\Omega)) \in \mathfrak{G}. \end{cases}$$

To guarantee the existence of solutions to the abstract problem above, one needs an appropriate compactness property for \mathfrak{G} and lower semicontinuity of J .

Definition 1.4.1. We suppose the following property of \mathfrak{G} and of J holds.

Compactness Property of \mathfrak{G} : For any sequence $\{(\Omega_n, u(\Omega_n))\} \in \mathfrak{G}$, there is a subsequence $\{(\Omega_{n_k}, u(\Omega_{n_k}))\}$ and an element $(\Omega, u(\Omega)) \in \mathfrak{G}$ such that $\Omega_{n_k} \xrightarrow{\tilde{\mathcal{O}}_{\text{ad}}} \Omega$ and $u(\Omega_{n_k}) \rightsquigarrow u(\Omega)$, as $k \rightarrow \infty$.

Lower semicontinuity of J : If $\Omega_n \xrightarrow{\tilde{\mathcal{O}}_{\text{ad}}} \Omega$, $\Omega_n, \Omega \in \tilde{\mathcal{O}}_{\text{ad}}$, and $u(\Omega_{n_k}) \rightsquigarrow u(\Omega)$, where $u(\Omega_{n_k}) \in \mathcal{X}(\Omega_{n_k})$ and $u(\Omega) \in \mathcal{X}(\Omega)$, then $\liminf_{n \rightarrow \infty} J(\Omega_n, u(\Omega_n)) \geq J(\Omega, u(\Omega))$.

Finally, the existence of optimal shape solution to the shape optimization problem (1.22) is given as follows.

Theorem 1.4.1. If the compactness property of \mathfrak{G} and the lower semicontinuity of J are satisfied, then the abstract shape optimization problem (1.22) has at least one solution.

1.4.2 Existence of Optimal Solution to the Proposed Shape Problems

The main purpose of this subsection is to prove the existence of optimal solution to the proposed shape optimization reformulations of (1.3) formally stated in Theorem 1.4.2. This will be accomplished based on the theory developed in [71] that was reviewed previously.

To start off, let us first state the respective weak forms of the state problems (1.7) and (1.15) as well as their equivalent variational formulations that we will utilize in this section.

Find $u_N \in H^1(\Omega)$, with $u_N = 1$ on Γ , such that

$$(1.23) \quad \int_{\Omega} \nabla u_N \cdot \nabla \varphi \, dx = \int_{\Sigma} \lambda \varphi \, d\sigma, \quad \forall \varphi \in H_{\Gamma,0}^1(\Omega);$$

Find $u_R \in H^1(\Omega)$, with $u_R = 1$ on Γ , such that

$$(1.24) \quad \int_{\Omega} \nabla u_R \cdot \nabla \varphi \, dx + \int_{\Sigma} \beta u_R \varphi \, d\sigma = \int_{\Sigma} \lambda \varphi \, d\sigma, \quad \forall \varphi \in H_{\Gamma,0}^1(\Omega),$$

where $H_{\Gamma,0}^1(\Omega)$ is the space of test functions in the introduction.

It is well-known that the variational equation (1.23) has a unique solution in $H^1(\Omega)$. Meanwhile, it can be shown (for instance, by means of Lax-Milgram theorem) that the variational problem (1.24) also has a *unique weak solution* in $H^1(\Omega)$ (see, e.g., [62, 88]).

To address the issue of existence of optimal solutions to the shape problems introduced in subsection 1.3.2, we consider the following equivalent formulations of (1.23) and (1.24).

Definition 1.4.2. The weak equations (1.23) and (1.24) are respectively equivalent to the following variational equations.

- Find $z_N = u_N - u_{N0} \in H_{\Gamma,0}^1(\Omega)$ such that

$$(1.25) \quad \int_{\Omega} \nabla z_N \cdot \nabla \varphi \, dx + \int_{\Omega} \nabla u_{N0} \cdot \nabla \varphi \, dx - \int_{\Sigma} \lambda \varphi \, d\sigma = 0, \quad \forall \varphi \in H_{\Gamma,0}^1(\Omega).$$

- Find $z_R = u_R - u_{R0} \in H_{\Gamma,0}^1(\Omega)$ such that

$$(1.26) \quad \int_{\Omega} \nabla z_R \cdot \nabla \varphi \, dx + \int_{\Omega} \nabla u_{R0} \cdot \nabla \varphi \, dx + \int_{\Sigma} \beta z_R \varphi \, d\sigma - \int_{\Sigma} \lambda \varphi \, d\sigma = 0, \quad \forall \varphi \in H_{\Gamma,0}^1(\Omega).$$

In above equations, u_{N0} and u_{R0} are two fixed functions in $H^1(U)$ such that $u_{N0} = u_{R0} = 1$ on Γ .

We have three different shape optimization problems that we need to deal with in this thesis. The existence analysis that we will present here actually applies to any of the shape optimization formulations that were introduced in the previous section. Therefore, we will only demonstrate a detailed examination of the existence question to one of the shape problems. In particular, we will focus on the existence of optimal shape solution to the third minimization problem (1.18) subject to the state problems (1.7) and (1.15). We will state, however, an existence result for the other two formulations but without proof.

Now, given the unique solvability of the variational problems (1.25) and (1.26) in $H^1(\Omega)$, we introduce the map $\Omega \mapsto (z_N, z_R) := (z_N(\Omega), z_R(\Omega))$ and denote its graph by

$$\mathfrak{G}_3 = \{(\Omega, z_N(\Omega), z_R(\Omega)) : \Omega \in \mathcal{O}_{\text{ad}}, z_N \text{ and } z_R \text{ satisfies (1.25) and (1.26) on } \Omega, \text{ respectively}\},$$

where \mathcal{O}_{ad} is the set of all admissible domains which we will specify further below. Hence, the minimization problem “ $\min_{\Omega \in \mathcal{O}_{\text{ad}}} J_3(\Sigma)$ subject to (1.23) and (1.24)” is equivalent to the problem of finding a solution $(\Omega, z_N(\Omega), z_R(\Omega))$ that minimizes $J_3(\Omega) = J_3(\Omega, z_N(\Omega), z_R(\Omega))$ on \mathfrak{G}_3 . As was seen in subsection 1.4.1, such minimization problem is usually solved by endowing the set \mathfrak{G}_3 with a topology for which \mathfrak{G}_3 is compact and the cost functional J_3 is lower semicontinuous. To this end, several propositions furnished in [21, 68] will be utilized.

Let us now characterize the set of admissible domains \mathcal{O}_{ad} and then describe the appropriate topology that we will use in our analysis. We assume that Ω has a $C^{1,1}$ smooth free boundary Σ . Our main problem is given as follows:

$$(1.27) \quad \begin{cases} \text{Find } (\Omega^*, z_N(\Omega^*), z_R(\Omega^*)) \in \mathfrak{G}_3 \text{ such that} \\ J_3(\Omega^*, z_N(\Omega^*), z_R(\Omega^*)) \leq J_3(\Omega, z_N(\Omega), z_R(\Omega)), \forall (\Omega, z_N(\Omega), z_R(\Omega)) \in \mathfrak{G}_3. \end{cases}$$

Given the assumed regularity of Ω , we let Σ be parametrized by a vector valued function $\boldsymbol{\phi} \in C^{1,\mu}(\mathbb{R}, \mathbb{R}^2)$, $0 \leq \mu < 1$; that is, $\Sigma := \Sigma(\boldsymbol{\phi}) = \{\boldsymbol{\phi} = (\phi_1(t), \phi_2(t)) : t \in (0, 1], \boldsymbol{\phi} \in C^{1,\mu}(\mathbb{R}, \mathbb{R}^2)\}$. We consider a collection \mathfrak{U}_{ad} of $\boldsymbol{\phi}$ which is defined as follows.¹

Definition 1.4.3. The parametric function $\boldsymbol{\phi}$ parameterizing Σ is in \mathfrak{U}_{ad} if $\boldsymbol{\phi}$ satisfies the following properties:

(P1) $\boldsymbol{\phi}$ is injective on $(0, 1]$ and is 1-periodic;

(P2) there exist positive real numbers c_0, c_1, c_2 , and c_3 such that

$$|\boldsymbol{\phi}(t)| \leq c_0, \quad c_1 \leq |\dot{\boldsymbol{\phi}}(t)| \leq c_2, \quad |\ddot{\boldsymbol{\phi}}(t)| \leq c_3,$$

for all $t \in (0, 1]$.

¹It is actually sufficient to assume that $\boldsymbol{\phi} : \mathbb{R} \rightarrow \mathbb{R}^2$ to be only C^1 regular and drop the uniform boundedness of $\ddot{\boldsymbol{\phi}}(t)$ for all $t \in (0, 1]$.

(P3) $\bar{\Omega} := \bar{\Omega}(\boldsymbol{\phi}) \subset U$, U is a fixed, connected, bounded open subset of \mathbb{R}^2 ;

(P4) lastly, there is a real number $\gamma > 0$ such that $\text{dist}(\Gamma, \Sigma(\boldsymbol{\phi})) \geq \gamma$.

In **(P2)**, the notations $(\dot{\cdot})$ and $(\ddot{\cdot})$ denote the usual first- and second-order time derivatives with respect to the (pseudo) time variable t , respectively.

Finally, we define the set of admissible domains \mathcal{O}_{ad} as

$$\mathcal{O}_{\text{ad}} := \{\Omega = \Omega(\boldsymbol{\phi}) \subset U : \boldsymbol{\phi} \in \mathfrak{A}_{\text{ad}}\},$$

where \mathfrak{A}_{ad} is a compact subset of \mathfrak{A}_{ad} . Examples of \mathfrak{A}_{ad} are the sets

$$\left\{ \boldsymbol{\phi} \in \mathfrak{A}_{\text{ad}} : |\dot{\boldsymbol{\phi}}(t) - \dot{\boldsymbol{\phi}}(s)| \lesssim |t - s|^\nu, 0 \leq \mu < \nu \leq 1, t, s \in (0, 1] \right\}$$

and

$$\left\{ \boldsymbol{\phi}(t) \in \mathfrak{A}_{\text{ad}} : \boldsymbol{\phi}(t) \in C^{2,\nu}(\mathbb{R}, \mathbb{R}^2) : 0 \leq \mu < \nu \leq 1 \right\},$$

which are compact in $C^{1,\nu}(\mathbb{R}, \mathbb{R}^2)$.² We shall also consider the larger set

$$\tilde{\mathcal{O}}_{\text{ad}} := \{\Omega = \Omega(\boldsymbol{\phi}) \subset U : \boldsymbol{\phi} \in \mathfrak{A}_{\text{ad}}\}.$$

We emphasize that in property **(P3)** of $\boldsymbol{\phi}$, we are assuming that all admissible domains $\Omega(\boldsymbol{\phi})$ are contained in the so-called *hold-all* domain U .³ Also, we assume that U is sufficiently large that it contains the optimal domain Ω^* that solves the exterior Bernoulli FBP (1.3). Consequently, we require that $\text{dist}(\Sigma(\boldsymbol{\phi}), \partial U) > 0$, for all $\boldsymbol{\phi} \in \mathfrak{A}_{\text{ad}}$, and, of course, we want $\text{dist}(\Sigma^*, \partial U) > 0$. By this means, we can say that the minimization problem “ $\min_{\Omega \in \mathcal{O}_{\text{ad}}} J_3(\Sigma)$ subject to (1.23) and (1.24)” is indeed equivalent to the free boundary problem (1.3).

Meanwhile, in view of (1.4.2), recalling Remark 1.2.1, we see that every admissible domain $\Omega(\boldsymbol{\phi})$ is a uniformly open set in \mathbb{R}^2 and therefore satisfy the well-known *uniform cone property* (see [30, Definition 1] or [73, Definition 2.4.1, p. 54]). As a consequence, these admissible domains satisfy a very important extension property. More precisely, for every $m \geq 1$, $p > 1$, and domain $\Omega \in \mathcal{O}_{\text{ad}}$, there exists an extension operator

$$(1.28) \quad E_\Omega : W^{m,p}(\Omega) \rightarrow W^{m,p}(U)$$

such that $\|E_\Omega \varphi\|_{W^{m,p}(U)} \leq c \|\varphi\|_{W^{m,p}(\Omega)}$, where c is a positive constant independent of the domain Ω (see [30]). By these properties, we can ensure a uniform extension $\tilde{\varphi} \in H^1(U)$ from Ω to U of every function $\varphi \in H^1(\Omega)$.

²If we only assume that $\boldsymbol{\phi}$ is $C^1(\mathbb{R}, \mathbb{R}^2)$, then an example of \mathfrak{A}_{ad} is the set $\left\{ \boldsymbol{\phi} \in \mathfrak{A}_{\text{ad}} : |\dot{\boldsymbol{\phi}}(t) - \dot{\boldsymbol{\phi}}(s)| \lesssim |t - s|^\mu, 0 < \mu \leq 1, t, s \in (0, 1] \right\}$ which is compact in $C^{1,\mu}(\mathbb{R}, \mathbb{R}^2)$.

³In subsection 2.1.2, we will use the same notation U to denote the *universal set* that holds all the possible deformations of the reference domain Ω .

We are now in the position to define the topology we shall use in this thesis, and this we give in the following definition.

Definition 1.4.4. Let $\boldsymbol{\phi} \in \mathcal{U}_{\text{ad}}$, $\{\boldsymbol{\phi}_n\} \subset \mathcal{U}_{\text{ad}}$, $\Omega := \Omega(\boldsymbol{\phi}) \in \tilde{\mathcal{O}}_{\text{ad}}$, $\{\Omega_n\} := \{\Omega(\boldsymbol{\phi}_n)\} \subset \tilde{\mathcal{O}}_{\text{ad}}$, and z_N and z_R be the respective solutions to (1.25) and (1.26) on Ω . Also, consider the sequences $\{z_{Nn}\}$ and $\{z_{Rn}\}$ of solutions to (1.25) and (1.26) on Ω_n , respectively. Denote the extensions of these functions by $\tilde{z}_i := E_\Omega z_i$ and $\tilde{z}_{in} := E_\Omega z_{in}$, for $i = N, R$, where E_Ω is the extension operator (1.28). Then, the topology we introduce on \mathfrak{G}_3 is the one induced by the convergence defined by

$$(1.29) \quad (\Omega_n, z_{Nn}, z_{Rn}) \rightarrow (\Omega, z_N, z_R) \quad \text{if and only if} \quad \begin{cases} \boldsymbol{\phi}_n \xrightarrow{C^1} \boldsymbol{\phi} \\ z_{Nn} \rightsquigarrow z_N \\ z_{Rn} \rightsquigarrow z_R \end{cases},$$

where the latter convergences are defined as follows:

$$(1.30) \quad \boldsymbol{\phi}_n \xrightarrow{C^1} \boldsymbol{\phi} \iff \boldsymbol{\phi}_n \rightarrow \boldsymbol{\phi} \text{ and } \dot{\boldsymbol{\phi}}_n \rightarrow \dot{\boldsymbol{\phi}} \text{ uniformly on } [0, 1],$$

$$(1.31) \quad z_{Nn} \rightsquigarrow z_N \iff \tilde{z}_{Nn} \rightharpoonup \tilde{z}_N \text{ weakly in } H^1(U),$$

$$(1.32) \quad z_{Rn} \rightsquigarrow z_R \iff \tilde{z}_{Rn} \rightharpoonup \tilde{z}_R \text{ weakly in } H^1(U).$$

Moreover, using the convergence (1.30) in the C^1 -topology, we define the convergence of a sequence of domains $\{\Omega_n\} := \{\Omega(\boldsymbol{\phi}_n)\} \subset \tilde{\mathcal{O}}_{\text{ad}}$ by

$$(1.33) \quad \Omega_n \xrightarrow{\tilde{\mathcal{O}}_{\text{ad}}} \Omega \quad \text{if and only if} \quad \boldsymbol{\phi}_n \xrightarrow{C^1} \boldsymbol{\phi}.$$

Before we give the main result of this section, let us also state the corresponding graphs and shape problems of the first and second proposed shape optimization reformulations of the Bernoulli problem introduced in subsection 1.3.2. The first proposed minimization problem “ $\min_{\Omega \in \mathcal{O}_{\text{ad}}} J_1(\Sigma)$ subject to (1.24)” is equivalent to the problem of finding a solution $(\Omega, z_R(\Omega))$ that minimizes $J_1(\Omega) = J_1(\Omega, z_R(\Omega))$ on the graph \mathfrak{G}_1 of the map $\Omega \mapsto z_R := z_R(\Omega)$ given by

$$\mathfrak{G}_1 = \{(\Omega, z_R(\Omega)) : \Omega \in \mathcal{O}_{\text{ad}} \text{ and } z_R(\Omega) \text{ satisfies (1.26) on } \Omega\}.$$

The customary problem corresponding to the first proposed shape problem is as follows.

$$(1.34) \quad \begin{cases} \text{Find } (\Omega^*, z_R(\Omega^*)) \in \mathfrak{G}_1 \text{ such that} \\ J_1(\Omega^*, z_R(\Omega^*)) \leq J_1(\Omega, z_R(\Omega)), \forall (\Omega, z_R(\Omega)) \in \mathfrak{G}_1. \end{cases}$$

Similarly, for the second proposed shape problem, we have

$$(1.35) \quad \begin{cases} \text{Find } (\Omega^*, z_N(\Omega^*), z_R(\Omega^*)) \in \mathfrak{G}_2 \text{ such that} \\ J_2(\Omega^*, z_N(\Omega^*), z_R(\Omega^*)) \leq J_2(\Omega, z_N(\Omega), z_R(\Omega)), \forall (\Omega, z_N(\Omega), z_R(\Omega)) \in \mathfrak{G}_2, \end{cases}$$

where \mathfrak{G}_2 is the same graph defined by \mathfrak{G}_3 .

Finally, we can now state the main result of this section.

Theorem 1.4.2. The minimization problem (1.27) (respectively, (1.34) and (1.35)) admits a solution in \mathfrak{G}_3 (respectively, \mathfrak{G}_1 and \mathfrak{G}_2).

As we have already mentioned earlier, we will focus on the proof of the case of the third proposed shape problem because the corresponding results for the first two shape problems can be proven in a similar fashion. Now, we reiterate here that the existence proof is reduced to proving the compactness of \mathfrak{G}_3 (see Proposition 1.4.1) and the lower semi-continuity of J_3 (see Proposition 1.4.2). Regarding the former, we point out that the convergence $\boldsymbol{\phi}_n \xrightarrow{C^1} \boldsymbol{\phi}$ is simply a consequence of the compactness of \mathfrak{V}_{ad} together with the application of the Arzelà-Ascoli theorem. Hence, the compactness of \mathfrak{G}_3 with respect to the convergence (1.29) is easily verified. Consequently, we only need to prove the continuity of the state problems (1.7) and (1.15) with respect to the domain in order to finish the proof of compactness of \mathfrak{G}_3 , and we give this desired result in the proposition below.

Continuity of the State Problems

Proposition 1.4.1 ([98, 99]). With the convergence of a sequence of domains $\{\Omega_n\} \subset \tilde{\mathfrak{O}}_{\text{ad}}$ to $\Omega \in \tilde{\mathfrak{O}}_{\text{ad}}$ given in (1.33), we let $\{(\boldsymbol{\phi}_n, z_{Nn}, z_{Rn})\}$ be a sequence in \mathfrak{G}_3 where $z_{Nn} := z_N(\boldsymbol{\phi}_n)$ and $z_{Rn} := z_R(\boldsymbol{\phi}_n)$ are the weak solutions of (1.25) and (1.26) on $\Omega_n := \Omega(\boldsymbol{\phi}_n)$, respectively. Then, there exists a subsequence $\{(\boldsymbol{\phi}_k, z_{Nk}, z_{Rk})\}$ and elements $\boldsymbol{\phi} \in \mathfrak{U}_{\text{ad}}$ and $z_N, z_R \in H^1(U)$ such that

$$\boldsymbol{\phi}_k \xrightarrow{C^1} \boldsymbol{\phi}, \quad \tilde{z}_{Nk} \rightharpoonup z_N \text{ in } H^1(U), \quad \tilde{z}_{Rk} \rightharpoonup z_R \text{ in } H^1(U),$$

where $z_N = z_N(\boldsymbol{\phi}) = \tilde{z}_N|_{\Omega(\boldsymbol{\phi})}$ and $z_R = z_R(\boldsymbol{\phi}) = \tilde{z}_R|_{\Omega(\boldsymbol{\phi})}$ are the unique solutions of equations (1.25) and (1.26) on $\Omega := \Omega(\boldsymbol{\phi})$, respectively.

To prove the above proposition, we shall utilize three essential auxiliary results listed in the lemma below. The first result is the uniform Poincaré inequality established in [19, Corollary 3(ii)]. The second one pertains to the uniform continuity of the trace operator with respect to the domain exhibited in [21, Theorem 4], and the last one is about uniform extensions of the state variables from Ω_n to U such that their respective $H^1(U)$ -norms are bounded above by a positive number. More precisely, we have the following lemma.

Lemma 1.4.3. Let $\boldsymbol{\phi}_n, \boldsymbol{\phi} \in \mathfrak{A}_{\text{ad}}$ and $\Omega(\boldsymbol{\phi}_n), \Omega(\boldsymbol{\phi}) \in \tilde{\mathfrak{O}}_{\text{ad}}$. Then, the following results hold.

- (i) For every $\varphi \in H_{\Gamma,0}^1(\Omega)$, we have the estimate $\|\varphi\|_{L^2(\Omega)} \lesssim |\varphi|_{H^1(\Omega)}$ [19, Corollary 3(ii)].
- (ii) For all real number q such that $\frac{1}{2} < q \leq 1$ and functions $\varphi \in H^1(U)$, we have

$$\|\varphi\|_{L^2(\Sigma(\boldsymbol{\phi}))} \lesssim \|\varphi\|_{H^q(U)},$$

where $\|\cdot\|_{H^q(U)}$ denotes the $H^q(U)$ -norm [21, Theorem 4].

- (iii) There exists a uniform extension \tilde{z}_{Rn} (respectively \tilde{z}_{Nn}) of z_{Rn} (respectively z_{Nn}) from Ω_n to U and a real number $c_R > 0$ independent of n such that $\|\tilde{z}_{Rn}\|_{H^1(U)} \leq c_R$ (respectively $\|\tilde{z}_{Nn}\|_{H^1(U)} \leq c_N$, where $c_N > 0$ is a real number).

Note that we only need to prove the third result stated above because the first two results were already proven in [19, 21]. Before we do that, we first make the following comments. Regarding Lemma 1.4.3(ii), we mention that due to assumption **(P3)** and the uniform cone property of the domain $\Omega(\boldsymbol{\phi}) \in \tilde{\mathfrak{O}}_{\text{ad}}$, the norm of the trace map $\gamma(\cdot) = \cdot|_{\Sigma} : H_0^1(U) \rightarrow L^2(\Sigma(\boldsymbol{\phi}))$ can actually be bounded uniformly with respect to $\Omega(\boldsymbol{\phi}) \in \tilde{\mathfrak{O}}_{\text{ad}}$, see [90]. On the other hand, we note that Lemma 1.4.3(iii) assures the existence of a subsequence of $\{\tilde{z}_{Rn}\}$ (respectively $\{\tilde{z}_{Nn}\}$) which weakly converges in $H^1(U)$ to a limit denoted by \tilde{z}_R (respectively \tilde{z}_N). Hence, the proof of Proposition 1.4.1 is completed by showing that the restriction of \tilde{z}_R (respectively \tilde{z}_N) in $\Omega(\boldsymbol{\phi})$ coincides with the unique solution of (1.26) (respectively (1.25)). We provide the proof of the third result from the previous lemma below.

Proof of Lemma 1.4.3(iii) For simplicity, we use the notation $(\cdot)_n := (\cdot)(\boldsymbol{\phi}_n)$. From [30], we know that the solution z_{Rn} of (1.26) on Ω_n admits an extension \tilde{z}_{Rn} in $H^1(U)$ such that

$$\|\tilde{z}_{Rn}\|_{H^1(U)} \lesssim \|z_{Rn}\|_{H^1(\Omega_n)}.$$

Therefore, to obtain our desired result, we need to show that $\|z_{Rn}\|_{H^1(\Omega_n)}$ is bounded with respect to n . In view of (1.24), taking $\varphi = z_{Rn} \in H_{\Gamma,0}^1(\Omega_n)$, we have

$$\int_{\Omega_n} |\nabla z_{Rn}|^2 dx + \int_{\Sigma_n} \beta |z_{Rn}|^2 d\sigma = - \int_{\Omega_n} \nabla u_{R0} \cdot \nabla z_{Rn} dx + \int_{\Sigma_n} \lambda z_{Rn} d\sigma.$$

This leads to

$$(1.36) \quad \|z_{Rn}\|_{H^1(\Omega_n)}^2 \leq |u_{R0}|_{H^1(U)} \|z_{Rn}\|_{H^1(\Omega_n)} + |\lambda| |U|^{1/2} \|z_{Rn}\|_{L^2(\Sigma_n)}.$$

Next, we show that $\|z_{Rn}\|_{L^2(\Sigma_n)}$ can be bounded by $\|z_{Rn}\|_{H^1(\Omega_n)}$. To do this, we utilize the first two results stated in Lemma 1.4.3 to obtain

$$\|z_{Rn}\|_{L^2(\Sigma_n)} \lesssim \|\tilde{z}_{Rn}\|_{H^1(U)} \lesssim \|z_{Rn}\|_{H^1(\Omega_n)} \lesssim \|z_{Rn}\|_{H^1(\Omega_n)}.$$

Going back to (1.36), we get

$$|z_{Rn}|_{H^1(\Omega_n)} \lesssim \|u_{R0}\|_{H^1(U)} + |\lambda||U|^{1/2}.$$

Applying Lemma 1.4.3(i) once more, we obtain

$$\|z_{Rn}\|_{H^1(\Omega_n)} \lesssim \|u_{R0}\|_{H^1(U)} + |\lambda||U|^{1/2}.$$

This establishes the boundedness of $\{\|\tilde{z}_{Rn}\|_{H^1(U)}\}$. Using a similar line of arguments, we can also show that there exists a uniform extension \tilde{z}_{Nn} of z_{Nn} from Ω_n to U and a constant $c_N > 0$ independent of n such that $\|\tilde{z}_{Nn}\|_{H^1(U)} \leq c_N$. (In fact, taking $\beta = 0$ in the proof easily verifies the statement.) ■

The following result, which is a consequence of Lemma 1.4.3(ii) (see [21, Corollary 2] and also [20, Corollary 1]), is also central to the proof of Proposition 1.4.1 (as well as in showing the lower semi-continuity of the cost functionals) that we will provide shortly.

Lemma 1.4.4 ([20, 21]). Let $\phi \in \mathfrak{V}_{\text{ad}}$ and $\{\phi_n\} \subset \mathfrak{V}_{\text{ad}}$ such that $\phi_n \xrightarrow{C^1} \phi$ on $[0, 1]$. Then, for any $\varphi \in H^1(U)$, we have $\lim_{n \rightarrow \infty} \varphi \circ \phi_n = \varphi \circ \phi$ in $L^2([0, 1])$.

Proof of Proposition 1.4.1 The first convergence easily follows from the compactness of \mathfrak{V}_{ad} and the Arzelà-Ascoli theorem 1.2.1. Hence, we only need to show the validity of the last two convergences. We only prove the convergence $\tilde{z}_{Rk} \rightarrow z_R$ in $H^1(U)$ since the proof for the other one is similar.

Firstly, from Lemma 1.4.3(iii), we know $\{\tilde{z}_{Rn}\}$ is a bounded sequence in $H^1(U)$. Therefore, we can extract a subsequence $\{\tilde{z}_{Rk}\}$ of $\{\tilde{z}_{Rn}\}$ which weakly converges in $H^1(U)$ to a limit denoted by \tilde{z}_R ; that is, $\tilde{z}_{Rk} \rightharpoonup \tilde{z}_R$ in $H^1(U)$. Now, the boundedness of the trace operator implies that $z_R = \tilde{z}_R|_{\Omega(\phi)}$ is in $H_{\Gamma,0}^1(\Omega(\phi))$. Indeed, for Lipschitz (fixed) boundary Γ , the trace operator $\cdot|_{\Gamma} : H^1(U) \rightarrow L^2(\Gamma)$ is compact, hence, it takes weakly convergent sequences into strongly convergent sequences. In particular, we have the limit $\lim_{k \rightarrow \infty} \tilde{z}_{Rk}|_{\Gamma} = \tilde{z}_R|_{\Gamma}$ in $L^2(\Gamma)$. Note that $\tilde{z}_{Rk}|_{\Omega(\phi_k)} = z_{Rk}$. Hence, $z_R|_{\Gamma} = \lim_{k \rightarrow \infty} \tilde{z}_{Rk}|_{\Gamma} = \lim_{k \rightarrow \infty} z_{Rk}|_{\Gamma} = 0$ which implies that $z_R \in H_{\Gamma,0}^1(\Omega(\phi))$.

Then, we will show that $z_R(\phi) = \tilde{z}_R|_{\Omega(\phi)}$ is the solution of (1.24) on $\Omega(\phi)$. In fact, we will show that the variational equation

$$(1.37) \quad \int_{\Omega(\phi)} \nabla z_R \cdot \nabla \varphi \, dx + \int_{\Omega(\phi)} \nabla u_{R0} \cdot \nabla \varphi \, dx + \int_{\Sigma(\phi)} \beta z_R \varphi \, d\sigma - \int_{\Sigma(\phi)} \lambda \varphi \, d\sigma = 0, \quad \forall \varphi \in H_{\Gamma,0}^1(\Omega(\phi)),$$

also holds for all test functions $\varphi \in H_{\Gamma,0}^1(U) = \{\tilde{\varphi} \in H^1(U) : \tilde{\varphi} = 0 \text{ on } \Gamma\}$. Clearly, the restriction on $\Omega_k := \Omega(\phi_k)$ of any element φ of $H_{\Gamma,0}^1(U)$ is in $H_{\Gamma,0}^1(\Omega_k)$, for all k , which is exactly the test space of (1.24) on Ω_k . Therefore, we have

$$(1.38) \quad \int_{\Omega_k} \nabla z_{Rk} \cdot \nabla \varphi \, dx + \int_{\Omega_k} \nabla u_{R0} \cdot \nabla \varphi \, dx + \int_{\Sigma_k} \beta z_{Rk} \varphi \, d\sigma - \int_{\Sigma_k} \lambda \varphi \, d\sigma = 0, \quad \forall \varphi \in H_{\Gamma,0}^1(U).$$

Next, we prove that, by passing to the limit, we will obtain (1.37) from (1.38). To see this, we simply take the difference of equations (1.37) and (1.38) and then let $k \rightarrow \infty$. As for the difference of the last two integrals, we have

$$\begin{aligned}
 \mathbb{I}_4(k) &:= \left| \int_{\Sigma(\phi_k)} \lambda \varphi \, d\sigma - \int_{\Sigma(\phi)} \lambda \varphi \, d\sigma \right| \\
 &\lesssim \left| \int_0^1 \{(\varphi \circ \phi_k)(t) |\dot{\phi}_k(t)| - (\varphi \circ \phi)(t) |\dot{\phi}(t)|\} \, dt \right| \\
 &\lesssim \left| \int_0^1 (\varphi \circ \phi_k - \varphi \circ \phi) |\dot{\phi}_k(t)| \, dt \right| + \left| \int_0^1 (\varphi \circ \phi) (|\dot{\phi}_k(t)| - |\dot{\phi}(t)|) \, dt \right| \\
 &\lesssim \|\varphi \circ \phi_k - \varphi \circ \phi\|_{L^2([0,1])} + \sup_{[0,1]} |\dot{\phi}_k - \dot{\phi}| \|\varphi\|_{L^2(\Sigma(\phi))},
 \end{aligned}$$

where we applied assumption **(P2)** in the last inequality. Because $\varphi \in H_{\Gamma,0}^1(U) \subset H^1(U)$, then by [20, Corollary 1] we have the limit $\lim_{k \rightarrow \infty} \|\varphi \circ \phi_k - \varphi \circ \phi\|_{L^2([0,1])} = 0$, for any sequence $\{\phi_k\} \subset \mathfrak{A}_{\text{ad}}$ and element $\phi \in \mathfrak{A}_{\text{ad}}$ such that $\phi_k \xrightarrow{C^1} \phi$ (cf. Lemma 1.4.4). Furthermore, in view of Lemma 1.4.3(ii) we get the estimate $\|\varphi\|_{L^2(\Sigma(\phi))} \lesssim \|\varphi\|_{H^1(U)}$. Thus, by the uniform convergence $\dot{\phi}_k \rightarrow \dot{\phi}$ in $[0, 1]$ (cf. (1.30)), we deduce that $\lim_{k \rightarrow \infty} \mathbb{I}_4(k) = 0$, as desired.

Similarly, we have

$$\begin{aligned}
 \mathbb{I}_3(k) &:= \left| \int_{\Sigma(\phi_k)} \beta z_{\text{R}k} \varphi \, d\sigma - \int_{\Sigma(\phi)} \beta z_{\text{R}} \varphi \, d\sigma \right| \\
 &\lesssim \left| \int_0^1 \{(z_{\text{R}k} \circ \phi_k)(\varphi \circ \phi_k)(t) |\dot{\phi}_k(t)| - (z_{\text{R}} \circ \phi)(\varphi \circ \phi)(t) |\dot{\phi}(t)|\} \, dt \right| \\
 &\lesssim \left| \int_0^1 (z_{\text{R}k} \circ \phi_k - z_{\text{R}} \circ \phi)(\varphi \circ \phi_k) |\dot{\phi}_k| \, dt \right| + \left| \int_0^1 (z_{\text{R}k} \circ \phi - z_{\text{R}} \circ \phi)(\varphi \circ \phi_k) |\dot{\phi}_k| \, dt \right| \\
 &\quad + \left| \int_0^1 (z_{\text{R}} \circ \phi)(\varphi \circ \phi_k - \varphi \circ \phi) |\dot{\phi}_k| \, dt \right| + \left| \int_0^1 (z_{\text{R}} \circ \phi)(\varphi \circ \phi) (|\dot{\phi}_k| - |\dot{\phi}|) \, dt \right| \\
 &\lesssim \|\varphi\|_{L^2(\Sigma(\phi_k))} \|z_{\text{R}k} \circ \phi_k - z_{\text{R}} \circ \phi\|_{L^2([0,1])} + \|\varphi\|_{L^2(\Sigma(\phi_k))} \|z_{\text{R}k} - z_{\text{R}}\|_{L^2(\Sigma(\phi))} \\
 &\quad + \|z_{\text{R}}\|_{L^2(\Sigma(\phi))} \|\varphi \circ \phi_k - \varphi \circ \phi\|_{L^2([0,1])} + \sup_{[0,1]} |\dot{\phi}_k - \dot{\phi}| \|z_{\text{R}}\|_{L^2(\Sigma(\phi))} \|\varphi\|_{L^2(\Sigma(\phi))}.
 \end{aligned}$$

Now, using the fact that $z_{\text{R}k} = \tilde{z}_{\text{R}k}|_{\Omega(\phi_k)} \in H^1(U)$, together with Lemma 1.4.3(ii), we deduce, via the application of [20, Corollary 1], that the first and the third summands in the last inequality above eventually vanished. Again, from Lemma 1.4.3(ii), and the compactness of the injection of $H^1(U)$ into $H^q(U)$ for $q \in (\frac{1}{2}, 1)$, we get

$$\|\varphi\|_{L^2(\Sigma(\phi_k))} \|z_{\text{R}k} - z_{\text{R}}\|_{L^2(\Sigma(\phi))} \lesssim \|\varphi\|_{H^1(U)} \|\tilde{z}_{\text{R}k} - \tilde{z}_{\text{R}}\|_{H^q(U)} \xrightarrow{k \rightarrow \infty} 0.$$

Likewise, we have

$$\sup_{[0,1]} |\dot{\phi}_k - \dot{\phi}| \|z_{\text{R}}\|_{L^2(\Sigma(\phi))} \|\varphi\|_{L^2(\Sigma(\phi))} \lesssim \sup_{[0,1]} |\dot{\phi}_k - \dot{\phi}| \|\tilde{z}_{\text{R}}\|_{H^1(U)} \|\varphi\|_{H^1(U)} \xrightarrow{k \rightarrow \infty} 0$$

because of (1.30). Therefore, we also have $\lim_{k \rightarrow \infty} \mathbb{I}_3(k) = 0$.

Last but not least, we have the differences

$$\begin{aligned} \mathbb{l}_1(k) &:= \int_{\Omega(\phi_k)} \nabla z_{Rk} \cdot \nabla \varphi \, dx - \int_{\Omega(\phi)} \nabla z_R \cdot \nabla \varphi \, dx \\ &= \int_U \chi_\Omega (\nabla \tilde{z}_{Rk} - \nabla \tilde{z}_R) \cdot \nabla \varphi \, dx + \int_U (\chi_{\Omega(\phi_k)} - \chi_\Omega) \nabla \tilde{z}_{Rk} \cdot \nabla \varphi \, dx; \\ \mathbb{l}_2(k) &:= \int_{\Omega(\phi_k)} \nabla u_{R0} \cdot \nabla \varphi \, dx - \int_{\Omega(\phi)} \nabla u_{R0} \cdot \nabla \varphi \, dx = \int_U (\chi_{\Omega(\phi_k)} - \chi_\Omega) \nabla u_{R0} \cdot \nabla \varphi \, dx. \end{aligned}$$

The desired limits $\lim_{k \rightarrow \infty} \mathbb{l}_1(k) = 0$ and $\lim_{k \rightarrow \infty} \mathbb{l}_2(k) = 0$ are obtained by applying the weak convergence $\tilde{z}_{Rk} \rightharpoonup \tilde{z}_R$ in $H^1(U)$ combined with the convergence of characteristic functions (see, e.g., [73, Prop. 2.2.28, p. 45]):

$$(1.39) \quad \chi_{\Omega_k} \rightarrow \chi_\Omega \quad \text{in } L^\infty(U)\text{-weak}^*,$$

and the fact that the sequence $\{\|\tilde{z}_{Rk}\|_{H^1(U)}\}$ is bounded.

In conclusion, $z_R(\phi) = \tilde{z}_R|_{\Omega(\phi)}$ is the solution of (1.24) on $\Omega(\phi)$.

Adopting a similar line of arguments, we can also show that there exists a sequence of uniform extensions $\{\tilde{z}_{Nk}\}$ of $\{z_{Nk}\}$ which is uniformly bounded in $H^1(U)$; that is, $\{\|\tilde{z}_{Nk}\|_{H^1(U)}\}$ is bounded. By this result, we can also prove that the limit of that sequence is $z_N(\phi) = \tilde{z}_N|_{\Omega(\phi)}$ which is in fact the solution of (1.23) on $\Omega(\phi)$. This completes the proof of Proposition 1.4.1. \blacksquare

Lower Semi-Continuity of the Cost Functions

To complete the proof of Proposition 1.4.2, let us now establish the lower semi-continuity of the cost functions J_i , $i = 1, 2, 3$, in the next proposition. Here, we will use the equivalence between the variational equations (1.23) (respectively (1.24)) and (1.25) (respectively (1.26)).

Proposition 1.4.2. The cost functionals

$$\begin{aligned} J_1(\Sigma) &:= J_1(\Omega, z_N(\Omega), z_R(\Omega)) = \frac{1}{2} \int_\Sigma \left| \frac{\partial}{\partial \mathbf{n}} z_R(\Omega) - \lambda \right|^2 \, d\sigma, \\ J_2(\Omega) &:= J_2(\Omega, z_N(\Omega), z_R(\Omega)) = \frac{1}{2} \int_\Omega |\nabla(z_R(\Omega) - z_N(\Omega))|^2 \, dx, \\ J_3(\Sigma) &:= J_3(\Omega, z_N(\Omega), z_R(\Omega)) = \frac{1}{2} \int_\Sigma |z_R(\Omega) - z_N(\Omega)|^2 \, d\sigma, \end{aligned}$$

are lower semicontinuous on \mathfrak{G}_1 , \mathfrak{G}_2 , and \mathfrak{G}_3 in the topology induced by (1.29), respectively.

To prove the proposition, we will exploit the parametrization of the free boundary defined in Definition 1.4.3. Its properties stated in assumption **(P3)** will be used implicitly many times in the proof.

Proof. Let $\{(\Omega_n, z_{Nn}, z_{Rn})\}$ be a sequence in \mathfrak{G}_2 , $\Omega_n := \Omega(\boldsymbol{\phi}_n)$, and assume that $(\Omega_n, z_{Nn}, z_{Rn}) \rightarrow (\Omega, z_N, z_R)$ as $n \rightarrow \infty$, where $\Omega := \Omega(\boldsymbol{\phi})$ and the triple (Ω, z_N, z_R) is in \mathfrak{G}_2 . We point out here that the graph \mathfrak{G}_2 is basically the same with \mathfrak{G}_3 , so, we may view $\{(\Omega_n, z_{Nn}, z_{Rn})\}$ as a sequence in \mathfrak{G}_3 and that the triple (Ω, z_N, z_R) is also in \mathfrak{G}_3 . For convenience, we let $w = z_N - z_R$ and $w_n = z_{Nn} - z_{Rn}$ and their extensions in $H^1(U)$ by \tilde{w}_n and \tilde{w} , respectively. Here, we emphasize that $w = \tilde{w}|_\Omega$ is in $H_{\Gamma,0}^1(\Omega)$ which is of course due to the boundedness of the trace operator. Also, we recall that for any $\varphi \in H_{\Gamma,0}^1(U)$, the restriction $\varphi|_{\Omega_n}$ is in $H_{\Gamma,0}^1(\Omega_n)$.

We only prove the case for J_2 and J_3 since the proof for the lower semi-continuity of J_1 is essentially the same with that of J_3 . Also, we emphasize we can use the lower semicontinuity of J_2 to prove the lower semicontinuity of J_3 . However, we shall prove the lower semicontinuity of the latter using a slightly different approach from the former one.

Lower semi-continuity of the cost function J_2 .

We start with the proof of the lower semi-continuity of J_2 . In doing so, we apply the identity $a^2 - b^2 = (a - b)^2 + 2b(a - b)$. First, we note that

$$\begin{aligned} J_2(\Omega(\boldsymbol{\phi}_n)) - J_2(\Omega(\boldsymbol{\phi})) &= \frac{1}{2} \int_{\Omega_n} |\nabla \tilde{w}_n|^2 dx - \frac{1}{2} \int_{\Omega} |\nabla \tilde{w}|^2 dx \\ &= \frac{1}{2} \int_U (\chi_{\Omega_n} - \chi_{\Omega}) |\nabla \tilde{w}_n|^2 dx + \frac{1}{2} \int_U \chi_{\Omega} (|\nabla \tilde{w}_n|^2 - |\nabla \tilde{w}|^2) dx \\ &=: \mathbb{I}_1(n) + \mathbb{I}_2(n). \end{aligned}$$

Using (1.39) and the fact that $\{\tilde{w}_n\}$ is a bounded sequence in $H^1(U)$ (see Lemma 1.4.3(iii)), we obtain $\lim_{n \rightarrow \infty} \mathbb{I}_1(n) = 0$. Meanwhile, by the (weak) lower semicontinuity of the $H^1(\Omega)$ -norm (see, e.g., [28, Remark 1.3.1]) and the equivalence of the $H^1(\Omega)$ -seminorm and the $H^1(\Omega)$ -norm on $H_{\Gamma,0}^1(\Omega)$, we know that

$$\liminf_{n \rightarrow \infty} \left\{ \int_{\Omega} (|\nabla \tilde{w}_n|^2 - |\nabla \tilde{w}|^2) dx \right\} \geq 0.$$

Therefore, $\liminf_{n \rightarrow \infty} \{J_2(\Omega(\boldsymbol{\phi}_n)) - J_2(\Omega(\boldsymbol{\phi}))\} \geq 0$, or equivalently,

$$J_2(\Omega, z_N, z_R) \leq \liminf_{n \rightarrow \infty} J_2(\Omega_n, z_{Nn}, z_{Rn}),$$

which is desired.

Lower semi-continuity of the cost function J_3 .

For the third cost function J_3 , we have

$$\begin{aligned} |J_3(\Sigma(\boldsymbol{\phi}_n)) - J_3(\Sigma(\boldsymbol{\phi}))| &= \frac{1}{2} \left| \int_{\Sigma(\boldsymbol{\phi}_n)} |w_n|^2 d\sigma - \int_{\Sigma(\boldsymbol{\phi})} |w|^2 d\sigma \right| \\ &\lesssim \left| \int_0^1 \left\{ |(w_n \circ \boldsymbol{\phi}_n)(t)|^2 |\dot{\boldsymbol{\phi}}_n(t)| - |(w \circ \boldsymbol{\phi})(t)|^2 |\dot{\boldsymbol{\phi}}(t)| \right\} dt \right| \\ &\lesssim \left| \int_0^1 \left\{ (w_n \circ \boldsymbol{\phi}_n)^2 - (w \circ \boldsymbol{\phi})^2 \right\} |\dot{\boldsymbol{\phi}}_n| dt \right| + \left| \int_0^1 (w \circ \boldsymbol{\phi})^2 (|\dot{\boldsymbol{\phi}}_n| - |\dot{\boldsymbol{\phi}}|) dt \right| \\ &=: \mathbb{J}_1(n) + \mathbb{J}_2(n), \end{aligned}$$

where $\Sigma_n := \Sigma(\boldsymbol{\phi}_n)$. We first look for an estimate for the second integral \mathbb{J}_2 . Towards this end, we apply the estimates in Lemma 1.4.3 and the compactness of the injection of $H^1(U)$ into $H^q(U)$ for $q \in (\frac{1}{2}, 1)$, to obtain

$$\mathbb{J}_2(n) \lesssim \sup_{[0,1]} |\dot{\boldsymbol{\phi}}_n - \dot{\boldsymbol{\phi}}| \|w\|_{L^2(\Sigma(\boldsymbol{\phi}))}^2 \lesssim \sup_{[0,1]} |\dot{\boldsymbol{\phi}}_n - \dot{\boldsymbol{\phi}}| \|\tilde{w}\|_{H^1(U)}^2 \lesssim \sup_{[0,1]} |\dot{\boldsymbol{\phi}}_n - \dot{\boldsymbol{\phi}}|.$$

Using the assumption that $\boldsymbol{\phi}_n \xrightarrow{C^1} \boldsymbol{\phi}$ on $[0, 1]$ (see (1.30)), we get the limit $\lim_{n \rightarrow \infty} \mathbb{J}_2(n) = 0$.

On the other hand, to get an estimate for the first integral \mathbb{J}_1 , we again make use of the identity $a^2 - b^2 = (a - b)^2 + 2b(a - b)$ to obtain

$$\begin{aligned} \mathbb{J}_1 &\lesssim \left| \int_0^1 (w_n \circ \boldsymbol{\phi}_n - w \circ \boldsymbol{\phi})^2 |\dot{\boldsymbol{\phi}}_n| dt \right| + \left| \int_0^1 (w \circ \boldsymbol{\phi})(w_n \circ \boldsymbol{\phi}_n - w \circ \boldsymbol{\phi}) |\dot{\boldsymbol{\phi}}_n| dt \right| \\ &=: \mathbb{J}_{11} + \mathbb{J}_{12}. \end{aligned}$$

For \mathbb{J}_{12} , we have the estimate

$$\begin{aligned} \mathbb{J}_{12} &\leq \left| \int_0^1 (w \circ \boldsymbol{\phi})(w_n \circ \boldsymbol{\phi}_n - w \circ \boldsymbol{\phi}_n) |\dot{\boldsymbol{\phi}}_n| dt \right| + \left| \int_0^1 (w \circ \boldsymbol{\phi})(w \circ \boldsymbol{\phi}_n - w \circ \boldsymbol{\phi}) |\dot{\boldsymbol{\phi}}_n| dt \right| \\ &\lesssim \|w\|_{L^2(\Sigma)} (\|w_n - w\|_{L^2(\Sigma_n)} + \|w \circ \boldsymbol{\phi}_n - w \circ \boldsymbol{\phi}\|_{L^2([0,1])}) \\ &\lesssim \|\tilde{w}_n - \tilde{w}\|_{H^q(U)} + \|w \circ \boldsymbol{\phi}_n - w \circ \boldsymbol{\phi}\|_{L^2([0,1])}. \end{aligned}$$

Meanwhile, for \mathbb{J}_{11} , we have

$$\begin{aligned} \mathbb{J}_{11} &\lesssim \left| \int_0^1 (w_n \circ \boldsymbol{\phi}_n - w \circ \boldsymbol{\phi}_n)^2 |\dot{\boldsymbol{\phi}}_n| dt \right| + \left| \int_0^1 (w_n \circ \boldsymbol{\phi}_n - w \circ \boldsymbol{\phi}_n)(w \circ \boldsymbol{\phi}_n - w \circ \boldsymbol{\phi}) |\dot{\boldsymbol{\phi}}_n| dt \right| \\ &\quad + \left| \int_0^1 (w \circ \boldsymbol{\phi}_n - w \circ \boldsymbol{\phi})^2 |\dot{\boldsymbol{\phi}}_n| dt \right| \\ &\lesssim \|w_n - w\|_{L^2(\Sigma_n)}^2 + \|w_n - w\|_{L^2(\Sigma_n)} (\|w\|_{L^2(\Sigma_n)} + \|w\|_{L^2(\Sigma)}) + \|w \circ \boldsymbol{\phi}_n - w \circ \boldsymbol{\phi}\|_{L^2([0,1])} \\ &\lesssim \|\tilde{w}_n - \tilde{w}\|_{H^q(U)} + \|w \circ \boldsymbol{\phi}_n - w \circ \boldsymbol{\phi}\|_{L^2([0,1])}. \end{aligned}$$

The previous two estimates were obtained using the inequalities in Lemma 1.4.3. Putting them together yields

$$\mathbb{J}_1 \lesssim \|\tilde{w}_n - \tilde{w}\|_{H^q(U)} + \|w \circ \boldsymbol{\phi}_n - w \circ \boldsymbol{\phi}\|_{L^2([0,1])}.$$

Again, applying Lemma 1.4.4, the compactness of the injection of $H^1(U)$ into $H^q(U)$ for $q \in (\frac{1}{2}, 1)$, the convergences $\tilde{w}_n \rightharpoonup \tilde{w}$ in $H^1(U)$ -weak, and the uniform convergence $\boldsymbol{\phi}_n \rightarrow \boldsymbol{\phi}$ in the $C^1([0, 1], \mathbb{R}^2)$ -norm (see (1.30)), we finally obtain $\lim_{n \rightarrow \infty} \mathbb{J}_1 = 0$. This, together with the first result established earlier, proves the limit $\lim_{n \rightarrow \infty} |J_3(\Sigma(\boldsymbol{\phi}_n)) - J_3(\Sigma(\boldsymbol{\phi}))| = 0$. Consequently, we find that

$$\lim_{n \rightarrow \infty} J_3(\Omega_n, z_{Nn}, z_{Rn}) = J_3(\Omega, z_N, z_R);$$

that is, J_3 is continuous, and in particular, lower semicontinuous. ■

To end this section, let us finally provide the proof of Proposition 1.4.2 using propositions 1.4.1 and 1.4.2.

Proof of Theorem 1.4.2 We only prove the case for the third proposed formulation since the proofs for the first two are similar. So, we let $(\Omega_n, z_{Nn}, z_{Rn})$, $\Omega_n = \Omega(\phi_n)$, be a minimizing sequence for the cost function J_3 ; that is, $(\Omega_n, z_{Nn}, z_{Rn})$ is such that

$$\lim_{n \rightarrow \infty} J_3(\Omega_n, z_{Nn}, z_{Rn}) = \inf\{J_3(\Omega, z_N, z_R) : (\Omega, z_N, z_R) \in \mathfrak{G}_3\}.$$

We apply Proposition 1.4.1 to obtain a subsequence $(\Omega_k, z_{Nk}, z_{Rk})$ and an element $\Omega = \Omega(\phi) \in \mathcal{O}_{\text{ad}}$ such that $\Omega_k \rightarrow \Omega$ (i.e., $\phi_k \rightarrow \phi$ uniformly in the C^1 topology), $\tilde{z}_{Nk} \rightarrow \tilde{z}_N$, $\tilde{z}_{Rk} \rightarrow \tilde{z}_R$ in $H^1(U)$, and the functions $\tilde{z}_N|_{\Omega}$ and $\tilde{z}_R|_{\Omega}$ are the solutions to the variational equations (1.23) and (1.24) in Ω , respectively. Using these, together with the continuity of J_3 proved in Proposition 1.4.2, we conclude, by virtue of [71, Theorem 2.10])

$$J_3(\Omega, \tilde{z}_N|_{\Omega}, \tilde{z}_R|_{\Omega}) = \lim_{k \rightarrow \infty} J_3(\Omega_k, z_{Nk}, z_{Rk}) = \inf\{J_3(\Omega, z_N, z_R) : (\Omega, z_N, z_R) \in \mathfrak{G}_3\}.$$

■

It is worth emphasizing that in [1, 13–15, 49–51, 100, 101], the authors did not tackle the question of existence of optimal solution of the shape optimization problems examined in their papers. Nevertheless, in [49–51], the authors tacitly supposed the existence of optimal domains and assumed that the domains in consideration are sufficiently regular to accomplish their objectives. Moreover, the regularities of the domains examined in the rest of the aforementioned papers also possess enough regularity for the existence of optimal shapes. Here, as already mentioned, we followed the ideas in [21, 68, 71] to address the existence issue for our proposed shape problems. Of course, similar analyses can be done for the classical settings if one wishes to carry out the same issue.

SHAPE SENSITIVITY ANALYSES

Contents

	Page
2.1 Tools for Shape Optimization	34
2.1.1 Two Methods for Domain Perturbation	34
2.1.2 Some Properties of the Perturbation of the Identity Operator	36
2.1.3 Some Identities from Tangential Calculus	39
2.1.4 Material and Shape Derivatives	40
2.2 Shape Derivative of J_1	45
2.2.1 The Minimax Formulation	45
2.2.2 The Shape Gradient of J_1	49
2.3 Shape Derivative of J_2	55
2.3.1 The Shape Gradient of J_2	56
2.3.2 The Shape Hessian of J_2	59
2.4 Shape Derivative of J_3	63
2.4.1 The Shape Gradient of J_3	63
2.4.2 The Shape Hessian of J_3	66
2.4.3 The Shape Derivative of the Adjoint State	68
2.4.4 Symmetricity of the Shape Hessian of J_3 at a Critical Shape	72
2.5 Coercivity Estimates for the Shape Hessians at the Optimal Solution	76

The main goal of this chapter is to characterize the shape derivatives of the cost functions introduced in the last chapter. In this direction, we will derive the first-order *Eulerian semi-derivative* of the cost function J_1 using the *minimax formulation* while we will derive the

expressions for both the first- and second-order Eulerian semi-derivatives of the cost functions J_2 and J_3 using the chain rule approach. We intend to derive the first-order Eulerian semi-derivative of J_1 via the minimax formulation in order to showcase the advantage of using the Robin problem over the Dirichlet problem as a state constraint in proving the shape differentiability of the Neumann-data-tracking cost functional with respect to a local perturbation of the domain.

2.1 Tools for Shape Optimization

In this section we lay out the tools and essentials for the shape sensitivity analysis of the cost functionals J_i , $i = 1, 2, 3$. Also, the formal definitions of the terminology discussed in the previous section are given here. We reiterate that in the framework of shape optimization, the domain Ω does not belong to a vector space. This issue leads to the development of shape calculus to make sense of a “derivative” or a “gradient”. To date, the three most commonly used techniques in computing the Eulerian semi-derivative of a cost functional are the *Hadamard’s normal variation* method [63], the *perturbation of the identity* (POI) operator method due to [104], and the *velocity* method which involves the other two techniques (see, e.g., [29, 43, 114]).

In the next subsection, we will briefly discuss the latter two strategies for perturbing a domain as well as their equivalence under appropriate conditions. Although the results can be given in d -dimensional space, we will simply state them in \mathbb{R}^2 case.

2.1.1 Two Methods for Domain Perturbation

In this subsection, for the sake of simplicity, we use the notations $\mathcal{C}^0 := C([0, t_{\max}]; \mathbb{R}^2)$ and $\mathcal{C}^1 := C^1([0, t_{\max}]; \mathbb{R}^2)$, where t_{\max} is a (fixed) positive real number.

Velocity or Speed Method

We denote the vector \hat{V} as a time-dependent velocity fields so as to make distinction with velocity fields denoted by V which are not time dependent.

Let $\hat{V} : [0, t_{\max}] \times \mathbb{R}^2 \rightarrow \mathbb{R}^2$ be a given velocity field. The map \hat{V} can be viewed as a family $\{\hat{V}(t)\}$ of *non-autonomous* velocity fields on \mathbb{R}^2 defined by

$$x \mapsto \hat{V}(t)(x) := \hat{V}(t, x) : \mathbb{R}^2 \mapsto \mathbb{R}^2.$$

Here we suppose that \hat{V} is continuous in t and Lipschitz-continuous in spatial variables; that is,

$$(V1) \quad \forall x \in \mathbb{R}^2, \hat{V}(\cdot, x) \in \mathcal{C}^0, \text{ and}$$

$$(V2) \quad \forall x, y \in \mathbb{R}^2, \|\hat{V}(\cdot, y) - \hat{V}(\cdot, x)\|_{\mathcal{C}^0} \lesssim \|y - x\|,$$

where $\hat{V}(\cdot, x)$ denotes the function $t \mapsto \hat{V}(t, x)$. Associate with \hat{V} the solution $x(t; X)$ of the ordinary differential equation

$$\frac{d}{dt}x(t) = \hat{V}(t, x(t)), \quad t \in [0, t_{\max}], \quad x(0) = X \in \mathbb{R}^2.$$

In the case of *autonomous* velocity fields, the condition is simply

$$(\mathbf{V2}^\circ) \quad \forall x, y \in \mathbb{R}^2, \quad \|\mathbf{V}(x) - \mathbf{V}(y)\| \lesssim \|x - y\|.$$

The above statement can be described equivalently as follows. Let $\hat{V} \in \mathcal{E}^k := C([0, t_{\max}]; \mathcal{D}^k(\mathbb{R}^2, \mathbb{R}^2))$, for some integer $k \geq 2$, where $\mathcal{D}^k(\mathbb{R}^2, \mathbb{R}^2)$ denotes the space of all k -times continuous differentiable functions with compact support contained in \mathbb{R}^2 . Assume that $\Omega \subset \mathbb{R}^2$ is a smooth bounded domain with boundary that is at least twice differentiable. Then, $\hat{V}(t, x) \in \mathcal{D}^k(\mathbb{R}^2, \mathbb{R}^2)$ which may depend on $t \geq 0$. It generates the transformations

$$T_t(\hat{V})(X) := T_t(X) = x(t; X), \quad t \geq 0, \quad X \in \mathbb{R}^2$$

through the differential equation

$$(2.1) \quad \frac{d}{dt}x(t; X) = \hat{V}(t, x(t; X)), \quad x(0; X) = X,$$

with the initial value X given. By definition $T_0(X) = X$ and T_0 is essentially the identity operator I . Moreover, we remark that T_t is an evolution operator that verifies the usual semigroup property [42].

Perturbation of the Identity Operator Method

Let us now describe the relation between the velocity method and the POI operator method. The theorem below tells us that we can either start from a family of velocity fields $\{\hat{V}(t)\}$ on \mathbb{R}^2 or a family of transformations $\{T_t\}$ of \mathbb{R}^2 provided that the map \hat{V} , verifies **(V1)** and **(V2)** or the map $T(t, \cdot) = T_t$ verifies assumptions **(T1)**–**(T3)** given below.

Theorem 2.1.1 ([37, 41]). (i) Under assumptions (V1) and (V2) on the map \hat{V} , the maps T_t defined previously have the following properties:

$$(\mathbf{T1}) \quad \forall X \in \mathbb{R}^2, \quad T(\cdot, X) \in C^1, \quad \text{and} \quad \forall X, Y \in \mathbb{R}^2, \quad \|T(\cdot, Y) - T(\cdot, X)\|_{C^1} \lesssim |Y - X|,$$

$$(\mathbf{T2}) \quad \forall t \in [0, t_{\max}], \quad X \mapsto T_t(X) = T(t, X) : \mathbb{R}^2 \rightarrow \mathbb{R}^2 \text{ is bijective,}$$

$$(\mathbf{T3}) \quad \forall x \in \mathbb{R}^2, \quad T^{-1}(\cdot, x) \in C^0, \quad \text{and} \quad \forall x, y \in \mathbb{R}^2, \quad \|T^{-1}(\cdot, y) - T^{-1}(\cdot, x)\|_{C^0} \lesssim |y - x|.$$

(ii) If there exists a real number $t_{\max} > 0$ and a map $T : [0, t_{\max}] \times \mathbb{R}^2 \rightarrow \mathbb{R}^2$ verifying assumptions **(T1)**–**(T3)**, then the map

$$(t, x) \mapsto \hat{V}(t, x) = \frac{\partial}{\partial t} T(t, T^{-1}(x))$$

verifies assumptions **(V1)** and **(V2)**, where T_t^{-1} is the inverse of $X \mapsto T_t(X)$.

Clearly, the solution $\hat{\mathbf{V}}$ to (2.1) is essentially the POI operator T_t . Conversely, the POI operator method can be recasted in the velocity framework by choosing the velocity field $\hat{\mathbf{V}}(t) = \mathbf{V} \circ T_t^{-1}$ which satisfies (2.1). This relationship can be further explained as follows. Consider the transformation $x(t) = I + t\mathbf{V}$. Then, we have

$$\frac{d}{dt}x(t; X) = \mathbf{V}(X) = \hat{\mathbf{V}}(t, x(t; X)), \quad x(0) = X,$$

from which we get the equation $\mathbf{V}(X) = \hat{\mathbf{V}}(t, (I + t\mathbf{V})(X))$. Now, replacing X by $(I + t\mathbf{V})^{-1}(X)$, we get $\mathbf{V}(T_t^{-1}(X)) = \hat{\mathbf{V}}(t, X)$, or simply, $\hat{\mathbf{V}}(t) = \mathbf{V} \circ T_t^{-1}$. This is why many results obtained by the POI operator method can be acquired as well through the velocity method. See [43, Section 4.5.1] for further details.

2.1.2 Some Properties of the Perturbation of the Identity Operator

Let us now specify the set of deformation fields appropriate to our focused problem. Since we want the boundary Γ to remain invariant after a deformation (i.e., $T_t(\mathbf{V})(\Gamma) = \Gamma$, for all $t \geq 0$), then we assume that every admissible velocity field \mathbf{V} vanishes at Γ . Moreover, we want every deformation to preserve the regularity of the reference domain Ω . For instance, if we assume that Ω is of class $C^{k,1}$, $k \geq 0$, we also want $T_t(\Omega) =: \Omega_t$ to be (at least) of the same regularity class. To do this, we require \mathbf{V} to be at least $C^{k,1}$ regular. Therefore, given an integer $k \geq 2$, we consider a family of deformation fields given by

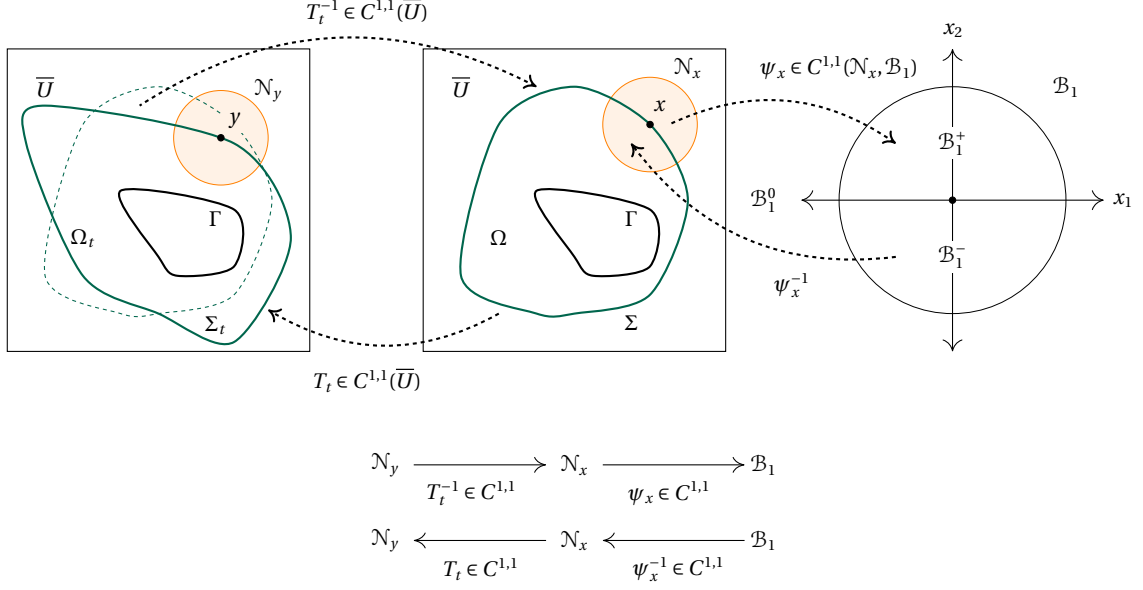
$$(2.2) \quad \Theta^k = \left\{ \mathbf{V} \in C^{k,1}(\bar{U}, \mathbb{R}^2) : \mathbf{V}|_{\Gamma \cup \partial U} = 0 \right\}.$$

Here, the larger set $U \subset \mathbb{R}^2$ denotes the *universal* or *hold-all* domain which contains all possible deformations of Ω (i.e., $\bar{\Omega}_t \subseteq U$, for all $t \geq 0$). Accordingly, we apply the POI operator method [43, Section 2.5.2, p. 147] to generate the desired class of perturbations of the domain Ω ; that is, we define T_t as follows

$$(2.3) \quad T_t = I + t\mathbf{V} : \bar{U} \rightarrow \mathbb{R}^2, \quad T_t(x) = x + t\mathbf{V}(x), \quad x \in \bar{U},$$

where the deformation field $\mathbf{V} := \mathbf{V}(x)$ is an element of Θ^k . For $t > 0$ sufficiently small, it can be shown that (i) $T_t : \bar{U} \rightarrow \bar{U}$ is a homeomorphism, and (ii) $T_t : U \rightarrow U$ is a $C^{k,1}$ diffeomorphism, and in particular, $T_t : \Omega \rightarrow \Omega_t$ is a $C^{k,1}$ diffeomorphism (cf. [14, Theorem 7]). Roughly speaking, these results tell us that, for sufficiently small t , the reference domain Ω and the perturbed domain Ω_t have the same topological structure and regularity under the POI operator T_t . An illustration of the action of T_t on a $C^{1,1}$ -domain is given in Figure 2.1.

In this thesis, we also want to derive the second-order Eulerian-semi derivative of the cost functionals J_i , $i = 1, 2, 3$. For this purpose, we need to perturb the reference domain Ω twice. Hence, for positive real numbers t and s , we consider the two transformations $T_t := T_t(\mathbf{V}) = I + t\mathbf{V}$ and $T_s := T_s(\mathbf{W}) = I + s\mathbf{W}$ where $\mathbf{V}, \mathbf{W} \in \Theta^2$. Note that, for sufficiently small positive real numbers t and s ,


 Figure 2.1: The action of T_t on a $C^{1,1}$ -domain

both T_t and T_s are $C^{2,1}$ diffeomorphisms. Therefore, the map $T_{t,s} := T_t \circ T_s : \Omega \rightarrow \Omega_{t,s}$ defined by

$$T_{t,s}(x) := T_t(T_s(x)) = x + s\mathbf{W}(x) + t\mathbf{V}(x + s\mathbf{W}(x)), \quad x \in \Omega,$$

may be shown to be a $C^{2,1}$ diffeomorphism too. Accordingly, we define the deformed domain $\Omega_{t,s}$ as $\Omega_{t,s} := T_t(T_s(\Omega)) = \{T_{t,s}(x) : x \in \Omega\}$. Consequently, for sufficiently small t and s , $\Omega_{t,s} \subset U$ is of class $C^{2,1}$.

Before we go further, it is worth to emphasize here that a direct of comparison between a function φ in Ω and a function φ_t defined in Ω_t is, in general, not possible because the functions are defined on different domains. To circumvent this issue, one maps φ_t back to the reference domain Ω by composing it with T_t ; that is, one utilizes the composition map $\varphi_t \circ T_t : \Omega \rightarrow \mathbb{R}$. Using this mapping, one can then define the domain and boundary integral transformations, derivatives of integrals over a perturbed domain, the material and the shape derivatives of a (scalar) function φ defined on Ω_t , as well as the Eulerian semi-derivatives of a shape functional.

Now, in what follows, we state some properties of the transformation $T_t = T_t(\mathbf{V})$ associated with the velocity field $\mathbf{V} \in \Theta^1$ which will serve useful in subsequent sections of this chapter. Throughout the rest of this thesis, we will denote the transformed domain $T_t(\mathbf{V})(\Omega)$ at $t \geq 0$ by $\Omega_t(\mathbf{V})$, or simply $\Omega_t := T_t(\Omega)$. We let t_{\max} be a sufficiently small positive number and denote the Jacobian matrix of T_t by DT_t . Then, for $t \in (0, t_{\max})$, the transformation T_t is invertible, $T_t, T_t^{-1} \in \mathcal{D}^1(\mathbb{R}^2, \mathbb{R}^2)$, and $\det DT_t > 0$. We identify $(DT_t)^{-1}$ and $(DT_t)^{-\top}$ as the inverse and inverse transpose of the Jacobian matrix DT_t , respectively, and, for convenience, we will use the notations

$$A(t) = \det DT_t (DT_t^{-1}) (DT_t)^{-\top} \quad \text{and} \quad B(t) = \det DT_t |(DT_t)^{-\top} \mathbf{n}|.$$

The latter expression is referred to as the cofactor matrix of the Jacobian matrix DT_t with respect to the boundary $\partial\Omega$ (see, e.g., [106, Proposition 2.47]). Using these notations, we recall the following integral transformations.

Lemma 2.1.2. Let $\varphi_t \in L^1(\Omega_t)$ and $\psi_t \in L^1(\partial\Omega_t)$, then $\varphi_t \circ T_t \in L^1(\Omega)$ and $\psi_t \circ T_t \in L^1(\partial\Omega)$, respectively. Moreover, the following transformations hold:

Domain Transformation [106, Section 2.16, p. 77]

$$\int_{\Omega_t} \varphi_t \, dx_t = \int_{\Omega} \det DT_t(\varphi_t \circ T_t) \, dx,$$

Boundary Transformation [106, Eq 2.116, p. 78]

$$\int_{\partial\Omega_t} \psi_t \, d\sigma_t = \int_{\partial\Omega} B(t)(\psi_t \circ T_t) \, d\sigma.$$

Moreover, we make the following observations for sufficiently small $t > 0$:

- | | |
|--|--|
| (i) $\det DT_t \in C^{0,1}(\bar{U})$, | (ii) $(DT_t)^{-1}, (DT_t)^{-\top} \in C(\bar{U}; \mathbb{R}^{2 \times 2})$, |
| (iii) $A(t) \in C(\bar{U}; \mathbb{R}^{2 \times 2})$, | (iv) $B(t) \in C(\Sigma; \mathbb{R})$. |

The following lemmas, whose proofs can be found in [43, 106], will be essential to our analysis.

Lemma 2.1.3. For a function $\varphi \in W_{loc}^{1,1}(\mathbb{R}^2)$ and $\mathbf{V} \in \Theta^1$, the following identities hold

- | | |
|--|--|
| (i) $\nabla(\varphi \circ T_t) = (DT_t)^\top (\nabla\varphi) \circ T_t$, | (ii) $\frac{d}{dt}(\varphi \circ T_t) = (\nabla\varphi \cdot \mathbf{V}(t)) \circ T_t$, |
| (iii) $\frac{d}{dt}(\varphi \circ T_t^{-1}) = -(\nabla\varphi \cdot \mathbf{V}(t)) \circ T_t^{-1}$, | (iv) $\frac{d}{dt} \det DT_t = (\operatorname{div}\mathbf{V}(t)) \circ T_t \det DT_t$. |

We emphasize that formula (iv) given in the previous lemma is well-defined because of Lemma 2.1.4(i) below.

Lemma 2.1.4. Let $\mathbf{V} \in \Theta^1$ and \mathcal{J} be the interval $(-t_{\max}, t_{\max})$ where $t_{\max} > 0$ is sufficiently small real number. Then, the following regularity properties of the transformation T_t hold

- | | |
|--|--|
| (i) $t \mapsto \det DT_t \in C^1(\mathcal{J}, C(\overline{\Omega}))$, | (ii) $t \mapsto A(t) \in C^1(\mathcal{J}, C^1(\overline{\Omega}))$, |
| (iii) $t \mapsto B(t) \in C^1(\mathcal{J}, C(\Sigma))$, | (iv) $\lim_{t \searrow 0} B(t) = 1$, |
| (v) $\frac{d}{dt} A(t) _{t=0} = A'(0) =: A$, | (vi) $\frac{d}{dt} B(t) _{t=0} = B'(0) =: B$, |

where

$$A'(0) = (\operatorname{div} \mathbf{V}) \mathbf{I}_2 - D\mathbf{V} - (D\mathbf{V})^\top \quad \text{and} \quad B'(0) = \operatorname{div}_\Sigma \mathbf{V} = \operatorname{div} \mathbf{V}|_\Sigma - (D\mathbf{V} \mathbf{n}) \cdot \mathbf{n},$$

and the limits defining the derivatives at $t = 0$ exist uniformly in $x \in \overline{\Omega}$.

The notation \mathbf{I}_2 appearing in $A'(0)$ denotes the identity matrix in two-dimension. Meanwhile, the operator $\operatorname{div}_\Sigma$ given above is referred to as the *tangential divergence* operator (see [43, p. 495]). Other tangential differential operators are given in the next subsection.

2.1.3 Some Identities from Tangential Calculus

We give below a formal definitions of some operators from tangential calculus that we will use in this work. For further details about these results, we refer the readers to [43, Chapter 9.5] or [106, Chapter 2] (see also [73]).

Definition 2.1.1. Let Σ be a boundary of a (sufficiently smooth) bounded domain $\Omega \subset \mathbb{R}^d$ and $\mathcal{N}(\Sigma)$ be a neighborhood of Σ . Consider a scalar function $\theta \in C^1(\Sigma)$ and let $\tilde{\theta}$ be any C^1 extension of θ into $\mathcal{N}(\Sigma)$. Similarly, consider a vector function $\boldsymbol{\theta} \in C^1(\Sigma, \mathbb{R}^d)$ and let $\tilde{\boldsymbol{\theta}}$ be any C^1 extension of $\boldsymbol{\theta}$ into $\mathcal{N}(\Sigma)$. Then, we have the following definitions.

Tangential Gradient The tangential gradient of a scalar function $\theta \in C^1(\Sigma)$ is given by

$$\nabla_\Sigma \theta := \nabla \tilde{\theta}|_\Sigma - \frac{\partial \tilde{\theta}}{\partial \mathbf{n}} \mathbf{n} \in C(\Sigma, \mathbb{R}^d).$$

Tangential Jacobian The tangential Jacobian matrix of $\boldsymbol{\theta} \in C^1(\Sigma, \mathbb{R}^d)$ is given by

$$D_\Sigma \boldsymbol{\theta} = D\tilde{\boldsymbol{\theta}}|_\Sigma - (D\tilde{\boldsymbol{\theta}} \mathbf{n}) \mathbf{n}^\top \in C(\Sigma, \mathbb{R}^{d \times d}).$$

Tangential Divergence For $\boldsymbol{\theta} \in C^1(\Sigma, \mathbb{R}^d)$, its tangential divergence is given by

$$\operatorname{div}_\Sigma \boldsymbol{\theta} = \operatorname{div} \tilde{\boldsymbol{\theta}}|_\Sigma - (D\tilde{\boldsymbol{\theta}} \mathbf{n}) \cdot \mathbf{n} \in C(\Sigma).$$

The details about the existence of extensions of θ and $\boldsymbol{\theta}$ can be found, for instance, in [43, Chapter 9.5]. It is worth remarking that the above definitions do not depend on the choice of the extension.

Let us also mention the following useful formulas.

Lemma 2.1.5. Consider a C^2 (or $C^{1,1}$) domain Ω with boundary $\partial\Omega = \Gamma \cup \Sigma$, $\Gamma \cap \Sigma = \emptyset$. Let $\theta \in H^1(\Sigma)$, $\mathbf{V} \in \Theta^1$, and κ denote the mean curvature of Σ . Then, the following formulas hold:

Tangential Divergence Formula [106, Eq. 2.140, p. 91]

$$\operatorname{div}_\Sigma(\theta \mathbf{V}) = \nabla_\Sigma \theta \cdot \mathbf{V} + \theta \operatorname{div}_\Sigma \mathbf{V};$$

Tangential Stokes' Formula [43, Eq. 5.26, p. 498]

$$\int_\Sigma \operatorname{div}_\Sigma \mathbf{V} \, d\sigma = \int_\Sigma \kappa \mathbf{V} \cdot \mathbf{n} \, d\sigma;$$

Tangential Green's Formula [43, Eq. 5.27, p. 498]

$$\int_\Sigma (\nabla_\Sigma \theta \cdot \mathbf{V} + \theta \operatorname{div}_\Sigma \mathbf{V}) \, d\sigma = \int_\Sigma \kappa \mathbf{V} \cdot \mathbf{n} \, d\sigma.$$

2.1.4 Material and Shape Derivatives

Here we formally state the definition of the material and shape derivatives of a scalar function φ defined in $[0, t_{\max}] \times U$.

Definition 2.1.2. Let φ be defined in $[0, t_{\max}] \times U$.

Material Derivative An element $\dot{\varphi} \in H^k(\Omega)$, called the material derivative of φ , is defined as

$$\dot{\varphi} = \lim_{t \searrow 0} \frac{\varphi(\Omega_t) \circ T_t - \varphi(\Omega)}{t} = \frac{d}{dt} (\varphi \circ T_t(\Omega)) \Big|_{t=0},$$

if the limit exists in $H^k(\Omega)$.

Shape Derivative An element $\varphi' \in H^k(\Omega)$, called the shape derivative of φ , is defined as

$$\varphi' = \lim_{t \searrow 0} \frac{\varphi(\Omega_t) - \varphi(\Omega)}{t},$$

where $(\varphi(\Omega_t) \circ T_t)(x) = \varphi(\Omega_t)(T_t(x))$.

Remark 2.1.1. In some literature, the material and shape derivatives of a (scalar) function φ is also expressed as

$$\dot{\varphi}(x) = \lim_{t \searrow 0} \frac{\varphi(t, T_t(x)) - \varphi(0, x)}{t} =: \left. \frac{d}{dt} \varphi(t, T_t(x)) \right|_{t=0} \quad \text{and} \quad \varphi'(x) = \lim_{t \searrow 0} \frac{\varphi(t, x) - \varphi(0, x)}{t},$$

respectively.

If the derivatives defined previously are obtained via the velocity field \mathbf{V} , then these expressions are related by

$$(2.4) \quad \varphi' = \dot{\varphi} - (\nabla \varphi \cdot \mathbf{V})$$

provided that $\nabla \varphi \cdot \mathbf{V}$ exists in some appropriate function space. In general, for bounded C^k domains, if $\dot{\varphi}$ and $\nabla \varphi \cdot \mathbf{V}$ both exist in the Sobolev space $W^{m,p}(\Omega)$, $0 \leq m \leq k$, $1 \leq p < \infty$, then φ' also exists in that space (see, e.g., [106, Section 2.30]).

We note here that the derivation of the Eulerian semi-derivative of the cost functionals J_i , $i = 1, 2, 3$, at Ω in the direction of a velocity field $\mathbf{V} \in \Theta^1$ may require the expression of the shape derivative of the state variables u_N and u_R , especially when one opts to apply the chain rule approach. This intermediate step is quite laborious but can be bypassed by employing, for instance, the minimax formulation to derive the shape differentiability of the cost functions. In this thesis, as already announced, we will apply the minimax formulation to compute the shape derivative of the shape functionals J_1 , and will use the chain rule approach to derive the shape derivative of J_2 and J_3 . For the cost function J_1 , we emphasize that we are only interested in its first-order shape derivative since the numerical results obtained from the formulation “ $\min_{\Sigma} J_1(\Sigma)$ subject to (1.15)” will serve as our benchmark for the other two formulations. In addition, we will see in the numerical part of this thesis that the advantage of using the Robin problem over the Dirichlet problem in the formulation is already apparent in the results of the first-order method. Nevertheless, the investigation of its corresponding second-order method will be the subject of our future work. Meanwhile, we will compute the shape derivatives of J_2 and J_3 up to the second-order using the chain rule approach, and carry out the numerical analyses also up to the second-order. However, a thorough investigation of a second-order numerical scheme will only be accomplished in the case of the last proposed formulation.

The shape derivative of a (scalar) function defined previously typically appears in the computation of the shape derivative of objective functionals when one, in particular, is applying the chain rule approach. In relation to this, the derivatives of integrals with respect to the domain of integration can be computed easily using the formulas given below. Here, the definition is stated for connected bounded domains $\Omega \subset U$ (U is, of course, the same hold-all domain defined in subsection 2.1.2) with disjoint (closed) boundaries Γ and Σ as in the Bernoulli problem. Moreover, the velocity fields are

autonomous (i.e., time-independent) and, in particular, are elements of Θ^k . For the first indicated result, the domain Ω is assumed to be at least $C^{0,1}$ regular while the second one requires Ω to be at least $C^{1,1}$ regular.

Theorem 2.1.6 (Hadamard's Differentiation Formulas). Let $t_{\max} > 0$ be sufficiently small, and $\Omega \subset U$ be a domain having disjoint (closed) boundaries Γ and Σ as in the Bernoulli problem. Also, suppose $\mathbf{V} \in \Theta^k$, for some integer $k \geq 0$. Then, we have the following formulas.

Domain Differentiation Formula Let $\varphi \in C((0, t_{\max}), W^{1,1}(U))$ and $\dot{\varphi}(0, \cdot) \in L^1(U)$. Then,

$$(2.5) \quad \left\{ \frac{d}{dt} \int_{\Omega_t} \varphi(t, x) dx_t \right\} \Big|_{t=0} = \int_{\Omega} \varphi'(0, x) dx + \int_{\Sigma} \varphi(0, s) \mathbf{V} \cdot \mathbf{n} d\sigma.$$

Boundary Differentiation Formula Let φ be defined in a neighborhood of Σ . If $\varphi \in C((0, t_{\max}), W^{2,1}(U))$ and $\dot{\varphi}(0, \cdot) \in W^{1,1}(U)$, then

$$(2.6) \quad \left\{ \frac{d}{dt} \int_{\partial\Omega_t} \varphi(t, x) d\sigma_t \right\} \Big|_{t=0} = \int_{\Sigma} \varphi'(0, s) d\sigma + \int_{\Sigma} \left(\frac{\partial}{\partial \mathbf{n}} \varphi(0, s) + \kappa \varphi(0, s) \right) \mathbf{V} \cdot \mathbf{n} d\sigma.$$

Proof. The results easily follow from formulas [106, Eq. 2.168, p. 113] and [106, Eq. 2.174, p. 116], respectively. See also [43, Theorem 4.2, p. 483-484] and [43, Theorem 4.3, p. 486], respectively. ■

Finally, to complete our preparation and end this section, let us formally define the first- and second-order shape derivatives of a shape functional $J(\Omega)$ at Ω in the direction of some (autonomous or time-independent) velocity fields \mathbf{V} and \mathbf{W} (see, e.g., [40, 43, 114]):

Definition 2.1.3 (Shape Gradient). Given a cost functional $J(\Omega)$ defined in some Sobolev spaces, we say that $J(\Omega)$ has a *Eulerian semi-derivative* at Ω in the direction $\mathbf{V} \in \mathcal{D}^k(\mathbb{R}^d, \mathbb{R}^d)$ if the limit

$$\lim_{t \searrow 0} \frac{J(\Omega_t(\mathbf{V})) - J(\Omega)}{t} =: dJ(\Omega)[\mathbf{V}]$$

exists and is finite. The shape functional $J(\Omega)$ is said to be *shape differentiable* if $dJ(\Omega)[\mathbf{V}]$ exists for all $\mathbf{V} \in \mathcal{D}^k(\mathbb{R}^d, \mathbb{R}^d)$ and the map $\mathbf{V} \mapsto dJ(\Omega)[\mathbf{V}] : \mathcal{D}^k(\mathbb{R}^d, \mathbb{R}^d) \rightarrow \mathbb{R}$ is well-defined, linear and continuous. In the distributional sense we have

$$dJ(\Omega)[\mathbf{V}] = \langle \mathfrak{J}, \mathbf{V} \rangle_{\mathcal{D}^k(\mathbb{R}^d, \mathbb{R}^d)' \times \mathcal{D}^k(\mathbb{R}^d, \mathbb{R}^d)}$$

and we say that \mathfrak{J} is the k -th order shape gradient of $J(\Omega)$ at Ω .

We have the following well-known structure theorem which is a fundamental result in shape optimization. Basically, it states that the shape derivative $dJ(\Omega)[\mathbf{V}]$ of a ‘regular’ functional $J(\Omega)$ only depends on the normal component $\mathbf{V} \cdot \mathbf{n}$ of the vector field \mathbf{V} .

Theorem 2.1.7 (Hadamard-Zolésio structure theorem). Assume that the boundary Γ of Ω is of class C^{k+1} for an integer $k \geq 0$. Then, there exists a scalar distribution g in $\mathcal{D}^k(\Gamma)'$ such that

$$dJ(\Omega)[\mathbf{V}] = \langle g, v_n \rangle_{\mathcal{D}^k(\Gamma)' \times \mathcal{D}^k(\Gamma)}$$

where $v_n = \mathbf{V} \cdot \mathbf{n}$ is the normal component of \mathbf{V} on Γ .

Corollary 2.1.8. Let Ω be a domain of class C^1 and denote $\Omega_V := \Omega_t(\mathbf{V})$. Assume that the application

$$\mathcal{D}^1(\mathbb{R}^d, \mathbb{R}^d) \ni \mathbf{V} \mapsto J(\Omega_V) \in \mathbb{R}$$

is of class C^1 . Then, for any vector field $\mathbf{V} \in \mathcal{D}^1(\mathbb{R}^d, \mathbb{R}^d)$ such that $\mathbf{V} \cdot \mathbf{n} = 0$ on $\partial\Omega$, one has

$$dJ(\Omega)[\mathbf{V}] = 0.$$

Clearly, based on the previous corollary, any two vector fields \mathbf{V}_1 and \mathbf{V}_2 belonging to $\mathcal{D}^1(\mathbb{R}^d, \mathbb{R}^d)$ with the same normal component will produce equal shape derivatives along the vector fields.

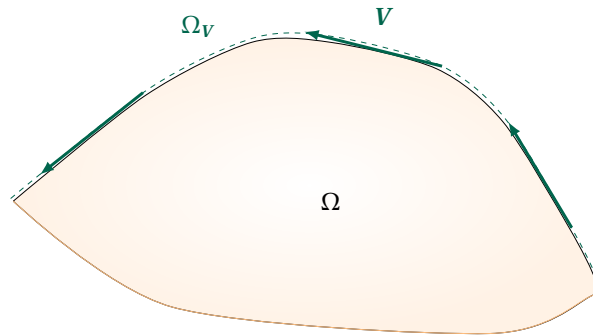


Figure 2.2: At first order, a *tangential vector field* \mathbf{V} (i.e., $\mathbf{V} \cdot \mathbf{n} = 0$) only results in a convection of the shape Ω , and it is expected that $dJ(\Omega)[\mathbf{V}] = 0$

Now, let \mathbf{V} and \mathbf{W} be two time-independent vector fields, i.e., $\mathbf{V}, \mathbf{W} \in \mathcal{D}^k(\mathbb{R}^d, \mathbb{R}^d)$ do not depend on $t \geq 0$. We associate to \mathbf{V} and \mathbf{W} with the transformations $T_t(\mathbf{V})$ and $T_t(\mathbf{W})$ and the transformed domains $\Omega_t(\mathbf{V})$ and $\Omega_t(\mathbf{W})$. We have the following definition.

Definition 2.1.4 (Shape Hessian). Assume that the first Eulerian semi-derivative $dJ(\Omega)[V]$ exists in some neighborhood of $t = 0$. We say that $J(\Omega)$ has the *second order Eulerian semi-derivative* at Ω in the directions (V, W) if the limit

$$\lim_{t \searrow 0} \frac{dJ(\Omega_t(W))[V] - dJ(\Omega)[V]}{t} =: d^2J(\Omega)[V, W]$$

exists and is finite. The shape functional $J(\Omega)$ is said to be *twice shape differentiable* if $dJ(\Omega)[V]$ exists for all $V, W \in \mathcal{D}^k := \mathcal{D}^k(\mathbb{R}^d, \mathbb{R}^d)$ and the map h defined as $(V, W) \mapsto dJ(\Omega)[V] : \mathcal{D}^k \times \mathcal{D}^k \rightarrow \mathbb{R}$ is well-defined, linear and continuous with the Fréchet space topology on $\mathcal{D}^k(\mathbb{R}^d, \mathbb{R}^d)$. We denote by $\mathfrak{H}(\Omega)$ the vector distribution in $(\mathcal{D}^k \otimes \mathcal{D}^k)'$ associated with h :

$$d^2J(\Omega)[V, W] = \langle \mathfrak{H}(\Omega), V \otimes W \rangle =: h(V, W),$$

where $V \otimes W$ is the tensor product of $V = (V_i)$ and $W = (W_j)$ defined as

$$(V \otimes W)_{i,j}(x, y) = V_i(x)W_j(y), \quad 1 \leq i, j \leq d.$$

In this case, $\mathfrak{H}(\Omega)$ will be called the *kth-order shape Hessian* of $J(\Omega)$ at Ω .

Next, we give an equivalent form of the Hadamard-Zolésio structure theorem for $d^2J(\Omega)[V, W]$.

Theorem 2.1.9. Let Ω be a domain in \mathbb{R}^d with boundary Γ and assume that the functional $J(\Omega)$ is twice shape differentiable at Ω .

- (i) Then, $\mathfrak{H}(\Omega)$ has support in $\Gamma \times \Gamma$. Moreover, the support of $\mathfrak{H}(\Omega)$ is compact when its order is finite.
- (ii) If $\mathfrak{H}(\Omega)$ is of finite order $k \geq 0$ and the boundary Γ is of class C^{k+1} , then there exists a linear and continuous vector distribution $h(\Gamma \otimes \Gamma)$ on $\mathcal{D}^k(\Gamma, \mathbb{R}^d) \otimes \mathcal{D}^k(\Gamma)$ of order k such that for all V and W in \mathcal{D}^k ,

$$d^2J(\Omega)[V, W] = \langle h(\Gamma \otimes \Gamma), (\gamma_\Gamma V) \otimes ((\gamma_\Gamma W) \cdot \mathbf{n}) \rangle$$

where γ_Γ denotes the trace operator on the boundary Γ .

Remark 2.1.2. In general, the shape Hessian is not symmetric; that is, we can find two (time-independent) vector fields V and W in \mathcal{D}^k such that $d^2J(\Omega)[V, W] \neq d^2J(\Omega)[W, V]$.

We are now in the position to derive the expressions for the derivatives of the cost functionals J_1 , J_2 , and J_3 with respect to domain variations.

2.2 Shape Derivative of J_1

In this section we derive the shape derivative of J_1 via the minimax formulation in the spirit of [38]. We start off the section with the following remark about an essential quality of the state solutions which is of key importance in the existence of the shape derivative of the cost functionals J_i s.

Remark 2.2.1. In Subsection 1.4.2, we already mentioned the existence of weak solutions to the Robin state problem (1.15). We remark here that, for $\beta > 0$, the uniqueness of the weak solution $u_R \in H^1(\Omega)$ to (1.24) is guaranteed. In fact, in general, if $\beta = \beta(x)$ is an $L^\infty(\Sigma)$ function and is positive almost everywhere in Σ , then we are assured that (1.15) admits only one solution in $H^1(\Omega)$ (see, e.g. [88, Lemma 7.36.3, p. 617]). It is worth to mention that both u_N and u_R possesses higher regularity because of the regularity assumption imposed on Ω . In fact, the weak solutions to (1.23) and (1.24) are even $H^2(\Omega)$ -regular since Ω is of class $C^{1,1}$. Generally, if Ω is of class $C^{k+1,1}$, where $k \geq 0$ is an integer, then $u_N, u_R \in H^1(\Omega)$ are also elements of $H^{k+2}(\Omega)$. This claim can easily be verified for u_N since the boundaries Γ and Σ are disjoint. See, for example, [14, Theorem 29]. The same is true for u_R as stated, for instance, in [81, Remark 3.5]. For more details about the existence and uniqueness of solutions to mixed Robin-Dirichlet problems in $W^{m,2}$ for bounded domains in \mathbb{R}^d , one may consult Section 7.36 in [88].

2.2.1 The Minimax Formulation

Here we want to review the minimax formulation of shape optimization problems that we will employ to examine the shape differentiability of J_1 . In this regard, we will also discuss a theorem due to Correa and Seeger [33] which is a powerful tool to differentiate a minimax function with respect to a parameter.

Let us first recall the definition of saddle points and briefly discuss their characterization.

Definition 2.2.1. Let \mathcal{A}, \mathcal{B} be sets and $\mathcal{G} : \mathcal{A} \times \mathcal{B} \rightarrow \mathbb{R}$ be a map. Then a pair $(u, p) \in \mathcal{A} \times \mathcal{B}$ is said to be a *saddle point* on $\mathcal{A} \times \mathcal{B}$ if $\mathcal{G}(u, \psi) \leq \mathcal{G}(u, p) \leq \mathcal{G}(\varphi, p)$, for all $(\varphi, \psi) \in \mathcal{A} \times \mathcal{B}$.

According to [44, Proposition 1.2, p. 167], a pair $(u, p) \in \mathcal{A} \times \mathcal{B}$ is a saddle point of $\mathcal{G}(\cdot, \cdot)$ if and only if ¹ $\min_{\hat{u} \in \mathcal{A}} \sup_{\hat{p} \in \mathcal{B}} \mathcal{G}(\hat{u}, \hat{p}) = \max_{\hat{p} \in \mathcal{B}} \inf_{\hat{u} \in \mathcal{A}} \mathcal{G}(\hat{u}, \hat{p})$, and it is equal to $\mathcal{G}(u, p)$, where u is the attained minimum and p is the attained maximum, respectively. For a convex-concave function \mathcal{G}

¹Here, the min and max indicate that the infimum and supremum are attained, respectively.

that is Gâteaux differentiable, it may be verified that $(u, p) \in \mathcal{A} \times \mathcal{B}$ is a saddle point of \mathcal{G} (see [44, Proposition 1.6, pp. 169–170]).

Proposition 2.2.1. Let \mathcal{X} and \mathcal{Y} be two Banach spaces. Let us suppose that $\mathcal{A} \subset \mathcal{X}$ and $\mathcal{B} \subset \mathcal{Y}$, \mathcal{A} , \mathcal{B} are closed, convex and non-empty. Moreover, let $\mathcal{G} : \mathcal{X} \times \mathcal{Y} \rightarrow \mathbb{R}$ be such that for all $p \in \mathcal{B}$, the function $u \mapsto \mathcal{G}(u, p)$ is lower semi-continuous, convex and Gâteaux differentiable, and for all $u \in \mathcal{A}$ the function $p \mapsto \mathcal{G}(u, p)$ is upper semi-continuous, concave and Gâteaux differentiable. Then, $(\hat{u}, \hat{p}) \in \mathcal{A} \times \mathcal{B}$ is a saddle point if and only if

$$\left\langle \frac{\partial \mathcal{G}}{\partial u}(\hat{u}, \hat{p}), u - \hat{u} \right\rangle \geq 0 \quad \text{and} \quad \left\langle \frac{\partial \mathcal{G}}{\partial p}(\hat{u}, \hat{p}), u - \hat{u} \right\rangle \leq 0,$$

for all $(u, p) \in \mathcal{A} \times \mathcal{B}$.

In what follows, we discuss the general idea about the inf-sup formulation of a perturbed problem in 2-dimensional space. So, we let Ω be a bounded open domain in \mathbb{R}^2 with a smooth boundary Γ . Let us suppose that $u = u(\Omega)$ be the solution of the variational problem

$$(2.7) \quad \inf_{\varphi \in H^1(\Omega)} E(\Omega, \varphi),$$

where E denotes some energy functional. We associate with u a cost function

$$J(\Omega) = F(\Omega, u(\Omega)).$$

Now, consider the deformed domain $\Omega_t = T_t(\Omega)$ of the reference domain Ω , where T_t is the perturbation of the identity operator. Let $u_t = u(\Omega_t)$ be the solution of problem (2.7) on the transformed domain Ω_t

$$(2.8) \quad \inf_{\varphi \in H^1(\Omega_t)} E(\Omega_t, \varphi),$$

and associate with u_t the cost function

$$(2.9) \quad J(\Omega_t) = F(\Omega_t, u(\Omega_t)).$$

To minimize the cost function J with respect to Ω , we transform the (2.8)-(2.9) into an inf-sup problem. Such approach is popular in the engineering and mathematical literature.

The solution of (2.8) is completely characterized by the variational equation

$$dE(\Omega_t, u_t; \varphi) = 0, \quad \forall \varphi \in H^1(\Omega_t).$$

Define

$$(2.10) \quad \mathcal{L}(t, \varphi, \psi) = F(\Omega_t, \varphi) + dE(\Omega_t, \varphi; \psi).$$

Noting that

$$\sup_{\psi \in H^1(\Omega_t)} \mathcal{L}(t, \varphi, \psi) = \begin{cases} F(\Omega_t, \varphi) & \text{if } \varphi \text{ is a solution of (2.8),} \\ +\infty & \text{otherwise,} \end{cases}$$

yields

$$J(\Omega_t) = \min_{\varphi \in H^1(\Omega_t)} \sup_{\psi \in H^1(\Omega_t)} \mathcal{L}(t, \varphi, \psi).$$

Notice that the functional spaces appearing in the inf-sup expression given above depend on the parameter t . So, before we can differentiate the inf-sup expression with respect to the parameter t , we need to fix the functional spaces first. To do this, we may apply either the *function space parametrization* technique or the *function space embedding* technique put forward in [43, Section 10.6.3].

Let us now discuss the differentiability of a saddle point with respect to the parameter t .

Consider a functional

$$\mathcal{G} : [0, t_{\max}] \times \mathcal{X} \times \mathcal{Y} \rightarrow \mathbb{R},$$

for some $t_{\max} > 0$ and topological spaces \mathcal{X} and \mathcal{Y} . For each t in $[0, t_{\max}]$, we define

$$\underline{M}(t) = \inf_{x \in \mathcal{X}} \sup_{y \in \mathcal{Y}} \mathcal{G}(t, x, y) \quad \text{and} \quad \overline{M}(t) = \sup_{y \in \mathcal{Y}} \inf_{x \in \mathcal{X}} \mathcal{G}(t, x, y)$$

and the associated sets

$$\hat{\mathcal{X}}(t) := \left\{ \hat{x} \in \mathcal{X} : \sup_{y \in \mathcal{Y}} \mathcal{G}(t, \hat{x}, y) = \underline{M}(t) \right\} \quad \text{and} \quad \hat{\mathcal{Y}}(t) := \left\{ \hat{y} \in \mathcal{Y} : \inf_{x \in \mathcal{X}} \mathcal{G}(t, x, \hat{y}) = \overline{M}(t) \right\}$$

To complete the set of notations, we introduce the *set of saddle points*

$$(2.11) \quad \mathcal{S}(t) := \{(\hat{x}, \hat{y}) \in \mathcal{X} \times \mathcal{Y} : \underline{M}(t) = \mathcal{G}(t, \hat{x}, \hat{y}) = \overline{M}(t)\},$$

which may be empty. Generally, we always have the inequality $\overline{M}(t) \leq \underline{M}(t)$. Further, for a fixed $t \in [0, t_{\max}]$, and for all $(x^t, y^t) = (\hat{x}, \hat{y}) \in \hat{\mathcal{X}}(t) \times \hat{\mathcal{Y}}(t)$, we have the inequality $\overline{M}(t) \leq \mathcal{G}(t, x^t, y^t) \leq \underline{M}(t)$, and when $\overline{M}(t) = \underline{M}(t)$, the set of saddle points $\mathcal{S}(t)$ is exactly $\hat{\mathcal{X}}(t) \times \hat{\mathcal{Y}}(t)$.

Now, the objective of this method is to seek realistic conditions under which the existence of the limit

$$d\underline{M}(0) = \lim_{t \searrow 0} \frac{\underline{M}(t) - \underline{M}(0)}{t}$$

is guaranteed. Here, we are particularly interested on the situation when \mathcal{G} admits saddle points for all $t \in [0, t_{\max}]$. It is basically an extension of [43, Theorem 2.1, pp. 58–59] which is about the differentiability of a min with respect to a parameter. It is used when we want to minimize a functional consisting of the state variable, which is itself a function of the domain through a BVP. In that case, the saddle point equations coincide with the “state equation” and the “adjoint state equation”. The main advantage of this approach is that it avoids the problem of the existence and characterization of the derivative of the state x^t with respect to t , which is in fact the directional derivative of the state with respect to the control variable in control problem. It is worth noting that it is not necessary

to invoke any implicit function theorem with possibly restrictive differentiability conditions, and it suffices to check two continuity conditions for the set-valued maps $\mathcal{X}(\cdot)$ and $\mathcal{Y}(\cdot)$ [43].

Finally, we state the theorem that we will utilize to differentiate a saddle point with respect to the parameter t . The result which we give below is an improved version [43, Theorem 5.1, pp. 556–559] of the theorem of Correa-Seeger. For the proof, see pages 557–588 of [43].

Theorem 2.2.1 (Correa and Seeger [33]). Let the sets \mathcal{X} and \mathcal{Y} , the real number $t_{\max} > 0$, and the functional

$$\mathcal{G} : [0, t_{\max}] \times \mathcal{X} \times \mathcal{Y} \rightarrow \mathbb{R}$$

be given. Assume that the following assumptions hold:

(H1) $\mathcal{S}(t) \neq \emptyset$, $0 \leq t \leq t_{\max}$;

(H2) for all $(x, y) \in [\cup\{\hat{\mathcal{X}}(t) : 0 \leq t \leq t_{\max}\} \times \hat{\mathcal{Y}}(0)] \cup [\hat{\mathcal{X}}(0) \times \cup\{\hat{\mathcal{Y}}(t) : 0 \leq t \leq t_{\max}\}]$, the partial derivative $\frac{\partial}{\partial t} \mathcal{G}(t, x, y)$ exists everywhere in $[0, t_{\max}]$;

(H3) there exists a topology \mathfrak{T}_X on \mathcal{X} such that for any sequence $\{t_n : 0 < t_n \leq t_{\max}\}$, $t_n \rightarrow t_0 = 0$, there exist an $x^0 \in \hat{\mathcal{X}}(0)$ and a subsequence $\{t_{n_k}\}$ of $\{t_n\}$, and for each $k \geq 1$, there exists $x_{n_k} \in \hat{\mathcal{X}}(t_{n_k})$ such that

(i) $x_{n_k} \rightarrow x^0$ in the \mathfrak{T}_X -topology, and

(ii) for all y in $\hat{\mathcal{Y}}(0)$,

$$\liminf_{\substack{t \searrow 0 \\ k \rightarrow \infty}} \frac{\partial}{\partial t} \mathcal{G}(t, x_{n_k}, y) \geq \frac{\partial}{\partial t} \mathcal{G}(0, x^0, y);$$

(H4) there exists a topology \mathfrak{T}_Y on \mathcal{Y} such that for any sequence $\{t_n : 0 < t_n \leq t_{\max}\}$, $t_n \rightarrow t_0 = 0$, there exist $y^0 \in \hat{\mathcal{Y}}(0)$ and a subsequence $\{t_{n_k}\}$ of $\{t_n\}$, and for each $k \geq 1$, there exists $y_{n_k} \in \hat{\mathcal{Y}}(t_{n_k})$ such that

(i) $y_{n_k} \rightarrow y^0$ in the \mathfrak{T}_Y -topology, and

(ii) for all x in $\hat{\mathcal{X}}(0)$,

$$\limsup_{\substack{t \searrow 0 \\ k \rightarrow \infty}} \frac{\partial}{\partial t} \mathcal{G}(t, x, y_{n_k}) \leq \frac{\partial}{\partial t} \mathcal{G}(0, x, y^0).$$

Then, there exists $(x^0, y^0) \in \hat{\mathcal{X}}(0) \times \hat{\mathcal{Y}}(0)$ such that

$$\underline{dM}(0) = \inf_{x \in \hat{\mathcal{X}}(0)} \sup_{y \in \hat{\mathcal{Y}}(0)} \frac{\partial}{\partial t} \mathcal{G}(0, x, y) = \frac{\partial}{\partial t} \mathcal{G}(0, x^0, y^0) = \sup_{y \in \hat{\mathcal{Y}}(0)} \inf_{x \in \hat{\mathcal{X}}(0)} \frac{\partial}{\partial t} \mathcal{G}(0, x, y).$$

Thus, (x^0, y^0) is a saddle point of $\frac{\partial}{\partial t} \mathcal{G}(0, x, y)$ on $\hat{\mathcal{X}}(0) \times \hat{\mathcal{Y}}(0)$.

In the literature, condition **(H3)**(i) is known as *sequential semicontinuity for set-valued functions*. When $\hat{\mathcal{X}}(0)$ is a singleton $\{x^0\}$ we readily get $d\bar{M}(0) = \partial_t \mathcal{G}(0, x^0, y)$.

Now we are in the position to compute the first-order shape derivative of the cost functional J_1 using the minimax formulation in the next subsection.

2.2.2 The Shape Gradient of J_1

In the derivation of the shape gradient of J_1 , it is sufficient to take $k = 1$ in (2.2) if one opt to apply the rearrangement method; see [67, 79]. However, since we wish to apply the minimax formulation [38] instead, we take $k = 2$. This in turn will simplify the derivation of the expression for the shape derivative of J_1 as we will demonstrate in the proof of the following proposition. Here, for convenience, we will denote the state variable u_R simply by u .

Proposition 2.2.2. Let Ω be of class $C^{2,1}$. Then, the shape derivative of J_1 at Ω along a deformation field $V \in \Theta^2$ is given by

$$\begin{aligned} dJ_1(\Sigma)[V] &= \int_{\Sigma} g_1 \mathbf{n} \cdot V \, d\sigma \\ &:= \int_{\Sigma} \left\{ \nabla u \cdot \nabla p + (\beta u - \lambda) \left(\frac{\partial p}{\partial \mathbf{n}} + \kappa p \right) + \beta p \frac{\partial u}{\partial \mathbf{n}} + \left(\frac{\partial u}{\partial \mathbf{n}} - \lambda \right) \frac{\partial^2 u}{\partial \mathbf{n}^2} + \frac{\kappa}{2} \left(\frac{\partial u}{\partial \mathbf{n}} - \lambda \right)^2 \right\} \mathbf{n} \cdot V \, d\sigma \end{aligned}$$

where the adjoint state p satisfies the PDE system

$$(2.12) \quad -\Delta p = 0 \text{ in } \Omega, \quad p = 0 \text{ on } \Gamma, \quad \frac{\partial p}{\partial \mathbf{n}} + \beta p = - \left(\frac{\partial u}{\partial \mathbf{n}} - \lambda \right) \text{ on } \Sigma.$$

If we choose β to be the mean curvature κ of Σ , i.e., $\beta = \kappa$, the kernel g_1 simplifies to

$$g_1 = \nabla u \cdot \nabla p - \kappa(u - p) \frac{\partial u}{\partial \mathbf{n}} + \left(\frac{\partial u}{\partial \mathbf{n}} - \lambda \right) \frac{\partial^2 u}{\partial \mathbf{n}^2} + \frac{\kappa}{2} \left(\frac{\partial u}{\partial \mathbf{n}} - \lambda \right)^2.$$

Additionally, at the shape solution Ω^* of the Bernoulli problem (1.3) wherein it holds that $\frac{\partial u}{\partial \mathbf{n}} = \lambda$ on Σ^* , we have the necessary optimality condition

$$dJ_1(\Sigma^*)[V] = 0, \quad \text{for all } V \in \Theta^2.$$

Before we proceed with proof, we recall, for convenience, the definition of the Hilbert space $H_{\Gamma,0}^1(\Omega)$ given by $H_{\Gamma,0}^1(\Omega) = \{\varphi \in H^1(\Omega) : \varphi|_{\Gamma} = 0\}$ which we endow with the norm $\|\varphi\|_{H_{\Gamma,0}^1(\Omega)} := \left(|\varphi|_{H^1(\Omega)}^2 + \|\varphi\|_{L^2(\Sigma)}^2 \right)^{1/2}$. We shall also consider throughout the rest of this thesis the linear manifold defined by

$$H_{\Gamma,f}^1(\Omega) = \{\varphi \in H^1(\Omega) : \varphi|_{\Gamma} = f \in H^{1/2}(\Gamma)\}.$$

Moreover, we reiterate with emphasis the equivalence of the $H^1(\Omega)$ -seminorm, $H_{\Gamma,0}^1(\Omega)$ -norm, and the usual Sobolev norm $H^1(\Omega)$ on $H_{\Gamma,0}^1(\Omega)$. Also, we point out that the properties of T_t listed in Lemma 2.1.4 will be used many times in proof.

Proof. The proof will be accomplished in several steps.

Step 1: Construction of the appropriate functional. We consider the following functional composed of the objective function and the weak formulation of the state system (over the perturbed domain Ω_t):

$$\mathcal{L}(t, \varphi, \psi) = \int_{\Omega_t} \nabla \varphi \cdot \nabla \psi \, dx_t + \int_{\Sigma_t} \left[(\beta \varphi - \lambda) \psi + \frac{1}{2} (\partial_{\mathbf{n}} \varphi - \lambda)^2 \right] d\sigma_t + \int_{\Gamma} (\varphi - 1) \mu \, d\sigma_t.$$

Here, the Lagrange multiplier $\mu := \partial_{\mathbf{n}} \psi$ is introduced to penalize the Dirichlet condition on the fixed boundary. Because Γ is invariant during deformation (i.e., $\Gamma_t = \Gamma$ for all t), we can actually drop t in Γ_t in above expression.

One can easily check that, at $t = 0$,

$$J_1(\Sigma) = \min_{\varphi \in H^1(\Omega)} \sup_{\psi \in H_{\Gamma,0}^1(\Omega)} \mathcal{L}(0, \varphi, \psi)$$

since

$$\sup_{\psi \in H_{\Gamma,0}^1(\Omega)} \mathcal{L}(0, \varphi, \psi) = \begin{cases} \frac{1}{2} \int_{\Sigma} \left(\frac{\partial u}{\partial \mathbf{n}} - \lambda \right)^2 d\sigma & \text{if } \varphi = u, \\ +\infty & \text{otherwise.} \end{cases}$$

In addition, one can also show that the functional $\mathcal{L}(0, \varphi, \psi)$ is convex continuous with respect to φ and concave continuous with respect to ψ . Hence, according to Proposition 2.2.1, the functional admits a saddle point (u, p) provided that the pair (u, p) satisfies the variational forms of the systems (1.15) and (2.12):

$$(2.13) \quad \begin{aligned} & \text{find } u \in H_{\Gamma,1}^1(\Omega) \text{ such that } \int_{\Omega} \nabla u \cdot \nabla \psi \, dx + \int_{\Sigma} \beta u \psi \, d\sigma = \int_{\Sigma} \lambda \psi \, d\sigma, \quad \forall \psi \in H_{\Gamma,0}^1(\Omega); \\ & \text{find } p \in H_{\Gamma,0}^1(\Omega) \text{ such that } \int_{\Omega} \nabla p \cdot \nabla \varphi \, dx + \int_{\Sigma} \beta p \varphi \, d\sigma = - \int_{\Sigma} (\partial_{\mathbf{n}} u - \lambda) \varphi \, d\sigma, \quad \forall \varphi \in H_{\Gamma,0}^1(\Omega). \end{aligned}$$

The saddle point (u, p) is unique because (1.24) and (2.13) are uniquely solvable in $H^1(\Omega)$. A similar analysis also holds on the transformed domain Ω_t . In fact, we have the equality

$$(2.14) \quad J_1(\Sigma_t) = \min_{\varphi \in H^1(\Omega_t)} \sup_{\psi \in H_{\Gamma,0}^1(\Omega_t)} \mathcal{L}(t, \varphi, \psi).$$

The corresponding saddle point of $\mathcal{L}(t, \varphi, \psi)$, (u_t, p_t) , for non-zero small t , is characterized by the same weak forms (1.24) and (2.13), only that the integrals are defined over Ω_t , (u_t, p_t) lives in $H^1(\Omega_t) \times H_{\Gamma,0}^1(\Omega_t)$, and the test functions are taken from $H_{\Gamma,0}^1(\Omega_t)$.

Step 2: Getting rid of the time-dependence of the function spaces. Our goal is to get the derivative of the minimax functional $\mathcal{L}(t, \varphi, \psi)$ with respect to the parameter $t \geq 0$ through the application of Correa-Seeger's Theorem [33]. However, the function spaces appearing in the minimax in (2.14)

depend on the parameter t . To get around this difficulty, we make use of the so-called *function space parametrization technique* (see, e.g., [43, Section 10.6.3]).² That is, we parametrize the functions in $H^1(\Omega_t)$ by elements of $H^1(\Omega)$ using the map

$$\varphi \mapsto \varphi \circ T_t^{-1} : H^1(\Omega) \rightarrow H^1(\Omega_t).$$

Of course, we do the same for the functions in $H_{\Gamma,f}^1(\Omega_t)$. This parametrization does not change the values of the saddle points. Thus, we have a new functional $\mathcal{L}(t, \varphi \circ T_t^{-1}, \psi \circ T_t^{-1})$ with the same saddle point for $\mathcal{L}(t, \varphi, \psi)$. We rewrite the resulting functional and the systems characterizing its saddle points into their respective equivalent forms via domain and boundary transformations (see Lemma 2.1.2). Particularly, we have

$$\mathcal{G}(t, \varphi, \psi) := \int_{\Omega} A(t) \nabla \varphi \cdot \nabla \psi \, dx + \int_{\Gamma} (\varphi - 1) \partial_n \psi \, d\sigma + \int_{\Sigma} B(t) \left[(\beta \varphi - \lambda) \psi + \frac{1}{2} (\partial_n \varphi - \lambda)^2 \right] d\sigma.$$

Here, we used the fact that $const. \circ T_t = const.$, and $T_t(x) = x$ and $B(t) = 1$ on $\Gamma_t = \Gamma$. The saddle point $(u^t, p^t) := (u^t \circ T_t, p^t \circ T_t) \in H^1(\Omega) \times H_{\Gamma,0}^1(\Omega)$ of this new functional is characterized by the systems

(2.15)

$$u^t \in H_{\Gamma,1}^1(\Omega) : \int_{\Omega} A(t) \nabla u^t \cdot \nabla \psi \, dx + \int_{\Sigma} \beta B(t) u^t \psi \, d\sigma = \int_{\Sigma} B(t) \lambda \psi \, d\sigma, \quad \forall \psi \in H_{\Gamma,0}^1(\Omega),$$

(2.16)

$$p^t \in H_{\Gamma,0}^1(\Omega) : \int_{\Omega} A(t) \nabla p^t \cdot \nabla \varphi \, dx + \int_{\Sigma} \beta B(t) p^t \varphi \, d\sigma = - \int_{\Sigma} B(t) (\partial_n u^t - \lambda) \varphi \, d\sigma, \quad \forall \varphi \in H_{\Gamma,0}^1(\Omega).$$

Step 3: Verifying the four assumptions of Correa-Seeger's Theorem. To get the shape derivative of J_1 at Ω along a deformation field \mathbf{V} , we evaluate the limit

$$\lim_{t \searrow 0} \left(\min_{\varphi \in H^1(\Omega)} \sup_{\psi \in H_{\Gamma,0}^1(\Omega)} \frac{\mathcal{G}(t, \varphi, \psi) - \mathcal{G}(0, \varphi, \psi)}{t} \right).$$

To do this, we apply Theorem 2.2.1. But first, we need to verify its four assumptions.

We let $\mathbf{V} \in \Theta^1$ and choose a sufficiently small number $t_{\max} > 0$, such that, for all $t \in [0, t_{\max}]$, there exist some constants a_1, a_2, b_1 and b_2 satisfying $0 < a_1 \leq a_2$, $0 < b_1 \leq b_2$ and such that $a_1 |\xi|^2 \leq A(t) \xi \cdot \xi \leq a_2 |\xi|^2$, for all $\xi \in \mathbb{R}^2$ and $b_1 \leq B(t) \leq b_2$ (see, e.g., [13]). We define the sets

$$\mathcal{X}(t) := \left\{ x^t \in H^1(\Omega) : \sup_{y \in H_{\Gamma,0}^1(\Omega)} \mathcal{G}(t, x^t, y) = \inf_{x \in H^1(\Omega)} \sup_{y \in H_{\Gamma,0}^1(\Omega)} \mathcal{G}(t, x, y) \right\},$$

$$\mathcal{Y}(t) := \left\{ y^t \in H_{\Gamma,0}^1(\Omega) : \inf_{x \in H^1(\Omega)} \mathcal{G}(t, x, y^t) = \sup_{y \in H_{\Gamma,0}^1(\Omega)} \inf_{x \in H^1(\Omega)} \mathcal{G}(t, x, y) \right\}.$$

²An alternative approach to address the issue is to use the *function space embedding technique*, see [43, Section 10.6.3].

The functions u^t and p^t satisfy the inequality $\mathcal{L}(t, u^t, \psi) \leq \mathcal{L}(t, u^t, p^t) \leq \mathcal{L}(t, \varphi, p^t)$. Hence, it is evident that $\mathcal{X}(t)$ and $\mathcal{Y}(t)$ are non-empty, since, in particular, we have $\mathcal{X}(t) = \{u^t\}$ and $\mathcal{Y}(t) = \{p^t\}$. Thus, we get

$$\forall t \in [0, t_{\max}] : \mathcal{S}(t) := \mathcal{X}(t) \times \mathcal{Y}(t) = \{u^t, p^t\} \neq \emptyset.$$

This shows that condition **(H1)** is satisfied.

To verify condition **(H2)**, let us compute the derivative of $\mathcal{G}(t, \varphi, \psi)$ with respect to $t \geq 0$:

$$\frac{\partial}{\partial t} \mathcal{G}(t, \varphi, \psi) = \int_{\Omega} A'(t) \nabla \varphi \cdot \nabla \psi \, dx + \int_{\Sigma} B'(t) \left[(\beta \varphi - \lambda) \psi + \frac{1}{2} \left(\frac{\partial \varphi}{\partial \mathbf{n}} - \lambda \right)^2 \right] d\sigma.$$

Since $\mathbf{V} \in \mathcal{D}^1(\mathbb{R}^2, \mathbb{R}^2)$ and the maps $t \mapsto DT_t$ are continuous in $[0, t_{\max}]$ (see Lemma 2.1.4), the partial derivative $\partial_t \mathcal{G}(t, \varphi, \psi)$ exists everywhere in $[0, t_{\max}]$. Hence, **(H2)** is satisfied.

To check **(H3)**(i) and **(H4)**(i), we first show the boundedness of (u^t, p^t) . We take $\psi = u^t$ in (2.15). With the choice of t_{\max} , we can use the bounds for $A(t)$ and $B(t)$ to get the estimate $\|u^t\|_{H_{\Gamma,0}^1(\Omega)}^2 \lesssim |\lambda| |\Sigma|^{1/2} \|u^t\|_{L^2(\Sigma)}$. Since the norm $\|\cdot\|_{H_{\Gamma,0}^1(\Omega)}$ is equivalent to the usual $H^1(\Omega)$ Sobolev norm on $H_{\Gamma,0}^1(\Omega)$, we actually have $\|u^t\|_{H^1(\Omega)} \lesssim |\lambda| |\Sigma|^{1/2}$. Applying the same technique, we can also show that p^t is bounded.

Next, we show the continuity of the pair (u^t, p^t) . To prove the continuity of u^t , we subtract in (2.15) at $t > 0$, $t = 0$ and let $\psi = u^t - u$ to obtain

$$\begin{aligned} \|u^t - u\|_{H_{\Gamma,0}^1(\Omega)}^2 &= \int_{\Omega} (A(t) - \mathbf{I}_2) \nabla u^t \cdot \nabla (u^t - u) \, dx + \int_{\Sigma} (\lambda \circ T_t B(t) - \lambda) (u^t - u) \, d\sigma \\ &\quad - \beta \int_{\Sigma} u^t (B(t) - 1) (u^t - u) \, d\sigma \\ &\leq \|A(t) - \mathbf{I}_2\|_{L^\infty(\Omega)} \|u^t\|_{H^1(\Omega)} \|u^t - u\|_{L^2(\Omega)} + |\lambda| \|B(t) - 1\|_{\infty} \|u^t - u\|_{L^2(\Sigma)} \\ &\quad + \beta \|B(t) - 1\|_{\infty} \|u^t\|_{L^2(\Sigma)} \|u^t - u\|_{L^2(\Omega)}, \end{aligned}$$

where $|\cdot|_{\infty}$ is the supremum norm. Using the boundedness of u^t , and the equivalence of the norms $\|\cdot\|_{H_{\Gamma,0}^1(\Omega)}$ and $\|\cdot\|_{H^1(\Omega)}$, we get the bound

$$\|u^t - u\|_{H^1(\Omega)} \lesssim \|A(t) - \mathbf{I}_2\|_{L^\infty(\Omega)} + \|B(t) - 1\|_{\infty}.$$

Hence, $u^t \rightarrow u$ in $H^1(\Omega)$ because $A(t) - \mathbf{I}_2 \rightarrow 0$ and $B(t) \rightarrow 1$ as $t \rightarrow 0$ (Lemma 2.1.4). For Ω at least $C^{1,1}$ regular we can show via the application of a classical regularity theorem [60], and standard arguments, that u^t is also bounded in $H^2(\Omega)$ because u^t is in $H^2(\Omega)$. This implies the continuity of u^t in $H^2(\Omega)$, and thus verifies **(H3)**(i) for $H^2(\Omega)$ -strong. Using a similar argument, we can also show that $p^t \rightarrow p$ strongly in $H^1(\Omega)$ as $t \rightarrow 0$. Moreover, since $u^t \in H^2(\Omega)$, $\partial_{\mathbf{n}} u^t - \lambda \in H^{1/2}(\Sigma)$. By regularity theorem, p^t is also in $H^2(\Omega)$, and so the continuity of p^t in $H^2(\Omega)$. Hence, condition **(H4)**(i) is true for the $H^2(\Omega)$ -strong topology.³

³It should be recognized here that we only need the domain Ω to be of class $C^{1,1}$ to guarantee the continuity of u^t and p^t in $H^2(\Omega)$. The continuity of the adjoint state in $H^2(\Omega)$ when the Robin state problem (1.15) is replaced by the pure Dirichlet problem (1.9) however cannot be achieved since the corresponding adjoint of the formulation does not actually live in $H^2(\Omega)$ in that case, see [67].

Finally, conditions **(H3)**(ii) and **(H4)**(ii) are easily verified by the strong continuity of the maps $(t, \varphi) \mapsto \partial_t \mathcal{G}(t, \varphi, \psi)$ and $(t, \psi) \mapsto \partial_t \mathcal{G}(t, \varphi, \psi)$.

Consequently, we have verified all assumptions of Theorem 2.2.1 from which we conclude that following equation holds

$$dJ_1(\Sigma)[\mathbf{V}] = \left. \frac{\partial}{\partial t} \mathcal{G}(t, u, p) \right|_{t=0} = \int_{\Omega} A \nabla u \cdot \nabla p \, dx + \int_{\Sigma} B \left[(\beta u - \lambda) p + \frac{1}{2} (\partial_{\mathbf{n}} u - \lambda)^2 \right] d\sigma,$$

where $A = (\operatorname{div} \mathbf{V}) \mathbf{I}_2 - D\mathbf{V} - (D\mathbf{V})^\top$ and $B = \operatorname{div}_{\Sigma} \mathbf{V}$ (see Lemma 2.1.4), and $(u, p) \in H^1(\Omega) \times H^1(\Omega)$ is the unique solution pair to systems (1.15) and (2.12).

Step 4: Characterization of the shape gradient in terms of just a boundary expression. Let us now assume that $\mathbf{V} \in \Theta^2$. It can be checked without difficulty that the map $\mathbf{V} \mapsto dJ_1(\Sigma)[\mathbf{V}] : \mathcal{D}^1(\mathbb{R}^2, \mathbb{R}^2) \rightarrow \mathbb{R}$ is linear and continuous. Therefore, according to Hadamard-Zolésio structure theorem [43, Section 9.3.4], there exists, for a $C^{2,1}$ domain Ω , a scalar distribution $g_1(\Omega) \in \mathcal{D}^1(\Sigma)$ such that $dJ_1(\Sigma)[\mathbf{V}] = \langle g_1(\Omega), \mathbf{V} \cdot \mathbf{n} \rangle_{L^2(\Sigma)}$.

Now we further characterize this boundary expression as follows. Firstly, we note that for a $C^{2,1}$ domain Ω , the unique solution pair to (1.15) and (2.12) possesses more regularity. In fact, u and p are elements of $H^3(\Omega)$ for Ω of class $C^{2,1}$ (see, e.g., [81, Remark 3.5]). These regularities allow us to use Hadamard's domain and boundary differentiation formulas (2.5) and (2.6) That is, we have

$$\begin{aligned} \left. \frac{\partial}{\partial t} \mathcal{L}(t, \varphi \circ T_t^{-1}, \psi \circ T_t^{-1}) \right|_{t=0} &= \int_{\Omega} (\nabla \dot{\varphi} \cdot \nabla \psi + \nabla \varphi \cdot \nabla \dot{\psi}) \, dx + \int_{\Sigma} [(\beta \varphi - \lambda) \dot{\psi} + \beta \dot{\varphi} \psi + (\partial_{\mathbf{n}} \varphi - \lambda) \partial_{\mathbf{n}} \dot{\varphi}] \, d\sigma \\ &\quad + \int_{\Sigma} \nabla \varphi \cdot \nabla \psi \mathbf{V} \cdot \mathbf{n} \, d\sigma + \int_{\Sigma} \partial_{\mathbf{n}} \left[(\beta \varphi - \lambda) \psi + \frac{1}{2} (\partial_{\mathbf{n}} \varphi - \lambda)^2 \right] \mathbf{V} \cdot \mathbf{n} \, d\sigma \\ &\quad + \int_{\Sigma} \kappa \left[(\beta \varphi - \lambda) \psi + \frac{1}{2} (\partial_{\mathbf{n}} \varphi - \lambda)^2 \right] \, d\sigma, \end{aligned}$$

where (by Lemma 2.1.3)

$$\dot{\varphi} = \left. \frac{d}{dt} \varphi \circ T_t^{-1} \right|_{t=0} = -\nabla \varphi \cdot \mathbf{V} \in H^1(\Omega) \quad \text{and} \quad \dot{\psi} = \left. \frac{d}{dt} \psi \circ T_t^{-1} \right|_{t=0} = -\nabla \psi \cdot \mathbf{V} \in H^1(\Omega).$$

Substituting (φ, ψ) by (u, p) , we see that the first and second integral vanish due to (1.24) with $\psi = -\nabla p \cdot \mathbf{V}$ and (2.12) with $\varphi = -\nabla u \cdot \mathbf{V}$. Consequently, we get

$$dJ_1(\Sigma)[\mathbf{V}] = \int_{\Sigma} g_1 \mathbf{n} \cdot \mathbf{V} \, d\sigma$$

where

$$g_1 = \nabla u \cdot \nabla p + (\beta u - \lambda) \partial_{\mathbf{n}} p + \beta p \partial_{\mathbf{n}} u + (\partial_{\mathbf{n}} u - \lambda) \partial_{\mathbf{nn}}^2 u + \kappa \left[(\beta u - \lambda) p + \frac{1}{2} (\partial_{\mathbf{n}} u - \lambda)^2 \right],$$

as desired.

If we take $\beta = \kappa$, g_1 simplifies to

$$g_1 = \nabla u \cdot \nabla p - \kappa(u - p) \partial_{\mathbf{n}} u + (\partial_{\mathbf{n}} u - \lambda) \partial_{\mathbf{nn}}^2 u + \frac{\kappa}{2} (\partial_{\mathbf{n}} u - \lambda)^2.$$

Moreover, if Ω^* is such that $u = u(\Omega^*)$ is the solution to the Bernoulli problem (1.3), i.e., it holds that $\partial_{\mathbf{n}}u = \lambda$ on Σ^* , then $p = p(\Omega^*)$ is identically equal to zero. Hence, $g_1 = 0$ on Σ^* , and this implies that $dJ_1(\Sigma)[\mathbf{V}] = \int_{\Sigma} (0) \mathbf{n} \cdot \mathbf{V} d\sigma = 0$. This finishes the proof of the proposition. ■

Evidently, the computed shape gradient of J_1 under the proposed formulation differs from the classical one (see [67, Theorem 3.1]). We recall that the cost function J_N with state variable u satisfying (1.9) has the shape derivative given by

$$dJ_N(\Sigma)[\mathbf{V}] = \int_{\Sigma} g_N \mathbf{V} \cdot \mathbf{n} d\sigma := - \int_{\Sigma} \left\{ \frac{\partial u}{\partial \mathbf{n}} \frac{\partial p}{\partial \mathbf{n}} + \kappa \left(\frac{1}{2} p^2 + \lambda p \right) \right\} \mathbf{n} \cdot \mathbf{V} d\sigma,$$

where the adjoint state p satisfies

$$(2.17) \quad -\Delta p = 0 \text{ in } \Omega, \quad p = 0 \text{ on } \Gamma, \quad p = \partial_{\mathbf{n}}u - \lambda \text{ on } \Sigma.$$

In the case of the interior problem, the shape derivative of J_N^{int} at Ω in the direction of the velocity field \mathbf{V} is given as follows.

Proposition 2.2.3. Let Ω be a $C^{2,1}$ bounded domain. Then, the shape derivative of the cost function $J_N^{\text{int}}(\Sigma)$ along a deformation field $\mathbf{V} \in \Theta^2$ is given by

$$dJ_N^{\text{int}}(\Sigma)[\mathbf{V}] = \int_{\Sigma} g_N^{\text{int}} \mathbf{n} \cdot \mathbf{V} d\sigma := \int_{\Sigma} \left\{ \nabla u \cdot \nabla p + \frac{\partial u}{\partial \mathbf{n}} \frac{\partial p}{\partial \mathbf{n}} + p \frac{\partial p}{\partial \mathbf{n}} + (u-1) \left(\frac{\partial^2 p}{\partial \mathbf{n}^2} + \kappa \frac{\partial p}{\partial \mathbf{n}} \right) + \frac{\kappa}{2} p^2 \right\} \mathbf{n} \cdot \mathbf{V} d\sigma,$$

where u is the unique solution to the pure Dirichlet BVP (1.14) and p is the corresponding adjoint state variable satisfying the same system 2.17 (where, of course, Γ represents the exterior boundary while Σ is the interior boundary).

Of course, one could also consider a reformulation of (1.5) similar to our proposed formulation for the exterior Bernoulli problem by constructing an associated state problem with a Robin condition. Instead of (1.14), we can use the PDE system

$$(2.18) \quad -\Delta u^{\text{int}} = 0 \text{ in } \Omega, \quad u^{\text{int}} = 0 \text{ on } \Gamma, \quad \partial_{\mathbf{n}}u^{\text{int}} + \beta u^{\text{int}} = \lambda + \beta \text{ on } \Sigma,$$

where $\beta > 0$, as the state problem. With this new state equation, the shape gradient of J_1^{int} has now a different structure as evident in the following result.

Proposition 2.2.4. Let Ω be a $C^{2,1}$ bounded domain. Then, the shape derivative of the cost function $J_1^{\text{int}}(\Sigma)$ (subject to (2.18)) along a deformation field $\mathbf{V} \in \Theta^2$ is given by

$$dJ_1^{\text{int}}(\Sigma)[\mathbf{V}] = \int_{\Sigma} g_1^{\text{int}} \mathbf{V} \cdot \mathbf{n} d\sigma,$$

where

$$g_1^{\text{int}} := \nabla u \cdot \nabla p + \left(\frac{\partial p}{\partial \mathbf{n}} + \kappa p \right) (\beta u - \lambda - \beta) + \beta p \frac{\partial u}{\partial \mathbf{n}} + \left(\frac{\partial u}{\partial \mathbf{n}} - \lambda \right) \frac{\partial^2 u}{\partial \mathbf{n}^2} + \frac{\kappa}{2} \left(\frac{\partial u}{\partial \mathbf{n}} - \lambda \right)^2,$$

and p is the adjoint state satisfying the same system (2.12) (where, of course, Γ represents the exterior boundary while Σ is the interior boundary).

If $\beta = \kappa$, the kernel g_1^{int} simplifies to

$$g_1^{\text{int}} = \nabla u \cdot \nabla p - \frac{\partial u}{\partial \mathbf{n}} \frac{\partial p}{\partial \mathbf{n}} + \left(\frac{\partial u}{\partial \mathbf{n}} - \lambda \right) \frac{\partial^2 u}{\partial \mathbf{n}^2} + \frac{\kappa}{2} \left(\frac{\partial u}{\partial \mathbf{n}} - \lambda \right)^2.$$

We omit the proofs of these two propositions since they are similar to that of Proposition 2.2.2.

2.3 Shape Derivative of J_2

Here we carry out the sensitivity analysis of the cost functional $J_2(\Omega)$ with respect to a local perturbation of the domain Ω . More precisely, we derive the first- and the second-order shape derivatives of J_2 through chain rule approach. This method requires, beforehand, the expressions for the shape derivatives of the states u_N and u_R . The shape derivatives of u_N and u_R were already obtained in [13, Theorem 6] and [109, Section 2], respectively, and their existence can be guaranteed if Ω is assumed to be at least $C^{2,1}$ regular.

Before we give the shape derivatives of u_R and u_N with respect to domain variations, let us first mention that on the perturbed domain Ω_t , the state solutions u_{Nt} and u_{Rt} satisfy

$$(2.19) \quad -\Delta u_{Nt} = 0 \text{ in } \Omega_t, \quad u_{Nt} = 1 \text{ on } \Gamma_t, \quad \nabla u_{Nt} \cdot \mathbf{n}_t = \lambda \text{ on } \Sigma_t;$$

$$(2.20) \quad -\Delta u_{Rt} = 0 \text{ in } \Omega_t, \quad u_{Rt} = 1 \text{ on } \Gamma_t, \quad \nabla u_{Rt} \cdot \mathbf{n}_t + \beta u_{Rt} = \lambda \text{ on } \Sigma_t,$$

respectively, where \mathbf{n}_t is the unit outward normal to Σ_t , and $\Gamma_t = \Gamma$, for all t .

Lemma 2.3.1 ([13]). Let Ω be a bounded $C^{2,1}$ domain and $V \in \Theta^2$ be a given velocity field. Then, $u_N \in H^3(\Omega)$ is shape differentiable with respect to the domain, and its shape derivative $u'_N \in H^1(\Omega)$ is the unique solution of the mixed Dirichlet-Neumann problem

$$(2.21) \quad \begin{cases} -\Delta u'_N = 0 & \text{in } \Omega, \\ u'_N = 0 & \text{on } \Gamma, \\ \partial_{\mathbf{n}} u'_N = \text{div}_{\Sigma}(V \cdot \mathbf{n} \nabla_{\Sigma} u_N) + \lambda \kappa V \cdot \mathbf{n} & \text{on } \Sigma, \end{cases}$$

where κ denotes the mean curvature of Σ .

Lemma 2.3.2 ([109]). Let Ω be a bounded $C^{2,1}$ domain and $\mathbf{V} \in \Theta^2$ be a given velocity field. Then, $u_R \in H^3(\Omega)$ is shape differentiable with respect to the domain, and its shape derivative $u'_R \in H^1(\Omega)$ is the unique solution of the mixed Robin-Neumann problem

$$(2.22) \quad \begin{cases} -\Delta u'_R = 0 & \text{in } \Omega, \\ u'_R = 0 & \text{on } \Gamma, \\ \partial_n u'_R + \beta u'_R = \operatorname{div}_\Sigma(\mathbf{V} \cdot \mathbf{n} \nabla_\Sigma u_R) + \lambda \kappa \mathbf{V} \cdot \mathbf{n} - \beta (\partial_n u_R + \kappa u_R) \mathbf{V} \cdot \mathbf{n} & \text{on } \Sigma. \end{cases}$$

If $\beta = \kappa$, then for the shape derivative u'_R of the solution of (1.15), it holds that $u'_R \equiv 0$ when Σ is the free boundary.

We elaborate briefly the last statement given in the previous lemma. Indeed, from (2.22), we note that the shape derivative u'_R satisfies the equation

$$\int_\Omega \nabla u'_R \cdot \nabla \varphi \, dx + \int_\Sigma \beta u'_R \varphi \, d\sigma = \int_\Sigma \left[-\nabla_\Sigma u'_R \cdot \nabla_\Sigma \varphi - \beta \left(\frac{\partial u_R}{\partial \mathbf{n}} + \kappa u_R \right) \varphi + \lambda \kappa \varphi \right] \mathbf{V} \cdot \mathbf{n} \, d\sigma, \quad \forall \varphi \in H_{\Gamma,0}^1(\Omega).$$

Hence, if Σ is the free boundary (i.e., $\Sigma = \Sigma^*$, where Σ^* denotes the optimal free boundary), then $u_R = 0$ on Σ , and so $-\nabla_\Sigma u'_R \cdot \nabla_\Sigma \varphi = 0$. This leaves us the equation

$$\int_\Omega \nabla u'_R \cdot \nabla \varphi \, dx + \int_\Sigma \beta u'_R \varphi \, d\sigma = \int_\Sigma \left(-\beta \frac{\partial u_R}{\partial \mathbf{n}} + \lambda \kappa \right) \varphi \mathbf{V} \cdot \mathbf{n} \, d\sigma, \quad \forall \varphi \in H_{\Gamma,0}^1(\Omega).$$

Since $\partial_n u_R = \lambda$ on Σ , then by choosing $\beta = \kappa$, the right side of the above equation vanishes and we get $u'_R \equiv 0$. This identity plays an important role in this present section (as well as in Section 2.4), particularly in simplifying the expression for the shape derivative of J_2 which would make the minimization problem more attractive in terms of numerical aspects. For this reason, throughout the rest of this thesis, we will refer to it as *Tiihonen's condition* (see [109, Lemma 1]):

(2.23) “ $\beta = \kappa$ and u'_R is the shape derivative of the solution of (1.15) where Σ is the free boundary.”

2.3.1 The Shape Gradient of J_2

The shape derivative of J_2 is given in the following proposition.

Proposition 2.3.1. Let Ω be of class $C^{2,1}$ and $\mathbf{V} \in \Theta^2$. Then, the energy-gap cost functional J_2 is shape differentiable with

$$(2.24) \quad dJ_2(\Omega)[\mathbf{V}] = \int_\Sigma g_2 \mathbf{n} \cdot \mathbf{V} \, d\sigma := \int_\Sigma [g_0 \mathbf{n} \cdot \mathbf{V} - \beta(u_R - u_N) u'_R] \, d\sigma,$$

where

$$g_0 = \lambda^2 - \lambda\beta u_R - \beta(u_R - u_N)(\nabla u_R \cdot \mathbf{n} + \kappa u_R) - \nabla u_R \nabla u_N \\ - (\nabla u_R \cdot \boldsymbol{\tau})(\nabla u_N \cdot \boldsymbol{\tau}) + \frac{1}{2} [\beta^2 u_R^2 - (\nabla u_R \cdot \boldsymbol{\tau})^2 - (\nabla u_N \cdot \boldsymbol{\tau})^2].$$

Here, of course, κ denotes the mean curvature of Σ . Moreover, $\boldsymbol{\tau}$ represents the unit tangent vector on Σ and it is oriented in such a way that Σ is at the left of $\boldsymbol{\tau}$; that is, if $\mathbf{n} = (n_1, n_2)^\top$, then $\boldsymbol{\tau} = (-n_2, n_1)^\top$.

If, in addition, u'_R is the shape derivative of the solution of (1.15) where Σ is the free boundary, then, for $\beta = \kappa$, the shape gradient considerably simplifies to

$$(2.25) \quad dJ_2(\Omega)[V] = \int_{\Sigma} g_2^\top \mathbf{n} \cdot V \, d\sigma := \int_{\Sigma} \left(\lambda \kappa u_N - \frac{1}{2} (\nabla u_N \cdot \boldsymbol{\tau})^2 \right) \mathbf{n} \cdot V \, d\sigma.$$

The proof of the above proposition, which we will give shortly, utilizes Hadamard's domain differentiation formula given by (2.5) and the tangential Green's identity in Lemma 2.1.5.

Proof. Let Ω be of class $C^{2,1}$ and $V \in \Theta^2$. Since u_N and u_R are sufficiently regular, we can apply (2.5) to obtain

$$dJ_2(\Omega)[V] = \int_{\Omega} \nabla(u_R - u_N) \cdot \nabla(u'_R - u'_N) \, dx + \frac{1}{2} \int_{\Sigma} |\nabla(u_R - u_N)|^2 V \cdot \mathbf{n} \, d\sigma =: \mathbb{I}_1 + \mathbb{I}_2,$$

where u'_N and u'_R satisfy (2.21) and (2.22), respectively. The second integral can be easily expanded as

$$\mathbb{I}_2 = \frac{1}{2} \int_{\Sigma} [\lambda^2 - 2\lambda\beta u_R + \beta^2 u_R^2 + (\nabla u_R \cdot \boldsymbol{\tau})^2] V \cdot \mathbf{n} \, d\sigma + \frac{1}{2} \int_{\Sigma} [-2\nabla u_R \nabla u_N + \lambda^2 + (\nabla u_N \cdot \boldsymbol{\tau})^2] V \cdot \mathbf{n} \, d\sigma.$$

On the other hand, we can express the first integral as follows

$$\begin{aligned} \mathbb{I}_1 &\stackrel{\langle 1 \rangle}{=} \int_{\Sigma} (u_R - u_N) \partial_{\mathbf{n}}(u'_R - u'_N) \, d\sigma \\ &\stackrel{\langle 2 \rangle}{=} \int_{\Sigma} (u_R - u_N) \operatorname{div}_{\Sigma}(V \cdot \mathbf{n} \nabla_{\Sigma}(u_R - u_N)) \, d\sigma - \int_{\Sigma} \beta(u_R - u_N) [(\partial_{\mathbf{n}} u_R + \kappa u_R) V \cdot \mathbf{n} + u'_R] \, d\sigma \\ &\stackrel{\langle 3 \rangle}{=} - \int_{\Sigma} [(\nabla u_R \cdot \boldsymbol{\tau})^2 + (\nabla u_N \cdot \boldsymbol{\tau})^2] V \cdot \mathbf{n} \, d\sigma - \int_{\Sigma} 2(\nabla_{\Sigma} u_R \cdot \nabla_{\Sigma} u_N) V \cdot \mathbf{n} \, d\sigma \\ &\quad - \int_{\Sigma} \beta(u_R - u_N) [(\partial_{\mathbf{n}} u_R + \kappa u_R) V \cdot \mathbf{n} + u'_R] \, d\sigma. \end{aligned}$$

Equality $\langle 1 \rangle$ is due to Green's formula. Meanwhile, $\langle 2 \rangle$ follows from (2.21) and (2.22). Lastly, equality $\langle 3 \rangle$ was derived through the identity

$$\int_{\Sigma} \varphi \operatorname{div}_{\Sigma}(V \cdot \mathbf{n} \nabla_{\Sigma} \varphi) \, d\sigma = - \int_{\Sigma} (\nabla \varphi \cdot \boldsymbol{\tau})^2 V \cdot \mathbf{n} \, d\sigma, \quad \varphi \in H^3(\Omega),$$

which holds true because $V \cdot \mathbf{n} \nabla_{\Sigma} \varphi \cdot \mathbf{n} = 0$ (cf. tangential Green's formula in Lemma 2.1.5). Furthermore, in $\langle 3 \rangle$, we note that we may write $\nabla_{\Sigma} u_R \cdot \nabla_{\Sigma} u_N = (\nabla u_R \cdot \boldsymbol{\tau})(\nabla u_N \cdot \boldsymbol{\tau})$. Thus, summing up the computed expressions for \mathbb{I}_1 and \mathbb{I}_2 , we get (2.24).

Employing Tiihonen's condition (2.23), we have $u_R = 0$ and $\partial_{\mathbf{n}} u_R = \lambda$ on Σ , and, in addition, $u'_R \equiv 0$. In addition, we get the relation $\nabla u_R = (\partial_{\mathbf{n}} u_R) \mathbf{n}$ on Σ from which we deduce that $\nabla u_R \cdot \boldsymbol{\tau} = 0$ on Σ . Direct substitutions of these identities in (2.24) eventually lead to (2.25), completing the proof of the proposition. ■

Remark 2.3.1. Because $u_N \in H^2(\Omega)$, we know that $(\nabla u_N \cdot \boldsymbol{\tau})^2 \in L^1(\Sigma)$. Also, for domains Ω of class $C^{1,1}$, the outward unit normal vector \mathbf{n} to Σ is Lipschitz continuous (cf. Remark 1.2.2). By Rademacher's theorem [102, Theorem 2.7.1], the mean curvature κ then belongs to $L^\infty(\Sigma)$. So, $\lambda \kappa u_N \in L^2(\Sigma)$. Since, in addition, $\mathbf{V} \cdot \mathbf{n} \in C^{0,1}(\Sigma) \subset L^\infty(\Sigma)$, we find that $dJ_2(\Omega)[\mathbf{V}]$ is well-defined. Moreover, J_2 is indeed shape differentiable at Ω because $dJ_2(\Omega)[\mathbf{V}]$ exists for all $\mathbf{V} \in \Theta^2$. Noting that $dJ_2(\Omega)[\mathbf{V}] \leq |g_2|_{L^1(\Sigma)} |\mathbf{V}|_{C^{1,1}(\overline{\Omega})}$, we also conclude that the map $\mathbf{V} \mapsto dJ_2(\Omega)[\mathbf{V}]$ is linear and continuous with respect to $\mathbf{V} \in \Theta^2$.

As an immediate consequence of Proposition 2.3.1, we have the following.

Corollary 2.3.3. Let the domain Ω^* be such that $u = u(\Omega^*)$ satisfies the overdetermined BVP (1.3); i.e., it holds that $u = u_R = u_N$ on $\overline{\Omega^*}$. Then, the domain Ω^* fulfils the necessary optimality condition

$$dJ_2(\Omega^*)[\mathbf{V}] = 0, \quad \text{for all } \mathbf{V} \in \Theta^2.$$

Proof. At the shape solution $\Omega = \Omega^*$ of the exterior Bernoulli problem (1.3), $u_N = 0$ on Σ . Hence, $\nabla u_N = (\partial_{\mathbf{n}} u_N) \mathbf{n}$ on Σ and it follows that $\nabla u_N \cdot \boldsymbol{\tau} = 0$ on Σ . Thus, $g_2 \equiv 0$ on $\overline{\Omega}$ implies the assertion. ■

We reiterate that, as opposed to the classical Kohn-Vogelius cost functional minimization problem (1.10) of (1.3), we only to solve (1.7) in order to evaluate the shape gradient of J_2 . We recall from [14, Theorem 33] (see also [1, Theorem 2] and [51, Theorem 1]) that in the case of the classical setting, the shape gradient is

$$(2.26) \quad dJ_{KV}(\Omega)[\mathbf{V}] = \int_{\Sigma} g_{KV} \mathbf{n} \cdot \mathbf{V} \, d\sigma := \frac{1}{2} \int_{\Sigma} \{ \lambda^2 - (\nabla u_D \cdot \mathbf{n})^2 + 2\lambda \kappa u_N - (\nabla u_N \cdot \boldsymbol{\tau})^2 \} \mathbf{n} \cdot \mathbf{V} \, d\sigma$$

where the state functions u_D and u_N are the unique solutions to (1.9) and (1.7), respectively. Apparently, the shape gradient of J_2 is obtained from (2.26) when $\partial_{\mathbf{n}} u_D = \lambda$. Of course, this condition holds in the case of (1.15) if one assumes that $\beta = \kappa$, and that u'_R is the shape derivative of the solution of (1.15) where Σ is the free boundary.

In the next subsection, we compute for the expression of the shape Hessian of J_2 . We only focus on the derivation of its shape Hessian under the assumption of Tiihonen's condition (2.23); that is, we suppose that $dJ_2(\Omega)[\mathbf{V}] = \int_{\Sigma} g_2^T \mathbf{n} \cdot \mathbf{V} \, d\sigma$.

2.3.2 The Shape Hessian of J_2

Let \mathbf{W} be another velocity field in Θ^2 . From Proposition 2.3.1 together with Remark 2.3.1, the derivative $dJ_2(\Omega_s(\mathbf{W}))[\mathbf{V}]$ exists for all sufficiently small s . Our next objective now is to find an expression for the limit

$$\lim_{s \searrow 0} \frac{dJ_2(\Omega_s(\mathbf{W}))[\mathbf{V}] - dJ_2(\Omega)[\mathbf{V}]}{s} =: d^2 J_2(\Omega)[\mathbf{V}, \mathbf{W}],$$

where

$$dJ_2(\Omega_s(\mathbf{W}))[\mathbf{V}] = \int_{\Sigma_s} \mathbf{g}_{2s}^\top \mathbf{n}_s \cdot \mathbf{V} \, d\sigma_s = \int_{\Sigma_s} \left(\lambda \kappa_s u_{N_s} - \frac{1}{2} (\nabla u_{N_s} \cdot \boldsymbol{\tau}_s)^2 \right) \mathbf{n}_s \cdot \mathbf{V} \, d\sigma_s.$$

Here, $\Sigma_s := \Sigma_s(\mathbf{W})$ denotes the free boundary of the deformed domain $\Omega_s := \Omega_s(\mathbf{W})$ perturbed via the velocity field $\mathbf{W} \in \Theta^2$, and $u_{N_s} \in H^3(\Omega_s)$ is the unique solution of the state system (1.7) on $\overline{\Omega} = \overline{\Omega}_s$ (cf. equation (2.19) with t replaced by s). In addition, $\kappa_s = \operatorname{div}_{\Sigma_s} \mathbf{n}_s$, and \mathbf{n}_s and $\boldsymbol{\tau}_s$ refer to the unit outward normal and unit tangent vectors on Σ_s , respectively.

Let us recall from Definition 2.1.4 that, if for all \mathbf{V} and \mathbf{W} , $d^2 J_2(\Omega)[\mathbf{V}, \mathbf{W}]$ exists and is bilinear and continuous with respect to \mathbf{V} and \mathbf{W} , then J_2 is said to be twice shape differentiable at Ω . In this case, the map $(\mathbf{V}, \mathbf{W}) \mapsto d^2 J_2(\Omega)[\mathbf{V}, \mathbf{W}]$ is the shape Hessian of J_2 in the directions of \mathbf{V} and \mathbf{W} .

Before we characterize the shape Hessian of J_2 , we first introduce some notations. For convenience, we use the following notations for $\mathbf{V} \in \Theta^2$:

$$V_n := \mathbf{V} \cdot \mathbf{n}, \quad \mathbf{v} = \mathbf{V}|_{\Sigma}, \quad \text{and} \quad \mathbf{v} = \mathbf{v}_\Sigma + v_n \mathbf{n} := (\mathbf{v} \cdot \boldsymbol{\tau}) \boldsymbol{\tau} + (v_n) \mathbf{n}.$$

Also, we denote by φ'_W the shape derivative of φ along a deformation field $\mathbf{W} \in \Theta^2$. Moreover, we recall the shape derivatives of the mean curvature κ and the tangential vector $\boldsymbol{\tau}$ with respect to Ω in the direction of \mathbf{W} which are respectively given as (see [43, 106])

$$(2.27) \quad \kappa'_W = \operatorname{trace} \{ D[(D\mathbf{W} \mathbf{n} \cdot \mathbf{n}) \mathbf{n} - (D\mathbf{W})^\top \mathbf{n}] - D\mathbf{n} D\mathbf{W} \} - \nabla \kappa \cdot \mathbf{W},$$

$$(2.28) \quad \boldsymbol{\tau}'_W = [(D\mathbf{W})^\top \mathbf{n} \cdot \boldsymbol{\tau}] \mathbf{n} - (D\boldsymbol{\tau}) \mathbf{W}.$$

We now state the shape Hessian of J_2 at Ω in the following proposition.

Proposition 2.3.2. The second-order shape derivative $d^2 J_2(\Omega)[\mathbf{V}, \mathbf{W}]$ of the cost functional J_2 at Ω in the directions of the deformation fields $\mathbf{V}, \mathbf{W} \in \Theta^2$ has the following structure:

$$(2.29) \quad d^2 J_2(\Omega)[\mathbf{V}, \mathbf{W}] = \int_{\Sigma} \left[\mathbf{g}_{2W}^{\top'} V_n + (\nabla \mathbf{g}_2^\top \cdot \mathbf{n} + \kappa \mathbf{g}_2^\top) V_n W_n - \mathbf{g}_2^\top \mathbf{K} + \mathbf{g}_2^\top (D\mathbf{V}) W_n \right] d\sigma,$$

where \mathbf{g}_2^\top is the kernel of $dJ_2(\Omega)[\mathbf{V}]$ given in (2.25) and

$$(2.30) \quad \mathbf{g}_{2W}^{\top'} = \lambda (\kappa'_W u_N + \kappa u'_{NW}) - (\nabla u_N \cdot \boldsymbol{\tau}) (\nabla u'_{NW} \cdot \boldsymbol{\tau} + \nabla u_N \cdot \boldsymbol{\tau}'_W),$$

$$(2.31) \quad \nabla \mathbf{g}_2^\top \cdot \mathbf{n} = \lambda u_N (\nabla \kappa \cdot \mathbf{n}) + \lambda^2 \kappa,$$

$$(2.32) \quad \mathbf{K} = \mathbf{v}_\Sigma \cdot (D_\Sigma \mathbf{n}) \mathbf{w}_\Sigma + \mathbf{n} \cdot (D_\Sigma \mathbf{v}) \mathbf{w}_\Sigma + \mathbf{n} \cdot (D_\Sigma \mathbf{w}) \mathbf{v}_\Sigma.$$

Proof. Hereon, for simplicity, we denote by g'_2 the expression $g_2^{\top'} W$ and drop \cdot^\top in g_2^\top . Now, using Stoke's formula, we write the gradient $dJ_2(\Omega_s)[V]$ as

$$dJ_2(\Omega_s)[V] = \int_{\Omega_s} \operatorname{div}(g_{2s} \mathbf{n}_s \cdot V) dx_s.$$

From (2.5), we easily find that

$$(2.33) \quad d^2 J_2(\Omega)[V, W] = \int_{\Sigma} g'_2 V \cdot \mathbf{n} d\sigma + \int_{\Sigma} \operatorname{div}(g_2 V) W \cdot \mathbf{n} d\sigma,$$

where g'_2 given by (2.30) is simply obtained by differentiating g_2 .

Note that the shape Hessian (2.33) is consistent with the Hadamard-Zolésio structure theorem provided that u'_{NW} is linear and continuous function of V_n on the boundary Σ (cf. [43]). Moreover, notice in equation (2.33) the non-symmetry of the second integral in V_n and W_n .

Now we further extract from the second integral in (2.33) a few more symmetric expressions of the shape Hessian. The non-symmetric part will be obtained from (2.25) applied to the deformation field DVW (cf. [92]). Since Ω is a $C^{2,1}$ domain and we have enough regularity for the state u_N , then in view of [43, Eq. 6.10, p. 505], the following identity actually holds

$$(2.34) \quad \int_{\Sigma} \operatorname{div}(g_2 V) W \cdot \mathbf{n} d\sigma = \int_{\Sigma} [(\partial_n g_2 + \kappa g_2) V_n W_n - g_2 \mathbf{K} + g_2 (DV) W_n] d\sigma,$$

where \mathbf{K} is given by (2.32). Here, the explicit form of $\partial_n g_2$ is computed as follows

$$\nabla \left(\kappa \lambda u_N - \frac{1}{2} (\nabla u_N \cdot \boldsymbol{\tau})^2 \right) \cdot \mathbf{n} = \lambda u_N (\nabla \kappa \cdot \mathbf{n}) + \lambda^2 \kappa - (\nabla u_N \cdot \boldsymbol{\tau}) \nabla [(\nabla u_N \cdot \mathbf{n}) \cdot \boldsymbol{\tau}].$$

Since $\partial_n u_N = \lambda$ on Σ , the last summand in right side of the above equation disappear and we immediately arrive at (2.31). Substituting this expression into (2.33) proves the expression for the shape Hessian given by (2.29). ■

Here, we point out that we may in fact consider velocity fields $V \in \Theta^2$ that are normal to Σ , i.e., $V|_{\Sigma} = V_n \mathbf{n}$. In this case, we observe that the expression in (2.32) vanishes. Moreover, the last integrand in (2.29) can be expressed as $g_2 (DV) W_n = g_2 \partial_n v_n w_n$ because we in fact have the identity $(DV) W_n \mathbf{n} = D(v_n \mathbf{n}) w_n \mathbf{n} \cdot \mathbf{n} = w_n \mathbf{n}^\top [\mathbf{n} (\nabla(v_n))^\top + v_n D\mathbf{n}] \mathbf{n}$ and $D\mathbf{n} \cdot \mathbf{n} = 0$ on Σ (cf. [106]). Thus, for deformation fields $V, W \in \Theta^2$ with null tangential part, the shape Hessian (2.29) simplifies to

$$d^2 J_2(\Omega)[V, W] = \int_{\Sigma} [g'_2 v_n + (\partial_n g_2 + \kappa g_2) v_n w_n + g_2 \partial_n v_n w_n] d\sigma.$$

Note that, in the proof of Proposition 2.3.2, we managed not to use the second-order shape derivative of the states in characterizing the second-order Eulerian semi-derivative of J_2 contrary to [45]. Thanks to identity (2.34), the characterization of the shape Hessian was easily accomplished.

Remark 2.3.2. Notice in (2.30) the term κ'_W which represents the shape derivative of the mean curvature κ along the deformation field $\mathbf{W} \in \Theta^2$. Note that the explicit form of κ'_W given in (2.27) essentially consists of a second-order tangential derivative of the vector field \mathbf{W} , and this derivative actually exists due to our assumption that Ω is of class $C^{2,1}$. Hence, we deduce that the shape Hessian defines a continuous bilinear form

$$d^2 J_2(\Omega)[\mathbf{V}, \mathbf{W}] : \mathbf{H}^1(\Sigma) \times \mathbf{H}^1(\Sigma) \rightarrow \mathbb{R};$$

that is, $|d^2 J_2(\Sigma)[\mathbf{V}, \mathbf{W}]| \lesssim \|\mathbf{V}\|_{\mathbf{H}^1(\Sigma)} \|\mathbf{W}\|_{\mathbf{H}^1(\Sigma)}$. Here, the notation $\mathbf{H}^1(\cdot)$ denotes the Sobolev space $\mathbf{H}^1(\cdot) := \{\boldsymbol{\varphi} := (\varphi_1, \varphi_2) : \varphi_1, \varphi_2 \in H^1(\cdot)\}$ and is equipped with the norm $\|\boldsymbol{\varphi}\|_{\mathbf{H}^1(\cdot)}^2 = \|\varphi_1\|_{H^1(\cdot)}^2 + \|\varphi_2\|_{H^1(\cdot)}^2$. Similar definition is also given for $\mathbf{H}_{\Gamma,0}^1(\cdot)$ -space.

To end this section, let us also consider the shape solution Ω^* of the exterior Bernoulli problem (1.3), focusing on the case wherein Tiihonen's condition is applied in obtaining the shape Hessian $d^2 J_2(\Omega^*)$. Accordingly, the characterization of the shape Hessian of J_2 along the deformation fields $\mathbf{V}, \mathbf{W} \in \Theta^2$ at Ω^* is given as follows.

Corollary 2.3.4. At the solution of the Bernoulli problem (1.3), i.e., $\Omega = \Omega^*$, we have

$$(2.35) \quad d^2 J_2(\Omega^*)[\mathbf{V}, \mathbf{W}] = \int_{\Sigma^*} \lambda \kappa u'_{NW} \mathbf{V} \cdot \mathbf{n} \, d\sigma + \int_{\Sigma^*} \lambda^2 \kappa (\mathbf{V} \cdot \mathbf{n}) \mathbf{W} \cdot \mathbf{n} \, d\sigma.$$

Proof. Using Stoke's theorem, we write

$$\begin{aligned} dJ_2(\Omega)[\mathbf{V}] &= \int_{\Sigma} \lambda \kappa u_N \mathbf{V} \cdot \mathbf{n} \, d\sigma - \frac{1}{2} \int_{\Sigma} (\nabla u_N \cdot \boldsymbol{\tau})^2 \mathbf{V} \cdot \mathbf{n} \, d\sigma \\ &= \int_{\Omega} \operatorname{div}(\lambda \kappa u_N \mathbf{V}) \, dx - \frac{1}{2} \int_{\Omega} \operatorname{div}[(\nabla u_N \cdot \boldsymbol{\tau})^2 \mathbf{V}] \, dx =: G_1 - G_2. \end{aligned}$$

Then, in the direction of the velocity field $\mathbf{W} \in \Theta^2$, the shape derivative of the integral G_1 is computed as follows:

$$\begin{aligned} dG_1(\Omega)[\mathbf{W}] &= \int_{\Omega} \operatorname{div}(\lambda \kappa u'_{NW} \mathbf{V}) \, dx + \int_{\Sigma} \operatorname{div}(\lambda \kappa u_N \mathbf{V}) W_n \, d\sigma \\ &= \int_{\Sigma} \lambda \kappa u'_{NW} V_n \, d\sigma + \int_{\Sigma} \operatorname{div} \mathbf{V} (\lambda \kappa u_N) W_n \, d\sigma \\ &\quad + \int_{\Sigma} \mathbf{V}_{\Sigma} \cdot \nabla (\lambda \kappa u_N) W_n \, d\sigma + \int_{\Sigma} [\nabla (\lambda \kappa u_N) \cdot \mathbf{n}] V_n W_n \, d\sigma, \end{aligned}$$

where $\mathbf{V}_{\Sigma} := \mathbf{V} - V_n \mathbf{n}$. At the shape solution $\Omega = \Omega^*$ of (1.3), we know that $u_N = 0$ on Σ . Hence, the second and the third integrals disappear, and we are left with

$$dG_1(\Omega^*)[\mathbf{W}] = \int_{\Sigma^*} \lambda \kappa u'_{NW} V_n \, d\sigma + \int_{\Sigma^*} \lambda^2 \kappa V_n W_n \, d\sigma.$$

On the other hand, for G_2 , we have

$$\begin{aligned} dG_2(\Omega)[\mathbf{W}] &= \int_{\Omega} \operatorname{div}[(\nabla u'_{NW} \cdot \boldsymbol{\tau})(\nabla u_N \cdot \boldsymbol{\tau})\mathbf{V}] dx + \frac{1}{2} \int_{\Sigma} \operatorname{div}((\nabla u_N \cdot \boldsymbol{\tau})^2 \mathbf{V}) W_n d\sigma \\ &= \int_{\Sigma} (\nabla u'_{NW} \cdot \boldsymbol{\tau})(\nabla u_N \cdot \boldsymbol{\tau}) V_n d\sigma + \frac{1}{2} \int_{\Sigma} \operatorname{div} \mathbf{V} (\nabla u_N \cdot \boldsymbol{\tau})^2 W_n d\sigma \\ &\quad + \frac{1}{2} \int_{\Sigma} \mathbf{V}_{\Sigma} \cdot \nabla [(\nabla u_N \cdot \boldsymbol{\tau})^2] W_n d\sigma + \frac{1}{2} \int_{\Sigma} \{\nabla [(\nabla u_N \cdot \boldsymbol{\tau})^2] \cdot \mathbf{n}\} V_n W_n d\sigma. \end{aligned}$$

Furthermore, at $\Omega = \Omega^*$, we know that $\nabla u_N \cdot \boldsymbol{\tau} = 0$ on Σ . Therefore, $dG_2(\Omega^*)[\mathbf{W}]$ vanishes, and we conclude that $d^2 J_2(\Omega^*)[\mathbf{V}, \mathbf{W}] = dG_1(\Omega^*)[\mathbf{W}]$ as desired. \blacksquare

Alternative Proof Of course, equation (2.35) can be proven directly from Proposition 2.3.2 together with Corollary 2.3.3. Indeed, at $\Omega = \Omega^*$, we get $g_2 = 0$ and (2.30) reduces to $g'_2 = \lambda \kappa u'_{NW}$. Moreover, we have $\partial_n g_2 = \lambda^2 \kappa$. Inserting these identities to

$$d^2 J_2(\Omega^*)[\mathbf{V}, \mathbf{W}] = \int_{\Sigma^*} (g'_2 V_n + \partial_n g_2 V_n W_n) d\sigma$$

yields (2.35) as announced. \blacksquare

We mention here that, with the help of the shape Hessian information, a regularized Newton method (see, e.g., [47]) could be used in the numerical realization of the shape optimization problem (1.17). However, we emphasize that our main purpose of introducing the formulation (1.17) of (1.3) is to reduce the number of associated PDE systems (by imposing Tiihonen's condition in the computation of the shape gradient) to be solved during the optimization procedure. Applying a second-order method will obviously lessen the number of iterations needed to reduce the cost at certain magnitude. The disadvantage, however, is the additional computational burden and time to carry out the task. Moreover, we note that u'_{NW} depends on the velocity field \mathbf{W} . Hence, applying a second-order method would require the solution of a system of PDEs for each velocity field \mathbf{W} . This, in turn, will make the computation of the descent direction more involved. Nevertheless, the said issue can be resolved by introducing the adjoint method. For the sake of comparison, we will also consider the utilization of the shape Hessian of J_2 in a second-order optimization algorithm in solving a concrete example of the minimization problem (1.17). Towards this end, we will use a modified version of the so-called *H¹ Newton method* (see, e.g., [9, Problem 4.2, Eq. (29)]) which utilizes the Hessian information to compute for an appropriate descent direction for a gradient-based second-order shape optimization algorithm (see subsection 3.1.5 for further details). In our case, we only use the shape Hessian information at the solution Ω^* of the exterior Bernoulli problem (1.3) instead of the full Hessian information. Therefore, with respect to (2.35), we introduce the adjoint variable $q_N \in H^1(\Omega)$ which is the only solution to the PDE system

$$(2.36) \quad -\Delta q_N = 0 \text{ in } \Omega, \quad q_N = 0 \text{ on } \Gamma, \quad \partial_n q_N = \lambda \kappa V_n \text{ on } \Sigma,$$

so that we may write the shape Hessian $d^2 J_2(\Omega)[\mathbf{V}, \mathbf{W}]$ at $\Omega = \Omega^*$ as

$$d^2 J_2(\Omega^*)[\mathbf{V}, \mathbf{W}] = \int_{\Sigma^*} (\lambda \kappa q_N + \lambda^2 \kappa V_n) \mathbf{n} \cdot \mathbf{W} d\sigma.$$

We formally write the above result as a corollary to Proposition 2.3.2.

Corollary 2.3.5. The shape Hessian $d^2 J_2$ at the solution of the Bernoulli problem (1.3) given by (2.35) is equivalent to

$$(2.37) \quad d^2 J_2(\Omega^*)[\mathbf{V}, \mathbf{W}] = \int_{\Sigma^*} (\lambda \kappa q_N + \lambda^2 \kappa V_n) \mathbf{n} \cdot \mathbf{W} \, d\sigma,$$

where $q_N \in H^1(\Omega)$ is the unique solution to the PDE system (2.36).

2.4 Shape Derivative of J_3

We now turn our attention on the computation of the first- and second-order shape derivatives of the newly proposed shape functional J_3 . As in the previous section, we will derive the shape gradient as well as the shape Hessian of J_3 using the chain rule approach.

2.4.1 The Shape Gradient of J_3

We first provide the characterization of the shape gradient of J_3 under Tiihonen's condition followed by its general expression.

Proposition 2.4.1. Let Ω be of class $C^{2,1}$ and $\mathbf{V} \in \Theta^2$. Also, let us assume that condition (2.23) holds true. Then, the Dirichlet-data-gap cost functional $J_3^\Gamma := J_3$ is shape differentiable with

$$(2.38) \quad dJ_3^\Gamma(\Sigma)[\mathbf{V}] = \int_{\Sigma} \left[\left(\lambda p_N + \frac{1}{2} u_N^2 \right) \kappa - \nabla_{\Sigma} u_N \cdot \nabla_{\Sigma} p_N \right] \mathbf{n} \cdot \mathbf{V} \, d\sigma,$$

where p_N is the adjoint state which is the unique solution to the PDE system

$$(2.39) \quad -\Delta p_N = 0 \text{ in } \Omega, \quad p_N = 0 \text{ on } \Gamma, \quad \partial_n p_N = u_N \text{ on } \Sigma,$$

and κ denotes the mean curvature of Σ .

Proof. We use chain rule approach coupled with the adjoint method to obtain the shape derivative of J_3 given by (2.38). Let Ω be of class $C^{2,1}$ and $\mathbf{V} \in \Theta^2$. Because the state variables u_N and u_R are sufficiently regular, we can apply Hadamard's boundary differentiation formula (2.6) to obtain

$$(2.40) \quad dJ_3(\Sigma)[\mathbf{V}] = \int_{\Sigma} (u_N - u_R)(u'_N - u'_R) \, d\sigma + \int_{\Sigma} \left[\beta u_R (u_N - u_R) + \frac{1}{2} \kappa (u_N - u_R)^2 \right] \mathbf{V} \cdot \mathbf{n} \, d\sigma.$$

Here, of course, u'_N and u'_R satisfy (2.21) and (2.22), respectively. Assuming Tiihonen's condition, we know that $u'_R \equiv 0$ on $\bar{\Omega}$. The expression for $dJ_3(\Sigma)[\mathbf{V}]$ given by (2.40) then simplifies to

$$(2.41) \quad dJ_3^\top(\Sigma)[\mathbf{V}] = \int_{\Sigma} u_N u'_N d\sigma + \frac{1}{2} \int_{\Sigma} \kappa u_N^2 \mathbf{V} \cdot \mathbf{n} d\sigma,$$

where we put the superscript “ $(\cdot)^\top$ ” simply to emphasize that condition (2.23) was imposed in the computation of the shape gradient (*see* also comment on notation below).

We point out here that the representation (2.41) of the shape derivative J_3 at Ω in the direction of \mathbf{V} is actually not useful for practical applications, especially in the numerical realization of the minimization problem (1.18) because it would require the solution of (2.21) for each velocity field \mathbf{V} . This issue can be resolved using the adjoint method, particularly by introducing the adjoint system (2.39). Using (2.21) and (2.39), we observe, via Green's second identity, that

$$(2.42) \quad \int_{\Sigma} u'_N u_N d\sigma = \int_{\Sigma} u'_N \partial_n p_N d\sigma = \int_{\Sigma} p_N \partial_n u'_N d\sigma = \int_{\Sigma} p_N [\operatorname{div}_{\Sigma}(\mathbf{V} \cdot \mathbf{n} \nabla_{\Sigma} u_N) + \lambda \kappa \mathbf{V} \cdot \mathbf{n}] d\sigma.$$

At this point, we apply the tangential Green's formula (Lemma 2.1.5), noting that $\mathbf{V} \cdot \mathbf{n} \nabla_{\Sigma} u_N \cdot \mathbf{n} = 0$, to obtain

$$(2.43) \quad \int_{\Sigma} p_N \operatorname{div}_{\Sigma}(\mathbf{V} \cdot \mathbf{n} \nabla_{\Sigma} u_N) d\sigma = - \int_{\Sigma} \nabla_{\Sigma} u_N \cdot \nabla_{\Sigma} p_N \mathbf{V} \cdot \mathbf{n} d\sigma.$$

Combining equations (2.41), (2.42) and (2.43), we get the desired result. ■

Remark 2.4.1. We recall from [78, Theorem 4.1] (with $g = \text{const.} = \lambda$ and $f \equiv 0$) (see also [50, Lemma 2.1]) that the shape gradient of J_D is given by

$$dJ_D(\Sigma)[\mathbf{V}] = \int_{\Sigma} g_D \mathbf{n} \cdot \mathbf{V} d\sigma := \int_{\Sigma} \left[\frac{\partial}{\partial \mathbf{n}} \left(\frac{1}{2} u_N^2 + \lambda p_N \right) + \left(\frac{1}{2} u_N^2 + \lambda p_N \right) \kappa - \nabla u_N \cdot \nabla p_N \right] \mathbf{n} \cdot \mathbf{V} d\sigma$$

It seems not obvious, but the kernel g_3^\top given in (2.38) only differs by $\frac{\partial}{\partial \mathbf{n}} \left(\frac{1}{2} u_N^2 \right)$ from g_D . This can be made more clear if we apply the identity

$$(2.44) \quad - \langle \nabla_{\Sigma} u_N, \nabla_{\Sigma} p_N \rangle = - \langle \nabla u_N, \nabla p_N \rangle + \frac{\partial u_N}{\partial \mathbf{n}} \frac{\partial p_N}{\partial \mathbf{n}} = - \langle \nabla u_N, \nabla p_N \rangle + \lambda \frac{\partial p_N}{\partial \mathbf{n}}$$

to (2.38). Thus, in addition, we can actually write the shape gradient of J_3 equivalently as follows

$$dJ_3^\top(\Sigma)[\mathbf{V}] = \int_{\Sigma} \left[\left(\lambda p_N + \frac{1}{2} u_N^2 \right) \kappa - \langle \nabla u_N, \nabla p_N \rangle + \lambda \frac{\partial p_N}{\partial \mathbf{n}} \right] \mathbf{n} \cdot \mathbf{V} d\sigma.$$

Notations. Throughout the rest of the discussion, we will denote the shape gradient of J_3 in the direction of \mathbf{V} at Ω obtained under condition (2.23) as dJ_3^\top and its corresponding kernel by g_3^\top ; i.e.,

$$(2.45) \quad g_3^\top := \left(\lambda p_N + \frac{1}{2} u_N^2 \right) \kappa - \langle \nabla u_N, \nabla p_N \rangle + \lambda \frac{\partial p_N}{\partial \mathbf{n}}$$

(cf. Proposition 2.4.1). Meanwhile, the expression dJ_3 simply refers to the shape gradient of J_3 obtained without imposing assumption (2.23). More precisely, the expression for dJ_3 is given by equation (2.40):

$$(2.46) \quad dJ_3(\Sigma)[\mathbf{V}] = \int_{\Sigma} \left[w w' + \left(\beta u_R w + \frac{1}{2} \kappa w^2 \right) \mathbf{V} \cdot \mathbf{n} \right] d\sigma,$$

where we use the notation $w = u_N - u_R$ and $w' = u'_N - u'_R$ for simplicity.

Before we go to the next subsection, let us also write $dJ_3(\Sigma)[\mathbf{V}]$ in an equivalent form using the adjoint method. To do this, we consider two harmonic functions Ξ_N and Ξ_R that both vanish on Γ , and such that $\partial_{\mathbf{n}} \Xi_N = w$ and $\partial_{\mathbf{n}} \Xi_R + \beta \Xi_R = w$ on Σ . Then, by Green's second identity together with equations (2.21) and (2.22), we get

$$\begin{aligned} \int_{\Sigma} w w' d\sigma &= \int_{\Sigma} [u'_N w - u'_R (\partial_{\mathbf{n}} \Xi_R + \beta \Xi_R)] d\sigma = \int_{\Sigma} [u'_N w - \Xi_R (\partial_{\mathbf{n}} u'_R + \beta u'_R)] d\sigma \\ &= \int_{\Sigma} \Xi_N \operatorname{div}_{\Sigma} (\mathbf{V} \cdot \mathbf{n} \nabla_{\Sigma} u_N) d\sigma - \int_{\Sigma} \Xi_R \{ \operatorname{div}_{\Sigma} (\mathbf{V} \cdot \mathbf{n} \nabla_{\Sigma} u_R) - \beta (\partial_{\mathbf{n}} u_R + \kappa u_R) \mathbf{V} \cdot \mathbf{n} \} d\sigma \\ &=: \mathbb{J}_1 - \mathbb{J}_2. \end{aligned}$$

Note that for any $\varphi, \psi \in H^3(\Omega)$ such that $\mathbf{V} \cdot \mathbf{n} \nabla_{\Sigma} \varphi = 0$, it can be verified using the tangential Green's formula (Lemma 2.1.5) that the integral $\int_{\Sigma} \psi \operatorname{div}_{\Sigma} (\mathbf{V} \cdot \mathbf{n} \nabla_{\Sigma} \varphi) d\sigma$ can be expressed as

$$\int_{\Sigma} \psi \operatorname{div}_{\Sigma} (\mathbf{V} \cdot \mathbf{n} \nabla_{\Sigma} \varphi) d\sigma = - \int_{\Sigma} (\nabla_{\Sigma} \varphi \cdot \nabla_{\Sigma} \psi) \mathbf{V} \cdot \mathbf{n} d\sigma = \int_{\Sigma} (\partial_{\mathbf{n}} \varphi \partial_{\mathbf{n}} \psi - \nabla \varphi \cdot \nabla \psi) \mathbf{V} \cdot \mathbf{n} d\sigma.$$

Hence, we have

$$\begin{aligned} \mathbb{J}_1 - \mathbb{J}_2 &= \int_{\Sigma} \{ \nabla_{\Sigma} u_R \cdot \nabla_{\Sigma} \Xi_R - \nabla_{\Sigma} u_N \cdot \nabla_{\Sigma} \Xi_N + \beta \Xi_R [\lambda + (\kappa - \beta) u_R] \} \mathbf{V} \cdot \mathbf{n} d\sigma \\ &= \int_{\Sigma} \{ \nabla u_R \cdot \nabla \Xi_R - \nabla u_N \cdot \nabla \Xi_N + \lambda w - (\lambda - \beta u_R)(w - \beta \Xi_R) + \beta \Xi_R [\lambda + (\kappa - \beta) u_R] \} \mathbf{V} \cdot \mathbf{n} d\sigma. \end{aligned}$$

Inserting the above expression in (2.46) yields the following result.

Proposition 2.4.2. Let Ω be of class $C^{2,1}$ and $\mathbf{V} \in \Theta^2$. Then, J_3 is shape differentiable with

$$(2.47) \quad \begin{aligned} dJ_3(\Sigma)[\mathbf{V}] &= \int_{\Sigma} \mathbf{g}_3 \mathbf{n} \cdot \mathbf{V} d\sigma \\ \mathbf{g}_3 &:= \nabla u_R \cdot \nabla \Xi_R - \nabla u_N \cdot \nabla \Xi_N + \lambda (u_N - u_R) - (\lambda - \beta u_R)(u_N - u_R - \beta \Xi_R) \\ &\quad + \beta \Xi_R [\lambda + (\kappa - \beta) u_R] + \beta u_R (u_N - u_R) + \frac{1}{2} \kappa (u_N - u_R)^2, \end{aligned}$$

and the quantities Ξ_N and Ξ_R are the respective solutions to the following adjoint systems

$$(2.48) \quad -\Delta \Xi_N = 0 \text{ in } \Omega, \quad \Xi_N = 0 \text{ on } \Gamma, \quad \partial_{\mathbf{n}} \Xi_N = u_N - u_R \text{ on } \Sigma;$$

$$(2.49) \quad -\Delta \Xi_R = 0 \text{ in } \Omega, \quad \Xi_R = 0 \text{ on } \Gamma, \quad \partial_{\mathbf{n}} \Xi_R + \beta \Xi_R = u_N - u_R \text{ on } \Sigma.$$

Again, similar to what has been pointed out in the proof of Proposition 2.4.1, we emphasize that the main reason for rewriting the shape gradient $dJ_3(\Sigma)[V]$ given in (2.46) into $dJ_3(\Sigma)[V] = \int_{\Sigma} g_3 \mathbf{n} \cdot \mathbf{V} d\sigma$ is to avoid the computations of solutions to the BVPs (2.21) and (2.22) for each velocity field \mathbf{V} which are impractical to use in an iterative procedure. As an immediate consequence of Proposition 2.4.2, we have the following optimality result.

Corollary 2.4.1. Let the domain Ω^* be such that $u = u(\Omega^*)$ satisfies the overdetermined BVP (1.3); i.e., it holds that $u = u_R = u_N$ on $\overline{\Omega^*}$. Then, the domain Ω^* fulfils the necessary optimality condition

$$dJ_3(\Sigma^*)[V] = 0, \quad \text{for all } V \in \Theta^2.$$

In addition, of course, it also holds that $dJ_3^T(\Sigma^*)[V] = 0$, for all $V \in \Theta^2$.

Proof. At the shape solution $\Omega = \Omega^*$ of (1.3), $u_N = 0$ on Σ^* . Hence, $\nabla u_N = (\partial_{\mathbf{n}} u_N) \mathbf{n}$ on Σ , and it follows that $\nabla u_N \cdot \boldsymbol{\tau} = 0$ on Σ^* . Moreover, we see that $\Xi_N \equiv 0$ and $\Xi_R \equiv 0$ (and also $p_N \equiv 0$) in $\overline{\Omega^*}$. Therefore, g_3 given by (2.47) is zero (so is g_3^T in (2.45)), which proves the assertion. ■

In the next subsection, we turn our attention in the computation of the second-order shape derivative of J_3 at Ω in the direction of two vector fields in Θ^2 . We first treat the case when condition (2.23) is imposed during the calculation of the shape derivative followed by the case when it is disregarded (see Subsection 2.4.4).

2.4.2 The Shape Hessian of J_3

Let us now focus on the computation of the shape Hessian of J_3 at Ω in the direction of two vector fields $\mathbf{V}, \mathbf{W} \in \Theta^2$. Firstly, we note that due to standard regularity theory for elliptic equations, we know that the $H^3(\Omega)$ regularity of u_N provides the same regularity $H^3(\Omega)$ to p_N . Hence, for sufficiently small s , it is clear that the derivative $dJ_3^T(\Omega_s(\mathbf{W}))[V]$ of J_3 (under assumption (2.23)) at $\Omega_s(\mathbf{W}) \subset U$ is well-defined.

Our goal, therefore, (as in subsection 2.3.2) is to find an expression for the limit

$$\lim_{s \searrow 0} \frac{dJ_3^T(\Omega_s(\mathbf{W}))[V] - dJ_3^T(\Omega)[V]}{s} =: d^2 J_3^T(\Sigma)[V, \mathbf{W}],$$

where

$$dJ_3^T(\Omega_s(\mathbf{W}))[V] = \int_{\Sigma_s} \left\{ \left(\lambda p_{Ns} + \frac{1}{2} u_{Ns}^2 \right) \kappa_s - \langle \nabla u_{Ns}, \nabla p_{Ns} \rangle + \lambda \frac{\partial p_{Ns}}{\partial \mathbf{n}_s} \right\} \mathbf{n}_s \cdot \mathbf{V} d\sigma_s.$$

Here, the expression appearing in the integrand of $dJ_3^T(\Omega_s(\mathbf{W}))[V]$ are of course of the same definitions as in subsection 2.3.2.

We will show, similar to what has been shown in the case of J_2 , that for an admissible domain Ω , the shape Hessian of J_3 has its support on the free boundary Σ , and it is independent on the

tangential component of \mathbf{W} on the boundary. Generally, however, the exact expression for the shape Hessian consists of the tangential component of \mathbf{V} (cf. (2.34)). This means, basically, that the shape Hessian is, in general, not symmetric as we have already seen in Proposition 2.3.2 in the case of J_2 (see, e.g., [43, Chapter 9, Section 6]). Nevertheless, at the optimal shape solution Ω^* of J_3 , it can be proved that only the normal components of \mathbf{V} and \mathbf{W} contributes to the shape Hessian. Here, we focus our attention on this situation because we are only interested in the expression for the shape Hessian of J_3 at the solution Ω^* of the exterior Bernoulli problem (1.3).

Proposition 2.4.3. Let Ω be of class $C^{2,1}$, $\mathbf{V}, \mathbf{W} \in \Theta^2$, and β be the mean curvature of Σ . Then, the shape Hessian of J_3 at Ω^* is given by

$$(2.50) \quad d^2 J_3^\top(\Sigma^*)[\mathbf{V}, \mathbf{W}] = \int_{\Sigma^*} \lambda \kappa p'_{\text{NW}} \mathbf{n} \cdot \mathbf{V} \, d\sigma,$$

where p'_{NW} denotes the shape derivative of the adjoint state p_N in the direction of \mathbf{W} satisfying the PDE system

$$(2.51) \quad -\Delta p'_{\text{NW}} = 0 \text{ in } \Omega^*, \quad p'_{\text{NW}} = 0 \text{ on } \Gamma, \quad \partial_{\mathbf{n}} p'_{\text{NW}} = u'_{\text{NW}} + \lambda \mathbf{W} \cdot \mathbf{n} \text{ on } \Sigma^*,$$

where u'_{NW} denotes the shape derivative of u_N in the direction of \mathbf{W} .

Proof. For convenience, we denote the shape derivative of φ in the direction \mathbf{W} by φ' (i.e., $\varphi' = \varphi'_{\mathbf{W}}$) throughout the proof. Let $\mathbf{N}_s = \mathbf{N}_s(\mathbf{W})$ be a smooth extension of \mathbf{n}_s (see, e.g. [43, Equation (4.37), p. 491]). Using (2.6) with $\varphi(s, \sigma) = g_{3s}^\top \mathbf{n}_s \cdot \mathbf{V} = g_{3s}^\top \mathbf{N}_s \cdot \mathbf{V}$, and \mathbf{V} replaced by \mathbf{W} , we get

$$d^2 J_3^\top(\Sigma)[\mathbf{V}, \mathbf{W}] = \int_{\Sigma} (g_3^{\top'} \mathbf{N} + g_3^{\top} \mathbf{N}') \cdot \mathbf{V} \, d\sigma + \int_{\Sigma} \{ \partial_{\mathbf{n}} g_3^{\top} (\mathbf{N} \cdot \mathbf{V}) + g_3^{\top} \partial_{\mathbf{n}} (\mathbf{N} \cdot \mathbf{V}) + \kappa g_3^{\top} \mathbf{N} \cdot \mathbf{V} \} \mathbf{n} \cdot \mathbf{W} \, d\sigma.$$

By Corollary 2.4.1, we know that $g_3^{\top} = 0$ on Σ^* . Then, since $\mathbf{N}|_{\Sigma} = \mathbf{n}$, we have

$$(2.52) \quad d^2 J_3^\top(\Sigma^*)[\mathbf{V}, \mathbf{W}] = \int_{\Sigma^*} \{ g_3^{\top'} \mathbf{n} \cdot \mathbf{V} + \partial_{\mathbf{n}} g_3^{\top} (\mathbf{n} \cdot \mathbf{V}) \mathbf{n} \cdot \mathbf{W} \} \, d\sigma.$$

Here, because $p_N \equiv 0$, and $u_N = 0$, and $\partial_{\mathbf{n}} u_N = \lambda$ on Σ^* , we see that $g_3^{\top'}|_{\Sigma^*}$ is given by

$$\begin{aligned} g_3^{\top'}|_{\Sigma^*} &= \left\{ (\lambda p'_N + u_N u'_N) \kappa + \left(\lambda p_N + \frac{1}{2} u_N^2 \right) \kappa' - \langle \nabla u'_N, \nabla p_N \rangle - \langle \nabla u_N, \nabla p'_N \rangle + \lambda (\nabla p'_N \cdot \mathbf{n} + \nabla p_N \cdot \mathbf{n}') \right\} \Big|_{\Sigma^*} \\ &= \lambda \kappa p'_N. \end{aligned}$$

On the other hand, we note that, for $\varphi, \psi \in H^3(\Omega)$, $\nabla(\nabla\varphi \cdot \nabla\psi) \cdot \mathbf{n} = (\nabla^2\varphi \nabla\psi + \nabla^2\psi \nabla\varphi) \cdot \mathbf{n}$ which holds true since the Hessian $\nabla^2\varphi$ of φ is actually symmetric. Hence, the term $\partial_{\mathbf{n}} g_3^{\top}$ vanishes on Σ^* because

$$\begin{aligned} \frac{\partial g_3^{\top}}{\partial \mathbf{n}} \Big|_{\Sigma^*} &= \left\{ (\lambda \partial_{\mathbf{n}} p_N + u_N \partial_{\mathbf{n}} u_N) \kappa + \left(\lambda p_N + \frac{1}{2} u_N^2 \right) \partial_{\mathbf{n}} \kappa - (\nabla^2 u_N \nabla p_N + \nabla^2 p_N \nabla u_N) \cdot \mathbf{n} + \lambda \nabla^2 p_N \mathbf{n} \cdot \mathbf{n} \right\} \Big|_{\Sigma^*} \\ &= 0. \end{aligned}$$

Thus, we have

$$d^2 J_3^T(\Sigma^*)[\mathbf{V}, \mathbf{W}] = \int_{\Sigma^*} \lambda \kappa p'_{NW} \mathbf{n} \cdot \mathbf{V} \, d\sigma,$$

where p'_{NW} satisfies the PDE system (2.51). This proves the proposition. \blacksquare

In view of the previous proposition, we observe that in order to evaluate the shape Hessian of J_3 , we first need to compute the solution p'_{NW} of (2.51) which depends on u'_{NW} , and hence to the perturbation field \mathbf{W} . In terms of numerical aspect, this step is quite problematic to implement in an iterative procedure because it would require the solution of (2.51) for each deformation field \mathbf{W} at every iteration. To resolve the issue, we can again apply the adjoint method (see Remark 2.4.2 in Section 2.4.4) as done in the proof of Proposition 2.4.1. Before we do this, let us first validate our claim that the shape derivative p'_{NW} of p_N indeed satisfies the PDE system (2.51). Afterwards, we will examine the symmetry of the shape Hessian $d^2 J_3(\Sigma^*)$ of J_3 with respect to the velocity fields \mathbf{V} and \mathbf{W} , then finally demonstrate how to eliminate the shape derivatives of the state and adjoint state variables by employing a nested application of the adjoint method.

2.4.3 The Shape Derivative of the Adjoint State

Before we derive the shape derivative of p_N , and for completeness, let us first prove the unique solvability of the adjoint problem on the perturbed domain Ω_t .

Lemma 2.4.2. For any $t > 0$ sufficiently small, the variational problem:

$$(2.53) \quad \text{find } p_N^t \in H_{\Gamma,0}^1(\Omega): \quad \int_{\Omega} A(t) \nabla p_N^t \cdot \nabla \varphi \, dx - \int_{\Sigma} B(t) u_{Nt}^t \varphi \, d\sigma = 0, \quad \forall \varphi \in H_{\Gamma,0}^1(\Omega).$$

admits a unique solution p_N^t in $H^1(\Omega)$.

Proof. We first note that the variational problem being examined is obtained from the problem:

$$(2.54) \quad \text{find } p_{Nt} \in H_{\Gamma,0}^1(\Omega_t) \text{ such that } \int_{\Omega_t} \nabla p_{Nt} \cdot \nabla \varphi \, dx_t - \int_{\Sigma_t} u_{Nt} \varphi \, d\sigma_t = 0, \quad \forall \varphi \in H_{\Gamma,0}^1(\Omega_t),$$

via the application of domain and boundary transformation formulas (see Lemma 2.1.2) In fact, the functions $\phi_t : \Omega_t \rightarrow \mathbb{R}$ and $\phi^t : \Omega \rightarrow \mathbb{R}$ are related through the equation $\phi^t = \phi_t \circ T_t$. Hence, if p_{Nt} solves the variational equation (2.54), then $p_N^t = p_{Nt} \circ T_t$ satisfies (2.53). Additionally, the boundary condition $p_N^t = p_{Nt} \circ T_t = 0$ on Γ implies that p_N^t is actually in $H_{\Gamma,0}^1(\Omega)$.

Now, consider the bilinear form $b_t(\cdot, \cdot) : H_{\Gamma,0}^1(\Omega) \rightarrow \mathbb{R}$ defined by

$$(2.55) \quad b_t(\phi^t, \varphi) = \int_{\Omega} A(t) \nabla \phi^t \cdot \nabla \varphi \, dx, \quad \forall \phi^t, \varphi \in H_{\Gamma,0}^1(\Omega).$$

Note that, as a consequence of Lemma 2.1.4, $A(t)$ is bounded. Hence, it is clear that $b_t(\cdot, \cdot)$ is continuous because $|b_t(\phi^t, \varphi)| = \left| \int_{\Omega} A(t) \nabla \phi^t \cdot \nabla \varphi \, dx \right| \lesssim \|A(t)\|_{L^\infty(\Omega)} \|\phi^t\|_{H^1(\Omega)} \|\varphi\|_{H^1(\Omega)}$. Moreover, $b_t(\cdot, \cdot)$

is coercive. Indeed, from the fact that $A(t) \rightarrow \mathbf{I}_2$ uniformly on $\bar{\Omega}$ as $t \rightarrow 0$, we know that there exist sufficiently small values for $t > 0$ such that $\|A(t) - \mathbf{I}_2\|_{L^\infty(\Omega)} < 1$. So, we have

$$\begin{aligned} b_t(\phi^t, \phi^t) &= \int_{\Omega} A(t) \nabla \phi^t \cdot \nabla \phi^t \, dx = \left| \int_{\Omega} (A(t) - \mathbf{I}_2) \nabla \phi^t \cdot \nabla \phi^t + |\nabla \phi^t|^2 \, dx \right| \\ &\geq \|\nabla \phi^t\|_{L^2(\Omega)}^2 - \|A(t) - \mathbf{I}_2\|_{L^\infty(\Omega)} \|\nabla \phi^t\|_{L^2(\Omega)}^2 \\ &\gtrsim |\nabla \phi^t|_{H^1(\Omega)}^2. \end{aligned}$$

Next, we consider the functional $\omega : H_{\Gamma,0}^1(\Omega) \rightarrow \mathbb{R}$ defined by $\langle \omega, \varphi \rangle = \int_{\Sigma} B(t) u_N^t \varphi \, d\sigma$. Evidently, this functional is continuous because of the boundedness of $|B(t)|_\infty$ and due to the sequence of inequalities

$$\left| \int_{\Sigma} B(t) u_N^t \varphi \, d\sigma \right| \lesssim |B(t)|_\infty \|u_N^t\|_{L^2(\Sigma)} \|\varphi\|_{L^2(\Sigma)} \lesssim |B(t)|_\infty \|u_N^t\|_{H^1(\Omega)} \|\varphi\|_{H^1(\Omega)}.$$

Thus, by Lax-Milgram theorem, the function p_N^t , vanishing on Γ , is the unique solution to the variational equation (2.53) in $H^1(\Omega)$. This proves the lemma. \blacksquare

Proposition 2.4.4. Let Ω be a bounded $C^{2,1}$ domain. The shape derivative of the adjoint state variable $p_N \in H^3(\Omega)$ at $\Omega = \Omega^*$ satisfying the mixed Dirichlet-Neumann problem (2.39) is a solution to the following mixed boundary value problem:

$$-\Delta p'_{NW} = 0 \text{ in } \Omega^*, \quad p'_{NW} = 0 \text{ on } \Gamma, \quad \partial_n p'_{NW} = u'_{NW} + \lambda \mathbf{W} \cdot \mathbf{n} \text{ on } \Sigma^*.$$

Proof. The proof mainly contains two parts; we first prove the existence of the material derivative of p_N , then we formally proceed on the derivation of its shape derivative.

Step 1. Existence of the material derivative of p_N . The variational formulation of (2.39) on the reference domain Ω is given as follows: find $p_N \in H_{\Gamma,0}^1(\Omega)$ such that

$$(2.56) \quad \int_{\Omega} \nabla p_N \cdot \nabla \varphi \, dx - \int_{\Sigma} u_N \varphi \, d\sigma = 0, \quad \forall \varphi \in H_{\Gamma,0}^1(\Omega).$$

Subtracting (2.53) with $t = 0$ from the case where $t > 0$, for all $\varphi \in H_{\Gamma,0}^1(\Omega)$, we obtain

$$\int_{\Omega} \{A(t) \nabla p_N^t - \nabla p_N^t + \nabla p_N^t - \nabla p_N\} \cdot \nabla \varphi \, dx - \int_{\Sigma} \{B(t) u_N^t - u_N^t + u_N^t - u_N\} \varphi \, d\sigma = 0.$$

Hence, we have a unique solution $p_N^t - p_N \in H_{\Gamma,0}^1(\Omega)$ to the variational equation

$$(2.57) \quad \int_{\Omega} \nabla (p_N^t - p_N) \cdot \nabla \varphi \, dx = - \int_{\Omega} (A(t) - \mathbf{I}_2) \nabla p_N^t \cdot \nabla \varphi \, dx + \int_{\Sigma} (B(t) - 1) u_N^t \varphi \, d\sigma + \int_{\Sigma} (u_N^t - u_N) \varphi \, d\sigma,$$

for all $\varphi \in H_{\Gamma,0}^1(\Omega)$. We note that ∇p_N^t is uniformly bounded in $L^2(\Omega; \mathbb{R}^2)$ and we have the convergence $\nabla p_N^t \rightarrow \nabla p_N$ also in that space. Indeed, using the boundedness of $\|A(t)\|_{L^\infty(\Omega)}$ from below, we get the

estimate

$$\|\nabla p_N^t\|_{L^2(\Omega)}^2 \lesssim \int_{\Omega} A(t) \nabla p_N^t \cdot \nabla p_N^t \, dx = \int_{\Sigma} B(t) u_N^t p_N^t \, d\sigma \lesssim |B(t)|_{\infty} \|u_N^t\|_{H^1(\Omega)} \|p_N^t\|_{L^2(\Omega)}.$$

Because u_N^t is uniformly bounded in $H^1(\Omega)$ (cf. [14, Theorem 23], see also [78, Proposition 3.1]), the uniform boundedness of ∇p_N^t in $L^2(\Omega; \mathbb{R}^2)$ immediately follows, and so the convergence $\nabla p_N^t \rightarrow \nabla p_N$ in $L^2(\Omega; \mathbb{R}^2)$. Next, we divide both sides of (2.57) by t and denote $\phi^t := \frac{1}{t}(p_N^t - p_N)$ to obtain

$$\int_{\Omega} \nabla \phi^t \cdot \nabla \varphi \, dx = - \int_{\Omega} \left(\frac{A(t) - I_2}{t} \right) \nabla p_N^t \cdot \nabla \varphi \, dx + \int_{\Sigma} \left(\frac{B(t) - 1}{t} \right) u_N^t \varphi \, d\sigma + \int_{\Sigma} \left(\frac{u_N^t - u_N}{t} \right) \varphi \, d\sigma,$$

for all $\varphi \in H_{\Gamma,0}^1(\Omega)$. We choose a sequence $\{t_n\}$ such that $t_n \rightarrow 0$ as $n \rightarrow \infty$. Our goal is to show that the limit $\lim_{n \rightarrow \infty} \phi^{t_n}$ exists. Using the boundedness of $\frac{1}{t_n}(A(t) - I_2)$ and $\frac{1}{t_n}(B(t) - 1)$ in L^∞ , we deduce that $\nabla p_N^{t_n}$ is bounded in $L^2(\Omega; \mathbb{R}^2)$, and thus the boundedness of ϕ^{t_n} in $H_{\Gamma,0}^1(\Omega)$. Hence, we can extract a subsequence, which we still denote by $\{t_n\}$, such that $\lim_{n \rightarrow \infty} t_n = 0$. Moreover, there exists an element ϕ of $H_{\Gamma,0}^1(\Omega)$ such that $\phi^{t_n} \rightharpoonup \phi$ weakly in $H_{\Gamma,0}^1(\Omega)$. From the convergences $\nabla p_N^{t_n} \rightarrow \nabla p_N$ in $L^2(\Omega; \mathbb{R}^2)$ and $u_N^{t_n} \rightarrow u_N$ in $L^2(\Sigma)$, together with Lemma 2.1.4(v)–(vi), we get

$$\int_{\Omega} \nabla \phi \cdot \nabla \varphi \, dx = - \int_{\Omega} A \nabla p_N \cdot \nabla \varphi \, dx + \int_{\Sigma} u_N \varphi \operatorname{div}_{\Sigma} \mathbf{W} \, d\sigma + \int_{\Sigma} \dot{u}_N \varphi \, d\sigma,$$

for all $\varphi \in H_{\Gamma,0}^1(\Omega)$, where $\dot{u}_N = \lim_{t \searrow 0} \frac{1}{t}(u_N^t - u_N)$ which is exactly the material derivative of u_N at $t = 0$ in the direction \mathbf{W} . This function exists and is actually an element of $H_{\Gamma,0}^1(\Omega)$ as shown, for example, in [13]. Hence, the above equation admits a unique solution in $H^1(\Omega)$ and we deduce that $\phi^{t_n} \rightarrow \phi$ for any sequence $\{t_n\}$. This implies the strong convergence of ϕ^{t_n} to ϕ in $L^2(\Sigma)$. Now, taking $\varphi = \phi^{t_n} \in H_{\Gamma,0}^1(\Omega)$, we obtain

$$\begin{aligned} \lim_{t_n \searrow 0} |\phi^{t_n}|_{H^1(\Omega)}^2 &= - \lim_{t_n \searrow 0} \left\{ \int_{\Omega} \left(\frac{A(t_n) - I_2}{t_n} \right) \nabla p_N^{t_n} \cdot \nabla \phi^{t_n} \, dx \right\} + \lim_{t_n \searrow 0} \left\{ \int_{\Sigma} \left(\frac{B(t_n) - 1}{t_n} \right) u_N^{t_n} \phi^{t_n} \, d\sigma \right\} \\ &\quad + \lim_{t_n \searrow 0} \left\{ \int_{\Sigma} \left(\frac{u_N^{t_n} - u_N}{t_n} \right) \phi^{t_n} \, d\sigma \right\} \\ &= - \int_{\Omega} A \nabla p_N \cdot \nabla \phi \, dx + \int_{\Sigma} u_N \phi \operatorname{div}_{\Sigma} \mathbf{W} \, d\sigma + \int_{\Sigma} \dot{u}_N \phi \, d\sigma = |\phi|_{H^1(\Omega)}. \end{aligned}$$

The norm convergence and the weak convergence of ϕ^{t_n} in $H_{\Gamma,0}^1(\Omega)$ implies the strong convergence of ϕ^{t_n} to $\phi \in H_{\Gamma,0}^1(\Omega)$. This guarantees the existence of the material derivative of p_N .

Step 2. Computing the shape derivative of p_N at $\Omega = \Omega^$ along the deformation field \mathbf{W} .* From the previous step, we showed the existence of the material derivative of p_N in $H_{\Gamma,0}^1(\Omega)$. Denoting this derivative by \dot{p}_N , we know that it satisfies the variational equation

$$(2.58) \quad \int_{\Omega} \nabla \dot{p}_N \cdot \nabla \varphi \, dx = - \int_{\Omega} A \nabla p_N \cdot \nabla \varphi \, dx + \int_{\Sigma} u_N \varphi \operatorname{div}_{\Sigma} \mathbf{W} \, d\sigma + \int_{\Sigma} \dot{u}_N \varphi \, d\sigma, \quad \forall \varphi \in H_{\Gamma,0}^1(\Omega).$$

In addition, it is clear that $\dot{p}_N = 0$ on Γ . Applying Green's formula to variational equation given above, we get

$$-\int_{\Omega} \varphi \Delta \dot{p}_N dx + \int_{\Sigma} \varphi \partial_n \dot{p}_N d\sigma = \int_{\Omega} \varphi \operatorname{div}(A \nabla p_N) dx - \int_{\Sigma} \varphi A \partial_n p_N d\sigma + \int_{\Sigma} u_N \varphi \operatorname{div}_{\Sigma} \mathbf{W} d\sigma + \int_{\Sigma} \dot{u}_N \varphi d\sigma, \quad \forall \varphi \in H_{\Gamma,0}^1(\Omega).$$

First, let us choose $\varphi \in H_0^1(\Omega)$. Then, we have $-\int_{\Omega} \varphi \Delta \dot{p}_N dx = \int_{\Omega} \varphi \operatorname{div}(A \nabla p_N) dx$. Since, $H_0^1(\Omega)$ is dense in $L^2(\Omega)$, we obtain $-\Delta \dot{p}_N = \operatorname{div}(A \nabla p_N)$ in Ω . Next, we choose $\varphi \in H_{\Gamma,0}^1(\Omega)$ such that φ is arbitrary in Σ . This gives us

$$\int_{\Sigma} \varphi \partial_n \dot{p}_N d\sigma = - \int_{\Sigma} \varphi A \partial_n p_N d\sigma + \int_{\Sigma} u_N \varphi \operatorname{div}_{\Sigma} \mathbf{W} d\sigma + \int_{\Sigma} \dot{u}_N \varphi d\sigma.$$

Because the traces of functions in $H_{\Gamma,0}^1(\Omega)$ are dense in $L^2(\Sigma)$, we arrive at $\partial_n \dot{p}_N = -A \partial_n p_N + u_N \operatorname{div}_{\Sigma} \mathbf{W} + \dot{u}_N$ on Σ . Summarizing these results, we see that \dot{p}_N satisfies the following boundary value problem:

$$-\Delta \dot{p}_N = \operatorname{div}(A \nabla p_N) \text{ in } \Omega, \quad \dot{p}_N = 0 \text{ on } \Gamma, \quad \partial_n \dot{p}_N = -A \partial_n p_N + u_N \operatorname{div}_{\Sigma} \mathbf{W} + \dot{u}_N \text{ on } \Sigma.$$

From above equations, and due to the fact that \mathbf{W} vanishes on Γ , we immediately obtain (using identity (2.4) in Remark 2.1.1) $p'_N = \dot{p}_N - \mathbf{W} \cdot \nabla p_N = 0$ on Γ . Now, we consider $\varphi \in H^2(\Omega)$. Note that for $C^{1,1}$ domain, we have that $u_N \in H^2(\Omega)$. Hence, $u_N \in H^{3/2}(\Sigma)$ which, in turn, means that $p_N \in H^2(\Omega)$ by standard elliptic regularity theory. Given this regularity of p_N and since $-\Delta p_N = 0$ in Ω , we can therefore write $-\int_{\Omega} A \nabla p_N \cdot \nabla \varphi dx$ as follows (see [78, Lemma 4.1])

$$(2.59) \quad - \int_{\Omega} A \nabla p_N \cdot \nabla \varphi dx = \int_{\Omega} \nabla(\mathbf{W} \cdot \nabla p_N) \cdot \nabla \varphi dx + \int_{\Sigma} \partial_n p_N (\mathbf{W} \cdot \nabla \varphi) d\sigma - \int_{\Sigma} (\nabla p_N \cdot \nabla \varphi) \mathbf{W} \cdot \mathbf{n} d\sigma,$$

for all $\varphi \in H^2(\Omega)$. Hence, using the identity (2.4), we have the equation

$$\int_{\Omega} \nabla \dot{p}_N \cdot \nabla \varphi dx = \int_{\Omega} \nabla p'_N \cdot \nabla \varphi dx + \int_{\Omega} \nabla(\mathbf{W} \cdot \nabla p_N) \cdot \nabla \varphi dx, \quad \forall \varphi \in H_{\Gamma,0}^1(\Omega).$$

Combining this equation with (2.58) and (2.59) yields

$$\begin{aligned} & \int_{\Omega} \nabla(\mathbf{W} \cdot \nabla p_N) \cdot \nabla \varphi dx + \int_{\Sigma} \partial_n p_N (\mathbf{W} \cdot \nabla \varphi) d\sigma - \int_{\Sigma} (\nabla p_N \cdot \nabla \varphi) \mathbf{W} \cdot \mathbf{n} d\sigma + \int_{\Sigma} u_N \varphi \operatorname{div}_{\Sigma} \mathbf{W} d\sigma + \int_{\Sigma} \dot{u}_N \varphi d\sigma \\ &= \int_{\Omega} \nabla p'_N \cdot \nabla \varphi dx + \int_{\Omega} \nabla(\mathbf{W} \cdot \nabla p_N) \cdot \nabla \varphi dx, \quad \forall \varphi \in H^2 \cap H_{\Gamma,0}^1(\Omega). \end{aligned}$$

Applying Green's formula on the right side of the above equation we arrive at

$$\begin{aligned} - \int_{\Omega} \varphi \Delta p'_N dx + \int_{\Sigma} \varphi \partial_n p'_N d\sigma &= \int_{\Sigma} \partial_n p_N (\mathbf{W} \cdot \nabla \varphi) d\sigma - \int_{\Sigma} (\nabla p_N \cdot \nabla \varphi) \mathbf{W} \cdot \mathbf{n} d\sigma \\ &+ \int_{\Sigma} u_N \varphi \operatorname{div}_{\Sigma} \mathbf{W} d\sigma + \int_{\Sigma} \dot{u}_N \varphi d\sigma, \quad \forall \varphi \in H^2 \cap H_{\Gamma,0}^1(\Omega). \end{aligned}$$

Now, we choose $\varphi \in C_0^\infty(\Omega)$. This leads us to $-\Delta p'_N = 0$ in Ω . Moreover, we get

$$\int_{\Sigma} \varphi \partial_n p'_N d\sigma = \int_{\Sigma} (u_N \mathbf{W} - \nabla p_N \mathbf{W} \cdot \mathbf{n}) \cdot \nabla \varphi d\sigma + \int_{\Sigma} u_N \varphi \operatorname{div}_{\Sigma} \mathbf{W} d\sigma + \int_{\Sigma} \dot{u}_N \varphi d\sigma.$$

Observe that $(u_N \mathbf{W} - \nabla p_N \mathbf{W} \cdot \mathbf{n}) \cdot \mathbf{n} = 0$. Hence, we can replace $\nabla \varphi|_\Sigma$ by the tangential gradient $\nabla_\Sigma \varphi$. Using the tangential Green's formula (see Lemma 2.1.5) thrice, noting that $\mathbf{W} \cdot \mathbf{n} \nabla_\Sigma p_N \cdot \mathbf{n} = 0$, and then using the relation $\dot{u}'_N = u'_N + \mathbf{W} \cdot \nabla u_N$, we obtain

$$\begin{aligned} \int_\Sigma \varphi \partial_n p'_N \, d\sigma &= \int_\Sigma \varphi \operatorname{div}_\Sigma (\nabla p_N \mathbf{W} \cdot \mathbf{n}) \, d\sigma + \int_\Sigma \dot{u}'_N \varphi \, d\sigma \\ &= \int_\Sigma \varphi \kappa (\nabla p_N \mathbf{W} \cdot \mathbf{n}) \cdot \mathbf{n} \, d\sigma - \int_\Sigma (\nabla_\Sigma \varphi \cdot \nabla p_N) \mathbf{W} \cdot \mathbf{n} \, d\sigma + \int_\Sigma \dot{u}'_N \varphi \, d\sigma \\ &= \int_\Sigma \varphi \kappa u_N \mathbf{W} \cdot \mathbf{n} \, d\sigma - \int_\Sigma (\nabla_\Sigma \varphi \cdot \nabla_\Sigma p_N) \mathbf{W} \cdot \mathbf{n} \, d\sigma + \int_\Sigma \dot{u}'_N \varphi \, d\sigma \\ &= \int_\Sigma \varphi \kappa u_N \mathbf{W} \cdot \mathbf{n} \, d\sigma + \int_\Sigma \varphi \operatorname{div}_\Sigma (\nabla_\Sigma p_N \mathbf{W} \cdot \mathbf{n}) \, d\sigma + \int_\Sigma (u'_N + \mathbf{W} \cdot \nabla u_N) \varphi \, d\sigma, \end{aligned}$$

for all $\varphi \in H^2(\Omega) \cap H^1_{\Gamma,0}(\Omega)$. Since the trace of functions from $H^2(\Omega)$ is dense in $L^2(\Sigma)$, we deduce the boundary condition on for p'_N given by $\partial_n p'_N = \operatorname{div}_\Sigma (\nabla_\Sigma p_N \mathbf{W} \cdot \mathbf{n}) + \kappa u_N \mathbf{W} \cdot \mathbf{n} + u'_N + \mathbf{W} \cdot \nabla u_N$. Summarizing these results, and letting $\Omega = \Omega^*$, we get

$$-\Delta p'_N = 0 \text{ in } \Omega^*, \quad p'_N = 0 \text{ on } \Gamma, \quad \partial_n p'_N = u'_N + \lambda \mathbf{W} \cdot \mathbf{n} \text{ on } \Sigma^*,$$

as desired. ■

It is worth remarking that the existence of the shape derivative p'_N of p_N can only be justified if u_N is H^3 -regular. Hence, we require that Ω be at least of class $C^{2,1}$ so that u_N (as well as u_R) is in $H^3(\Omega)$.

2.4.4 Symmetricity of the Shape Hessian of J_3 at a Critical Shape

In this subsection, we derive the shape Hessian $d^2 J_3(\Sigma^*)[\mathbf{V}, \mathbf{W}]$ of J_3 without imposing assumption (2.23) in expressing its shape gradient (see expression (2.46)). We will show that, in this case, the corresponding expression for the shape Hessian is symmetric with respect to \mathbf{V} and \mathbf{W} . For this very purpose, the calculation is accomplished in a slightly different fashion to the proof of Proposition 2.4.3. We again denote $w = u_N - u_R$, and suppose $\mathbf{N}_s = \mathbf{N}_s(\mathbf{W})$ to be a smooth extension of \mathbf{n}_s . Then, $J_3(\Sigma) = \frac{1}{2} \int_\Sigma |w|^2 \, d\sigma$, and from (2.6), we have

$$dJ_3(\Sigma)[\mathbf{V}] = \int_\Sigma \{w w'_V + g_3 \mathbf{V} \cdot \mathbf{n}\} \, d\sigma,$$

where $g = w \nabla w \cdot \mathbf{n} + \frac{1}{2} \kappa w^2$. Applying (2.6) once more, we get

$$\begin{aligned} d^2 J_3(\Sigma)[\mathbf{V}, \mathbf{W}] &= \int_\Sigma \{w'_W w'_V + w w''_{VW} + [\partial_n w w'_V + w \partial_n w'_V + \kappa w w'_V] \mathbf{W} \cdot \mathbf{n}\} \, d\sigma \\ (2.60) \quad &+ \int_\Sigma \{g'_3 \mathbf{V} \cdot \mathbf{N} + g_3 \mathbf{V} \cdot \mathbf{N}'_W + [\partial_n g_3 \mathbf{V} \cdot \mathbf{N} + g_3 \partial_n (\mathbf{V} \cdot \mathbf{N}) + \kappa g_3 \mathbf{V} \cdot \mathbf{N}] \mathbf{W} \cdot \mathbf{n}\} \, d\sigma, \end{aligned}$$

where w''_{VW} denotes the shape derivative of w along the directions of \mathbf{V} and \mathbf{W} (applied consecutively) and $g'_3 \mathbf{V} \cdot \mathbf{N} = w'_W \nabla w \cdot \mathbf{N} + w \nabla w'_W \cdot \mathbf{N} + w \nabla w \cdot \mathbf{N}'_W + \frac{1}{2} \kappa'_W w^2 + \kappa w w'_W$. Now, according to Corollary 2.4.1,

we have $w \equiv 0$ and $g_3 \equiv 0$ at $\Sigma = \Sigma^*$ which also gives us $g_3'_{\mathbf{W}} \equiv 0$ on Σ^* . Therefore, $d^2 J_3(\Sigma^*)[\mathbf{V}, \mathbf{W}] = \int_{\Sigma^*} w'_V w'_W d\sigma$. Meanwhile, for $\beta = \kappa$, we know that $u'_R \equiv 0$ on $\overline{\Omega}^*$ by Lemma 2.3.2. Thus, we obtain

$$(2.61) \quad d^2 J_3(\Sigma^*)[\mathbf{V}, \mathbf{W}] = \int_{\Sigma^*} u'_{NV} u'_{NW} d\sigma,$$

which clearly shows the symmetry (with respect to the deformation fields \mathbf{V} and \mathbf{W}) of the shape Hessian at a critical shape Ω^* .

Let us now write (2.61) in its equivalent form using the adjoint method. For this purpose, we will denote the corresponding adjoint of u'_{NV} and u'_{NW} by Φ_W and Φ_V , respectively. (The choice of subscripts for these adjoints will be made clear shortly.)

Clearly, both Φ_W and Φ_V are harmonic functions and both vanishes on Γ . Meanwhile, on Σ^* , we take $\partial_{\mathbf{n}} \Phi_W = u'_{NW}$ and $\partial_{\mathbf{n}} \Phi_V = u'_{NV}$, so that (via Green's second identity) we obtain the following equalities

$$\begin{aligned} \int_{\Sigma^*} u'_{NV} u'_{NW} d\sigma &= \int_{\Sigma^*} u'_{NV} \partial_{\mathbf{n}} \Phi_W d\sigma = \int_{\Sigma^*} \Phi_W \partial_{\mathbf{n}} u'_{NV} d\sigma = \int_{\Sigma^*} \Phi_W (\lambda \kappa \mathbf{V} \cdot \mathbf{n}) d\sigma \\ &= \int_{\Sigma^*} u'_{NW} \partial_{\mathbf{n}} \Phi_V d\sigma = \int_{\Sigma^*} \Phi_V \partial_{\mathbf{n}} u'_{NW} d\sigma = \int_{\Sigma^*} \Phi_V (\lambda \kappa \mathbf{W} \cdot \mathbf{n}) d\sigma. \end{aligned}$$

Consequently, the adjoint states Φ_W and Φ_V satisfy the PDE systems

$$(2.62) \quad -\Delta \Phi_W = 0 \text{ in } \Omega^*, \quad \Phi_W = 0 \text{ on } \Gamma, \quad \partial_{\mathbf{n}} \Phi_W = u'_{NW} \text{ on } \Sigma^*;$$

$$(2.63) \quad -\Delta \Phi_V = 0 \text{ in } \Omega^*, \quad \Phi_V = 0 \text{ on } \Gamma, \quad \partial_{\mathbf{n}} \Phi_V = u'_{NV} \text{ on } \Sigma^*,$$

respectively. Hence, we conclude that (2.61) can also be expressed as

$$(2.64) \quad d^2 J_3(\Sigma^*)[\mathbf{V}, \mathbf{W}] = \int_{\Sigma^*} \lambda \kappa \Phi_W \mathbf{V} \cdot \mathbf{n} d\sigma = \int_{\Sigma^*} \lambda \kappa \Phi_V \mathbf{W} \cdot \mathbf{n} d\sigma,$$

where Φ_W and Φ_V satisfy (2.62) and (2.63), respectively. Evidently, this shows that, at the optimal shape solution Ω^* of J_3 , only the normal components of \mathbf{V} and \mathbf{W} contributes to the shape Hessian.

At this juncture, it is also worth to emphasize that the shape Hessian issued in Proposition 2.4.3 is also impractical to use in numerical calculation. Again, this is primarily due to the fact that an appropriate choice for the deformation field \mathbf{W} is difficult to determine directly from the given expression for the shape Hessian. To address this problem, we again apply the adjoint method. In this respect, we let Ψ be harmonic on Ω such that it vanishes on Γ . Letting $\partial_{\mathbf{n}} \Psi = \lambda \kappa \mathbf{V} \cdot \mathbf{n}$ on Σ , we get (via Green's second identity and equation (2.51)) the following equalities $\int_{\Sigma} \lambda \kappa p'_{NW} \mathbf{n} \cdot \mathbf{V} d\sigma = \int_{\Sigma} (\Psi u'_{NW} + \lambda \Psi) \mathbf{n} \cdot \mathbf{W} d\sigma$. Next, we let another function Π to be harmonic on Ω such that $\Pi = 0$ on Γ . Also, we let $\partial_{\mathbf{n}} \Pi = \Psi$, so that (via Green's second identity) we have $\int_{\Sigma} \Psi u'_{NW} d\sigma = \int_{\Sigma} \lambda \kappa \Pi \mathbf{n} \cdot \mathbf{W} d\sigma$. To summarize, we make the following remark.

Remark 2.4.2. Using the adjoint method, the shape Hessian $d^2 J_3^\Gamma(\Sigma^*)[\mathbf{V}, \mathbf{W}]$ can also be expressed as

$$(2.65) \quad d^2 J_3^\Gamma(\Sigma^*)[\mathbf{V}, \mathbf{W}] = \int_{\Sigma^*} \lambda \kappa p'_{\text{NV}} \mathbf{n} \cdot \mathbf{V} \, d\sigma = \int_{\Sigma^*} \lambda (\Psi + \lambda \kappa \Pi) \mathbf{n} \cdot \mathbf{W} \, d\sigma,$$

where Ψ and Π satisfy the following PDE systems

$$(2.66) \quad -\Delta \Psi = 0 \text{ in } \Omega^*, \quad \Psi = 0 \text{ on } \Gamma, \quad \partial_{\mathbf{n}} \Psi = \lambda \kappa \mathbf{V} \cdot \mathbf{n} \text{ on } \Sigma^*;$$

$$(2.67) \quad -\Delta \Pi = 0 \text{ in } \Omega^*, \quad \Pi = 0 \text{ on } \Gamma, \quad \partial_{\mathbf{n}} \Pi = \Psi \text{ on } \Sigma^*,$$

respectively. Here, we notice that $\Psi \equiv u'_{\text{NV}}$ on $\overline{\Omega^*}$. Hence, looking back to equation (2.63), we also find that $\Phi_{\mathbf{V}}$ is exactly equal to Π satisfying (2.67). This means that we may actually write the shape Hessian given in (2.64) as

$$(2.68) \quad d^2 J_3(\Sigma^*)[\mathbf{V}, \mathbf{W}] = \int_{\Sigma^*} \lambda \kappa \Pi \mathbf{n} \cdot \mathbf{W} \, d\sigma.$$

Remark 2.4.3. Similar to 2.3.2, we notice from (2.60) the dependence of the shape Hessian $d^2 J_3(\Sigma)[\mathbf{V}, \mathbf{W}]$ (for Ω different from the optimal domain Ω^*) to the shape derivative κ'_W of the mean curvature κ along $\mathbf{W} \in \Theta^2$ appearing on g'_{3W} . From this observation, we deduce that the shape Hessian currently in consideration also defines a continuous bilinear form

$$d^2 J_3(\Sigma) : \mathbf{H}^1(\Sigma) \times \mathbf{H}^1(\Sigma) \rightarrow \mathbb{R};$$

that is, $|d^2 J_3(\Sigma)[\mathbf{V}, \mathbf{W}]| \lesssim \|\mathbf{V}\|_{\mathbf{H}^1(\Sigma)} \|\mathbf{W}\|_{\mathbf{H}^1(\Sigma)}$.

In view of the previous remark, it is natural to ask whether it is true that

$$d^2 J_3(\Sigma^*)[\mathbf{V}, \mathbf{V}] \gtrsim \|\mathbf{V}\|_{\mathbf{H}^1(\Sigma^*)}^2.$$

This question actually refers to the *stability* of a local minimizer Ω^* of J_3 . In relation to this, we recall from [35, 36] (a result regarding *sufficient* second-order conditions) that a local minimizer Ω^* is stable *if and only if* the shape Hessian $d^2 J_3(\Sigma^*)$ is strictly coercive in its corresponding energy space $\mathbf{H}^1(\Sigma^*)$. Unfortunately, this kind of strict coercivity cannot be established for the shape Hessian $d^2 J_3(\Sigma^*)$ of J_3 (as well as in the case of J_2). Nevertheless, we will show in the next subsection that sufficient condition can be derived to obtain strict coercivity in a weaker space of $\mathbf{H}^1(\Sigma^*)$. We note that the derived coercivity criterion is exactly the same as in the case of the shape Hessian $d^2 J_i$ of the cost functional J_i , for $i = \text{D}, \text{N}, \text{KV}, 2$, as shown in [49–51, 98], respectively. It is worth remarking that, among these cost functions, only the shape Hessian $d^2 J_{\text{N}}(\Sigma^*)$ of J_{N} is $\mathbf{H}^1(\Sigma^*)$ -coercive under the derived coercivity criterion (see [49, Proposition 2.12]). In connection with this, we will also establish a coercivity estimate for the shape Hessian $d^2 J_2(\Sigma^*)$ of J_2 in the next subsection.

Before we continue to the last section of this chapter, and for the sake of comparison, let us also compute the shape Hessian of the cost functional $J_D(\Sigma)$ at $\Sigma = \Sigma^*$. From Remark 2.4.1, we know that the gradient of $J_D(\Sigma)$ only differs by the addition of the integral $\int_{\Sigma} (u_N \nabla u_N \cdot \mathbf{n}) \mathbf{n} \cdot \mathbf{V} \, d\sigma =: \int_{\Sigma} \tilde{v} \mathbf{n} \cdot \mathbf{V} \, d\sigma$ from the shape gradient of $J_3(\Sigma)$. Computing the shape derivative of \tilde{v} at $\Omega = \Omega^*$ along the deformation field $\mathbf{W} \in \Theta^2$, we get $\tilde{v}'_{1W}|_{\Sigma^*} = u'_{NW}(\nabla u_N \cdot \mathbf{N}) + u_N(\nabla u'_{NW} \cdot \mathbf{N} + \nabla u_N \cdot \mathbf{N}'_W)|_{\Sigma^*} = \lambda u'_{NW}$. Meanwhile, we have $\nabla(u_N \nabla u_N \cdot \mathbf{n}) \cdot \mathbf{n} = (\nabla u_N \cdot \mathbf{n})^2 + u_N [(\nabla^2 u_N) \mathbf{n}] \cdot \mathbf{n} = \lambda^2$ on Σ^* . Hence, from (2.52) with $g_3^{\top'}$ replaced by \tilde{v} , together with equation (2.50) in Proposition 2.4.3, we get the final expression for the shape Hessian of J_D at $\Omega = \Omega^*$ (cf. [50, Eq. (21)]):

Proposition 2.4.5. Let Ω be of class $C^{2,1}$ and $\mathbf{V}, \mathbf{W} \in \Theta^2$. Then, the shape Hessian of J_D at Ω^* is given by

$$(2.69) \quad d^2 J_D(\Sigma^*)[\mathbf{V}, \mathbf{W}] = \int_{\Sigma^*} \{ \lambda(\kappa p'_{NW} + u'_{NW}) \mathbf{n} \cdot \mathbf{V} + \lambda^2 (\mathbf{n} \cdot \mathbf{V}) \mathbf{n} \cdot \mathbf{W} \} \, d\sigma.$$

Here, we mention that the above expression was also computed in [50] but through shape calculus for star shape domains, hence, we refer the readers to the aforementioned reference for comparison.

Meanwhile, following Remark 2.4.2, we can also write $d^2 J_D(\Sigma^*)[\mathbf{V}, \mathbf{W}]$ in terms of appropriate adjoint states. To do this, we let Υ be harmonic in Ω and be zero on Γ . Moreover, we let $\partial_{\mathbf{n}} \Upsilon = \lambda \mathbf{V} \cdot \mathbf{n}$ on Σ , so that by Green's second identity we have $\int_{\Sigma} u'_{NW} (\lambda \mathbf{n} \cdot \mathbf{V}) \, d\sigma = \int_{\Sigma} \lambda \kappa \Upsilon \mathbf{n} \cdot \mathbf{W} \, d\sigma$. Hence, using the results from Remark 2.4.2, we therefore have the following corollary of Proposition 2.4.5 regarding an equivalent expression for (2.69) in terms of the adjoint variable Υ .

Corollary 2.4.3. Let Ω be of class $C^{2,1}$ and $\mathbf{V}, \mathbf{W} \in \Theta^2$. Then, the shape Hessian of J_D at Ω^* given by (2.69) can be written as

$$(2.70) \quad d^2 J_D(\Sigma^*)[\mathbf{V}, \mathbf{W}] = \int_{\Sigma^*} \{ \lambda^2 \kappa \Pi + \lambda \kappa \Upsilon + \lambda \Psi + \lambda^2 (\mathbf{n} \cdot \mathbf{V}) \} \mathbf{n} \cdot \mathbf{W} \, d\sigma,$$

where the adjoint states Ψ and Π satisfy the BVPs (2.66) and (2.67), respectively, while Υ is the unique solution to the PDE system

$$(2.71) \quad -\Delta \Upsilon = 0 \text{ in } \Omega^*, \quad \Upsilon = 0 \text{ on } \Gamma, \quad \partial_{\mathbf{n}} \Upsilon = \lambda \mathbf{V} \cdot \mathbf{n} \text{ on } \Sigma^*.$$

Here, it is worth to stress out that the shape Hessian $d^2 J_D(\Sigma^*)[\mathbf{V}, \mathbf{W}]$ depends on the solutions of three BVPs as opposed to the case of $d^2 J_3^{\top}(\Sigma^*)[\mathbf{V}, \mathbf{W}]$ which depends only on the solutions of two PDE systems. In terms of numerical implementation, this obviously means that we need to solve an additional variational problem in order to evaluate the descent direction for a gradient-based

descent algorithm (which may then require additional computing times) when using the classical formulation (1.6).

2.5 Coercivity Estimates for the Shape Hessians at the Optimal Solution

We close out this chapter with the discussion about the coercivity estimate for the shape Hessian of the cost functions J_2 and J_3 . More precisely, we determine which weaker space of $\mathbf{H}^1(\Sigma^*)$ does the shape Hessians $d^2 J_2(\Sigma^*)$ and $d^2 J_3(\Sigma^*)$ are strictly coercive. To this end, we use the method already used in [47] (see also [49–51, 98]). We start by introducing the following operators which are linear continuous as a multiplier by a smooth function (see [98, Section 3.4]):

$$\begin{aligned}\Lambda : \mathbf{H}^{1/2}(\Sigma^*) &\rightarrow H^{1/2}(\Sigma^*), & \Lambda \mathbf{V} &:= \lambda V_n; \\ \mathcal{M} : H^{1/2}(\Sigma^*) &\rightarrow H^{1/2}(\Sigma^*), & \mathcal{M} v &:= \kappa v.\end{aligned}$$

Here, of course, $V_n := \mathbf{V} \cdot \mathbf{n}$ and κ is the mean curvature of Σ^* . The continuity of these operators follows from the following result.

Lemma 2.5.1. Let $\Omega \subset \mathbb{R}^2$ be a bounded Lipschitz domain with boundary $\Gamma := \partial\Omega$. Then, the map $v \mapsto \varphi v$ is continuous in $H^{1/2}(\Gamma)$ for any $v \in H^{1/2}(\Gamma)$ and $\varphi \in C^{0,1}(\Gamma)$.

Proof. We recall that the fractional Sobolev space $H^{1/2}(\Gamma)$ (the trace space for $H^1(\Omega)$) is equipped with the norm

$$\|v\|_{1/2,2} = \|v\|_{L^2(\Gamma)} + |v|_{1/2,2,\Gamma}, \quad |v|_{1/2,2,\Gamma} = \left(\int_{\Gamma} \int_{\Gamma} \frac{|v(x) - v(y)|^2}{|x - y|^2} d\sigma_x d\sigma_y \right)^{1/2}.$$

Let φ be a Lipschitz function. Then, we have the inequality

$$|\varphi(x)v(x) - \varphi(y)v(y)| \lesssim \|\varphi\|_{\infty} |v(x) - v(y)| + |v(y)| |x - y|.$$

Hence, $|\varphi v|_{1/2,2,\Gamma}$ can be estimated as follows

$$\begin{aligned}|\varphi v|_{1/2,2,\Gamma} &= \left(\int_{\Gamma} \int_{\Gamma} \frac{|\varphi(x)v(x) - \varphi(y)v(y)|^2}{|x - y|^2} d\sigma_x d\sigma_y \right)^{1/2} \\ &\lesssim \|\varphi\|_{\infty} |v|_{1/2,2,\Gamma} + \left(\int_{\Gamma} \int_{\Gamma} |v(y)|^2 dx dy \right)^{1/2} \\ &\lesssim \|\varphi\|_{\infty} |v|_{1/2,2,\Gamma} + |\Gamma|^{1/2} \|v\|_{L^2(\Gamma)}.\end{aligned}$$

Because $\|\varphi v\|_{L^2(\Gamma)} \leq \|\varphi\|_{\infty} \|v\|_{L^2(\Gamma)}$, then the assertion is proved. ■

In addition to the operators introduced above, let us also define the map \mathcal{S} as the *Steklov-Poincaré* operator on Σ^* which is defined by (see, e.g., [109])

$$(2.72) \quad \mathcal{S} : H^{1/2}(\Sigma^*) \rightarrow H^{-1/2}(\Sigma^*), \quad \mathcal{S}(\Phi) := \left. \frac{\partial \Psi}{\partial \mathbf{n}} \right|_{\Sigma^*},$$

where $\Psi \in H^1(\Omega^*)$ satisfies

$$-\Delta \Psi = 0 \quad \text{in } \Omega^*, \quad \Psi = 0 \quad \text{on } \Gamma, \quad \Psi = \Phi \quad \text{on } \Sigma^*.$$

The operator \mathcal{S} , also called the *Dirichlet-to-Neumann* map, is $H^{1/2}(\Sigma^*)$ -coercive (cf. [51, Lemma 2]). Its inverse \mathcal{R} called the *Neumann-to-Dirichlet* map is defined by

$$\mathcal{R} : H^{-1/2}(\Sigma^*) \rightarrow H^{1/2}(\Sigma^*), \quad \mathcal{R}\left(\left. \frac{\partial \Psi}{\partial \mathbf{n}} \right|_{\Sigma^*}\right) := \Phi|_{\Sigma^*},$$

where $\Phi \in H^1(\Omega^*)$ satisfies

$$-\Delta \Phi = 0 \quad \text{in } \Omega^*, \quad \Phi = 0 \quad \text{on } \Gamma, \quad \partial_{\mathbf{n}} \Phi = \partial_{\mathbf{n}} \Psi \quad \text{on } \Sigma^*.$$

Now, using the operators Λ , \mathcal{M} , \mathcal{R} , and denoting the $L^2(\Sigma^*)$ -inner product by $(\cdot, \cdot)_{L^2(\Sigma^*)}$, we can write (2.50) as

$$d^2 J_3^\top(\Omega^*)[\mathbf{V}, \mathbf{W}] = (\mathcal{M}\Lambda\mathbf{V}, \mathcal{R}(\Lambda\mathbf{W} + \mathcal{R}(\mathcal{M}\Lambda\mathbf{W})))_{L^2(\Sigma^*)}.$$

By the continuity of the maps Λ and \mathcal{M} , and the bijectivity of \mathcal{R} , we deduce that the shape Hessian $d^2 J_3^\top$ at Ω^* is $L^2(\Sigma^*)$ -coercive (whenever κ is non-negative) and we state this result formally as follows.

Proposition 2.5.1. For Σ^* with non-negative mean curvature κ , the shape Hessian $d^2 J_3^\top$ at Ω^* is $L^2(\Sigma^*)$ -coercive; i.e.,

$$d^2 J_3^\top(\Sigma^*)[\mathbf{V}, \mathbf{V}] \gtrsim \|\mathbf{V}\|_{L^2(\Sigma^*)}^2.$$

The above result also means that the minimization problem (1.18) (with condition (2.23) imposed in computing the gradient) is (algebraically) *ill-posed*. We further discuss this notion of ill-posedness (in the case of the present shape optimization formulation (1.18)) briefly as follows. As alluded in the previous subsection, the shape optimization problem is *well-posed* if its local minimum is stable; that is, if the shape Hessian $d^2 J_3^\top(\Sigma^*)$ is strictly coercive in its energy space $\mathbf{H}^1(\Sigma^*)$, or equivalently, if $d^2 J_3^\top(\Sigma^*)[\mathbf{V}, \mathbf{V}] \gtrsim \|\mathbf{V}\|_{\mathbf{H}^1(\Sigma^*)}^2$. However, if the positivity of the shape Hessian at Σ^* only holds on a weaker (Sobolev) space, then the shape optimization problem is said to be (algebraically) ill-posed (cf. [50, 53]). This means, in particular, that tracking the Dirichlet data in the L^2 -norm is not sufficient, and as strongly assumed by the authors in [52], they have to be tracked relative to H^1 . This aforementioned *lack of coercivity* is known from other PDE-constrained optimal control problems as the so-called *two-norm discrepancy* (see, e.g., [53] and the references therein) and this concept of

norm discrepancy under shape optimization framework was first observed in [35, 36, 45, 46], among others.

In the case of the cost functional $J_2(\Omega) = \frac{1}{2}|u_N - u_R|_{H^1(\Omega)}^2$ examined in subsection 2.3.2 (See [98]), the shape Hessian is likewise a continuous bilinear form; that is, as also pointed out in Remark 2.3.2, $d^2 J_2(\Omega) : \mathbf{H}^1(\Sigma) \times \mathbf{H}^1(\Sigma) \rightarrow \mathbb{R}$. Using the operators introduced above, the shape Hessian $d^2 J_2$ at Ω^* is therefore expressible as

$$d^2 J_2(\Omega^*)[\mathbf{V}, \mathbf{W}] = (\mathcal{M}\Lambda\mathbf{V}, \mathcal{R}(\mathcal{M} + \mathcal{S})\Lambda\mathbf{W})_{L^2(\Sigma^*)},$$

which is $\mathbf{H}^{1/2}(\Sigma^*)$ -coercive provided that Σ^* has non-negative mean curvature κ . More formally, we have the following proposition.

Proposition 2.5.2. For Σ^* with non-negative mean curvature κ , the shape Hessian $d^2 J_2$ at Ω^* is $\mathbf{H}^{1/2}(\Sigma^*)$ -coercive; i.e.,

$$d^2 J_2(\Sigma^*)[\mathbf{V}, \mathbf{V}] \gtrsim \|\mathbf{V}\|_{\mathbf{H}^{1/2}(\Sigma^*)}^2.$$

We finish this chapter with the following remark.

Remark 2.5.1. Similarly, we have that $d^2 J_D(\Omega) : \mathbf{H}^1(\Sigma) \times \mathbf{H}^1(\Sigma) \rightarrow \mathbb{R}$ and using the operators introduced above, we may write the shape Hessian of J_D at $\Omega = \Omega^*$ given in Proposition 2.4.5 as follows:

$$d^2 J_D(\Omega^*)[\mathbf{V}, \mathbf{W}] = (\mathcal{R}(\mathcal{M} + \mathcal{S})\Lambda\mathbf{V}, \mathcal{R}(\mathcal{M} + \mathcal{S})\Lambda\mathbf{W})_{L^2(\Sigma^*)},$$

This expression is also $\mathbf{H}^{1/2}(\Sigma^*)$ -coercive; that is,

$$d^2 J_D(\Sigma^*)[\mathbf{V}, \mathbf{V}] \gtrsim \|\mathbf{V}\|_{\mathbf{H}^{1/2}(\Sigma^*)}^2,$$

provided that Σ^* has non-negative mean curvature κ .

On the other hand, in case of the shape Hessian $d^2 J_3(\Sigma^*)[\mathbf{V}, \mathbf{W}]$, we deduce (via the continuity of the maps Λ and \mathcal{M} , and the bijectivity of \mathcal{R}) that

$$d^2 J_3(\Sigma^*)[\mathbf{V}, \mathbf{V}] = \|\mathcal{R}(\mathcal{M}\Lambda\mathbf{V})\|_{L^2(\Sigma^*)}^2 \sim \|\mathcal{M}\Lambda\mathbf{V}\|_{H^{-1}(\Sigma^*)}^2,$$

whenever κ is non-negative.

NUMERICAL ANALYSES

Contents

	Page
3.1 Numerical Algorithm	80
3.1.1 The Sobolev Gradient Method	80
3.1.2 Step Size for the First-Order Method	81
3.1.3 The Boundary Variation Algorithm	83
3.1.4 Stopping Criteria	83
3.1.5 The Sobolev Newton Method	85
3.1.6 Step Size for the Second-Order Method	86
3.2 Numerical Examples	88
3.2.1 Examples for the First Proposed Shape Problem	90
3.2.2 Examples for the Second Proposed Shape Problem	108
3.2.3 Examples for the Third Proposed Shape Problem	120

In this chapter we demonstrate how the computed shape gradients and shape Hessians of the cost functions can be utilized in a gradient-based descent algorithm to solve some concrete examples of the Bernoulli problems. Therefore, this chapter is divided into two major sections. The first half contains the details of the numerical scheme we will use to carry out our numerical explorations. The second half, on the other hand, contains the set of numerical examples that illustrates the feasibility of the proposed numerical schemes. In these numerical experiments, the results obtain from the proposed methods are compared with those generated using the classical shape optimization reformulations.

3.1 Numerical Algorithm

As far as we know, there are at least three different computational strategies for the numerical resolution of the Bernoulli problem. The first one is the classical *fixed-point* approach wherein a sequence of elliptic problems are solved in a sequence of converging domains with one of the conditions on the free boundary omitted, and then the remaining boundary condition is used to update the free boundary (see [18, 57]). This approach does not require any gradient information in contrast to the second approach which considers an equivalent shape optimization formulation of the problem, see, for example, the numerical approaches used in [1, 67, 70, 78, 100, 101]. Another strategy, built from the theory of complex analysis, is the use of *conformal mapping* method. This solution method was recently developed by Haddar and Kress in [64] which relates the Bernoulli problem in the context of inverse problems. In a more recent study, another method was also introduced by Kress in [83] in an attempt to improve the use of boundary integral equations for numerically solving the Bernoulli problem. In terms of numerical performance, it was revealed in [83] that this recently proposed method inspired by Trefftz' integral equation method [111] is more robust and wider applicable than that of [64]. We mention that Trefftz' approach, in principle, can be considered as a so-called *trial method* which is also a prominent numerical method for solving free boundary value problems such as the Bernoulli problem (see [65, 66, 84, 109]).

In this thesis, we will use a classical gradient scheme for the numerical realization of the shape optimization methods discussed in Section 1.3 by means of a Lagrangian-like method. It consists in adopting an iterative procedure that decreases the value of the cost functional J at each iteration. One could also use an Eulerian-like approach such as the level-set method that was applied, for instance, in [1, 79]. Alternatively, one could also apply a variant of Newton's method to numerically solve the minimization problems. This method, however, also requires the knowledge of the shape Hessian of J which is considerably more difficult to obtain and utilize (see, e.g., [93, 105], and the references cited therein). In the subsequent parts of this section, we will describe the details of the numerical algorithms that we will use to solve some concrete examples of the Bernoulli problem.

3.1.1 The Sobolev Gradient Method

Let us consider a shape functional $J(\Omega)$ whose shape gradient is given by $dJ(\Omega)[V] = \int_{\Sigma} g \mathbf{n} \cdot \mathbf{V} d\sigma$. Also, suppose that Ω_k is the shape of the domain at the k th iteration. Then, at the $(k+1)$ th iteration, the shape $\Omega = \Omega_k$ can be updated as $\Omega_{k+1} := \Omega_{t_{k+1}} = (\mathbf{I}_2 + t_k \mathbf{V})\Omega$, where $t_k \geq 0$ is some small step size parameter and \mathbf{V} represents the descent deformation field \mathbf{V}_k at the k th iterate. In perturbing the domain Ω , we may take $\mathbf{V}|_{\Sigma} = -g\mathbf{n}$ as the descent direction. Indeed, in this case, we have $dJ(\Omega)[V] = -\int_{\Sigma} |g|^2 d\sigma < 0$. However, this choice of the descent direction may cause undesirable oscillations on the free boundary of the shape solution Ω^* . To avoid such phenomena, we compute the descent direction \mathbf{V} using the so-called H^1 *gradient method* [8]; that is, we take \mathbf{V} as the unique

solution in $\mathbf{H}_{\Gamma,0}^1(\Omega)$ of the variational problem

$$(3.1) \quad \int_{\Omega} (\nabla \mathbf{V} : \nabla \boldsymbol{\varphi} + \mathbf{V} \cdot \boldsymbol{\varphi}) \, dx = - \int_{\Sigma} g \mathbf{n} \cdot \boldsymbol{\varphi} \, d\sigma, \quad \forall \boldsymbol{\varphi} \in \mathbf{H}_{\Gamma,0}^1(\Omega).$$

In this sense, the deformation field \mathbf{V} , also termed in some literature as a *Sobolev gradient* (see, e.g., [89]), provides a smooth extension of $g \mathbf{n}$ over the entire domain Ω , which not only smoothes the free boundary after a deformation [10], but also provides a preconditioning of the descent direction. The method of regularizing the descent direction using (3.1) is similar to the idea behind the so-called *traction method* introduced and popularized in [6, 10–12].

In the previous chapter, we saw that the computed shape gradients corresponding to each cost functions J_i , $i \in \{1, 2, 3\}$ (as well as to each cost functions J_i , $i \in \{D, N, KV\}$), depends not only on the state and adjoint state variables, but also on the value of the mean curvature κ of the free boundary Σ . Consequently, this means that we first need to calculate $\kappa := \kappa(\Sigma)$ in order to determine the vector field \mathbf{V} . In this investigation, we will evaluate κ by first creating a smooth extension of \mathbf{n} using the idea of the H^1 gradient method, and then calculate κ as the divergence of that smooth extension. This technique is certainly numerically doable, and in fact theoretically justifiable. From Proposition 5.4.8 of [73, p. 218] (see also [60, Lemma 16.1, p. 390]), we know that, for a domain Ω of class C^2 , there exists a unitary C^1 extension $\tilde{\mathbf{n}}$ of \mathbf{n} such that the mean curvature may be defined as

$$\kappa = \operatorname{div}_{\Sigma} \mathbf{n} = \operatorname{div} \tilde{\mathbf{n}}.$$

Therefore, based on this idea, we may numerically compute κ through the equation $\kappa = \operatorname{div} \mathbf{N}$, where \mathbf{N} is the smoothed extension of \mathbf{n} satisfying the equation

$$(3.2) \quad \int_{\Omega} \nabla \mathbf{N} : \nabla \boldsymbol{\varphi} \, dx + \int_{\Sigma} \mathbf{N} \cdot \boldsymbol{\varphi} \, d\sigma = \int_{\Sigma} \mathbf{n} \cdot \boldsymbol{\varphi} \, d\sigma, \quad \forall \boldsymbol{\varphi} \in \mathbf{H}^1(\Omega).$$

We can also use the same idea to compute for higher-order derivatives of (scalar) functions if the function is defined (or only supported) on the boundary. For example, the shape gradient of J_1 consists of the second-order normal derivative of the state variable u ; that is, the derivative $\partial^2 u / \partial \mathbf{n}^2$ appears in the kernel of $dJ_1(\Sigma)$. In the classical Neumann-data-tracking cost functional minimization approach (1.8), the derivative $\partial^2 u / \partial \mathbf{n}^2$ can actually be simplified as $-\partial^2 u / \partial \mathbf{n}^2 = \kappa \partial u / \partial \mathbf{n}$ because $\Delta u = \Delta_{\Sigma} u + \kappa \partial u / \partial \mathbf{n} + \partial^2 u / \partial \mathbf{n}^2$ and $u|_{\Sigma} = 0$. However, in our numerical procedure, we will calculate $\partial^2 u / \partial \mathbf{n}^2$ using a similar idea in computing κ . More precisely, we will evaluate $\partial^2 u / \partial \mathbf{n}^2$ by computing the normal derivative of a smooth extension of $\partial u / \partial \mathbf{n}$. We mention here that, to the best of our knowledge, such method for numerically computing a second-order normal derivative is also novel to our work.

3.1.2 Step Size for the First-Order Method

Let us now turn our attention to the computation of the step size to be used in our algorithm. It is worth mentioning that the choice for t_k can be decided in many ways. Here, we will update $t_k \in (0, \varepsilon]$

(where $\varepsilon > 0$ is some sufficiently small real number) by following a heuristic approach inspired by the Armijo-Goldstein line search strategy similar to the one offered in [78], but for level-set methods. Given the choice of descent direction $\mathbf{V}|_{\Sigma} = -g\mathbf{n}$ (this means, basically, that $a(\cdot, \cdot)$ in equation (3.4) below is the usual inner product in $L^2(\Sigma)$), and the definition of the domain Ω_ε , we have the formal expansion

$$J(\Omega_\varepsilon) \simeq J(\Omega_0) + \varepsilon dJ(\Omega_0)[\mathbf{V}] = J(\Omega_0) - \varepsilon \|g\|_{L^2(\Sigma_0)}^2 < J(\Omega_0).$$

Suppose that, for some $\alpha \in (0, 1)$, $J(\Omega_\varepsilon) = (1 - \alpha)J(\Omega_0)$. Then, equating the previous estimate $J(\Omega_0) + \varepsilon dJ(\Omega_0)[\mathbf{V}]$ with $(1 - \alpha)J(\Omega_0)$ suggests that

$$\varepsilon = \alpha \frac{J(\Omega_0)}{\|g\|_{L^2(\Sigma_0)}^2}.$$

Clearly, this choice for the step size with $\mathbf{V}|_{\Sigma} = -g\mathbf{n}$ as the descent direction can be used to perturb the domain Ω . However, since in our case we are regularizing \mathbf{V} through the variational problem (3.1), we need to replace the L^2 -norm of g appearing in the denominator of the previous formula with the $\mathbf{H}^1(\Omega)$ -norm of \mathbf{V} , and then finally define the step size t_k as

$$(3.3) \quad t_k = \alpha \frac{J(\Omega_k)}{\|\mathbf{V}\|_{\mathbf{H}^1(\Omega)}^2}.$$

We explain this choice in more detail as follows. In general, we may in fact consider the variational equation

$$(3.4) \quad a(\mathbf{V}, \boldsymbol{\varphi}) = -\langle g\mathbf{n}, \boldsymbol{\varphi} \rangle_{L^2(\Sigma)}, \quad \forall \boldsymbol{\varphi} \in \mathcal{X},$$

where $a(\cdot, \cdot)$ is some bounded coercive bilinear form on an appropriate space \mathcal{X} , to produce a regularized descent direction using $-g\mathbf{n}$ (see, e.g., [10, Section 6.3]). Using (3.4), and the requirement that the relation

$$J(\Omega_\varepsilon) = (1 - \alpha)J(\Omega_0) = J(\Omega_0) + \varepsilon \langle g\mathbf{n}, \mathbf{V} \rangle_{L^2(\Sigma)}$$

holds for some $\alpha \in (0, 1)$, we therefore end up with

$$\varepsilon = -\alpha \frac{J(\Omega_0)}{\langle g\mathbf{n}, \mathbf{V} \rangle_{L^2(\Sigma)}} = \alpha \frac{J(\Omega_0)}{a(\mathbf{V}, \mathbf{V})},$$

for any $\mathbf{V} \in \mathbf{H}_{\Gamma,0}^1(\Omega)$. Thus, at each iteration, we may in fact choose, for a fixed α , the step size parameter t_k as

$$(3.5) \quad t_k = \alpha \frac{J(\Omega_k)}{a(\mathbf{V}, \mathbf{V})}.$$

Clearly, this formula for t_k provides a logical choice for the magnitude of the step size when the descent direction \mathbf{V} is regularized using equation (3.4). Even so, we will see through various numerical experiments in the first part of the next section that it is possible to change the denominator in (3.5) to get a better step size (see the numerical section of [97]). In fact, by changing the $\mathbf{H}^1(\Omega)$ -norm in

(3.3) by either the $H_{\Gamma,0}^1(\Omega)$ - or the $L^2(\Sigma)$ -norm, for instance, we can speed up the convergence of the algorithm given below, as exhibited in [97]. Indeed, this claim can easily be supported by the fact that the sequence of inequalities $\|\mathbf{V}\|_{H^1(\Omega)}^{-2} \lesssim \|\mathbf{V}\|_{H_{\Gamma,0}^1(\Omega)}^{-2} \lesssim \|\mathbf{V}\|_{L^2(\Omega)}^{-2}$ obviously holds.

Now, with $\alpha \in (0, 1)$ fixed, the step size will be decided according to the following rule: we take t_k as in (3.3) whenever there is a *strict* decrease in the computed cost value from the previous to the next iteration loop; that is, if $J(\Omega_{k+1}) < J(\Omega_k)$. Otherwise, if the cost value increases, we reduce the step size and go backward: the next iteration is initialized with the previous shape Ω_k . We also reduce the step size t_k if reversed triangles are detected within the mesh update.

3.1.3 The Boundary Variation Algorithm

The main steps required for the computation of the k th domain using a first-order method can be summarized as follows:

Step 1 First, fix the step size parameter $\alpha \in (0, 1)$, and choose an initial shape Ω_0 .

Step 2 Next, solve the state and adjoint state equations on Ω_k , and if needed, compute the mean curvature k of the current free boundary Σ_k .

Step 3 Then, compute the descent direction \mathbf{V}_k using (3.1). Also, calculate the step size t_k by (3.3).

Step 4 Finally, using \mathbf{V}_k and t_k , perturb the current domain by $\Omega_{k+1} = (\mathbf{I}_2 + t_k \mathbf{V}_k)\Omega$ with $\Omega = \Omega_k$.

We shall implement the above procedures in the programming software FREEFEM++ (see [72]), and to be more precise with our calculation process, we give below (see Algorithm 3.1) the exact first-order boundary variation algorithm we will use in our numerical experiments. In Algorithm 3.1, the quantities $\mathbf{u}(\Omega)$ and $\mathbf{p}(\Omega)$ respectively denote the state and adjoint variables. For instance, in the case of the third proposed shape problem (1.18), $\mathbf{u}(\Omega)$ is essentially composed of the state variables $u_N(\Omega)$ and $u_R(\Omega)$.

3.1.4 Stopping Criteria

To complete the iterative procedure presented in the previous subsection, we need to specify the stopping condition of the algorithm. A typical stopping criterion for a gradient-type method is to find that whether the shape gradients in some suitable norm are small enough. However, since we are using continuous shape gradients, it is hopeless for us to expect very small gradient norm because of numerical discretization errors. Another option, however, is to use the inequality condition

$$(3.6) \quad |J(\Omega_{k+1}) - J(\Omega_k)| < \text{Tol}$$

as a stopping rule, where $\text{Tol} > 0$ is a predetermined small tolerance value.

In our numerical experiments, we will compare the results obtained from the proposed formulation (1.16) with that of the classical Neumann-data tracking cost functional minimization approach

Algorithm 3.1 Boundary Variation Algorithm (First-Order)

Initialization: Let $k = 0$, $J_{\text{old}} = 10^{32}$, initialize domain Ω_0 , and choose a step size $\alpha \in (0, 1)$. Set $\text{back} = \text{false}$.

```

1: while stopping condition not satisfied do
2:   For  $\Omega = \Omega_k$ , compute  $\mathbf{u}(\Omega)$  and  $\mathbf{p}(\Omega)$ 
3:   Evaluate  $\kappa = \text{div } \mathbf{N}$  where  $\mathbf{N}(\Omega)$  solves (3.2)
4:   Compute  $\mathbf{V}_k(\Omega)$  using (3.4)
5:   Evaluate  $J(\Omega_k)$ 
6:    $J_{\text{new}} = J(\Omega_k)$ 
7:   if  $J_{\text{new}} < J_{\text{old}}$  then
8:      $t_k = \alpha \frac{J(\Omega_k)}{\|\mathbf{V}_k\|_{\mathcal{X}^2}^2}$ 
9:   end if
10:   $\Omega_{\text{old}} = \Omega_k$ 
11:  if  $(J_{\text{new}} > J_{\text{old}}) \wedge (\text{back} = \text{false})$  then
12:     $t_k \leftarrow 0.5 t_k$ 
13:     $\Omega_k = \Omega_{\text{old}}$ 
14:     $\text{back} = \text{true}$ 
15:  end if
16:  if  $\text{back} = \text{false}$  then
17:     $\Omega_{k+1} = \{x + t_k \mathbf{V}_k(x) : x \in \Omega_k\}$ 
18:     $J_{\text{old}} = J_{\text{new}}$ 
19:     $k \leftarrow k + 1$ 
20:  end if
21: end while

```

(1.8). For this reason, the proper choice for Tol in (3.6) may be different for each of the two formulations. Because of this issue, we need to consider a stopping rule that is independent of the cost or the gradient value. In this regard, the most reasonable choice would be to use the computing time (i.e., the maximum number of seconds before timing out) as the stopping condition. Note that we could also stop the iteration process with a predetermined maximum number of iterations. However, since the step size t_k is chosen on the basis of formula (3.3), the total number of iterations the algorithm needed to process in order to obtain good enough approximation of the optimal shape solution (given that α and \mathcal{X} are fixed) may differ greatly from each formulation. Nevertheless, we emphasize that we could still utilize the inequality condition given in (3.6) to choose an optimal iteration number that provides reasonable approximation of the optimal solution. This can be done by first running the algorithm for a certain amount of time and then examine afterwards the convergence history of the cost function (or possibly the history of Hausdorff distances between the k th and final computed shape) to decide for the best choice of the tolerance value. The index k that satisfies the condition (3.6) with the chosen value for Tol can then be regarded as the optimal iteration number when the said stopping rule is applied.

On the other hand, for the case of the second proposed shape optimization problem (1.17),

we will compare our numerical findings with that of the classical Kohn-Vogelius cost functional minimization approach (1.10). In this case, we again consider (3.6) as our stopping condition. This seems proper for this case because our main objective in this part of the investigation is to show numerically that the proposed formulation (1.17) indeed, coupled with Tiihonen's condition (2.23), provides less computing time per iteration than in the case of the classical energy-gap cost functional minimization setting (1.10).

Lastly, for the case of the third proposed shape optimization problem (1.18), we will compare our numerical results with that of the classical Dirichlet-data-tracking cost functional minimization approach (1.6). In this regard, we will finish our algorithm as soon as the cost, normalized with respect to its initial value, is less than some small (positive) tolerance value. We deem this criterion more appropriate than (3.6) in evaluating the computational qualities of the two methods since their corresponding cost values actually differ by two orders of magnitude. In this respect, we therefore stop the algorithm as soon as the inequality condition

$$(3.7) \quad \frac{J(\Omega_k)}{J(\Omega_0)} < \text{Tol},$$

is satisfied for some sufficiently small real number $\text{Tol} > 0$ (of course, the choice for this tolerance value is different from the case of the first proposed shape optimization problem (1.16)), or if the algorithm already completed a specified (maximum) computing time.

3.1.5 The Sobolev Newton Method

Note, by incorporating the shape Hessian information in the numerical procedure, we can obviously improve the convergence of the iterative scheme given in the previous subsection in terms of the number of iterations required to complete the optimization procedure (see, e.g., [47, 98, 109]). However, the drawback of a second-order method is that, in most cases, it demands additional computational burden and time to carry out the task. In this section, we will formulate a second-order optimization algorithm to solve the minimization problems (1.17) and (1.18) following an idea first proposed by Azegami in [7] (see also [9, Problem 4.2, Eq. (29)]). Particularly, we use a variant of the so-called H^1 Newton (or Sobolev Newton) method which utilizes the Hessian information to compute the descent direction. The basic idea of this method is that it incorporates the shape Hessian in obtaining a regularized descent direction for the algorithm similar to equation (3.4) (see the next subsection 3.1.6 below). In our case, however, we propose to use only the shape Hessian information at the solution of the FBP (1.3) (i.e., we use (2.65)).

To do the task, we define the descent direction $\mathbf{W} \in \mathbf{H}_{\Gamma,0}^1(\Omega)$ as the unique solution of the variational equation

$$(3.8) \quad \int_{\Omega} (\nabla \mathbf{W} : \nabla \boldsymbol{\varphi} + \mathbf{W} \cdot \boldsymbol{\varphi}) dx = - \int_{\Sigma} (g + h[\mathbf{V}]) \mathbf{n} \cdot \boldsymbol{\varphi} d\sigma, \quad \forall \boldsymbol{\varphi} \in \mathbf{H}_{\Gamma,0}^1(\Omega),$$

where g , as before, is the kernel of the shape gradient $dJ(\Omega)[\mathbf{V}] = \int_{\Sigma} g \mathbf{n} \cdot \mathbf{V} d\sigma$, while $h[\mathbf{V}]$, in this case, denotes only the *kernel of the shape Hessian at the solution of the FBP (1.3)*. For example,

in the case of the minimization problem (1.18), we have $\int_{\Sigma^*} h_3[\mathbf{V}]\mathbf{n} \cdot \mathbf{W} \, d\sigma := d^2 J_3(\Sigma^*)[\mathbf{V}, \mathbf{W}]$ (see (2.68)). Meanwhile, in the case of the shape gradient computed under Tiihonen's condition (2.23), the corresponding expression which we denote by $h^\top[\mathbf{V}]$ is given by the kernel of the shape Hessian $d^2 J_3^\top(\Sigma^*)[\mathbf{V}, \mathbf{W}] =: \int_{\Sigma^*} h_3^\top[\mathbf{V}]\mathbf{n} \cdot \mathbf{W} \, d\sigma$ (see (2.65)). More precisely, these kernels of the shape Hessians are given by

$$(3.9) \quad h_3[\mathbf{V}] = \lambda\kappa\Pi[\mathbf{V}] \quad \text{and} \quad h_3^\top[\mathbf{V}] = \lambda(\Psi[\mathbf{V}] + \lambda\kappa\Pi[\mathbf{V}]),$$

respectively. Here, of course, Ψ and Π are the respective unique solutions of equations (2.66) and (2.67). In above expressions, we added the notation $(\cdot)[\mathbf{V}]$ to emphasize that the expression it is attached to is dependent to the deformation field \mathbf{V} .

Let us discuss the additional procedures needed to utilize the shape Hessian information in an iterative scheme. We illustrate, in particular, the case for the third proposed shape optimization approach (1.18). We emphasize that the main steps to compute the k th domain Ω_k using a second-order method are essentially the same with that of the first-order method given in Section 3.1.3. However, in order to take into account the procedure in computing \mathbf{W} , we divide the third step of the original algorithm as follows:

Step 3.1 Compute the descent direction \mathbf{V}_k using (3.1).

Step 3.2 Compute Ψ and Π by solving the PDE systems (2.66) and (2.67) at $\Omega = \Omega_k$.

Step 3.3 Compute the descent direction \mathbf{W}_k using (3.8).

Moreover, in **Step 4** of the original algorithm, we replace \mathbf{V}_k with the new deformation field \mathbf{W}_k ; that is, we perturb the k th domain by $\Omega_{k+1} = (\mathbf{I}_2 + t_k \mathbf{W}_k)\Omega_k$. Here, the step size t_k can still chosen on the basis of the formula given in (3.3). However, in our experience, this formula for the step size does not give much improvement in terms of convergence speed for the second-order shape optimization algorithm. To exploit the advantage of utilizing the shape Hessian information, an appropriate step size formula has to be used to achieve at least a superlinear (or even quadratic) convergence rate for the algorithm (see Remark 3.1.1 below).

3.1.6 Step Size for the Second-Order Method

Again, let us suppose that $J(\Omega)$ is a shape functional whose shape gradient is given by $dJ(\Omega)[\mathbf{V}] = \int_{\Sigma} \mathbf{g}\mathbf{n} \cdot \mathbf{V} \, d\sigma$. Then, its corresponding shape Hessian (under sufficient regularity) can be shown to be given by

$$d^2 J(\Omega)[\mathbf{V}, \mathbf{W}] = \int_{\Sigma} [g'_W V_n + (\partial_n g + \kappa g) V_n W_n - g\mathbf{K} + g(D\mathbf{V})W_n] \, d\sigma,$$

(cf. (2.29) or see, e.g., [43, Eq. (5.2), p. 495]). Evidently, as already remarked in the previous chapter, the above expression of the shape Hessian $d^2 J(\Omega)[\mathbf{V}, \mathbf{W}]$ consists of symmetric and non-symmetric parts with respect to the deformation fields \mathbf{V} and \mathbf{W} . This lack of symmetry and complexity in

form of the shape Hessian provides much difficulty for its utilization and numerical implementation ([93, 105]). Nevertheless, as proposed by Simon in [105], one can still utilize the shape Hessian in an optimization procedure in a much simpler way by dropping the non-symmetrical part of the Hessian (see, e.g., [77]), allowing one to obtain a second order expansion of the form

$$J(\Omega) + dJ(\Omega)[V] + d^2J(\Omega)[V, V]$$

of $J(\Omega)$ with respect to the descent direction V . Note that, at the optimal shape solution $\Omega = \Omega^*$, the necessary optimality condition give rise to the variational formulation of the Newton equation

$$d^2J(\Omega)[V, W] = -dJ(\Omega)[V], \quad \forall V \in \mathbf{H}_{\Gamma,0}^1(\Omega),$$

whose solution W may be used as a descent direction in a gradient-based descent algorithm (cf. equation in Step 3 of [71, Section 4.1.1, Algorithm 4.1, p. 131]). Following this idea, and employing a smoothing technique such as (3.4), we arrive at equation (3.8) which gives us a new regularized descent direction W .

Remark 3.1.1. As pointed out by Simon in [105] (see his remark in Section 2.1), we mention here that the velocity of gradient methods (such as Algorithm 3.1) can be improved by choosing the step size as the negative ratio between the shape gradient over the shape Hessian. For example, the k th approximation of Ω_0 can be computed as $\Omega_{k+1} = (\mathbf{I}_2 + t_k^f \mathbf{V}_k) \Omega_k$ where $t_k^f = -dJ(\Omega_k)[\mathbf{V}_k] / d^2J(\Omega_k)[\mathbf{V}_k, \mathbf{V}_k]$. Here, the step generated by the formula for t^f is commonly called as the *(full) Newton step* (see, e.g., [91, Section 3.3]).

In our case, since we are using regularized descent directions, the above idea is, in a sense, equivalent to taking t_k as a scalar multiple of the ratio of the square of the $\mathbf{H}^1(\Omega)$ -norm of V over the squared $\mathbf{H}^1(\Omega)$ -norm of W . Indeed, from a similar proposition issued in subsection 3.1.2, we can naturally take

$$(3.10) \quad t_k = \tilde{\alpha} \frac{\|\mathbf{V}\|_{\mathbf{H}^1(\Omega_k)}^2}{\|\mathbf{W}\|_{\mathbf{H}^1(\Omega_k)}^2},$$

for a fixed $\tilde{\alpha} \in (0, 1]$, as the k th step size of the second-order optimization algorithm proposed in subsection 3.1.5.

In (3.10), we introduced the step size parameter $\tilde{\alpha}$ simply to control the magnitude of the descent step during each iteration. We recall that, in most optimization problems, the introduction of a step size parameter to Newton's method is primarily due to the fact that the method is quite sensitive if the initial guess is too bad. Common strategies to globalize the method is to introduce a *line search strategy* or to work with the so-called *trust region methods* (see, e.g., Section 3.4 and Chapter 4 of [91]). In practice, the former strategy is accomplished by scaling the Newton's step by some

coefficient $0 < \tilde{\alpha} \leq 1$ in every iteration (as we have done in (3.10)). Taking $\tilde{\alpha} = 1$ obviously amounts to a full Newton step and choosing $\tilde{\alpha} < 1$ yields the so-called *damped Newton method* (see, e.g., [22, Section 9.5.2, p. 487]) which has an increased convergence radius (this, however, does not work well in general), and also has a reduced convergence order (not quadratically anymore). Nevertheless, when the approximant is judged to be near to a solution, $\tilde{\alpha} = 1$ is taken and the convergence would be as good as for the standard (or *pure*) Newton's method.

Here, we opted to apply a line search method in our proposed second-order (shape optimization) algorithm to address two main issues when taking the full Newton step. Firstly, we notice that, in some situations, choosing a full Newton step is not necessarily the best strategy to start the approximation procedure, especially if the initial guess is far from the (optimal shape) solution. Secondly, we observe that the full Newton step is sometimes too large that the cost functions become insensitive with respect to geometric perturbations, occasionally causing the algorithm to overshoot or converge prematurely to a less optimal solution (*see* Example 3.2.3.4). On the other hand, although the step size parameter $\tilde{\alpha}$ can be made at most equal to the unit value when the approximant is estimated to be close to the optimal solution, we only fixed $\tilde{\alpha}$ to be of constant value (≤ 1) throughout the iteration process. Nevertheless, a backtracking procedure as in subsection 3.1.2 will still be employed in the algorithm, meaning that the maximum step size at each iteration of the algorithm is only bounded above by a fraction (determined by the value of $\tilde{\alpha}$) of the full Newton step. Despite the fact that the idea is already known in the literature, we emphasize that the formula for the step size given by (3.10) is, to the best of our knowledge, new to this work.

Before we proceed to the numerical examples in the next section, let us be more precise with our second-order gradient-based optimization procedure that we will use in our numerical experiments. The exact iterative scheme is given in Algorithm 3.2. In this algorithm, the quantities $\mathbf{u}^\dagger(\Omega)[\mathbf{V}]$ and $\mathbf{p}^\dagger(\Omega)[\mathbf{V}]$ respectively denote the corresponding adjoint variables for $\mathbf{u}(\Omega)$ and $\mathbf{p}(\Omega)$ in the first-order optimization algorithm 3.1. The notation $(\cdot)[\mathbf{V}]$ is attached to emphasize that these unknowns are dependent on the vector field \mathbf{V} . For instance, in the case of classical Dirichlet-data-tracking cost functional minimization approach (1.6), $\mathbf{u}^\dagger(\Omega)[\mathbf{V}]$ refers to the adjoint variables $\Psi(\Omega)$ and $\Pi(\Omega)$ which are unique solutions to the PDE systems (2.66) and (2.67), respectively. Meanwhile, $\mathbf{p}^\dagger(\Omega)[\mathbf{V}]$ corresponds to the adjoint variable $\Upsilon(\Omega)$ which is the solution to the BVP (2.71), see Proposition 2.4.5 and Corollary 2.4.3.

3.2 Numerical Examples

In this section, we solve various concrete examples of the Bernoulli problem. The examples are sorted in accordance with the formulations presented in Section 1.3.2 of the first chapter. Therefore, this section is composed of three parts. The first part (subsection 3.2.1) contains the results of the improved Neumann-data-tracking cost functional minimization approach (1.16) which is compared with its classical counterpart (1.8). The second part (subsection 3.2.2), on the other hand, presents the nu-

Algorithm 3.2 Boundary Variation Algorithm (Second-Order)

Initialization: Let $k = 0$, $J_{\text{old}} = 10^{32}$, initialize domain Ω_0 , and choose a step size $\tilde{\alpha} \in (0, 1]$. Set $\text{back} = \text{false}$.

- 1: **while** stopping condition not satisfied **do**
- 2: For $\Omega = \Omega_k$, compute $\mathbf{u}(\Omega)$ and $\mathbf{p}(\Omega)$
- 3: Evaluate $\kappa = \text{div } \mathbf{N}$ where $\mathbf{N}(\Omega)$ solves (3.2)
- 4: Compute $\mathbf{V}_k(\Omega)$ using (3.4)
- 5: Compute $\mathbf{u}^\dagger(\Omega)[\mathbf{V}]$ and $\mathbf{p}^\dagger(\Omega)[\mathbf{V}]$
- 6: Compute \mathbf{W}_k using (3.8)
- 7: Evaluate $J(\Omega_k)$
- 8: $J_{\text{new}} = J(\Omega_k)$
- 9: **if** $J_{\text{new}} < J_{\text{old}}$ **then**
- 10:
$$t_k = \tilde{\alpha} \frac{\|\mathbf{V}_k\|_{\mathcal{X}^2}^2}{\|\mathbf{W}_k\|_{\mathcal{X}^2}^2}$$
- 11: **end if**
- 12: $\Omega_{\text{old}} = \Omega_k$
- 13: **if** $(J_{\text{new}} > J_{\text{old}}) \wedge (\text{back} = \text{false})$ **then**
- 14: $t_k \leftarrow 0.5 t_k$
- 15: $\Omega_k = \Omega_{\text{old}}$
- 16: $\text{back} = \text{true}$
- 17: **end if**
- 18: **if** $\text{back} = \text{false}$ **then**
- 19: $\Omega_{k+1} = \{x + t_k \mathbf{W}_k(x) : x \in \Omega_k\}$
- 20: $J_{\text{old}} = J_{\text{new}}$
- 21: $k \leftarrow k + 1$
- 22: **end if**
- 23: **end while**

merical results for the modified Kohn-Vogelius cost functional minimization approach (1.17) which is compared against the classical setting (1.10). Last but not least, the third part (subsection 3.2.3) exhibits the numerical findings for the Dirichlet-data-gap cost functional minimization approach (1.18) which is compared with the classical Dirichlet-data-tracking cost functional minimization approach (1.6).

All numerical experiments carried out in this investigation are performed in two-dimension using the programming software FREEFEM++ (see [72]). Moreover, all variational problems that need to be solved in order to evaluate the quantities in the algorithm are numerically computed using P2 finite element discretization where the number of discretization points on the free and fixed boundaries are initially set to $N_{\text{ext}} \times N_{\text{int}} = 120 \times 100$ discretization points. Meanwhile, we use the built-in function *movemesh* of FREEFEM++ in perturbing the reference domain Ω during the optimization process. In addition, we use the function *adaptmesh* with minimum edge size h_{min} and maximum edge size h_{max} (to be specified later in each of the subsection below) during mesh adaption to refine and avoid the degeneracy of the triangles in the meshes. Lastly, all computations

are carried out on a 1.6 GHz Intel Core i5 Macintosh computer with 4GB RAM processors.

3.2.1 Examples for the First Proposed Shape Problem

In this subsection, we provide a number of concrete examples of the Bernoulli problems, including both the exterior and interior case of the problem. The problems that we examine here, however, are only solved using first-order shape optimization methods. This is because the set of numerical experiments we perform here serves as a preliminary examination on the effect of the Robin problem (1.15) in the approximation procedure. Nevertheless, we will provide numerical results for second-order methods in the last two subsections of the chapter.

Now, in all test cases we examine here, we let β be the mean curvature of the free boundary Σ (i.e., we let $\beta = \kappa$). We mention that we have actually tested several values for this Robin coefficient, but it appears that the mean curvature κ of the free boundary is the best choice for the algorithm to work effectively in terms of convergence speed and stability, especially in the case of the classical approach.

Notations. In all examples we present in this subsection, Σ_k denotes the k th approximation of the optimal free boundary Σ^* , and the quantity $d_H(\Sigma_k, \Sigma)$ denotes the Hausdorff distance between Σ_k and Σ . Also, K denotes the *optimal termination index* when the stopping condition (3.6) is imposed with some prescribed value for Tol; i.e., $K := \min\{k \in \mathbb{N}_0 : |J(\Sigma_{k+1}) - J(\Sigma_k)| < \text{Tol}\}$. Moreover, for later use, we denote by the index M the last iteration loop of the algorithm before timing out (or equivalently, the maximum number of iterations completed by the algorithm after running it for a specified number of seconds).

Exterior case

3.2.1.1 Example 1: Accuracy Tests

We first test the accuracy of the computed gradient. For this purpose, we consider the exterior Bernoulli problem with

$$\Gamma = C(\mathbf{0}, r), \quad \lambda = \frac{1}{R(\log r - \log R)}, \quad 0 < r < R,$$

where $C(\mathbf{0}, r)$ denotes the circle centered at the origin with radius r . In this case, the only solution is the circle $C(\mathbf{0}, R)$.

We let $r = 0.3$ and $R = 0.5$ (hence, $\Sigma^* = C(\mathbf{0}, 0.5)$), giving us $\lambda = -3.9152$. We take $C(\mathbf{0}, 0.6)$ as the initial guess and compute the optimal shapes using the proposed formulation and the classical Neumann-data tracking approach.

In this example, since the evolution of the free boundary consists of concentric circles, we will often use the term ‘ k th mean radii’ which means the average distance from the origin of the nodes on the exterior boundary of the k th domain Ω_k . Throughout the discussion, this term will be denoted by \bar{R}_k . Furthermore, in all test cases, we take $h_{\max} = 0.02$ and end the optimization process after running

the algorithm for 300 seconds.

Comparisons of results for different choices of \mathcal{X} in (3.3). In this test case, we present the results of the optimization process when \mathcal{X} in the step size formula (3.3) for t_k is set to either $H^1(\Omega_k)$, $H_{\Gamma,0}^1(\Omega_k)$ or $L^2(\Sigma_k)$ with $\alpha = 0.01$. Figure 3.1a shows the histories of mean radii of the free boundary obtained using the proposed formulation. Looking at the said figure, it seems that the choice $\mathcal{X} = L^2(\Sigma_k)$ provides the fastest convergence to the optimal solution among the three choices. This is primarily due to the fact that when \mathcal{X} is set to $L^2(\Sigma_k)$, we have, on the average, larger values for the step size t_k (as expected) than when it is set to either $H^1(\Omega_k)$ or $H_{\Gamma,0}^1(\Omega_k)$ (see Figure 3.1b). Observe also that the latter two choices almost have the same rate of convergence, which is not surprising since their corresponding norms are actually equivalent. Meanwhile, in Table 3.1, we tabulate the computational results of the present experiment. The table shows, in particular, the Hausdorff distance between the K th approximation Σ_K of the free boundary and its exact optimal shape Σ^* , the mean radii \bar{R}_K and its corresponding standard deviation σ_K^{rad} at the K th iterate, where K is the optimal termination index when the tolerance Tol is set to the ones indicated in the first column of the table. Also listed in the table are the values of the cost at the K th iterate and the total computing time to reach convergence when the stopping rule (3.6) is imposed with Tol values given in the first column of the table. Here we mention that the Tol values listed in the table are actually the values of the tolerance in the stopping rule (3.6) that were satisfied (omitting the case when 10^{-1} and 10^{-2}) after running the algorithm for 300 seconds (except for the case when $\mathcal{X} = L^2(\Sigma_k)$ where we only present the results up to 10^{-6}). Based on the results, it appears that a reasonable choice for the tolerance Tol when imposing the stopping condition (3.6) when using the proposed formulation is to take it equal to 10^{-5} . Note also that, for all $\mathcal{X} \in \{H^1(\Omega_k), H_{\Gamma,0}^1(\Omega_k), L^2(\Sigma_k)\}$, the Hausdorff distance between Σ^* and the computed optimal free boundary Σ_K , with Tol = 10^{-5} in (3.6), is approximately equal to 0.005.

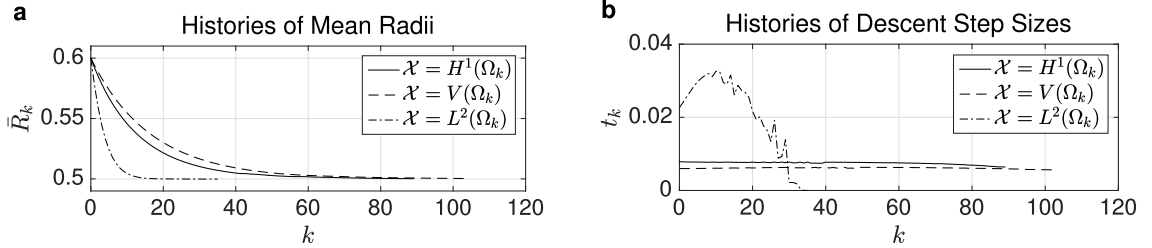


Figure 3.1: Histories of mean radii (plot **a**) and descent step sizes (plot **b**) when $\mathcal{X} = H^1(\Omega_k), H_{\Gamma,0}^1(\Omega_k), L^2(\Sigma_k)$ in (3.3) with $\alpha = 0.01$ using the proposed formulation, running the algorithm for 300 seconds

On the other hand, the results obtained from using the classical Neumann-data tracking approach are depicted in Figure 3.2. Figure 3.2a shows the histories of mean radii \bar{R}_k of the free boundary Σ_k while Figure 3.2b plots the graph of their corresponding standard deviations. Looking at the latter plot, we observe that the choice $\mathcal{X} = L^2(\Sigma_k)$ gives a very unstable approximation of the free boundary during the optimization process. In fact, we noticed during the optimization process that the exterior boundary Σ becomes very ‘jagged’ after some iterations. This possibly means that the algorithm,

Tol	$d_H(\Sigma_K, \Sigma^*)$	\bar{R}_K	σ_K^{rad}	$J(\Sigma_K)$	K	CPU time
$\mathcal{X} = H^1(\Omega_k)$						
10^{-3}	0.006660	0.504413	2.33×10^{-5}	0.004413	42	63.89 sec
10^{-4}	0.005371	0.501888	3.74×10^{-5}	0.001888	58	124.21 sec
10^{-5}	0.005004	0.500214	4.05×10^{-5}	0.000214	88	298.37 sec
$\mathcal{X} = H_{\Gamma,0}^1(\Omega_k)$						
10^{-3}	0.008084	0.506344	1.82×10^{-5}	0.038721	46	67.84 sec
10^{-4}	0.005146	0.501220	1.60×10^{-5}	0.001632	78	148.89 sec
10^{-5}	0.005053	0.500766	2.55×10^{-5}	0.000765	89	199.50 sec
$\mathcal{X} = L^2(\Sigma_k)$						
10^{-3}	0.005041	0.500586	3.93×10^{-5}	0.000927	15	23.60 sec
10^{-4}	0.005006	0.500198	4.09×10^{-5}	0.000108	17	29.45 sec
10^{-5}	0.005000	0.500055	2.94×10^{-5}	1.30×10^{-5}	22	49.19 sec
10^{-6}	0.004998	0.500101	3.15×10^{-5}	5.70×10^{-6}	25	74.39 sec

Table 3.1: Summary of results of the computational experiments when $\mathcal{X} = H^1(\Omega_k), H_{\Gamma,0}^1(\Omega_k), L^2(\Sigma_k)$ in (3.3) with $\alpha = 0.01$ using the proposed formulation

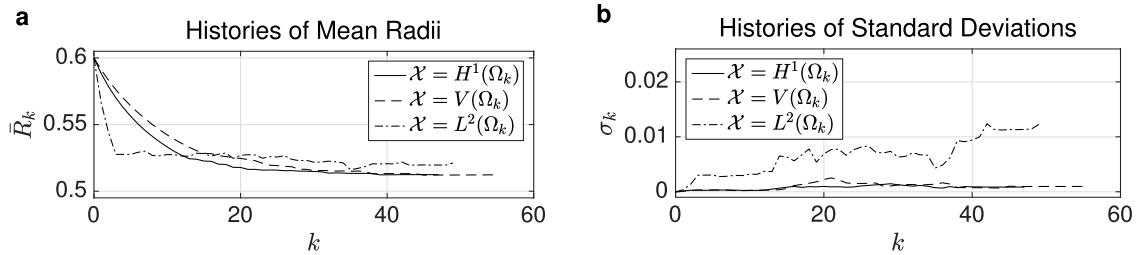


Figure 3.2: Histories of mean radii (plot **a**) and their corresponding histories of standard deviations (plot **b**) when $\mathcal{X} = H^1(\Omega_k), H_{\Gamma,0}^1(\Omega_k), L^2(\Sigma_k)$ in (3.3) with $\alpha = 0.01$ using the classical Neumann-data tracking approach after 300 seconds of run time

when employing the Neumann-data tracking approach, is very sensitive to large deformations, which, on the other hand, suggests that we need to take smaller values for α in order to get more stable approximation of the optimal free boundary. Setting α in (3.3) to smaller values, however, would then require the algorithm to process additional number of iterations (and therefore demands additional computing times) just in order to attain reasonable approximation of the exact optimal free boundary. Furthermore, even in the case when \mathcal{X} is set to either $H^1(\Omega_k)$ or $H_{\Gamma,0}^1(\Omega_k)$, the histories of mean radii obtained through the Neumann-data tracking approach is less smooth that in the case of when applying the proposed formulation (compare Figure 3.1a and Figure 3.2a). Moreover, it is also evident in the two plots shown in Figure 3.2 that the choices $H^1(\Omega_k)$ and $H_{\Gamma,0}^1(\Omega_k)$ for \mathcal{X} in (3.3) exhibit almost the same rate of convergence as in the case of using the proposed formulation. It seems, however, that the best choice for the algorithm to work effectively when applying the Neumann-data tracking

Tol	$d_H(\Sigma_K, \Sigma^*)$	\bar{R}_K	σ_K^{rad}	$J(\Sigma_K)$	K	CPU time
$\mathcal{X} = H^1(\Omega_k)$						
10^{-1}	0.020737	0.517855	0.000972	2.527479	20	22.70 sec
10^{-2}	0.017395	0.514585	0.001157	1.957065	31	38.98 sec
10^{-3}	0.014639	0.512422	0.000855	1.526704	44	195.86 sec
10^{-4}	0.014612	0.512444	0.000848	1.525842	47	288.12 sec
$\mathcal{X} = H_{\Gamma,0}^1(\Omega_k)$						
10^{-1}	0.030236	0.522901	0.002171	4.638160	22	29.40 sec
10^{-2}	0.019315	0.515450	0.001315	2.204293	32	49.77 sec
10^{-3}	0.015384	0.512289	0.000970	1.430624	55	276.75 sec
$\mathcal{X} = L^2(\Sigma_k)$						
10^{-1}	0.038000	0.527682	0.003034	7.934110	5	19.36 sec
10^{-2}	0.044922	0.528277	0.006324	5.996569	15	77.61 sec

Table 3.2: Summary of results of the computational experiments when $\mathcal{X} = H^1(\Omega_k), H_{\Gamma,0}^1(\Omega_k), L^2(\Sigma_k)$ in (3.3) with $\alpha = 0.01$ using the Neumann-data tracking approach

approach is to take \mathcal{X} as the space $H^1(\Omega_k)$. Meanwhile, the computational results corresponding to the case when using the Neumann-data tracking approach with $\alpha = 0.01$ in (3.3) are summarized in Table 3.2. Based on the table, it seems that the appropriate value for the tolerance Tol is 10^{-3} when imposing the stopping rule (3.6), in case of implementing the Neumann-data tracking approach.

Before we proceed further with our numerical investigations, let us comment and reiterate the most important findings drawn from the results of the computational experiments presented above. Firstly, it seems that the proposed formulation provides a more stable approximation of the free boundary (in a sense that the domain Ω is less prone to experience rapid oscillating exterior boundary during iterations) than the Neumann-data tracking approach, regardless of the choice of $\mathcal{X} \in \{H^1(\Omega_k), H_{\Gamma,0}^1(\Omega_k), L^2(\Sigma_k)\}$. This observation can actually be inferred easily by comparing the order of magnitude of σ_K^{rad} obtained from the two formulations. Secondly, it appears that the proposed formulation exhibits faster convergence behavior than the Neumann-data tracking approach, again irrespective of the choice of \mathcal{X} in the step size formula (3.3). In addition, the former formulation provides better approximation of the analytical solution than the latter approach. Furthermore, it seems that the appropriate choice for Tol when imposing the stopping condition (3.6) is to take it equal to 10^{-5} when using the proposed formulation and set it to 10^{-3} when applying the Neumann-data tracking approach. In relation to this remark, it appears that the best choice for \mathcal{X} in (3.3) that provides the fastest convergence rate when employing the proposed formulation is the space $L^2(\Sigma_k)$. On the other hand, it seems that the most practical choice for \mathcal{X} that provides the most stable and fastest convergence rate when applying the Neumann-data tracking approach is the space $H^1(\Omega_k)$. All these observations can all be inferred easily from the results shown in Table 3.1 and Table 3.2, and,

of course, from the graphs plotted in Figure 3.1 and Figure 3.2.

Examining the order of convergence of the iterative procedure. Next, we numerically examine the convergence behavior of the present iterative scheme. We do this by looking at the sequence of radii of the computed optimal free boundaries obtained from using each of the two formulations. For this purpose, we let $\epsilon_k = |\bar{R}_k - R^*|$ be the error in the k th approximation. Note that, for a ‘good’ numerical procedure, we want the approximate shape solution $\Omega_k := C(\mathbf{0}, \bar{R}_k)$ to be as close as possible to the analytical solution $\Omega^* := C(\mathbf{0}, R^*)$, $R^* = 0.5$. Now, let ρ be the order of convergence of R_k to R^* ; that is, we have that $\lim_{k \rightarrow \infty} \epsilon_{k+1} / \epsilon_k^\rho = \eta$. If we assume that the error progression is exactly of the form $\epsilon_{k+1} = \eta \epsilon_k^\rho$, then we can actually write $\log \epsilon_{k+1} = \rho \log \epsilon_k + \log \eta$. Hence, we can use a best-fit-line approach to find an approximation of ρ , given the sequence of errors ϵ_k . Figure 3.3 below depicts the order of convergences of the algorithm when using the proposed and the classical Neumann-data tracking approach which correspond to the computational results presented above. It shows, in particular, the order of convergences of the proposed formulation when the stopping condition (3.6) is imposed with $\text{Tol} = 10^{-5}$ (see Figure 3.3a and Figure 3.3b). It also presents the order of convergences of the algorithm when applying the Neumann-data tracking approach which is again terminated via the stopping rule (3.6) but with $\text{Tol} = 10^{-3}$ (refer to Figure 3.3c and Figure 3.3d). In these plots, the *dashed-line* passing through the origin has slope equal to the unity. Meanwhile, the solid-line plot represents the best fit line to the data $\log \epsilon_{k+1} = \rho \log \epsilon_k + \log \eta$ with slope equal to the value indicated in the figure. Clearly, based on these plots, the present algorithm exhibits linear convergence behavior regardless of the formulation used in the optimization procedure.

Effects of increasing the value of the step size parameter α . Let us now look at the effect of increasing the magnitude of the step size t_k in the optimization process by adjusting α to a higher value. Obviously, we could expect that, by increasing the value of α , we could improve the rate of convergence of the algorithm. Such improvement could be expected when employing the proposed formulation in the algorithm (at least for slightly higher values of α for the present case). However, this is not always the case for the other approach since increasing the magnitude of α , in general, would only cause the algorithm to become more unstable. These facts are apparent in the plots shown in Figure 3.4, and also in Table 3.3 wherein the results of the optimization process obtained through the proposed and the classical Neumann-data tracking approach with $\mathcal{X} = H^1(\Omega)$ and $\alpha \in \{0.02, 0.03, 0.04\}$ are summarized. In the table, the notation \bar{t} represents the computed mean step size for the entire optimization process when the stopping rule (3.6) is utilized (i.e., $\bar{t} = \sum_{k=0}^K t_k / K$). The notation σ^{step} , on the other hand, denotes the standard variation of the computed step sizes, also for the entire iteration process. Meanwhile, the last column in Table 3.3 indicates the coefficient of variation (C.V.) with respect to the step size t_k , i.e., $\text{C.V.} = \sigma^{\text{step}} / \bar{t}$. In relation to this, we note that having a coefficient of variation for the step size that is larger than the unity is an indication that the step size varies greatly from each iterate. This means, possibly, that the algorithm is very much less stable, and based on our experience, large fluctuations in step size could cause the algorithm to crash during iterations. These results further support our claim that the proposed formulation provides more stable approximation

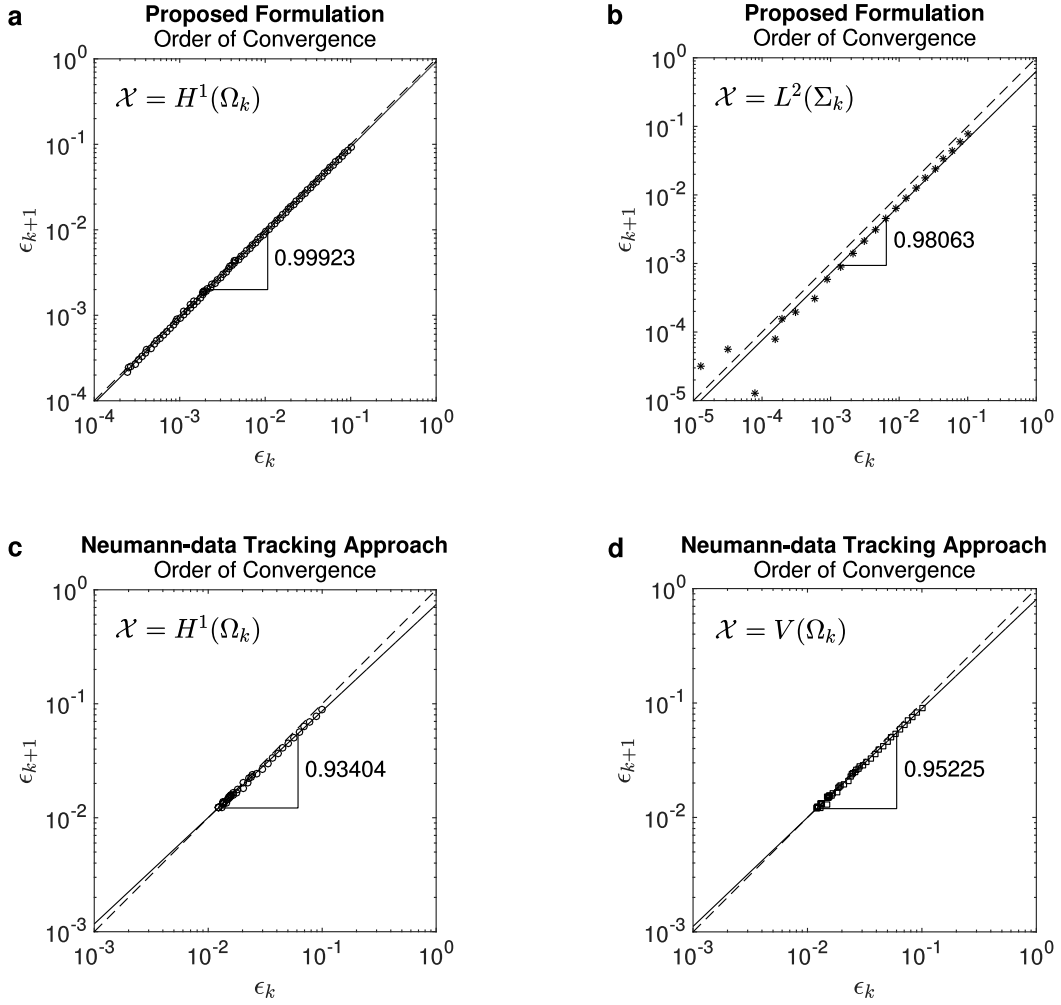


Figure 3.3: Order of convergences of the algorithm when applying the proposed formulation (plots **a** and **b**) and when using the Neumann-data tracking approach (plots **c** and **d**) with $\alpha = 0.01$, employing the stopping condition (3.6) with Tol = 10^{-5} and 10^{-3} for the first and second approach, respectively

of the exact optimal solution than the classical Neumann-data tracking approach. Moreover, it is clear from the table that the former approach is more accurate than the latter one. Lastly, notice from the table that the number of iterations (and hence, the computing times) required to reach convergence when imposing the stopping condition (3.6) is significantly less for the case of the proposed formulation than in the case of using the Neumann-data tracking approach. In the rest of the examples below, we utilize the main findings drawn above. More precisely, we take $\mathcal{X} = L^2(\Sigma_k)$ in (3.3) when the proposed formulation is being applied in the algorithm and, on the other hand, set $\mathcal{X} = H^1(\Omega_k)$ when the Neumann-data tracking approach is used in the optimization procedure.

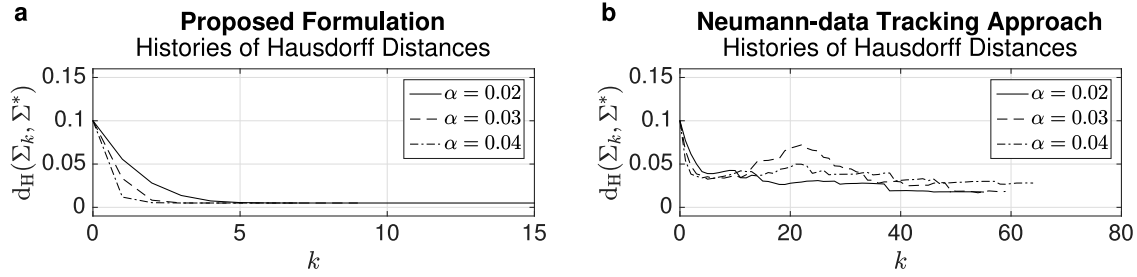


Figure 3.4: Histories of Hausdorff distances using the proposed formulation with $\mathcal{X} = L^2(\Sigma_k)$ (plot **a**) and when applying the Neumann-data tracking approach with $\mathcal{X} = H^1(\Omega_k)$ for some values of α

α	$d_H(\Sigma_K, \Sigma^*)$	\bar{R}_K	σ_K^{rad}	$J(\Sigma_K)$	K	time	\bar{t}	σ^{step}	C.V.
Proposed formulation with $\mathcal{X} = L^2(\Sigma_k)$ in (3.3) and terminated using (3.6) with Tol = 10^{-5}									
0.02	0.005002	0.499914	0.000037	4.81×10^{-6}	10	52 s	0.0375	0.0235	< 1
0.03	0.005002	0.499688	0.000062	3.09×10^{-7}	7	21 s	0.0524	0.0458	< 1
0.04	0.005014	0.499620	0.000074	1.49×10^{-9}	7	24 s	0.0926	0.0650	< 1
Neumann-data tracking approach with $\mathcal{X} = H^1(\Sigma_k)$ in (3.3) and stopped using (3.6) with Tol = 10^{-3}									
0.02	0.017956	0.513706	0.001123	1.697592	51	183 s	0.0009	0.0012	> 1
0.03	0.018772	0.513442	0.001803	1.721732	52	276 s	0.0012	0.0014	> 1
0.04	0.029857	0.515549	0.005606	1.826101	54	116 s	0.0010	0.0016	> 1

Table 3.3: Summary of results of the computational experiments corresponding to Figure 3.4

3.2.1.2 Example 2: An inverted T-shaped fixed boundary

Next, we consider $\Gamma = \partial S$ as the boundary of the inverted T-shape

$$S := ((-3/8, 3/8) \times (-1/4, 0)) \cup ((-1/8, 1/8) \times [0, 1/4]).$$

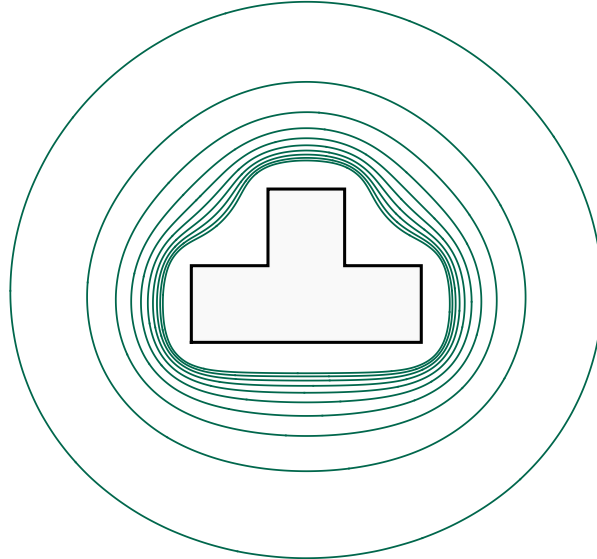
The optimal domain for $\lambda = -1, -2, \dots, -10$. First, we compute the optimal domain for all integers $\lambda = -1, -2, \dots, -10$ using the proposed formulation. We choose the unit circle as the initial guess and let $h_{\max} = 0.025$ for all cases. Furthermore, we terminate the iteration process after running the algorithm for 60 seconds. The resulting exterior boundaries are shown in Figure 3.5, where the outermost boundary corresponds to $\lambda = -1$ and the innermost boundary to $\lambda = -10$, and the shaded area represents the region bounded by the fixed boundary. Meanwhile, the results of the present computational experiments are summarized in Table 3.4 when the stopping rule (3.6) with Tol = 10^{-5} is used. The table shows in particular the computed cost value at the K th iterate and the total computing time to reach convergence for each values of λ . Also indicated in the table are the total number of iterations completed by the algorithm before timing out. The values shown in Table 3.4 were all obtained with the step size parameter α set to 0.10 except for the case when $\lambda = -3$ where we slightly adjusted α to 0.11 to reach convergence under the stopping condition (3.6) with Tol = 10^{-5} and within 60 seconds. On the other hand, we remark that the optimal free boundaries obtained

when the stopping rule (3.6) is employed are actually indistinguishable from the ones shown in Figure 3.5 (see Figure 3.6 for a direct comparison of the free boundaries Σ_K and Σ_M when $\lambda = -1, -8$). The evolution of the free boundary when $\lambda = -10$ is shown in Figure 3.7a.

Comparison of results obtained from the two formulations. Next, we compare the optimal free boundaries obtained from the two formulations for the present test case. We focus particularly on the case when $\lambda = -10$. So, we repeat the optimization process for the case $\lambda = -10$, but now using the Neumann-data tracking approach. Also, this time, we run the algorithm for 120 seconds and again take $\alpha = 0.10$. In contrast to the evolution of the free boundary shown in Figure 3.7a, we notice several oscillations appearing on Σ_k , at some iterations, when using the Neumann-data tracking approach. These unwanted irregularities on the free boundary are actually discernible from the evolution of Σ_k obtained through the said approach shown in Figure 3.7b. We emphasize that such phenomenon actually indicates that the algorithm is unstable for large deformations (which has already been observed in Example 3.2.1.1). These oscillations appearing on the free boundary during iterations can actually be avoided by taking smaller values for the step size; that is, by reducing the magnitude of α , in expense, of course, of processing additional number of iterations to attain good enough approximation of the optimal free boundary. In relation to this, the evolution of the free boundary using the classical approach under the same setup, but now with $\alpha = 0.01$, is shown in Figure 3.7c. Observe that, with the new value of α , we now have a smooth evolution of the free boundary (but smaller gaps between each consecutive shape deformations). Meanwhile, a direct comparison of the computed optimal free boundary Σ_M obtained from the two formulations (with $\alpha = 0.10$) are shown in Figure 3.7d. For the proposed formulation, the final cost value is $J_1(\Sigma_{23}) = 2.99 \times 10^{-8}$ and for the Neumann-data tracking approach, we obtain the value $J_N(\Sigma_{80}) = 4.10$ at the final iteration. We mention here that we have not actually satisfied the stopping condition (3.6) with $\text{Tol} = 10^{-3}$ when using the Neumann-data tracking approach, after running the algorithm for 120 seconds. Nevertheless, we are able to satisfy (3.6) for $\text{Tol} = 10^{-2}$ after $K = 42$ iterations (which was completed after 47.93 seconds of run time) with cost value $J_N(\Sigma_{42}) = 5.06$. Taking $\text{Tol} = 10^{-2}$ as the tolerance value when imposing the stopping rule (3.6), however, seems reasonable since the cost actually decreases very slow after reaching 39 iterations, as evident in Figure 3.8.

Remark 3.2.1. We remark here that we actually took slightly larger edge size for the mesh (in fact, we set $h_{\max} = 0.03$) during mesh adaptation in performing the optimization process with the Neumann-data tracking approach. The main reason for this different setup is that it is actually difficult to obtain stable approximation of the optimal free boundary when using the said approach with finer mesh during mesh adaptation. In fact, the algorithm crashes after a certain number of iterations when a smaller value for h_{\max} is used during mesh adaptation.

Below we provide a few more examples illustrating further the robustness of the proposed formulation in solving the exterior Bernoulli free boundary problem.

Figure 3.5: The optimal free (or exterior) boundaries Σ^* using the proposed formulation

λ	$J(\Sigma_K)$	K	CPU time	M
-1	3.68×10^{-5}	6	11.98 sec	18
-2	7.84×10^{-6}	13	22.21 sec	17
-3	5.37×10^{-5}	10	16.55 sec	16
-4	6.27×10^{-6}	14	27.72 sec	16
-5	1.51×10^{-5}	16	25.56 sec	20
-6	4.59×10^{-7}	15	31.99 sec	17
-7	9.52×10^{-6}	21	40.14 sec	24
-8	2.03×10^{-6}	17	41.61 sec	24
-9	1.94×10^{-6}	22	42.09 sec	24
-10	1.22×10^{-7}	21	55.82 sec	23

Table 3.4: Summary of computational results corresponding to the optimal free boundaries shown in Figure 3.5

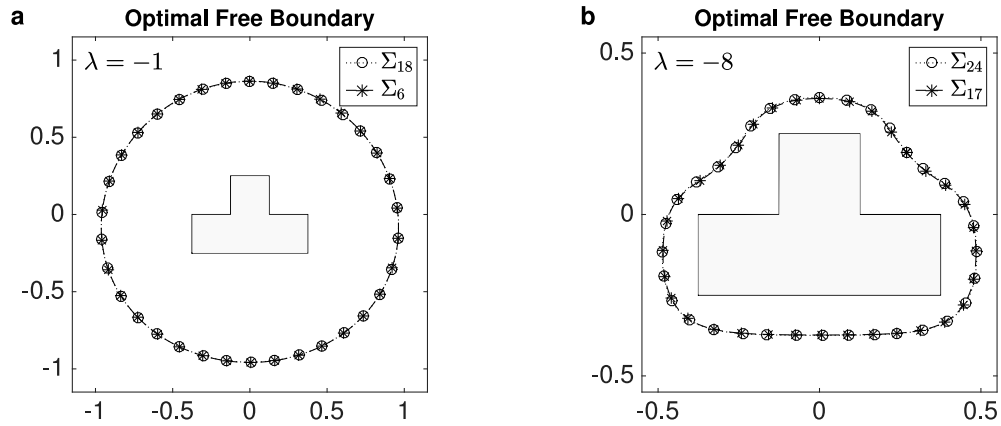


Figure 3.6: Optimal free (or exterior) boundaries obtained through the proposed formulation for Example 3.2.1.2 (the case where $\Gamma = \partial S$) when $\lambda = -1$ (plot **a**) and when $\lambda = -8$ (plot **b**)

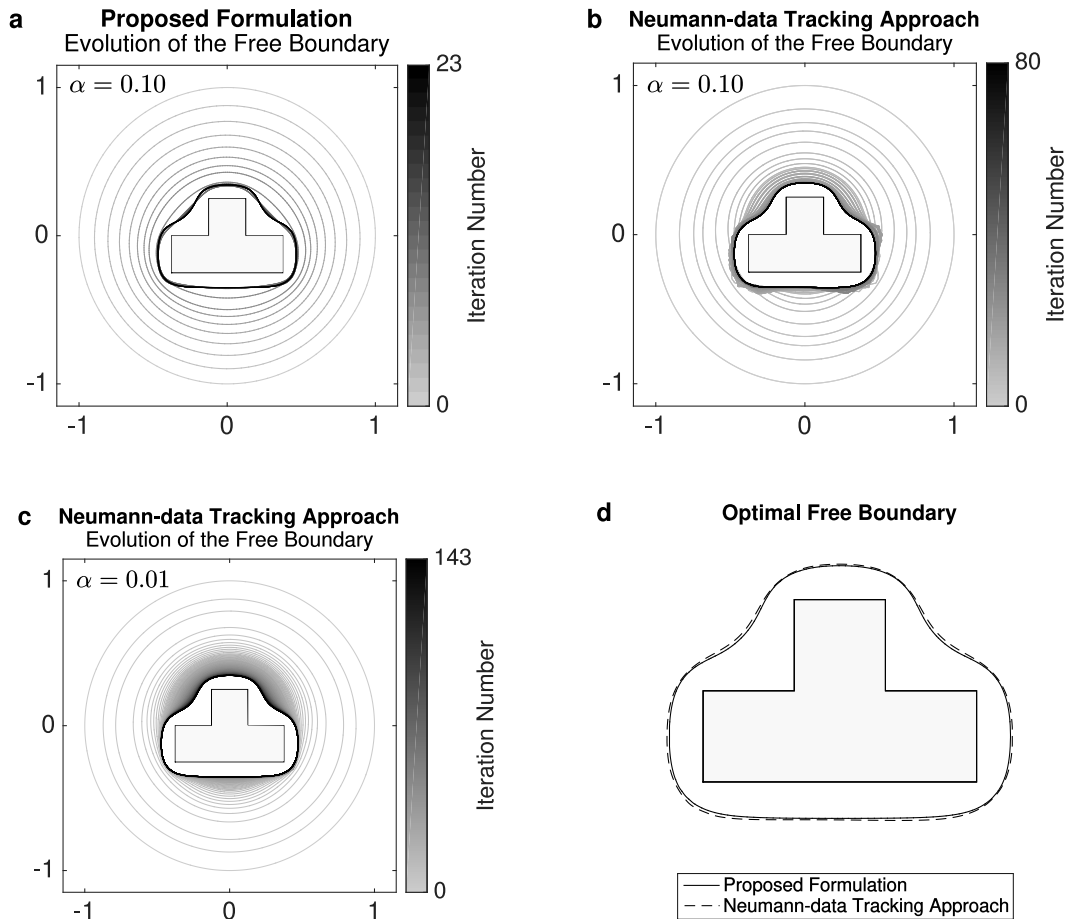


Figure 3.7: Evolutions of the free boundary for the case $\lambda = -10$ when the proposed formulation is employed with $\alpha = 0.10$ (plot **a**) and when the Neumann-data tracking approach is applied with $\alpha = 0.10, 0.01$ (plots **b**, and **c**, respectively); **d**: direct comparison between the optimal free boundaries obtained through the proposed and the classical Neumann-data tracking approach when $\alpha = 0.10$

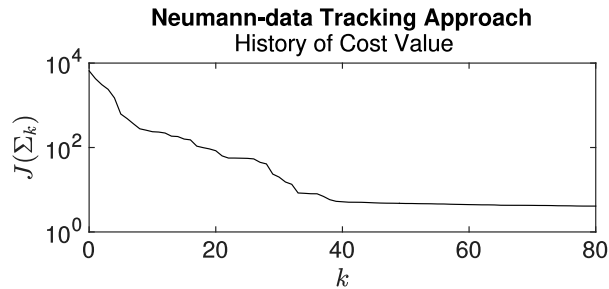


Figure 3.8: Convergence history of the cost function for Example 3.2.1.2 when $\lambda = -10$, applying the Neumann-data tracking approach with $\alpha = 0.10$

3.2.1.3 Example 3: An L-shaped fixed (interior) boundary

In this test case, we consider the boundary $\Gamma = \partial S$ of the L-shaped domain

$$S = (-0.25, 0.25)^2 \setminus [0, 0.25]^2$$

and let $\lambda = -10$. For the initial guess, we select the circle $C(\mathbf{0}, 0.6)$ and take $\alpha = 0.10$ for both approaches. Also, we run the algorithm for 300 seconds and we let $h_{\max} = 0.025$ when using the proposed formulation and take $h_{\max} = 0.03$ when applying the Neumann-data tracking approach. In case of using the proposed formulation, the algorithm completed 16 iterations (which was reached after 23.49 seconds of run time) with the final cost value $J_1(\Sigma_{16}) = 4.68 \times 10^{-11}$. The stopping rule (3.6) with $\text{Tol} = 10^{-5}$ is satisfied after 15 iterations which was completed after 19.77 seconds and the computed cost is $J_1(\Sigma_{15}) = 2.17 \times 10^{-7}$. The evolution of the free boundary obtained through the proposed formulation is shown in Figure 3.9a. On the other hand, when the Neumann-data tracking approach is applied, the optimization procedure completely processed 158 iterations with the final cost value $J_N(\Sigma_{158}) = 0.88$. Again, during the iteration process, we notice several oscillations on the free boundary, and these oscillations are noticeable from the evolution of the free boundary obtained through Neumann-data tracking approach depicted in Figure 3.10b. A direct comparison of the optimal free boundaries Σ_{16} and Σ_{158} obtained through the proposed formulation and from the classical Neumann-data tracking approach, respectively, are shown in Figure 3.10c. Observe that the two computed optimal free boundaries are almost indistinguishable from each other. However, it seems that Σ_{158} is slightly larger compared to Σ_{16} . The Hausdorff distance between the two is computed to be of order 10^{-2} . Meanwhile, for the classical approach, the stopping rule (3.6) with $\text{Tol} = 10^{-2}$ (respectively, 10^{-3}) is met after 49 (respectively, 139) iterations which was attained after 48.77 seconds (respectively, 244.66 seconds) of run time. Similar to the case of the previous example, setting the tolerance value in (3.6) to $\text{Tol} = 10^{-2}$ seems reasonable if the stopping rule is applied because the cost actually decreases slowly after reaching 49 iterations (see upper plot in Figure 3.9d). This observation is also apparent from the history of Hausdorff distances between the k th and the 139th approximations of the optimal free boundary depicted in the lower plot in Figure 3.9d.

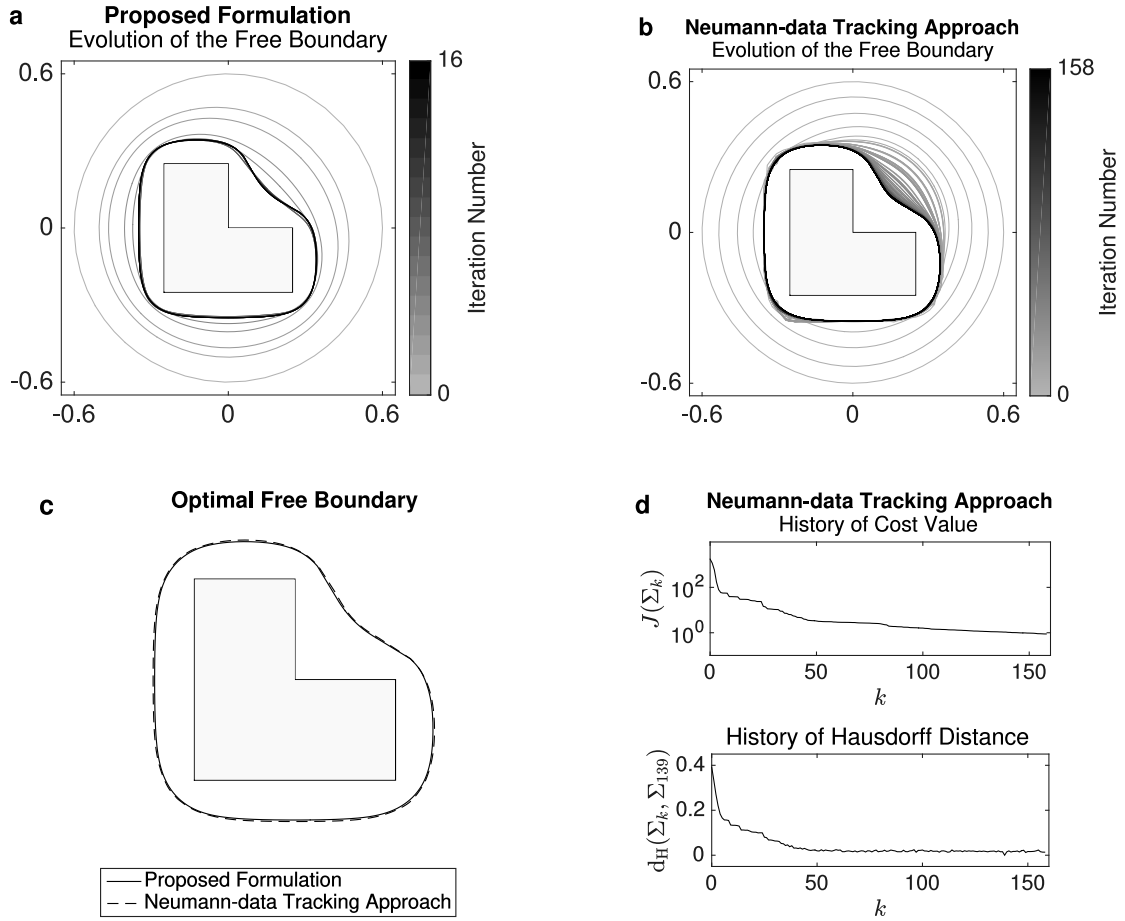


Figure 3.9: Evolutions of the free boundary for Example 3.2.1.3 when the proposed formulation is employed (plot **a**) and when the Neumann-data tracking approach is applied (plot **b**) where $\alpha = 0.10$ in both cases; **c**: direct comparison between the optimal free boundaries obtained through the proposed and the classical Neumann-data tracking approach when $\alpha = 0.10$; **d**: histories of cost values (*upper plot*) and Hausdorff distances (*lower plot*) obtained through the Neumann-data tracking approach corresponding to plot **b**

3.2.1.4 Example 4: A fixed boundary with two disjoint components

For the last example under the exterior case, we take $\lambda = -1.5$ and define the fixed boundary as the union of two disjoint kite-shaped figures given by the following parametrization

$$\begin{aligned}\Gamma_1 &= \{(1 + 0.7 \cos \theta - 0.4 \cos 2\theta, \sin \theta)^\top, 0 \leq \theta \leq 2\pi\}, \\ \Gamma_2 &= \{-2 + \cos \theta + 0.4 \cos 2\theta, 0.5 + 0.7 \sin \theta)^\top, 0 \leq \theta \leq 2\pi\}.\end{aligned}$$

For the initial guess, we choose the circle $C(\mathbf{0}, 5)$. In this case, the solution is known to be connected, hence the present scheme is suitable for numerically solving the problem (cf. [83]). Here, in all situations, the algorithm is ran for 600 seconds. Also, we use finer mesh during mesh adaptation when employing the proposed formulation than when applying the Neumann-data tracking approach. In particular, we use $h_{\max} = 0.05$ for the former approach and set $h_{\max} = 0.10$ for the latter method. We

choose coarser mesh when using the Neumann-data tracking approach for the same reason stated in Remark 3.2.1.

The evolution of the free boundary obtained through the application of the proposed formulation is depicted in Figure 3.10 when $\alpha = 0.10, 0.25$ and 0.50 (see plots a, b and c, respectively). Clearly, as α increases in magnitude, the convergence speed also increases (of course, this is only true up to some value of α as in the results shown in Table 3.3). In the same figure, particularly, in plots b, d and f, the evolution of the free boundary obtained using the Neumann-data tracking approach when $\alpha = 0.001, 0.010, 0.100$ are shown. Notice that, even at small step sizes, the free boundary is prone to oscillations as evident (although not too visible) in Figure 3.10b. Also, it is apparent from Figures 3.10d and f that increasing α , in case of using the Neumann-data tracking approach, only worsen the oscillations appearing on the free boundary during the optimization process. The numerical results of the present computational experiments are summarized in Table 3.5. The table shows, in particular, the computed cost value $J_i(\Sigma_K)$, $i \in \{1, N\}$, at the optimal termination number K when the stopping condition (3.6) is utilized with tolerance value $\text{Tol} = 10^{-5}$ for the proposed formulation and $\text{Tol} = 10^{-2}$ for the Neumann-data tracking approach (the reason behind these choices of Tol values will be issued later). Also, listed in the table are the corresponding final cost values $J_i(\Sigma_M)$ for each of the methods applied (and for each values of α used in the experiment). Surprisingly, the computing time to reach convergence (imposing the stopping rule (3.6)) when using the proposed formulation with $\alpha = 0.25$ is almost the same with the case when α is set to 0.50 . Meanwhile, the corresponding histories of cost values of the free boundaries shown in Figure 3.10 are plotted in Figure 3.11a. Observe that, in case of the Neumann-data tracking approach, the values 0.01 and 0.10 for α exhibits comparable convergence speed. Based on this, it seems that the rate of convergence of the optimization process when applying the Neumann-data tracking approach could not be further improved even when α is increased in magnitude. On the other hand, Figures 3.11b and c respectively plots the histories of Hausdorff distances between Σ_k and the final computed free boundary Σ_M obtained through the proposed formulation, for each $\alpha = 0.10, 0.25, 0.50$, and via the Neumann-data tracking approach, for each $\alpha = 0.001, 0.010, 0.100$. In these plots, the abbreviation ‘H.D.’ appearing on the vertical axes means the term ‘Hausdorff Distance’. In all situations, including the cross comparisons between the final optimal free boundaries obtained from using each of the values of α and the comparisons between the results obtained from each methods, the computed Hausdorff distances are all of order 10^{-2} (or lower). We emphasize that the said order of magnitude of the computed Hausdorff distances is reasonable since we used coarser mesh during the optimization process. Furthermore, the graphs depicted in Figures 3.11b and c show that the stopping rule (3.6) can indeed be effectively used to terminate the iteration process by taking the tolerance value $\text{Tol} = 10^{-5}$ when using the proposed formulation and setting it to $\text{Tol} = 10^{-2}$ when the Neumann-data tracking approach is being applied. Finally, a direct comparison between the computed optimal free boundaries Σ_{32} and Σ_{114} obtained through the proposed formulation (with $\alpha = 0.50$) and the classical Neumann-data tracking approach (with $\alpha = 0.10$), respectively, are shown in Figure 3.11d. As in Example 3.2.1.2, it seems that the optimal

free boundary due to the Neumann-data tracking approach is slightly larger compared to the one obtained through the proposed formulation.

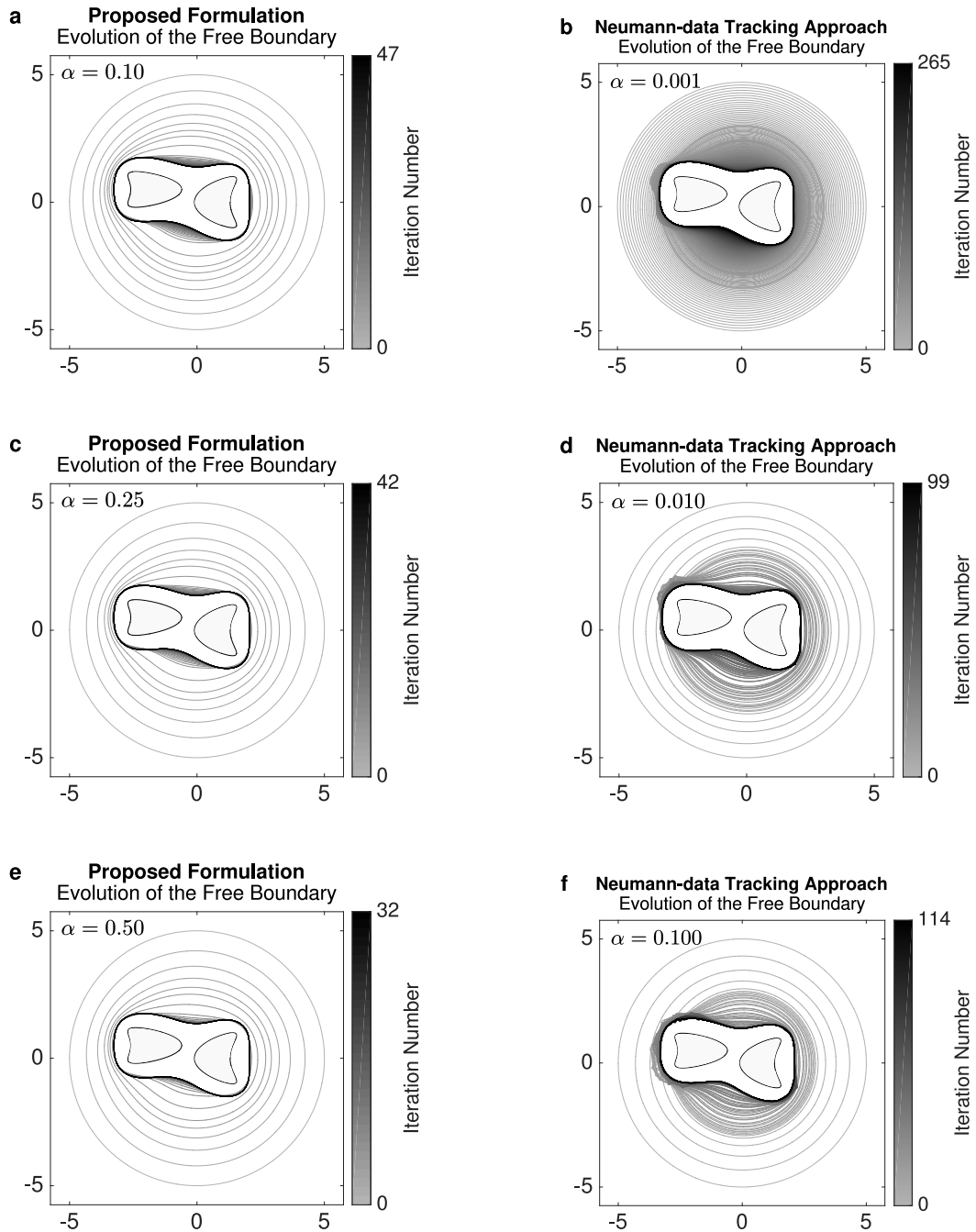


Figure 3.10: Evolutions of the free boundary corresponding to Example 3.2.1.4 when the proposed formulation is employed with $\alpha = 0.10, 0.25, 0.50$ (plots **a**, **c**, and **e**, respectively) and when the Neumann-data tracking approach is applied with $\alpha = 0.001, 0.010, 0.100$ (plots **b**, **d**, and **f**, respectively)

Interior case

We now provide some numerical examples for the interior case. This time we take $\mathcal{X} = L^2(\Omega_k)$ and

α	$J(\Sigma_K)$	K	CPU time	$J(\Sigma_M)$	M
Proposed formulation; Tol = 10^{-5}					
0.10	0.000762	38	146.68 sec	0.000473	47
0.25	0.000164	27	55.30 sec	1.26×10^{-6}	42
0.50	2.20×10^{-5}	22	55.28 sec	1.30×10^{-8}	32
Neumann-data tracking approach; Tol = 10^{-2}					
0.001	9.25	210	363.67 sec	5.73	265
0.010	8.02	71	86.95 sec	7.43	99
0.100	5.69	68	187.94 sec	4.60	114

Table 3.5: Summary of computational results corresponding to Example 3.2.1.4

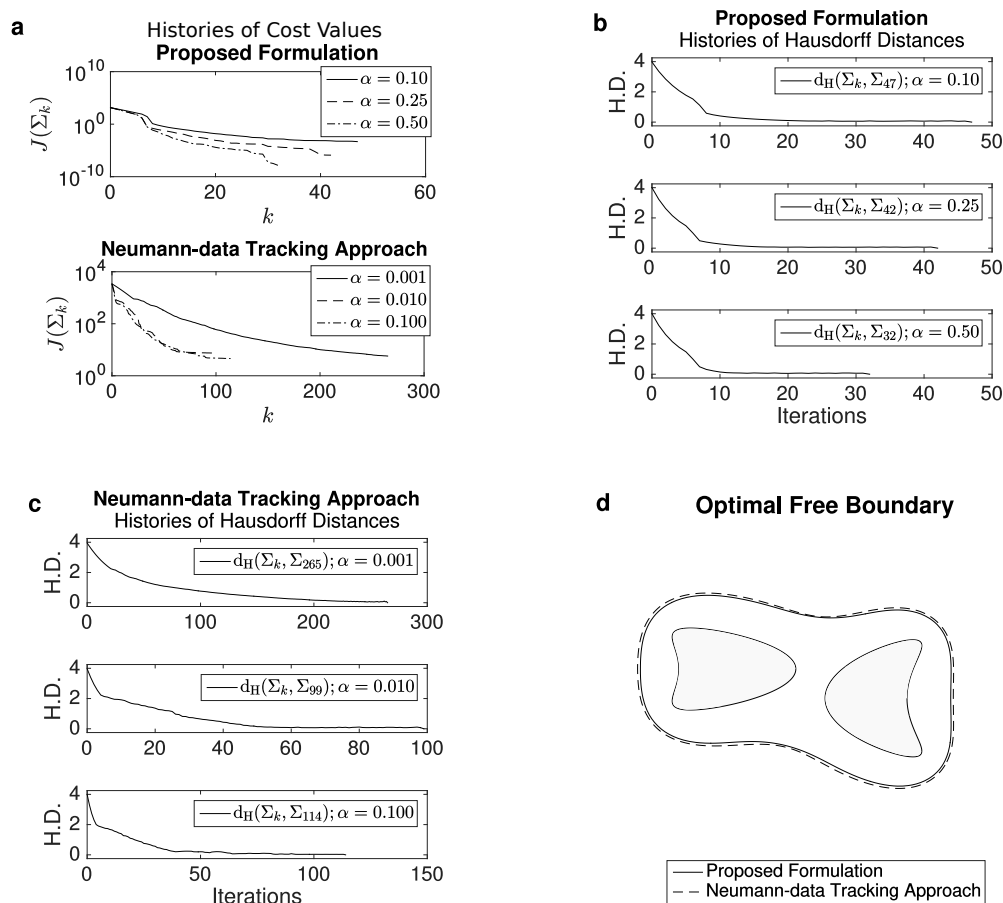


Figure 3.11: **a:** Convergence histories of the cost function for both the proposed and classical formulations with different values of α ; the histories of Hausdorff distances between Σ_k and the final computed free boundary Σ_M obtained through the proposed formulation, for each $\alpha = 0.10, 0.25, 0.50$ (plot **b**), and via the Neumann-data tracking approach, for each $\alpha = 0.001, 0.010, 0.100$ (plot **c**); **d:** direct comparison between the optimal free boundaries obtained through the proposed and the classical Neumann-data tracking approach

let $\alpha = 0.99$, for simplicity, in the step size formula (3.3) for both the proposed and the classical Neumann-data tracking approach. Also, we run the algorithm for 60 and 600 seconds in the first (Example 3.2.1.5) and second test case (Example 3.2.1.6), respectively.

3.2.1.5 Example 5: Accuracy Tests

For the first test case, we again check the accuracy of the computed gradient. To this end, we consider the interior Bernoulli problem with

$$\Gamma = C(\mathbf{0}, R), \quad \lambda = \frac{1}{r(\log R - \log r)}, \quad R/e < r < R.$$

For this case, the interior Bernoulli problem admits two possible solutions; namely, the *elliptic* solution which is the circle $C(\mathbf{0}, r)$, and the *hyperbolic* solution given by the circle $C(\mathbf{0}, r_h)$, where r_h is the unique real number such that

$$0 < r_h < R/e, \quad \frac{1}{r_h(\log R - \log r_h)} = \lambda.$$

Convergence to the elliptic or hyperbolic solution depends on the initial guess. In our test, we are interested only in the elliptic solution. We take $R = 0.9$ and $r = 0.5$, so $\lambda = 3.4026$ (and again, obviously, $\Sigma^* = C(\mathbf{0}, 0.5)$). We choose $C(\mathbf{0}, 0.6)$ as the initial guess. The histories of the mean radii and Hausdorff distances obtained through the application of the proposed formulation are plotted in Figures 3.12a and b, respectively, for some mesh sizes h_{\max} used during mesh adaptation. Observe from the said plots that the rate of convergence of the mean radii and of the Hausdorff distances slows down after four iterations. If we imposed the stopping condition (3.6), with $\text{Tol} = 10^{-4}$, the algorithm actually terminates after six iterations, irrespective of the magnitude of maximum edge size of the mesh h_{\max} used during mesh adaptation. Table 3.6 summarizes the results toward the elliptic solution when the stopping rule (3.6) with $\text{Tol} = 10^{-4}$ is utilized to terminate the algorithm. It is clear from the table that the accuracy of the computed optimal free boundary is improved as the magnitude of h_{\max} is reduced. Also, based on the computed value for the standard deviation σ_K^{rad} shown in the said table, we can actually say that the proposed method produces a very stable approximation of the optimal solution, in a sense that every domain Ω_k , $k = 1, 2, \dots, M$, has an exterior boundary Σ_k with no rapid oscillation. We have also ran the algorithm using the Neumann-data tracking approach. However, the algorithm was only able to process one complete iteration (regardless of the magnitude of h_{\max}) and the computed free boundary has mean radius $\bar{R}_1 = 0.5127$, Hausdorff distance of $d_H(\Sigma_1, \Sigma^*) = 0.0207$ from the exact optimal shape Σ^* and final cost value $J_N(\Sigma_1) = 0.0046$ when h_{\max} is set to $1/160$. It seems that the formula (3.3) produces a very small magnitude for t_1 which is already of order 10^{-3} , and apparently, this step size is not large enough to produce a variation of the current domain Ω_1 that would decrease the magnitude of the cost at the next iteration. In addition, we mention that the computed shape at the first iterate actually has some irregularities appearing on its exterior boundary. In fact, the computed standard deviation σ_1^{rad} is equal to 0.0029 which is one order higher compare to the order of magnitude of σ_K^{rad} 's listed in Table 3.6.

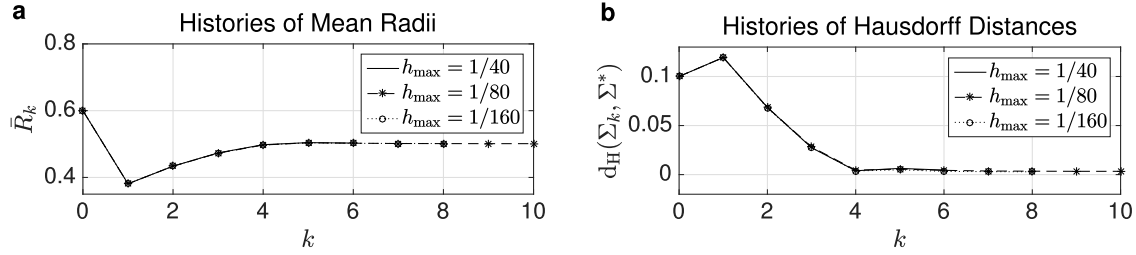


Figure 3.12: Histories of mean radii (plot **a**) and Hausdorff distances (plot **b**) obtained through the application of the proposed formulation after running the algorithm for 60 seconds

h_{\max}	$d_H(\Sigma_K, \Sigma^*)$	\bar{R}_K	σ_K^{rad}	$J(\Sigma_K)$	K	time	\bar{t}	σ^{step}	C.V.
1/40	0.004602	0.502944	0.000292	7.27×10^{-6}	6	12.83 s	0.6327	0.3545	< 1
1/80	0.004341	0.501177	0.000205	7.46×10^{-6}	6	17.63 s	0.5907	0.2780	< 1
1/160	0.003328	0.501606	0.000193	1.91×10^{-6}	6	17.37 s	0.6119	0.3010	< 1

Table 3.6: Summary of computational results corresponding to Example 3.2.1.5 using the proposed formulation terminated with the stopping rule (3.6) with $\text{Tol} = 10^{-4}$

3.2.1.6 Example 6: An L-shaped fixed (exterior) boundary

For the second test case, we consider the boundary $\Gamma = \partial S$ of the L-shaped domain

$$S = (-0.5, 0.5)^2 \setminus [0.1, 0.5]^2$$

and take $\lambda = 14$. We choose $C((-0.15, -0.15), 0.25)$ as the initial guess. The result of the computational experiments are summarized in Table 3.7. Clearly, based from the table, the proposed formulation converges significantly faster to the optimal solution than the classical Neumann-data tracking approach. The evolution of the free boundary using the proposed and the classical Neumann-data tracking approach are respectively depicted in Figures 3.13a and b (where the shaded region represents the final computed domain Ω_M). Observe from the latter figure that there are some irregularities appearing on the shape of the free boundary at several iterations. Meanwhile, a direct comparison between the free boundaries Σ_{17} and Σ_{104} , respectively obtained through the proposed formulation and the Neumann-data tracking approach, are shown in Figure 3.13c. These shapes have the corresponding cost values $J_1(\Sigma_{17}) = 1.55 \times 10^{-7}$ and $J_N(\Sigma_{104}) = 0.33$. Also, the computed Hausdorff distance between Σ_{17} and Σ_{104} are found to be equal to 0.02. Lastly, in Figure 3.13d, we plot the histories of cost values and Hausdorff distances $d_H(\Sigma_k, \Sigma_{104})$ obtained through the Neumann-data tracking approach. Notice that the value of $d_H(\Sigma_k, \Sigma_{104})$ fluctuates at a certain number after 44 iterations. So, based from Table 3.7, we can actually terminate the algorithm using (3.6) with $\text{Tol} = 10^{-2}$. On the other hand, the value $\text{Tol} = 10^{-5}$ seems a reasonable choice for the tolerance value when imposing the stopping rule (3.6).

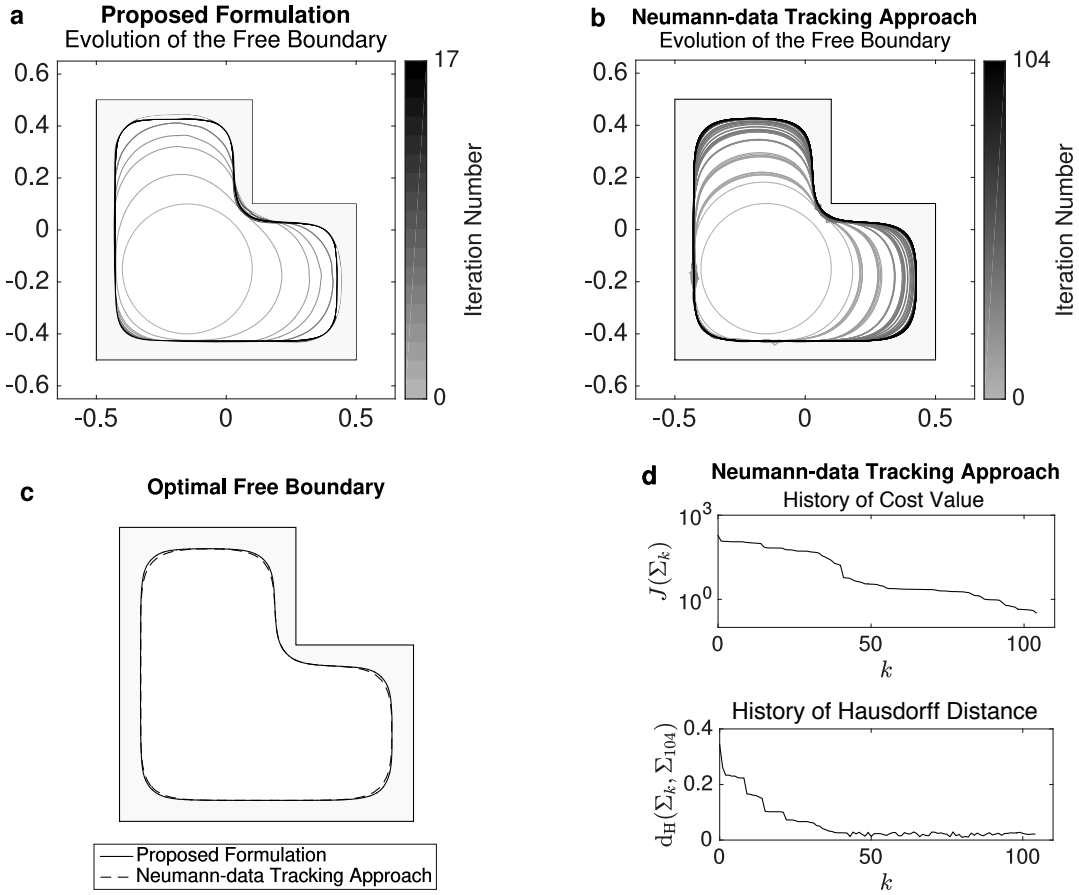


Figure 3.13: Evolutions of the free boundary for Example 3.2.1.6 when the proposed formulation is employed (plot **a**) and when the Neumann-data tracking approach is applied (plot **b**); **c**: direct comparison between the optimal free boundaries obtained through the proposed and the classical Neumann-data tracking approach; **d**: convergence history of the function (*upper plot*) and history of Hausdorff distances (*lower plot*) obtained through the Neumann-data tracking approach corresponding to plot **b**

Tol	$J(\Sigma_K)$	K	$d_H(\Sigma_K, \Sigma_M)$	CPU time
Proposed formulation				
10^{-3}	0.037359	7	0.017952	35.73 sec
10^{-4}	7.83×10^{-5}	11	0.004287	71.17 sec
10^{-5}	7.12×10^{-5}	12	0.004174	73.77 sec
Neumann-data tracking approach				
10^{-1}	112.97	7	0.223435	37.38 sec
10^{-2}	2.41	57	0.019425	194.46 sec
10^{-3}	2.23	70	0.025111	430.145 sec

Table 3.7: Summary of computational results corresponding to Example 3.2.1.6

3.2.2 Examples for the Second Proposed Shape Problem

This subsection is devoted to the numerical investigation of the second proposed shape problem (1.17) and its comparison with the classical Kohn-Vogelius cost functional minimization approach (1.10).

3.2.2.1 Example 1: Accuracy of the computed gradient

We begin by testing the accuracy of the computed gradient. To do this, we consider the exterior Bernoulli problem with

$$\Gamma = C(\mathbf{0}, r), \quad \lambda = \frac{1}{R(\log r - \log R)}, \quad 0 < r < R,$$

where $C(\mathbf{0}, r)$ is the circle centered at the origin with radius r . The only solution, in this case, is of course the circle $C(\mathbf{0}, R)$.

We let $r = 0.3$ and $R = 0.5$. These give us $\lambda = -3.9152$. We consider three different initial guesses defined as follows (see Figure 3.14a for illustration):

$$\text{Test 1: } \Sigma_0^1 = C(\mathbf{0}, 0.6);$$

$$\text{Test 2: } \Sigma_0^2 = C(\mathbf{0}, 0.4);$$

$$\text{Test 3: } \Sigma_0^3 = \{(0.01 + 0.6 \cos \theta, 0.01 + 0.4 \sin \theta)^\top, 0 \leq \theta \leq 2\pi\}.$$

In all cases, we take $h_{\max} = 0.01$ and set $\text{Tol} = 10^{-6}$, i.e., we stop the algorithm as soon as the inequality condition $|J(\Omega_{k+1}) - J(\Omega_k)| < 10^{-6}$ holds true. The results of the accuracy tests with parameter values $\alpha = 0.10, 0.50, 0.99$ are summarized in Table 3.8.

Σ_0^i	α	cost	$d_H(\Sigma^*, \Sigma_f^i)$	\bar{R}	$ R - \bar{R} /R$	iter.	cpu time
Σ_0^1	0.10	2.85×10^{-5}	0.005072	0.500888	0.001776	72	115 sec
	0.50	2.32×10^{-7}	0.004983	0.500002	0.000004	17	26 sec
	0.99	8.55×10^{-8}	0.004984	0.499865	0.000270	8	12 sec
Σ_0^2	0.10	1.77×10^{-5}	0.005044	0.499343	0.001314	70	103 sec
	0.50	9.26×10^{-7}	0.005003	0.499878	0.000244	16	28 sec
	0.99	3.91×10^{-9}	0.004998	0.499956	0.000088	7	14 sec
Σ_0^3	0.10	1.65×10^{-5}	0.005887	0.500051	0.000102	76	122 sec
	0.50	6.64×10^{-7}	0.004991	0.500002	0.000004	19	29 sec
	0.99	8.77×10^{-7}	0.005001	0.499993	0.000014	9	13 sec

Table 3.8: Convergence test toward exact solution using the proposed formulation via the modified H^1 -gradient method with initial free boundaries Σ_0^i , $i = 1, 2, 3$, and $\alpha = 0.10, 0.50, 0.99$ in (3.3)

The table shows, in particular, the final values of the cost, the Hausdorff distances between the computed optimal shape and the exact shape, the average distances \bar{R} of points on the computed

free boundaries to the origin, the relative errors between \bar{R} and the exact radius of the free boundary R , the number of iterations until termination of the algorithm and over-all computing times. Clearly, as α increases in value, the number of iterations, as well as the computing time, decreases. Moreover, except for the case when the initial guess is Σ_0^3 and $\alpha = 0.1$, the Hausdorff distance between the exact optimal shape $\Sigma^* = C(\mathbf{0}, 0.5)$ and each of the computed optimal (final) shape Σ_f^i , $i = 1, 2, 3$, is (approx.) equal to 0.005. Meanwhile, we notice large number of iterations required to reach convergence when α is set to 0.1. These values can obviously be reduced by applying a second-order method. Indeed, by employing the modified H^1 -Newton method presented in subsection 3.1.5, we obtain a significant reduction in the number of iterations needed to reach convergence as evident in Table 3.9.

α	Σ_0^i	cost	$d_H(\Sigma^*, \Sigma_f^i)$	\bar{R}	$ R - \bar{R} /R$	iter.	cpu time
0.1	Σ_0^1	6.17×10^{-7}	0.005007	0.500139	0.000278	7	25 sec
	Σ_0^2	1.57×10^{-8}	0.005003	0.500013	0.000026	8	41 sec
	Σ_0^3	4.47×10^{-6}	0.005130	0.500101	0.000202	14	35 sec

Table 3.9: Convergence test toward exact solution using the proposed formulation via the modified H^1 -Newton method with $\alpha = 0.1$ and different initial free boundary Σ_0^i , $i = 1, 2, 3$

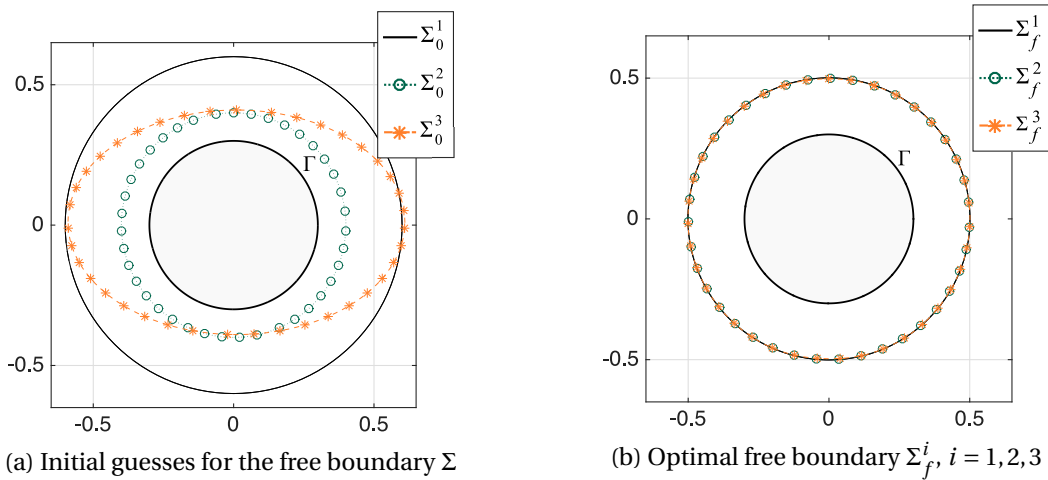


Figure 3.14: Initial (*left*) and final (*right*) free boundaries for Example 3.2.2.1 with $\alpha = 0.1$ in (3.3)

The computed optimal free boundaries when $\alpha = 0.1$, as well as the fixed boundary Γ , are depicted in Figure 3.14b. The histories of cost values and Hausdorff distances obtained through the first- and second-order method with $\alpha = 0.1$ and initial profiles Σ_0^i , $i = 1, 2, 3$, for the free boundary Σ are depicted in the plots shown in Figure 3.15. Looking at Figure 3.15a and Figure 3.15c, we observe that the first and second tests, where we respectively took Σ_0^1 and Σ_0^2 as initial guesses, have almost the same rate of convergence and are both faster compared to when taking Σ_0^3 as the initial profile for the free boundary Σ . However, in terms of convergence to the exact solution (measuring the Hausdorff distance between the k th approximation Σ_k of the free boundary and its exact profile $\Sigma^* = C(\mathbf{0}, 0.5)$), the choice Σ_0^2 gives the fastest rate of convergence among the three choices for Σ_0 (with the third

choice Σ_0^3 as the initial guess for the free boundary giving the slowest convergence rate to the exact solution) in case of using the first-order method is applied (see Figure 3.15b). On the other hand, it appears that the first and second test cases have almost the same convergence rate when using the second-order method (refer to Figure 3.15d). In testing the accuracy of the computed gradient, we

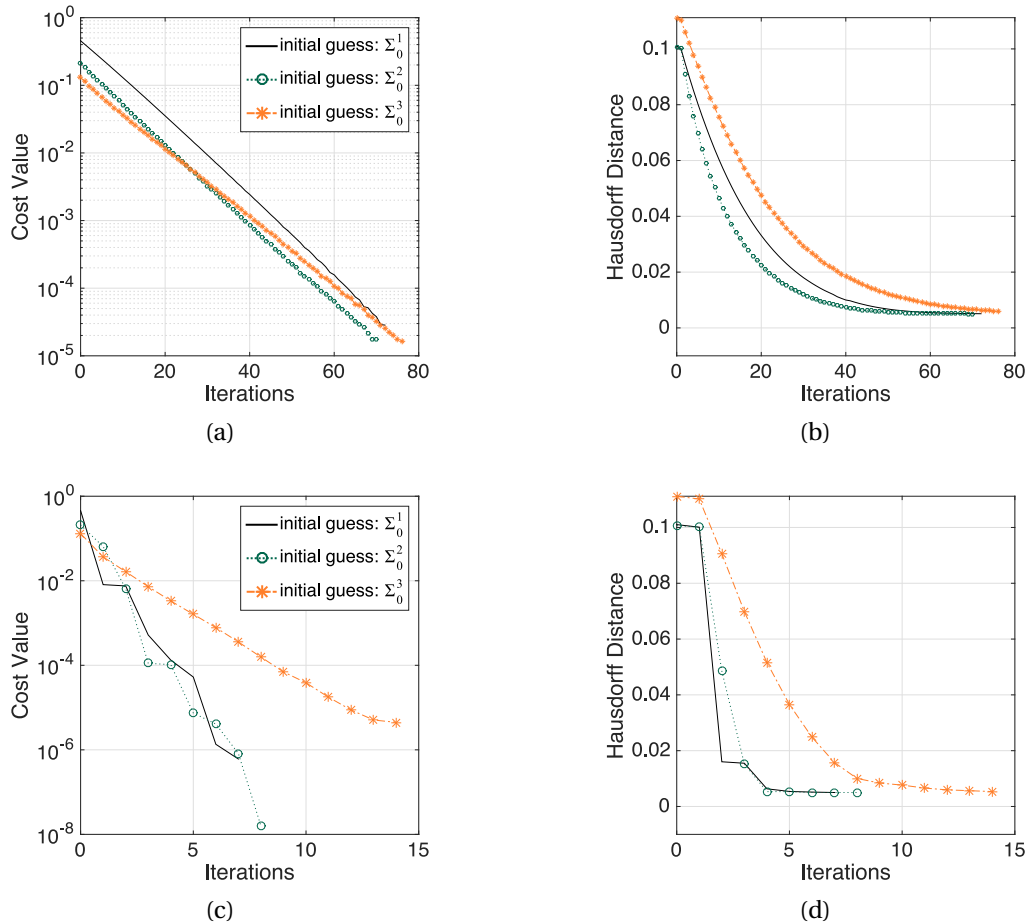


Figure 3.15: (a)-(b): Respective histories of cost values and Hausdorff distances via first-order method with $\alpha = 0.1$ in (3.3) and varying initial free boundary Σ_0^i , $i = 1, 2, 3$; (c)-(d): respective histories of cost values and Hausdorff distances via second-order method with $\alpha = 0.1$ in (3.3) and different initial free boundary Σ_0^i , $i = 1, 2, 3$

also considered coarser mesh in solving the PDE systems involved in the formulations. It seems that using coarser mesh requires less computing time to complete the optimization process (as expected). However, we obtained a more accurate final free boundary in all test cases when using finer mesh during the discretization process (also as expected).

3.2.2.2 Example 2: An L-shaped fixed domain

Next, we again consider the boundary $\Gamma = \partial S$ of the L-shaped domain $S = (-0.25, 0.25)^2 \setminus [0, 0.25]^2$ and compute the optimal shape for all integers $\lambda = -10, -9, \dots, -1$. In all situations, we take $\alpha = 0.99$

and choose $C(\mathbf{0}, 0.6)$ as the initial shape of the free boundary Σ . We compare our results with the ones obtained using the classical Kohn-Vogelius formulation (1.10). As in the previous example, we also set $\text{Tol} = 10^{-6}$ in the stopping condition (3.6) and set $h_{\max} = 0.01$. Table 3.10 summarizes the

λ	formulation	t_0	cost	iter.	cpu time
-10	proposed	0.228150	1.37×10^{-6}	14	14 sec
	classical	0.767890	0.000137	19	55 sec
-9	proposed	0.221636	6.25×10^{-7}	13	16 sec
	classical	0.738627	3.11×10^{-5}	25	96 sec
-8	proposed	0.213501	7.94×10^{-7}	12	14 sec
	classical	0.702851	7.17×10^{-5}	19	57 sec
-7	proposed	0.203058	1.23×10^{-6}	10	13 sec
	classical	0.658125	0.000628	12	34 sec
-6	proposed	0.189163	8.27×10^{-7}	10	14 sec
	classical	0.600640	0.000190	13	34 sec
-5	proposed	0.169783	2.61×10^{-7}	10	16 sec
	classical	0.524113	0.000948	18	54 sec
-4	proposed	0.140942	2.04×10^{-7}	10	17 sec
	classical	0.417590	0.000186	8	24 sec
-3	proposed	0.094111	5.68×10^{-7}	9	14 sec
	classical	0.262124	4.95×10^{-5}	11	29 sec
-2	proposed	0.039805	2.37×10^{-7}	10	17 sec
	classical	0.120956	6.48×10^{-6}	10	27 sec
-1	proposed	0.312388	1.08×10^{-6}	13	25 sec
	classical	0.615256	5.69×10^{-7}	9	24 sec

Table 3.10: Summary of computational results for an L-shaped fixed boundary $\Gamma = \partial S$ with $\lambda = -10, -9, \dots, -1$ where $\alpha = 0.99$ in (3.3) and $\text{Tol} = 10^{-6}$ in the stopping condition (3.6)

computational results for the present test cases obtained through the proposed shape optimization formulation (1.18) versus the classical Kohn-Vogelius formulation (1.10). The table shows, in particular, the initial step sizes, the final cost values, the number of iterations until termination of the algorithm and over-all computing times for each of the two formulations. Notice that when $\lambda = -9$, the computing time for the classical formulation is too large compared to other cases. Also, we observe that only in cases when $\lambda = -4, -1$ that the number of iterations of the proposed formulation is higher compared to the classical formulation. The resulting exterior boundaries are shown in Figure 3.16 (*forest-green-colored lines*) where the outermost boundary corresponds to $\lambda = -1$ and the innermost boundary to $\lambda = -10$. The fixed boundary Γ and the initial shape of the free boundary Σ are also depicted in the figure, and are respectively colored with *black* and *orange* colors.

We compared the computed optimal free boundaries from the two formulations and we noticed that, in all cases being considered, the results are indistinguishable from each other (see, e.g., Figure 3.17a for $\lambda = -9$). Also, we observed that the histories of cost values (as well as the L^2 -norms of the

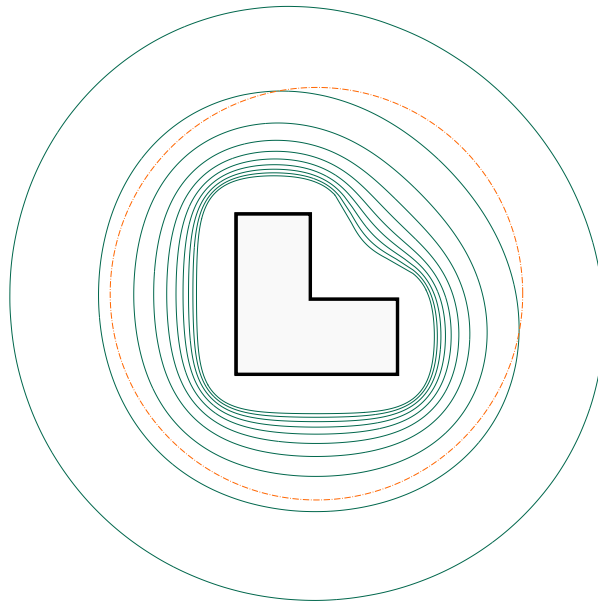


Figure 3.16: *Forest-green solid lines*: Optimal free boundaries for Example 3.2.2.2 when $\lambda = -10, -9, \dots, -1$ (the outermost boundary corresponds to $\lambda = -1$ and the innermost boundary to $\lambda = -10$); *dashed-dot orange line*: initial guess for the free boundary

descent direction V , and hence the descent step sizes) from the proposed formulation exhibit an almost uniform convergence rate, while the classical formulation do not (see, e.g., Figures 3.17b–3.17d for the case $\lambda = -9$). We believe that this is due to large deformations of the domain caused by large values of descent step sizes (and therefore has to be reduced) during the optimization process. In addition to these observations, we also mention the following important remarks regarding the computational results summarized in Table 3.10. Firstly, for $\alpha = 0.99$ and $\text{Tol} = 10^{-6}$ in (3.6), it seems that the proposed formulation requires less computing time to complete the optimization process than the classical formulation. Secondly, it appears that, for all values of $\lambda \in \{-10, -9, \dots, -1\}$, the initial step size for the classical formulation is larger (in fact, more than three times) than the magnitude of the initial step size for the proposed formulation. Lastly, we observed that the final cost values from the classical formulation are only of magnitude 10^{-4} (or lower) while the proposed formulation produces final cost values that in the magnitude 10^{-6} (or lower). Because of the last two remarks, it is actually difficult to say that the proposed formulation possesses faster convergence rate to the optimal solution than the classical Kohn-Vogelius formulation.

We further assess the quality of the two formulations in terms of numerically solving the exterior Bernoulli problem (1.3) by taking into account the above-mentioned key observations. To do this, instead of taking the same value of α for the two formulations, we choose α in such a way that the difference between the initial step sizes from the two formulations is small as possible. For simplicity, we take $\alpha = 0.99$ for the proposed formulation and adjust the value of α in the classical scheme so that the initial step size for the two formulations are as close as possible. Also, for this purpose, we focus our attention to the case when $\lambda = -9, -4, -1$ since these are the cases where we see some sort

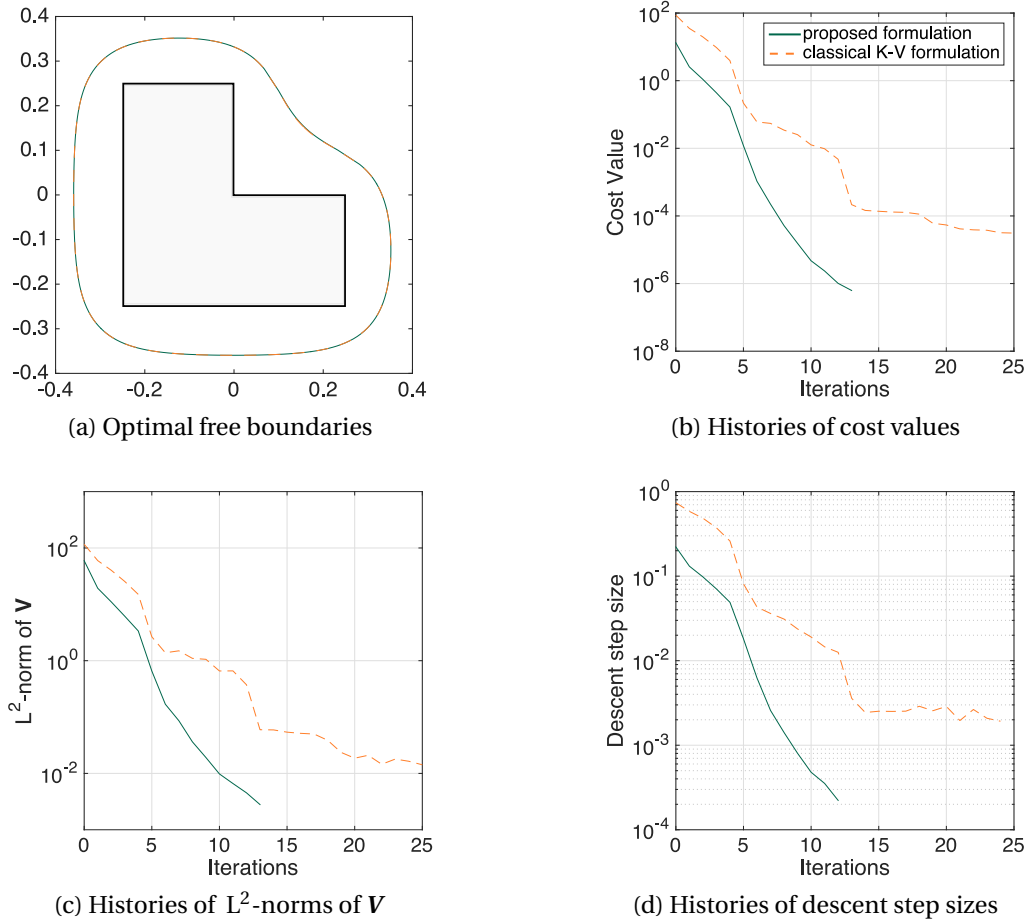


Figure 3.17: Results of Example 3.2.2.2 for $\lambda = -9$ when $\text{Tol} = 10^{-6}$ in the stopping condition (3.6) and $\alpha = 0.99$ in (3.3)

of inconsistencies in the number of iterations and computing times shown in Table 3.10. Table 3.11 shows the results of the computations using the classical Kohn-Vogelius formulation with $\text{Tol} = 10^{-6}$ in (3.6). It seems that for $\lambda = -9$ (and possibly for smaller values of λ), the computing time when using the classical formulation varies greatly with respect to a small change in the value of α . In contrast, for $\lambda = -1$ (and possibly for values of $\lambda < 0$ near zero), the computing time is not sensitive to small change in α . Meanwhile, we notice that, still, the proposed formulation (refer to Table 3.10) requires less number of iterations and computing times to reach convergence to the optimal solution than the classical formulation.

We also examine the results of the two formulations when Tol is set to 10^{-4} in the stopping condition (3.6) while taking the initial step size for the two formulations as close as possible. Among the three values of the parameter α listed in Table 3.11, we take the corresponding value of α_2 for each $\lambda = -9, -4, -1$ for the classical formulation. Table 3.12 shows the corresponding results for the given setup. Observe that, for the three cases considered, the proposed formulation requires less computing time than the classical one except for the case when $\lambda = -4$ where both formulations require 11

seconds to complete the optimization process. However, it seems that the classical formulation requires less number of iterations than the proposed scheme if we compare the number of iterations for the proposed formulation tabulated in Table 3.10 with that of the classical formulation shown in Table 3.12. Nevertheless, notice that, in most cases, the proposed formulation requires less computing time per iteration than the classical formulation. The histories of descent step sizes for the proposed and classical formulations are plotted in Figure 3.18a. Figure 3.18b, on the other hand, depicts the computed (optimal) exterior boundaries obtained through the proposed formulation versus the ones computed via the classical Kohn-Vogelius shape optimization formulation when $\text{Tol} = 10^{-4}$. We observe that, in all cases examined, the computed optimal free boundaries from the two formulations are almost indistinguishable.

λ	i	α_i	t_0	cost	iter.	cpu time
-9	1	0.2970642705	0.2216361137	1.34×10^{-5}	22	74 sec
	2	0.2970642710	0.2216361144	3.70×10^{-5}	18	102 sec
	3	0.2970642715	0.2216361144	6.40×10^{-5}	17	32 sec
-4	1	0.334138300	0.1409423055	1.03×10^{-5}	11	23 sec
	2	0.334138305	0.1409423076	4.57×10^{-6}	12	26 sec
	3	0.334138310	0.1409423098	4.92×10^{-5}	14	40 sec
-1	1	0.502658435	0.3123875250	1.34×10^{-6}	14	34 sec
	2	0.502658440	0.3123875282	1.17×10^{-6}	14	35 sec
	3	0.502658445	0.3123875313	1.24×10^{-6}	14	34 sec

Table 3.11: Computational results obtained via the classical formulation with $\text{Tol} = 10^{-6}$ in the stopping condition (3.6) for an L-shaped fixed boundary $\Gamma = \partial S$ when $\lambda = -9, -4, -1$ for different values of α in (3.3)

λ	formulation	α	t_0	cost	iter.	cpu time
-9	proposed	0.990000000	0.2216361144	1.55×10^{-5}	9	10 sec
	classical	0.297064271	0.2216361144	14.2×10^{-5}	12	16 sec
-4	proposed	0.990000000	0.1409423086	6.37×10^{-6}	7	11 sec
	classical	0.334138305	0.1409423076	4.57×10^{-6}	7	11 sec
-1	proposed	0.990000000	0.3123875327	4.39×10^{-5}	8	17 sec
	classical	0.502658440	0.3123875282	5.51×10^{-5}	9	24 sec

Table 3.12: Comparison of computational results obtained through the proposed and classical formulations with $\text{Tol} = 10^{-4}$ in (3.6) for an L-shaped fixed boundary $\Gamma = \partial S$ when $\lambda = -9, -4, -1$ with almost the same initial step size t_0 for both formulations

We provide a few more numerical examples comparing the results between the proposed and classical formulation when $\lambda = -10$ for $\text{Tol} = 10^{-4}, 10^{-5}, 10^{-6}$ in (3.6). In this test case, we consider two different initial guesses given in Example 3.2.2.1. Particularly, we consider Σ_0 as the circle Σ_0^1 and as the ellipse Σ_0^3 . For the proposed formulation, we again take $\alpha = 0.99$ which gives us $t_0 = 0.2281500068$ when $\Sigma_0 = \Sigma_0^1$ and $t_0 = 0.1918396442$ in case of taking $\Sigma_0 = \Sigma_0^3$. On the other hand,

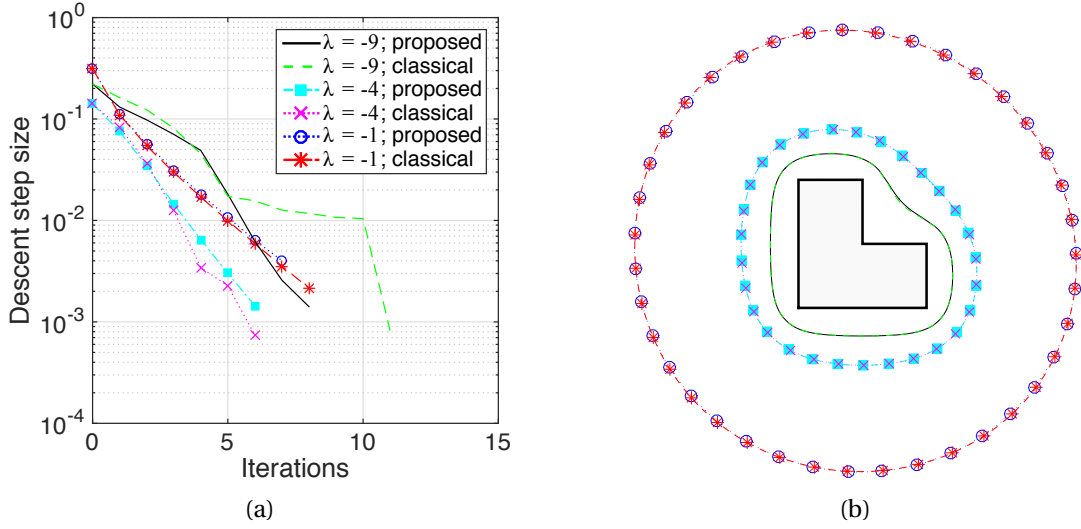


Figure 3.18: (a): Histories of descent step sizes for the proposed and classical formulations (with almost equal initial step size t_0 for the two formulations); (b): optimal free boundaries obtained when $\lambda = -9, -4, -1$ in Example 3.2.2.2 using the proposed and classical formulations with $\text{Tol} = 10^{-4}$ in the stopping condition (3.6)

by taking $\alpha = 0.2941418090$ when $\Sigma_0 = \Sigma_0^1$ in the classical formulation, we get $t_0 = 0.2281500069$. Also, with $\alpha = 0.2904954592$ when $\Sigma_0 = \Sigma_0^3$ in the classical formulation, we get $t_0 = 0.1918396442$. We examine the convergence of the approximate free boundaries to the optimal shape obtained through the two formulations. Because we do not know precisely the exact profile of the optimal domains corresponding to the solution of the test case in consideration, we use the computed optimal free boundary Σ^{in} obtained using the improved Neumann-data-tracking cost functional minimization approach (1.17) proposed in [97] as our benchmark. The results of the computations are summarized in Table 3.13 where we show the final cost values, the Hausdorff distance of the computed optimal free boundary Σ_f^i , $i = 1, 3$, with respect to Σ^{in} , the number of iterations and the total computing times for each of the two formulations. Comparing the results of the proposed formulation when $\text{Tol} = 10^{-6}$ with that of the classical formulation when $\text{Tol} = 10^{-4}$ (see highlighted rows), we observe that the former formulation needs less computing time per iteration to complete the iteration process than the latter one. In addition, it seems that the computed optimal free boundary obtained through the proposed formulation is closer (in terms of the Hausdorff distance) to Σ^{in} than the one obtained via the classical formulation when $\Sigma_0 = \Sigma_0^3$. However, when $\Sigma_0 = \Sigma_0^1$, the classical formulation produces smaller Hausdorff distance with respect to Σ^{in} than the proposed formulation. The evolutions of the domains or histories of free boundaries computed for each of the cases considered through the two formulations are shown in Figure 3.19. Looking at the plots depicted in the said figures, we notice that the proposed formulation yields a more stable convergence behavior (in the sense that the shape evolution is almost monotone) to the optimal solution than the classical formulation. We also looked at the histories of the minimum, the maximum and the mean curvatures (respectively

denoted by κ_2 , κ_1 , and κ) of the free boundaries (see Figure 3.20) plotted in Figure 3.19, and we found out that the mean curvatures of the computed optimal free boundaries Σ_f for all considered cases are positive. Hence, according to Proposition 2.5.2, the shape Hessian at the solution Ω^* of the Bernoulli problem (1.3) when $\Gamma = \partial S$ and $\lambda = -10$ (and therefore, for $-10 < \lambda < 0$) is strictly $H^{1/2}$ -positive. Moreover, we noticed that, after a certain number of iterations, the history of minimum curvatures that corresponds to the histories of free boundaries obtained through the proposed formulation (refer to Figure 3.20a and Figure 3.20b) projects a decreasing trend. This is in contrast to the behavior of the graph of the minimum curvatures corresponding to the history of free boundaries obtained via the classical setting where we noticed an increase in the value of the minimum curvature from the 7th to the 8th iteration (see Figure 3.20c and Figure 3.20d).

Σ_0^i	formulation	Tol	cost	$d_H(\Sigma^{\text{in}}, \Sigma_f^i)$	iter.	cpu time
Σ_0^1	proposed	10^{-4}	2.93×10^{-5}	0.023850	9	10 sec
		10^{-5}	4.46×10^{-6}	0.008586	12	13 sec
		10^{-6}	1.38×10^{-6}	0.008586	14	14 sec
	classical	10^{-4}	0.001627	0.008435	9	14 sec
		10^{-5}	0.001627	0.010512	9	14 sec
		10^{-6}	0.000224	0.007484	15	30 sec
Σ_0^3	proposed	10^{-4}	5.69×10^{-5}	0.026360	8	9 sec
		10^{-5}	1.22×10^{-5}	0.008565	10	10 sec
		10^{-6}	9.47×10^{-7}	0.007675	14	14 sec
	classical	10^{-4}	0.000644	0.008637	9	15 sec
		10^{-5}	0.000062	0.007394	15	30 sec
		10^{-6}	0.000027	0.007394	19	114 sec

Table 3.13: Comparison of computational results obtained through the proposed and classical formulations for an L-shaped fixed boundary $\Gamma = \partial S$ when $\lambda = -10$ with almost the same initial step size t_0 for both formulations

Before we go to our next and final set of examples, we reiterate the following key findings drawn in this subsection. For the same value of α , the classical formulation produces larger magnitude for t_0 than the proposed formulation. Moreover, it seems that the appropriate value of Tol in (3.6) is 10^{-4} for the classical formulation and 10^{-6} for the proposed formulation. One of the possible reason for this difference in the right choice for Tol is the fact that the classical formulation produces larger initial cost values than the proposed formulation. Furthermore, instead of simply comparing just the number of iterations or computing time to complete an iteration process, it seems reasonable to compare the mean computing time per iteration of the two formulations to evaluate their performance in numerically solving the optimization problem. This way of comparing the two formulations seems sensible because the two formulations almost have the same computing time. Moreover, we emphasize that we are actually applying the same algorithm for each of the two formulations, hence,

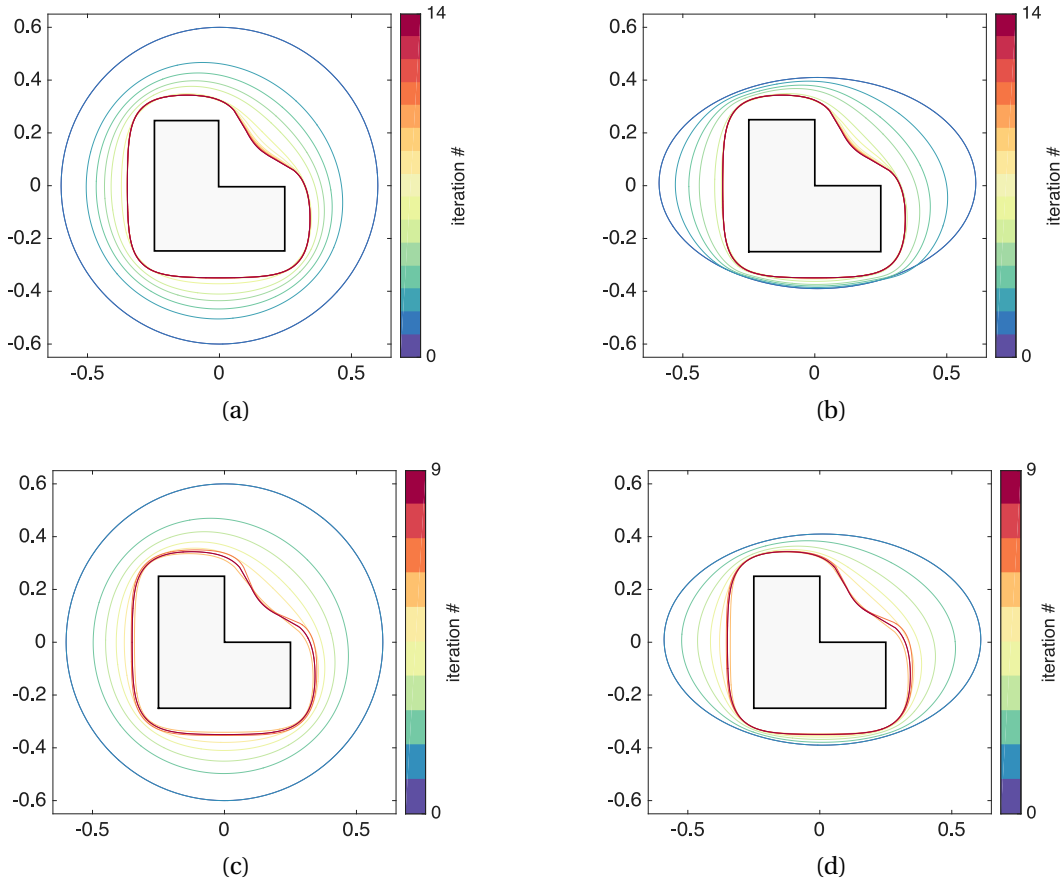


Figure 3.19: (a)-(b): histories of free boundaries obtained through the proposed formulation with initial guess Σ_0^1 and Σ_0^3 , respectively, where $\text{Tol} = 10^{-6}$ in (3.6); (c)-(d): Histories of free boundaries obtained via the classical Kohn-Vogelius formulation with initial guess Σ_0^1 and Σ_0^3 , respectively, where $\text{Tol} = 10^{-4}$ in (3.6)

considering the computing time per iteration as performance metrics in evaluating the two methods is justifiable. Lastly, we emphasize that the classical formulation requires less iteration number to complete an iteration process than the proposed formulation.

To end this section, let us complete Table 3.12 and compare the mean computing time per iteration and standard deviations for all $\lambda = -10, -9, \dots, -1$. Table 3.14 shows the final cost values, the number of iterations and computing times for all $\lambda \in \{-10, -8, -7, -6, -5, -3, -2\}$ when using the classical approach. The values of α chosen for each cases and the corresponding sizes of the initial step t_0 are also shown in the table. Meanwhile, in Table 3.15, we show the means and standard deviations of the number of iterations, computing time and computing time per iteration from the two formulations for the present optimization problem. Notice that the two formulations are comparable in terms of the mean over-all computing time. However, it requires two additional iterations for the proposed formulation to complete the optimization process than the classical formulation. Nevertheless, the proposed formulation needs less computing time per iteration than

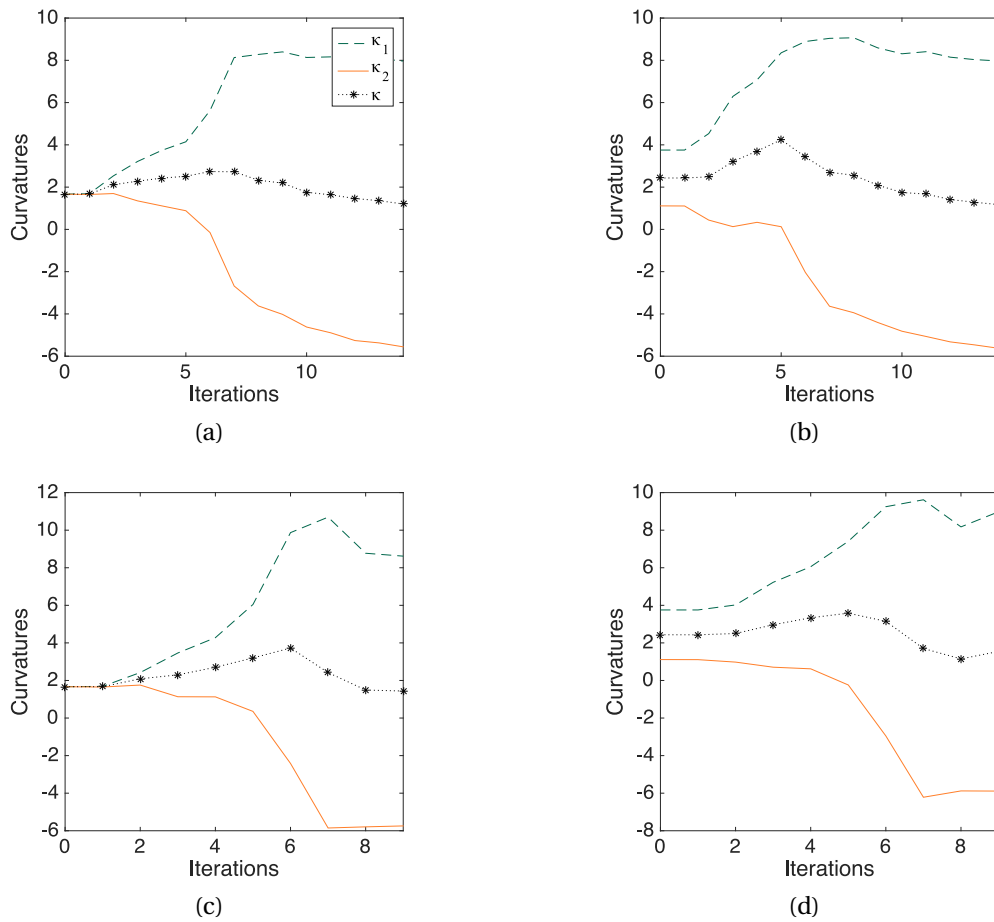


Figure 3.20: (a)-(b): corresponding histories of curvatures of the free boundaries obtained through the proposed formulation with initial guess Σ_0^1 and Σ_0^3 , respectively, shown in Figure 3.19a–3.19b; (c)-(d): Corresponding histories of curvatures of the free boundaries obtained via the classical Kohn-Vogelius formulation with initial guess Σ_0^1 and Σ_0^3 , respectively, shown in Figure 3.19c–3.19d

the classical setting.

λ	α	t_0	cost	iter.	cpu time
-10	0.29414181	0.22815001	0.001628	9	14 sec
-8	0.30072761	0.21350176	0.000119	12	17 sec
-7	0.30545458	0.20305801	0.001727	10	17 sec
-6	0.31178679	0.18916314	0.000137	8	13 sec
-5	0.32070413	0.16978307	0.000925	6	10 sec
-3	0.35544029	0.09411051	7.89×10^{-5}	6	14 sec
-2	0.32579718	0.03980505	2.08×10^{-5}	7	14 sec

Table 3.14: Computational results obtained through the classical formulation with $\text{Tol} = 10^{-4}$ in (3.6) for an L-shaped fixed boundary $\Gamma = \partial S$ for $\lambda = -10, -8, -7, -6, -5, -3, -2$ with almost the same initial step size t_0 with respect to that of the proposed formulation shown in Table 3.10

formulation	iteration		cpu time		$\frac{\text{cpu time}}{\text{iteration}}$	
	mean	std	mean	std	mean	std
proposed	≈ 11 (11.1)	≈ 2 (1.73)	16	3.46	1.46	0.29
classical	≈ 9 (8.6)	≈ 2 (2.22)	15	3.92	1.77	0.42

Table 3.15: Means and standard deviations (std) of the number of iterations, computing time and computing time per iteration for the proposed formulation with $\text{Tol} = 10^{-6}$ and classical formulation with $\text{Tol} = 10^{-4}$ in (3.6)

3.2.2.3 Example 3: A domain with fixed boundary having two disjoint components

For the third and final example, we look at a similar test case studied in [83]. Particularly, we define the fixed boundary Γ as the union of two disjoint kite-shaped figures which are parametrically defined as follows:

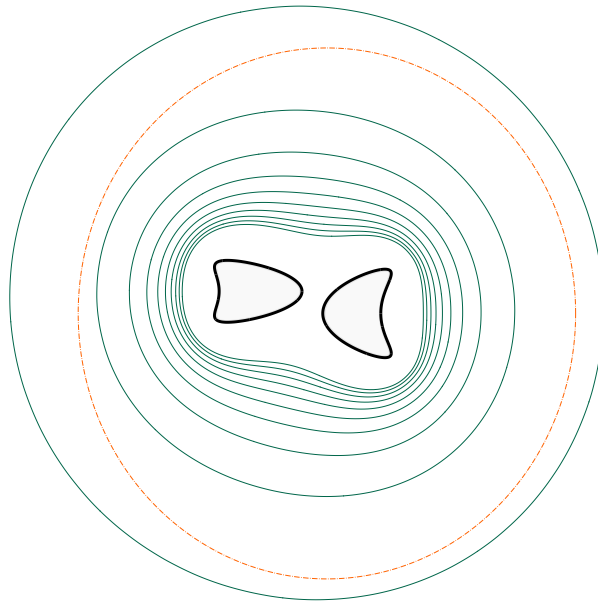
$$\begin{aligned}\Gamma^1 &:= \{(0.1 + 0.07 \cos \theta - 0.04 \cos 2\theta, 0.1 \sin \theta)^\top, 0 \leq \theta \leq 2\pi\}, \\ \Gamma^2 &:= \{(-0.2 + 0.1 \cos \theta + 0.04 \cos 2\theta, 0.05 + 0.07 \sin \theta)^\top, 0 \leq \theta \leq 2\pi\}.\end{aligned}$$

As in Example 3.2.2.2, we compute the optimal shape for all integers $\lambda = -10, -9, \dots, -1$ with $C(\mathbf{0}, 0.6)$ as the initial shape for the free boundary Σ . We set $\alpha = 0.99$ for the proposed formulation and choose α for the classical formulation in such a way that it results to an initial step size having (almost) the same value as that of the proposed setting. Moreover, we stop the algorithm with $\text{Tol} = 10^{-6}$ in (3.6) when using the proposed formulation and take $\text{Tol} = 10^{-4}$ for the classical formulation. Also, in all cases, $h_{\max} = 0.01$. The computed exterior boundaries are shown in Figure 3.21a (*forest-green-colored lines*) where the outermost boundary corresponds to $\lambda = -1$ and the innermost boundary to $\lambda = -10$. The fixed boundary Γ (*black line*) and the initial shape of the free boundary Σ (*dashed-dot orange line*) are also shown in the figure. Table 3.16 summarizes the computational results obtained through the two formulations. It shows in particular the values of α used for each of the two formulations, the resulting initial step sizes, the final values of the costs, the number of iterations and over-all computing time to reach convergence to the optimal solution. Meanwhile, in Figure 3.22, we show a comparison between the results obtained through the proposed and classical formulation for the case $\lambda = -10, -4, -1$. In Figure 3.22a, we see that the computed optimal free boundaries obtained from the two formulations are indistinguishable from each other. The histories of the costs values, the L^2 -norms of V and the histories of the descent step sizes are plotted in Figures 3.22b–3.22d, respectively. Looking at these figures, we observe that we get a more comparable convergence rate from the two formulations as $\lambda < 0$ closes to zero; that is, in case of $\lambda = -1$, the rate of convergence, for instance, of the cost for the proposed formulation is almost of the same value with that of the classical scheme. On the other hand, when $\lambda = -10$, the convergence rates of the two formulations differ greatly from each other. Meanwhile, in Figure 3.23, we show the evolutions or the histories of the free boundaries when $\lambda = -10$, for each of the two formulations (see, particularly, Figure 3.23a and Figure 3.23c for the respective results of the proposed and classical formulation). The figure also

shows the evolutions of the free boundaries (refer to Figure 3.23b and Figure 3.23d) when the initial shape Σ_0 of the free boundary is taken to be the ellipse

$$\Sigma_0^{\text{ell}} := \{(-0.1 + 0.4 \cos \theta, 0.05 + 0.5 \sin \theta)^\top, 0 \leq \theta \leq 2\pi\}.$$

As in the previous example, we noticed that the proposed formulation yields a more stable convergence behavior (again, in the sense that the shape evolution is monotone) to the optimal solution than the classical formulation. The histories of the minimum, the maximum and the mean curvatures of the free boundaries depicted in Figure 3.23 are plotted in the graphs shown in Figure 3.24. Clearly, the optimal free boundary for the present test case has positive mean curvature. Finally, in Table 3.17, we show the means and standard deviations of the number of iterations, computing times and computing times per iterations for the present test case. Looking at the results shown in the table, we see that the numerical algorithm presented in Subsection 3.1.3 requires 12 iterations to complete the optimization process when using the proposed formulation. This is two iterations higher compared to when using the classical formulation. However, we get a comparable result for the two formulations in terms of computing time which means that the proposed formulation actually requires less computing time per iteration than the classical setting.



(a) *Forest-green solid lines*: Optimal free boundaries for Example 3.2.2.3 when $\lambda = -10, -9, \dots, -1$ (the outermost boundary corresponds to $\lambda = -1$ and the innermost boundary to $\lambda = -10$); *dashed-dot orange line*: initial guess for the free boundary

3.2.3 Examples for the Third Proposed Shape Problem

This subsection is dedicated to the numerical investigation using the third proposed shape problem (1.18). In this respect, the numerical results will be compared with those obtained using the classical Dirichlet-data-tracking cost functional minimization approach (1.6).

λ	α	t_0	cost	iter.	cpu time
-10	0.990000000	0.337420581	1.33×10^{-7}	14	14 sec
	0.386646216	0.337420581	0.001223	15	24 sec
-9	0.990000000	0.331971040	5.73×10^{-7}	13	16 sec
	0.388463867	0.331971040	0.000473	11	20 sec
-8	0.990000000	0.325160189	5.07×10^{-7}	13	14 sec
	0.390736229	0.325160189	0.000582	10	17 sec
-7	0.990000000	0.316405255	3.36×10^{-7}	12	18 sec
	0.393657966	0.316405255	0.000745	10	16 sec
-6	0.990000000	0.304735585	3.79×10^{-7}	11	14 sec
	0.397552887	0.304735585	9.84×10^{-5}	12	20 sec
-5	0.990000000	0.288405794	3.33×10^{-7}	11	13 sec
	0.403001262	0.288405794	4.38×10^{-5}	13	18 sec
-4	0.990000000	0.263931464	2.09×10^{-7}	11	14 sec
	0.411150343	0.263931464	2.25×10^{-5}	9	16 sec
-3	0.990000000	0.223215311	1.45×10^{-7}	11	13 sec
	0.424571657	0.223215311	3.88×10^{-5}	7	11 sec
-2	0.990000000	0.142355886	1.70×10^{-7}	10	17 sec
	0.448686986	0.142355886	1.30×10^{-5}	7	13 sec
-1	0.990000000	0.111335863	9.21×10^{-7}	12	23 sec
	0.482819584	0.111335863	3.54×10^{-5}	8	16 sec

Table 3.16: Summary of computational results of Example 3.2.2.3 for $\lambda = -10, -9, \dots, -1$ where the highlighted rows correspond to the results due to the proposed formulation

formulation	iteration		cpu time		$\frac{\text{cpu time}}{\text{iteration}}$	
	mean	std	mean	std	mean	std
proposed	≈ 12 (11.8)	≈ 1 (1.23)	16.5	3.41	1.46	0.34
classical	≈ 10 (10.2)	≈ 3 (2.61)	17.1	3.70	1.77	0.17

Table 3.17: Means and standard deviations (std) of the number of iterations, computing time and computing time per iteration of the computational results shown in Table 3.16

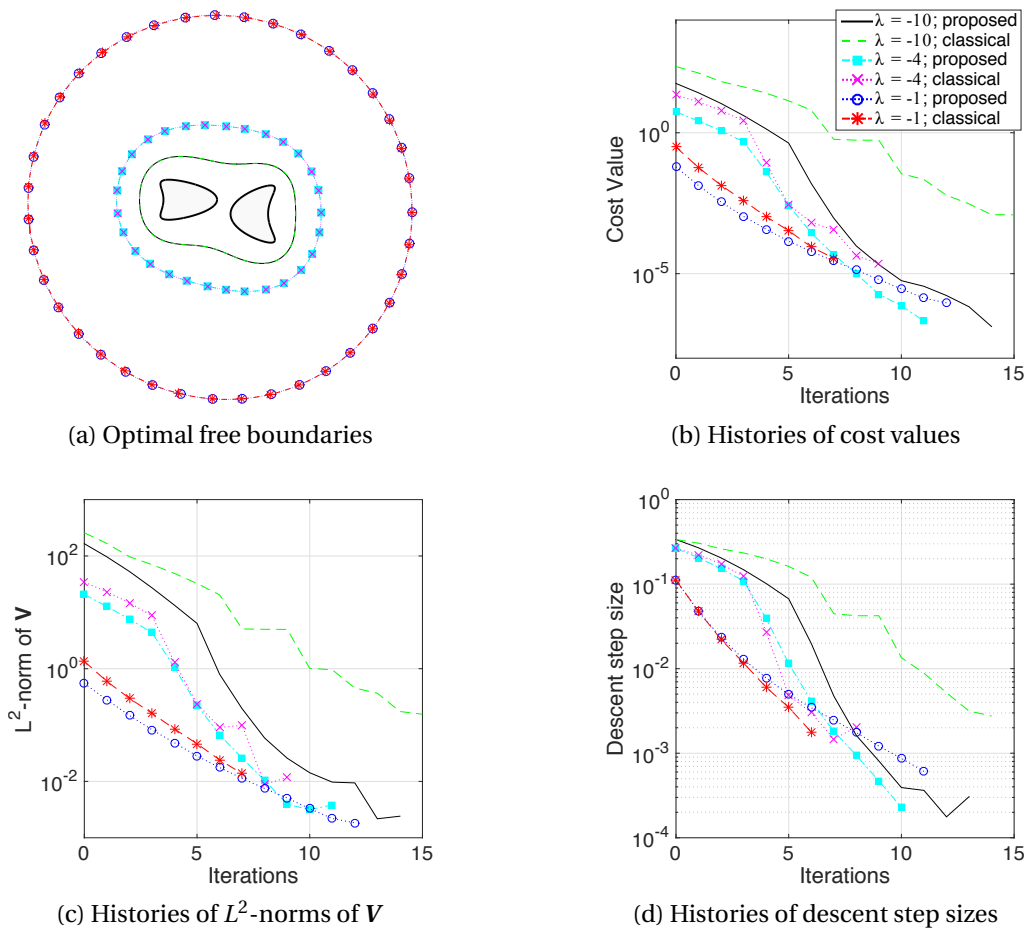


Figure 3.22: Results of Example 3.2.2.3 when $\lambda = -10, -4, -1$ for both of the proposed and classical formulations

In all numerical simulations conducted here, the minimum edge size h_{\min} and maximum edge size h_{\max} are set to $1/80$ and $1/40$, respectively, except for the third problem where we take $h_{\min} = 1/10$ and $h_{\max} = 1/5$. Moreover, we terminate the iterations as soon as $J(\Sigma_{k+1})/J(\Sigma_0) < 10^{-8}$ or if the algorithm already runs for 60 seconds of computing time. Furthermore, in this subsection, we consider three sets of algorithms, Algorithm A, Algorithm B, and Algorithm C, and each of them consists of two types: the first type essentially follows Algorithm 3.1, while the second type conforms to Algorithm 3.2. To be precise, we refer to the first-order methods as Algorithm A.1, Algorithm B.1, and Algorithm C.1, and to the second-order algorithms as Algorithm A.2, Algorithm B.2, and Algorithm C.2. Algorithm A utilizes the shape gradient and Hessian of J_3 computed under Tiihonen's condition (2.23). Particularly, it exploits equation (2.38) and (2.68) in computing for the descent directions in Algorithm 3.1 and Algorithm 3.2. On the other hand, Algorithm B simply refer to the case where the full versions of the shape gradient and shape Hessian of J_3 , given by $dJ_3(\Omega)[V]$ in Proposition 2.4.2 and (2.68), respectively, are utilized in the algorithm. Also, since we will compare our numerical results with those obtained using classical Dirichlet-data tracking approach, we will

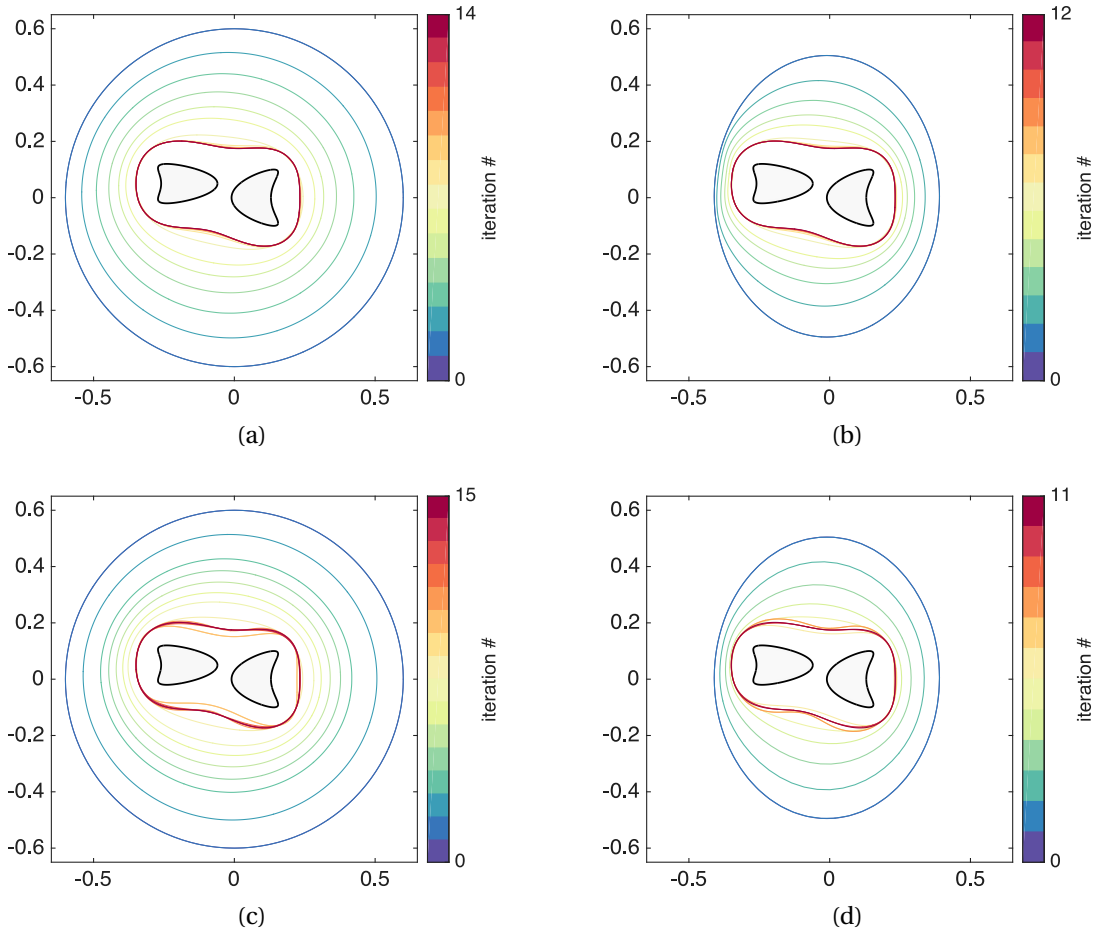


Figure 3.23: (a)-(b): histories of free boundaries obtained through the proposed formulation with initial guess $C(\mathbf{0}, 0.6)$ and Σ_0^{ell} , respectively, where $\text{Tol} = 10^{-6}$ in (3.6); (c)-(d): histories of free boundaries obtained via the classical Kohn-Vogelius formulation with initial guess $C(\mathbf{0}, 0.6)$ and Σ_0^{ell} , respectively, where $\text{Tol} = 10^{-4}$ in (3.6)

also run our propose iterative procedures Lastly, Algorithm C, refers the case when the corresponding shape gradient and shape Hessian from the classical Dirichlet-data tracking approach (1.6) is used in the algorithm. That is, when g in (3.4) is the kernel of the shape gradient $dJ_D(\Omega)[\mathbf{V}] = \int_{\Sigma} g_D \mathbf{n} \cdot \mathbf{V} d\sigma$ (see Remark 2.4.1), and when $h[\mathbf{V}]$ in (3.8) is given by (2.70).

3.2.3.1 Example 1: Axisymmetric case

We first consider a simple axisymmetric case. Given that $C(\mathbf{0}, r)$ and $C(\mathbf{0}, R)$ are the circles centered at the origin with radius $r > 0$ and $R > r$, respectively, the pure Dirichlet problem (1.9)

$$-\frac{\partial^2 u}{\partial \rho^2} - \frac{1}{\rho} \frac{\partial u}{\partial \rho} = 0 \text{ for } r < \rho < R, \quad u(r) = 1, \quad \text{and} \quad u(R) = 0,$$

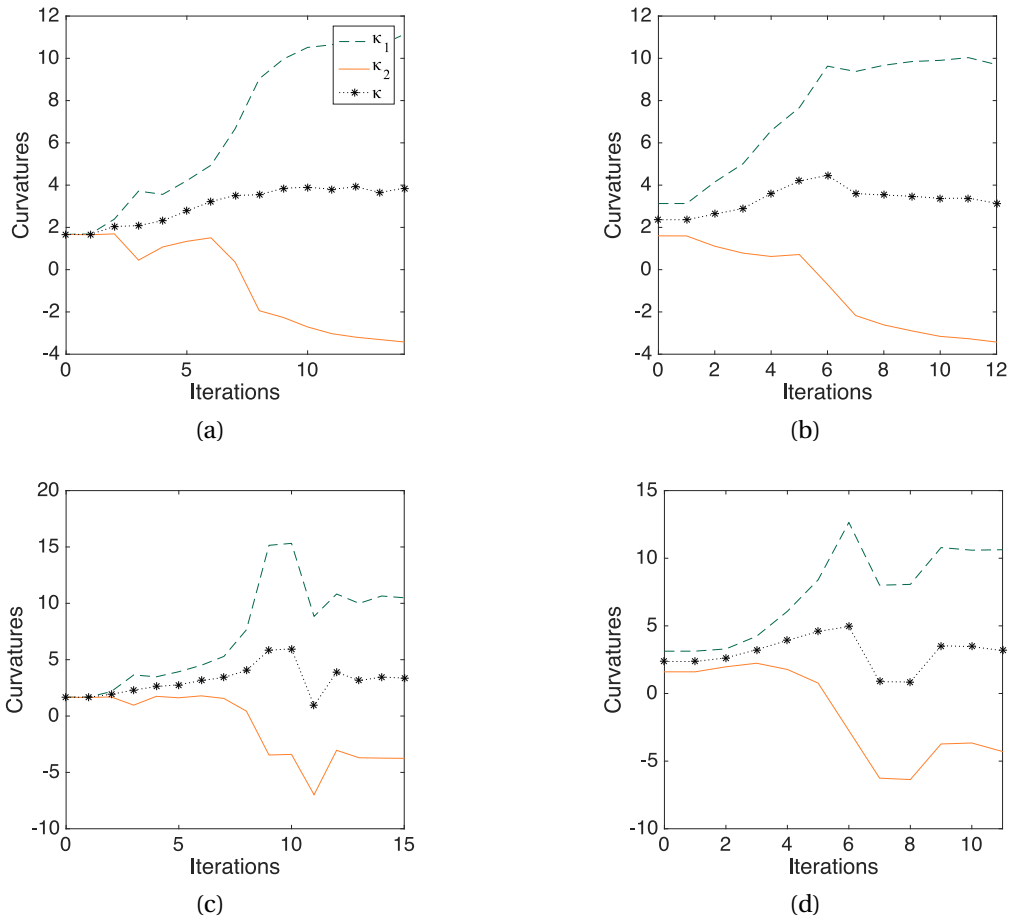


Figure 3.24: (a)-(b): Corresponding histories of curvatures of the free boundaries obtained through the proposed formulation with initial guess Σ_0^1 and Σ_0^3 shown in Figure 3.23a–3.23b, respectively; (c)-(d): corresponding histories of curvatures of the free boundaries obtained via the classical Kohn-Vogelius formulation with initial guess Σ_0^1 and Σ_0^3 shown in Figure 3.23c–3.23d, respectively

has the exact solution

$$u(\rho) = \frac{\log\left(\frac{\rho}{R}\right)}{\log\left(\frac{r}{R}\right)}.$$

In this case,

$$\frac{\partial}{\partial \mathbf{n}} u(R) = \frac{1}{R \log\left(\frac{r}{R}\right)}.$$

Hence, the exterior Bernoulli FBP (1.3) with

$$(3.11) \quad \Gamma = \{x \in \mathbb{R}^2 : |x| = r\} \quad \text{and} \quad \lambda = \frac{1}{R \log\left(\frac{r}{R}\right)}, \quad 0 < r < R,$$

has the unique exact free boundary solution $\Sigma^* = C(\mathbf{0}, R)$. Moreover, the explicit expression u_D satisfying (1.9) on Ω_ρ (the annular domain with inner radius r and outer radius ρ centered at the origin) is given by

$$u_D(\Omega_\rho) = \frac{\log|x| - \log\rho}{\log r - \log\rho}.$$

Similarly, for the mixed Dirichlet-Neumann problem (1.7) with assumptions given by (3.11), the explicit expression for its solution u_N is given by

$$u_N(\Omega_\rho) = \lambda\rho \log\left(\frac{|x|}{r}\right) + 1.$$

Meanwhile, for the mixed Dirichlet-Robin problem (1.15) with fixed $\beta > 0$ and λ in (3.11), the PDE system

$$-\frac{\partial^2 u}{\partial \rho^2} - \frac{1}{\rho} \frac{\partial u}{\partial \rho} = 0 \text{ for } r < \rho < R, \quad u(r) = 1, \quad \text{and} \quad \frac{\partial}{\partial \mathbf{n}} u(R) + \beta u(R) = \lambda,$$

has the solution $u = u_R(\Omega_\rho)$ explicitly given by

$$u_R(\Omega_\rho) = \frac{1 + \lambda\rho \log\left(\frac{|x|}{r}\right) - \beta\rho \log\left(\frac{|x|}{\rho}\right)}{1 - \beta\rho \log\left(\frac{r}{\rho}\right)}.$$

Thus, when the free boundary is given by $\Sigma_\rho = \{x : |x| = \rho\}$, the exact values of the functionals J_D , J_N , J_{KV} , J_1 , J_2 , and J_3 are respectively given by the following expressions:

$$\begin{aligned} J_D(\Sigma_\rho) &= \frac{1}{2} \int_{\Sigma_\rho} u_N^2 \, d\sigma = \pi\rho \left(1 - \lambda\rho \log\left(\frac{r}{\rho}\right)\right)^2, \\ J_N(\Sigma_\rho) &= \frac{1}{2} \int_{\Sigma_\rho} \left(\frac{\partial u_D}{\partial \mathbf{n}} - \lambda\right)^2 \, d\sigma = \frac{\pi}{\rho \left(\log\left(\frac{r}{\rho}\right)\right)^2} \left(1 - \lambda\rho \log\left(\frac{r}{\rho}\right)\right)^2, \\ J_{KV}(\Omega_\rho) &= \frac{1}{2} \int_{\Omega_\rho} |\nabla(u_N - u_D)|^2 \, dx = \frac{\pi}{\log\left(\frac{\rho}{r}\right)} \left(1 - \lambda\rho \log\left(\frac{r}{\rho}\right)\right)^2, \\ J_1(\Sigma_\rho) &= \frac{1}{2} \int_{\Sigma_\rho} \left(\frac{\partial u_D}{\partial \mathbf{n}} - \lambda\right)^2 \, d\sigma = \pi\beta\rho \left(\frac{1 - \lambda\rho \log\left(\frac{r}{\rho}\right)}{1 - \beta\rho \log\left(\frac{r}{\rho}\right)}\right)^2, \\ J_2(\Omega_\rho) &= \frac{1}{2} \int_{\Omega_\rho} |\nabla(u_N - u_R)|^2 \, dx = \frac{\pi}{\log\left(\frac{\rho}{r}\right)} \left(\frac{\beta\rho \log\left(\frac{r}{\rho}\right)}{1 - \beta\rho \log\left(\frac{r}{\rho}\right)}\right)^2 \left(1 - \lambda\rho \log\left(\frac{r}{\rho}\right)\right)^2, \\ J_3(\Sigma_\rho) &= \frac{1}{2} \int_{\Sigma_\rho} |u_N - u_R|^2 \, d\sigma = \pi\rho \left(\frac{\beta\rho \log\left(\frac{r}{\rho}\right)}{1 - \beta\rho \log\left(\frac{r}{\rho}\right)}\right)^2 \left(1 - \lambda\rho \log\left(\frac{r}{\rho}\right)\right)^2. \end{aligned}$$

Figure 3.25 shows that the algorithms using J_D , J_N , J_{KV} , J_1 , J_2 , and J_3 are not equivalent.

Next, we evaluate the efficiency of the first-order shape optimization methods presented in previous chapters (i.e., Algorithm A.1, Algorithm B.1, and Algorithm C.1) in solving a concrete example of the present test problem. For this purpose, we again let $r = 0.3$ and $R = 0.5$ (hence, $R^* = 0.5$), giving us $\lambda = -3.9152$ (as in Example 3.2.1.1). We choose the circle centered at the origin with radius 0.6 as our initial guess (i.e., we take $\Sigma_0 = C(\mathbf{0}, 0.6)$). The results of the convergence tests using Algorithm A.1, Algorithm B.1, and Algorithm C.1 for values of $\alpha = 0.1, 0.3, 0.5$ are depicted in

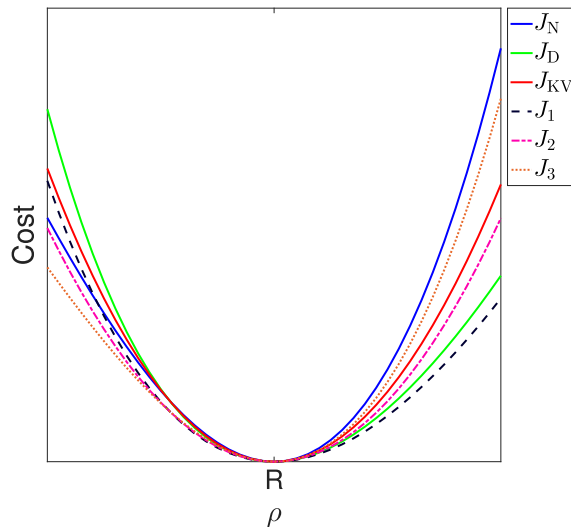


Figure 3.25: Variation of the cost functionals J_D , J_N , J_{KV} , J_1 , J_2 , and J_3 with respect to ρ

Figure 3.26. This includes the histories of mean radii shown in Figure 3.26(a), the histories of relative errors $\epsilon_k = |\bar{R}_k - R^*|$ shown in Figure 3.26(b), and the histories of cost values (normalized with its initial value) plotted on logarithmic scale in Figure 3.26(c). Similar to 3.2.1, the ‘ k th mean radii,’ denoted by \bar{R}_k , in these figures means the average distance from the origin of the nodes on the exterior boundary of the k th domain Ω_k , and Σ_k denotes the k th approximation of the optimal free boundary Σ^* . On the other hand, the computed values of the cost functionals at Σ_K that correspond to each algorithm, where K denotes the *optimal termination index* (i.e., $K := \min\{k \in \mathbb{N}_0 : \text{stopping condition is satisfied}\}$), are all found to be of magnitude less than 10^{-6} . Furthermore, the computed relative errors ϵ_k in all cases are of magnitude of order 10^{-4} . Meanwhile, we notice from Figure 3.26(a) that our proposed formulation coupled with our present numerical scheme with $\alpha = 0.3$ solves the solution of the test problem as fast as the Kohn-Vogelius formulation (combined with the level-set method) used in [1] in terms of the number of iterations required to complete its corresponding iteration process. In fact, our proposed method with the step size parameter α set to 0.5 is even faster than the said approach used by Ben Abda et al. in [1]. On the other hand, it is evident from the shown figures that Algorithm B.1 possesses faster convergence rate than Algorithm C.1. Hence, our proposed method (without, of course, imposing condition (2.23)) is more efficient than the classical Dirichlet-data tracking approach, at least in solving the present case problem. In contrary, however, Algorithm A.1 (in which condition (2.23) is assumed) converges to the solution of the test problem slower than Algorithm C.1.

Now, we resolve the present test problem using Algorithm A.2, Algorithm B.2, and Algorithm C.2. The computational results obtained from these second-order shape optimization methods are shown in Figure 3.27. Looking at the graphs depicted in the said figure, it seems that our proposed method, with or without condition (2.23) (respectively, Algorithm A.2, and Algorithm B.2) is faster than the second-order Dirichlet-data tracking approach (i.e., Algorithm C.2). In this case, however,

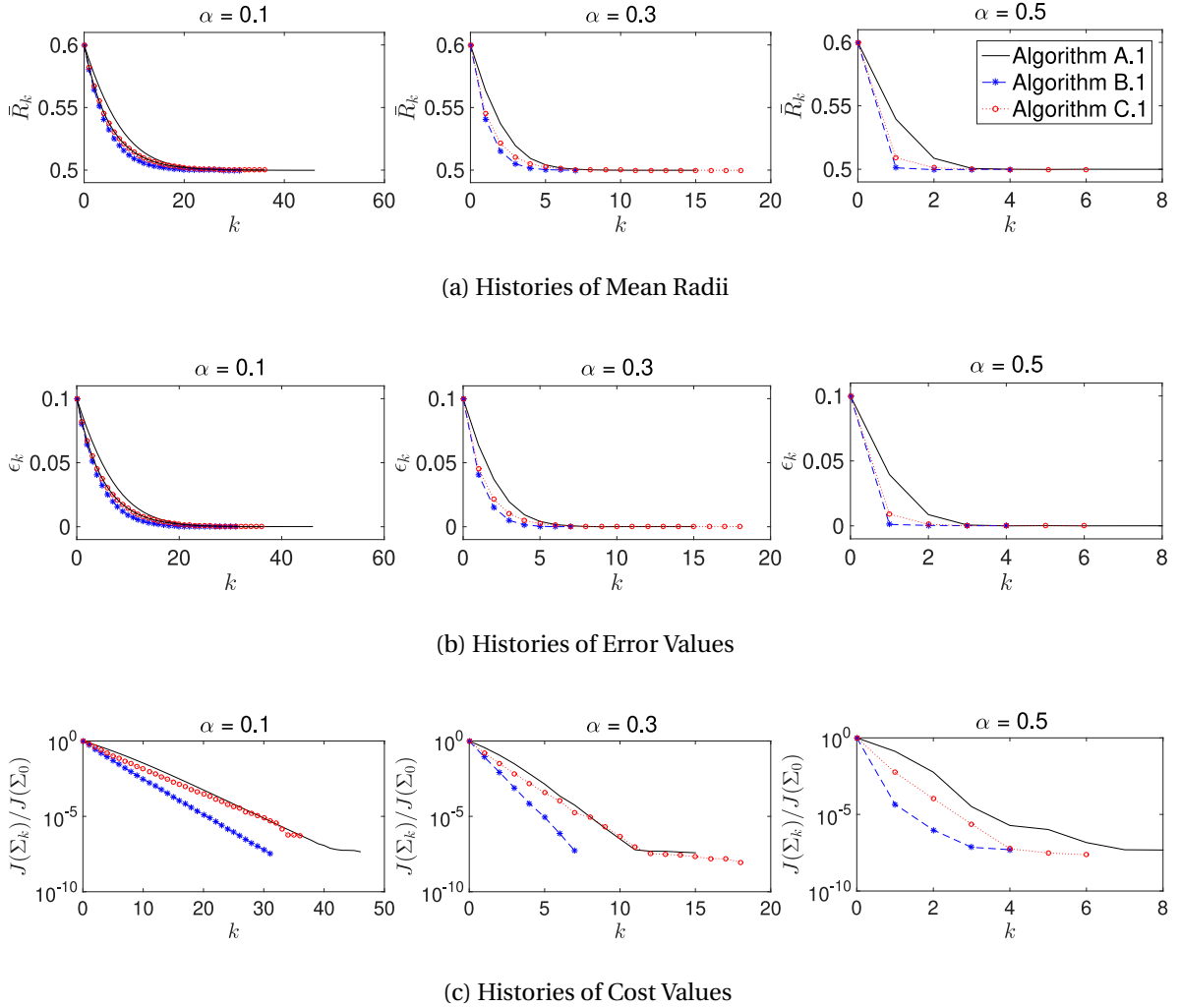


Figure 3.26: Histories of (a) mean radii, (b) error values and (c) cost values of Example 3.2.3.1 for values of $\alpha = 0.1, 0.3, 0.5$ (left, middle and right plots, respectively) using the gradient based algorithms A.1, B.1, and C.1

Algorithm B.2 and Algorithm C.2 were ran with $\tilde{\alpha} = 0.3$ while we used the full Newton step (i.e., $\tilde{\alpha} = 1$) for Algorithm A.2. Again, the computed final cost values, in all cases, are of magnitude less than 10^{-6} and the absolute errors at the final iterate ϵ_K are all found to be of magnitude of order 10^{-4} . Notice from the left most plot in Figure 3.27 that the first iterate of Algorithm A.2 already overshoots the solution. Even so, the second iterate is already close enough to the optimal solution as evident in the said plot.

In the next two examples, we further examine the effect of imposing condition (2.23) in the shape optimization process. This time we consider two concrete problems that have non-trivial fixed boundaries. Also, due to the limitation of the proposed shape optimization method coupled with condition (2.23) (see Remark 2.2.1), we only consider cases wherein the optimal shape solution are *nearly convex*. Specifically, for the first problem, we consider the case when the fixed boundary has a

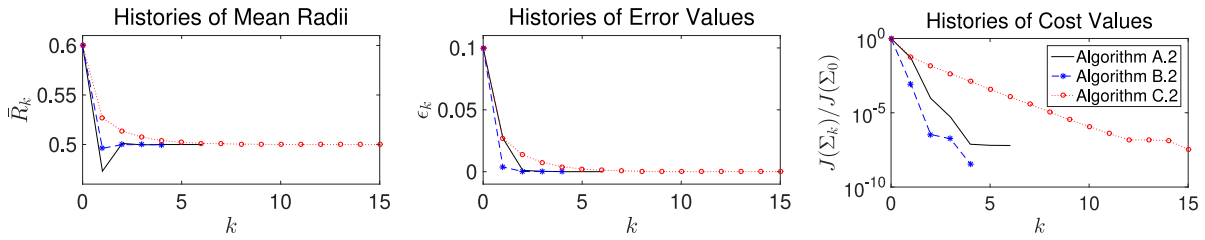


Figure 3.27: Histories of mean radii (*left plot*), error values (*mid plot*) and cost values (*right plot*) for Example 3.2.3.1 using the second-order shape optimization algorithms A.2, B.2 and C.2

shape like an inverted letter T. On the other hand, for the second case problem, we consider a fixed boundary that has two disjoint components similar to the one examined in [83]. In these cases, since the exact optimal free boundaries are difficult to solve analytically, we simply assume Σ^* as the final free boundary computed using finer meshes and at longer computing times.

3.2.3.2 Example 2: An inverted T-shaped fixed boundary

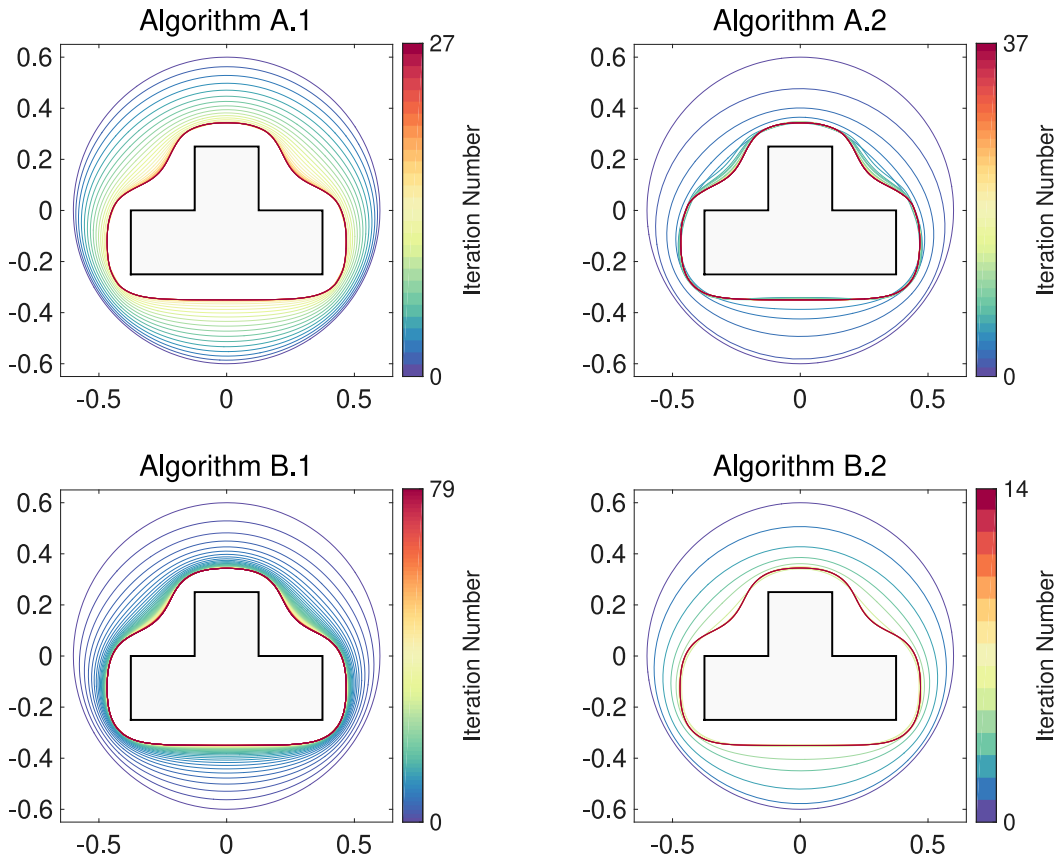
Next, we consider $\Gamma = \partial S$ as the boundary of the T-shape

$$S := ((-3/8, 3/8) \times (-1/4, 0)) \cup ((-1/8, 1/8) \times [0, 1/4]),$$

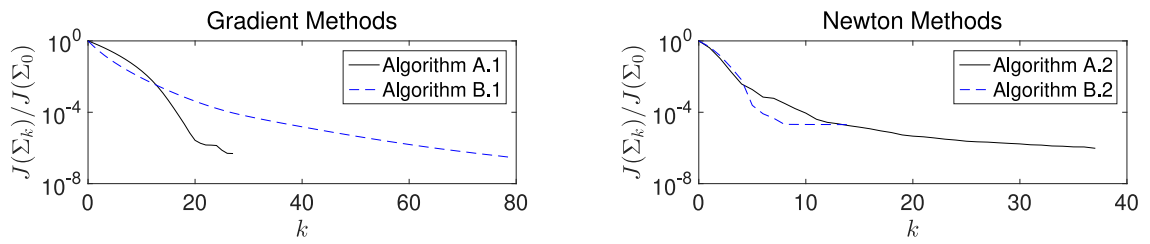
and let $\lambda = -10$. We solve the present problem using algorithms A.1, B.1, A.2, and B.2. For the first-order methods, we take $\alpha = 0.1$ while for the second-order algorithms, we choose $\tilde{\alpha} = 0.9$. The results of the computations are shown in Figure 3.28. Here, the evolution of the free boundaries with initial profile $\Sigma_0 = C(\mathbf{0}, 0.6)$ are illustrated in Figure 3.28(a). Observe from these figures that the evolution of the free boundaries are clearly different from each other (as expected), especially when the approximant is closing to the optimal free boundary. Meanwhile, a comparison between the histories of cost values and histories of Hausdorff distances between the k th approximation and the (approximate) optimal free boundaries (here, we denote by $d_H(\Sigma_k, \Sigma^*)$) obtained from the four algorithms are shown in Figure 3.28(b) and Figure 3.28(c), respectively. Looking at these figures, it seems that Algorithm B.1 is converging faster than Algorithm A.1 at first few iterations, but then the condition is reversed after 12 iterations. Meanwhile, comparing their corresponding second-order methods, it appears that Algorithm A.2 and Algorithm B.2 are comparable in terms of convergence speed. On the other hand, the second-order methods are obviously much faster than the first-order methods as expected. In these numerical tests, the computed cost values are all found to be of magnitude of order 10^{-4} . Furthermore, the calculated Hausdorff distances between the final free boundaries obtained from the four algorithms (including the approximate optimal free boundary) are found to be of order 10^{-3} . This means that the computed final free boundaries are almost identical.

3.2.3.3 Example 3: A domain with fixed boundary having two disjoint components

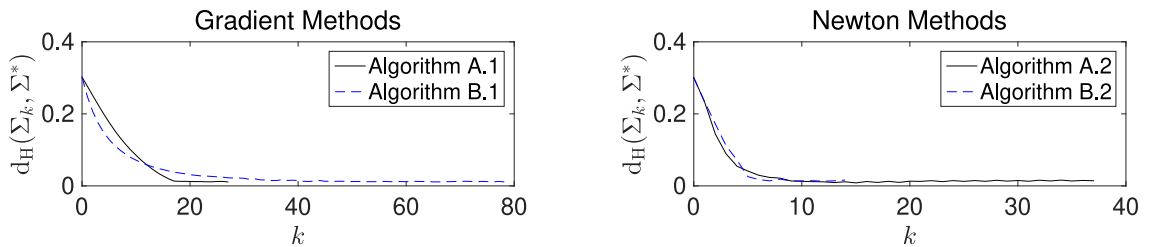
For the third example, we look at one of the test problems studied in [83]. Particularly, we let $\lambda = -1.5$ and again define the fixed boundary Γ as the union of two disjoint kite-shaped figures which are



(a) Evolution of the free boundaries generated by gradient methods (*left*) and by Newton methods (*right*)



(b) Histories of cost values



(c) Histories of Hausdorff distances

Figure 3.28: Computational results of Example 3.2.3.2 using algorithms A.1, B.1, A.2 and B.2

parametrically defined as follows:

$$\begin{aligned}\Gamma^1 &:= \{(1 + 0.7 \cos \theta - 0.4 \cos 2\theta, \sin \theta)^\top, 0 \leq \theta \leq 2\pi\}, \\ \Gamma^2 &:= \{(-2 + \cos \theta + 0.4 \cos 2\theta, 0.5 + 0.7 \sin \theta)^\top, 0 \leq \theta \leq 2\pi\}.\end{aligned}$$

Here, the initial guess Σ_0 for the free boundary is taken to be the circle $C(\mathbf{0}, 5.0)$. In addition, we again choose $\alpha = 0.1$ and $\tilde{\alpha} = 0.9$ in the first- and second-order methods. The results of the computations using algorithms A.1, B.1, A.2, and B.2 are shown in Figure 3.29. In particular, Figure 3.29(a) shows the evolutions of the free boundaries obtained using the four algorithms while the remaining plots, Figure 3.29(b) and Figure 3.29(c), illustrate the histories of cost values and Hausdorff distances $d_H(\Sigma_k, \Sigma^*)$, respectively. In this problem, it appears that Algorithm B.1 is completely much faster than Algorithm A.1 as oppose to the previous problem. However, we notice a similar convergence behavior on the second-order methods as in the previous example. More precisely, it seems that Algorithm B.2 converges faster than Algorithm A.2 as the approximant gets closer to the optimal free boundary. Meanwhile, as in the previous example, the computed cost values are all found to be of magnitude of order 10^{-4} , and the computed final free boundaries are almost identical with each other (i.e., their Hausdorff distances are computed to be of order 10^{-3}).

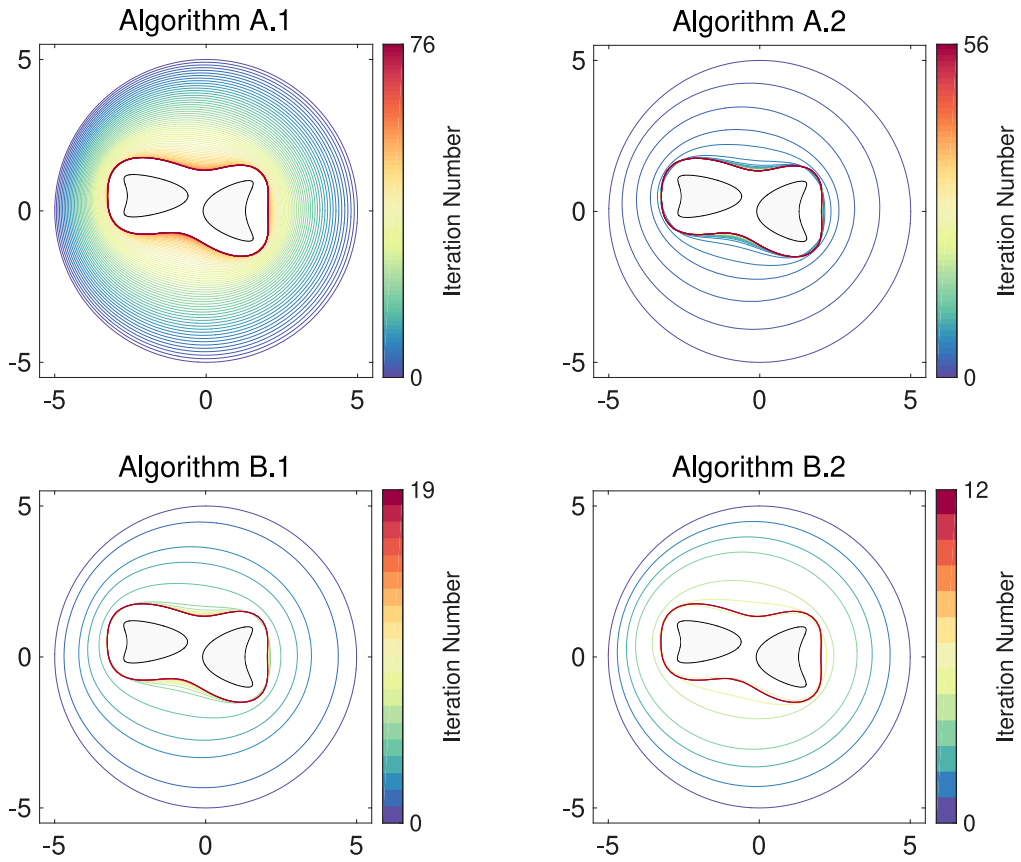
In the last two examples presented above, the computed final free boundaries are found to be *nearly* convex. To complete our numerical investigation, we need to consider another example wherein the optimal free boundary is clearly non-convex. For this purpose, however, we focus on comparing our proposed method with that of the classical Dirichlet-tracking approach (noting, of course, that condition (2.23) is not appropriate to take into account in solving this new last and final case problem).

3.2.3.4 Example 4: A dumb-bell like shape fixed boundary

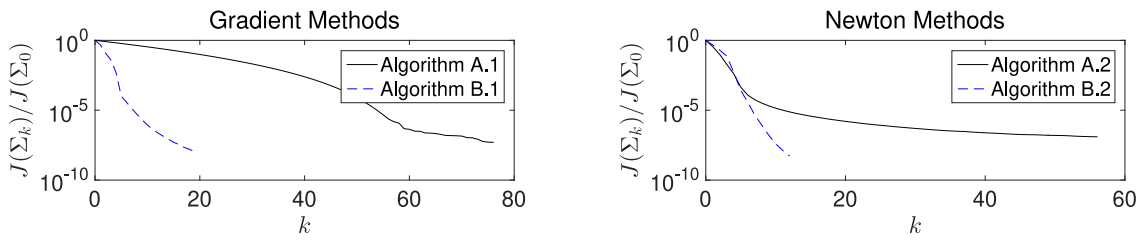
We consider $\Gamma = \partial D$ as the boundary of a dumbbell-like domain D similar to the one examined by Eppler and Harbrecht in [48] which has the following parametrization

$$D := \{(0.45 \cos \theta, 0.3 \sin \theta (1.25 + \cos 2\theta))^\top, 0 \leq \theta \leq 2\pi\},$$

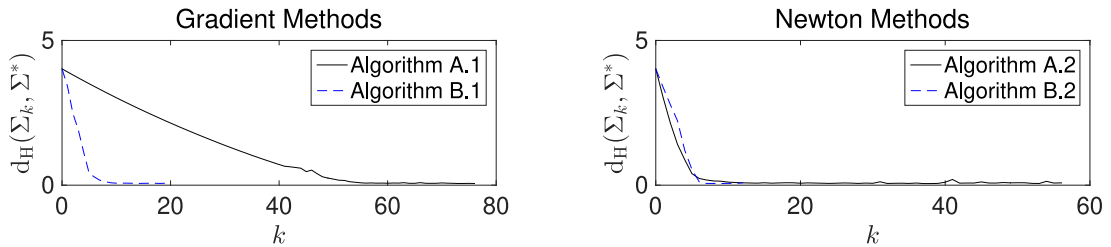
and take $\lambda = -10$. For this problem, we again choose the circle $C(\mathbf{0}, 0.6)$ as the geometric profile of the initial free boundary Σ_0 . Moreover, we let $\alpha = 0.3$ as the step-size parameter for the first-order methods and take $\tilde{\alpha} = 0.8$ for the second-order algorithms. The computational results using algorithms B.1, C.1, B.2, and C.2 are summarized in Figure 3.30. Looking at Figure 3.30(a), it is evident that the free boundaries evolve differently from each algorithm. In particular, referring to the results of the first-order methods shown in the other plots (Figure 3.30(b) and Figure 3.30(c)), it seems that our proposed method is somewhat faster than the classical Dirichlet-data tracking approach. Regarding second-order methods, however, it looks like that the classical approach is converging faster than the Dirichlet-data-gap tracking formulation. In fact, as early as the second iterate, the classical Dirichlet-data tracking approach was already able to detect the non-convexity of the optimal



(a) Evolution of the free boundaries generated by gradient methods (*left*) and by Newton methods (*right*)



(b) Histories of cost values

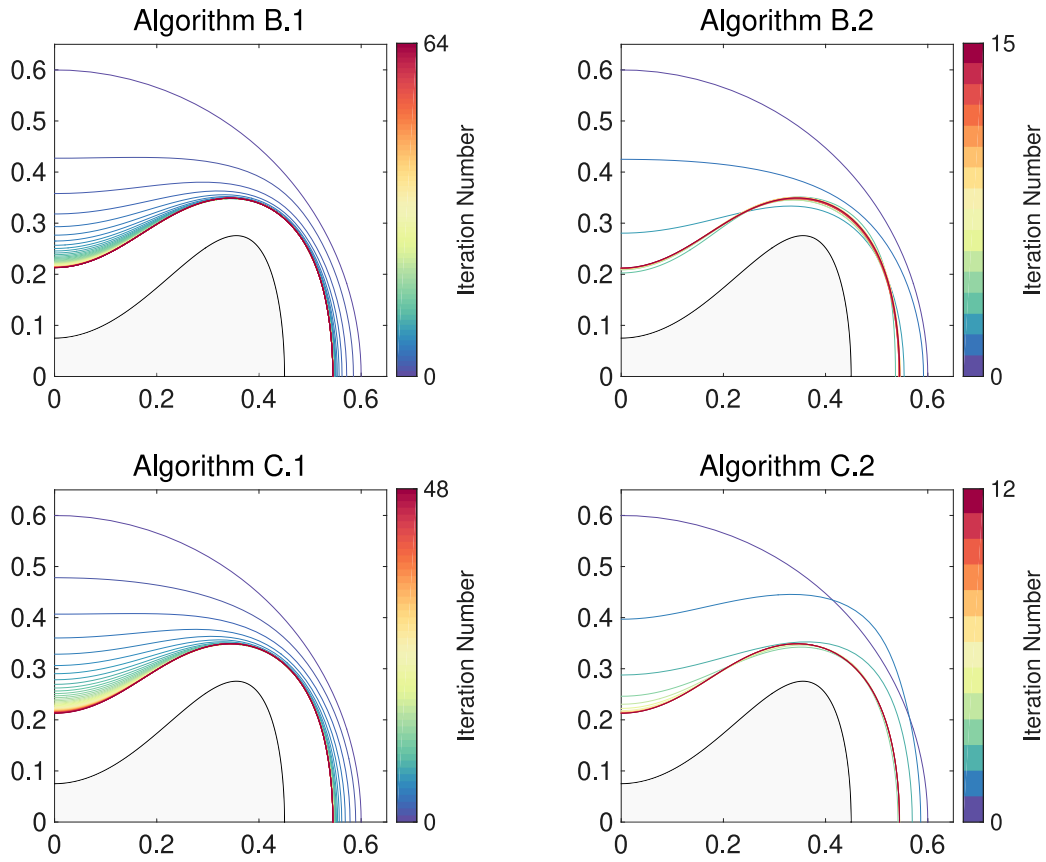


(c) Histories of Hausdorff distances

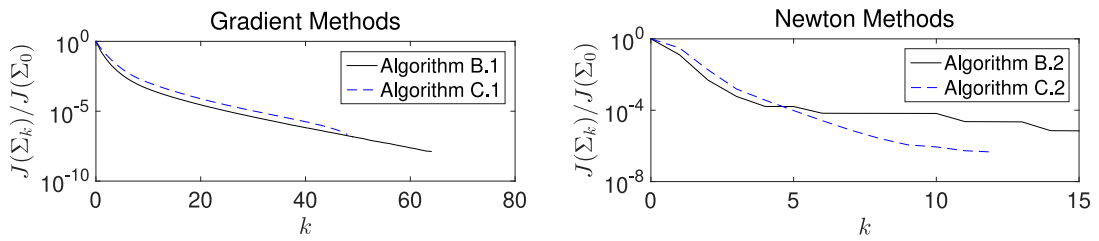
Figure 3.29: Computational results of Example 3.2.3.3 using algorithms A.1, B.1, A.2 and B.2

free boundary. Nevertheless, as the approximants get closer to the optimal free boundary, we observe that the proposed method then converge faster than the classical approach (at least based on the right plot depicted in Figure 3.30(c)). We also compared the computed optimal free boundaries obtained from the two formulations and found that they are almost identical. In fact, the computed Hausdorff distance between the computed final free boundaries obtained from the two formulations has magnitude of order 10^{-3} . Lastly, in all cases, the computed cost values are all found to be of magnitude of order 10^{-5} or lower. However, as we see in the right plot in Figure 3.30(b), it seems that the cost functional J_3 is less sensitive than the Dirichlet-data-tracking cost functional J_D in this example. We further explain this property of the cost function below, giving emphasis on the notion of ill-posedness of the proposed Dirichlet-data-gap cost functional minimization approach formulation (1.18) discussed in Section 2.5.

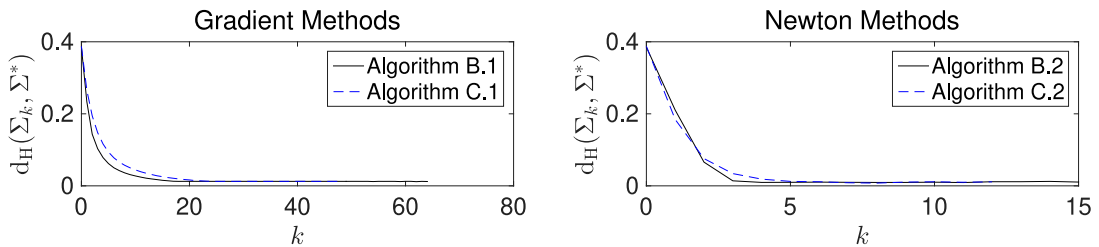
Sensitivity of the cost functionals J_3 and J_D . We conclude our numerical example by discussing the effect of the step size parameter $\tilde{\alpha}$ in the ‘sensitivity property’ of the cost functionals J_3 and J_D . As pointed out at the end of subsection 3.1.5, the main purpose of introducing a step size parameter in our second-order methods is to control the magnitude of the step size (i.e., to limit the maximum step) at every iteration. Recall that, at the k th iterate, we only accept the step size t_k only if it provides a decrease in the cost value (i.e., if $J(\Omega_{k+1}) \leq J(\Omega_k)$); otherwise, we do a backtracking procedure. In our numerical experiments, we observe that taking a full Newton step at every iterate is not a good strategy at all because the cost functional J_3 (as well as J_D) seems to be insensitive with respect to large geometric perturbations. For illustration, we refer to Figure 3.31(a) where we logarithmically plot the histories of cost values obtained from resolving the present case problem using Algorithm B.2 and Algorithm C.2 with the full Newton step $t_k = \|\mathbf{V}\|_{\mathbf{H}^1(\Omega_k)}^2 / \|\mathbf{W}\|_{\mathbf{H}^1(\Omega_k)}^2$ (i.e., $\tilde{\alpha} = 1.0$). Noticeably, several adjacent iterations differ only with very small values (and almost insignificant). Hence, the non-uniform sensitivity of the cost with respect to the descent directions. This observation can actually be viewed as a validation to our findings that the proposed formulation (1.18) is algebraically ill-posed (see Proposition 2.5.1 and Remark 2.5.1). That is, in this case, the ill-posedness of the present optimization formulation could also mean that larger deformations in the domains may have little effect on the cost functional. On the other hand, the evolution of the free boundaries with the full Newton step are shown in Figure 3.31(b) while a comparison between the computed free boundaries using the two second-order algorithms is depicted in Figure 3.32. In the latter figure, the difference between the two computed geometries is clearly discernible and, in this case, the final free boundary computed through the classical approach (i.e., Algorithm C.2) is more accurate than the one obtained via the proposed method (i.e., Algorithm B.2). Meanwhile, scaling the (full) Newton steps by a factor of $\tilde{\alpha} = 0.2$ at every iteration (in both Algorithm B.2 and Algorithm C.2) lead to the computational results shown in Figure 3.33. The figure shows, in particular, the histories of cost values and Hausdorff distances both plotted in Figure 3.33(a) (left and right plot, respectively). Referring, in particular, to the left plot shown in Figure 3.33(a), it is clear that the costs J_3 and J_D are decreasing almost uniformly from the initial to their respective final values. However, it is apparent from the figure



(a) Evolution of the free boundaries generated by gradient methods (*left*) and by Newton methods (*right*)



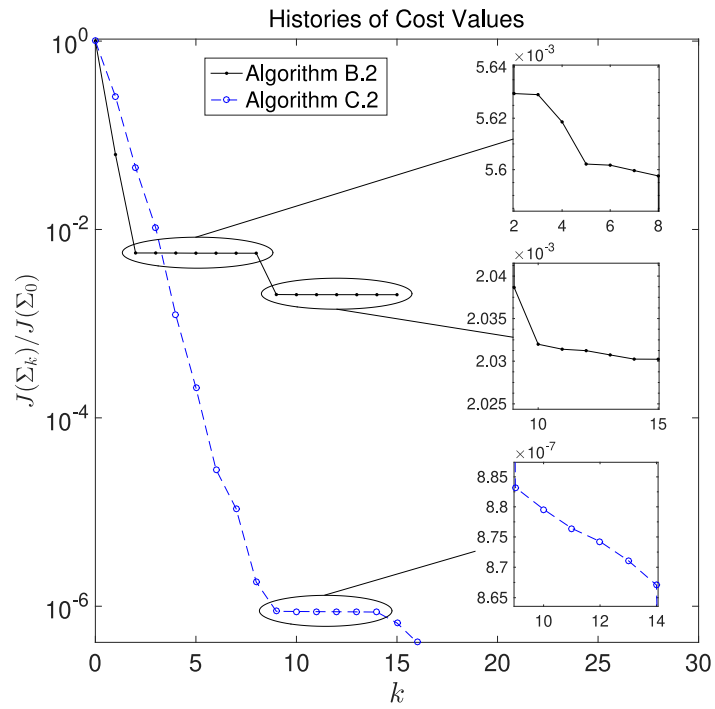
(b) Histories of cost values



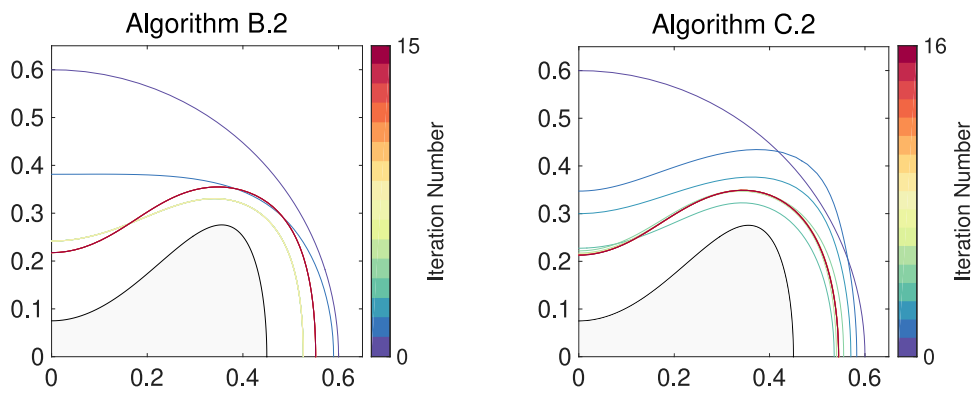
(c) Histories of Hausdorff distances

Figure 3.30: Computational results of Example 3.2.3.4 using algorithms B.1, C.1, B.2 and C.2

that the cost J_3 is more sensitive (and therefore has higher convergence behavior) than J_D . In fact, because the number of iterations required by Algorithm B.2 to reach the optimal free boundary is less than that of Algorithm C.2 (as evident in the right graph plotted in Figure 3.33(a)), we can conclude that the proposed method is indeed much faster than the classical Dirichlet-data-tracking cost functional minimization approach. This observation is, of course, also evident from the evolution of the free boundaries shown in Figure 3.33(b) wherein we recognized a big difference on how the two algorithms actually develop the initial free boundary into an optimal one. We mention here that we also ran the two algorithms using several other values for $\tilde{\alpha}$ between zero and the unit value (to solve the present case problem), and, as in the previous cases, we found that the proposed method is, in general, faster than the classical approach of minimizing the Dirichlet-data-tracking cost functional. Nevertheless, the cost function J_3 becomes more insensitive than J_D as the step size parameter $\tilde{\alpha}$ increases in value.



(a) Histories of cost values



(b) Evolution of the free boundaries using Algorithm B.2 (*left*) and Algorithm C.2 (*right*)

Figure 3.31: Computational results of Example 3.2.3.4 using Algorithm B.2 and Algorithm C.2 with the full Newton step (i.e., $\tilde{\alpha} = 1$.)

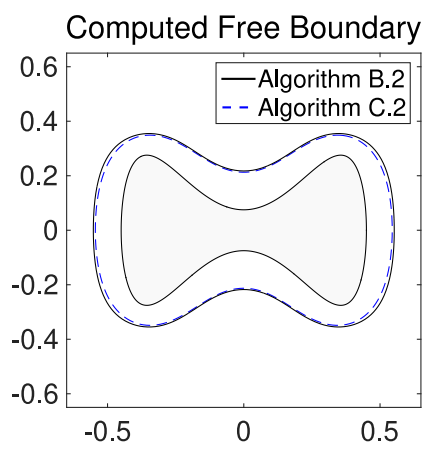
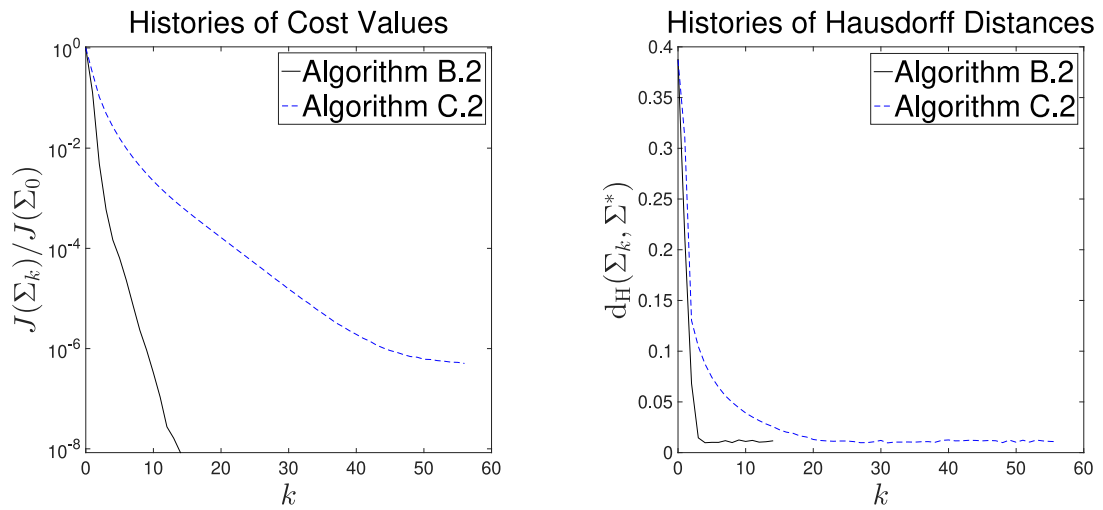
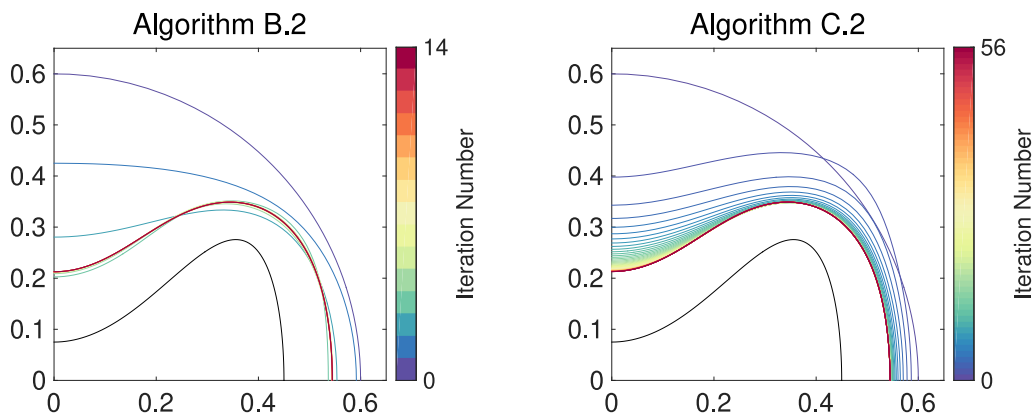


Figure 3.32: Direct comparison of the free boundaries corresponding to Figure 3.31

(a) Histories of cost values (*left*) and Hausdorff distances (*right*)

(b) Evolution of the free boundaries

Figure 3.33: Computational results of Example 3.2.3.4 using Algorithm B.2 and Algorithm C.2 with the scaled full Newton step (i.e., $\tilde{\alpha} = 0.2$)

CONCLUSION

This thesis has contributed in several ways to the mathematical understanding of shape optimization methods for solving free boundary problems as detailed here.

What have we done in this thesis?

In Chapter 1, we recalled the well-known Bernoulli free boundary problem and reviewed its ‘classical’ reformulations in the context of shape optimization. We also proposed, in the said chapter, three shape optimization formulations of the problem that have not been investigated yet in previous studies (by other authors). The main point of departure of the proposed formulations is the coupling of the overdetermined boundary conditions on the free boundary into one equation. In this respect, the first formulation is viewed as an improvement of the classical L^2 tracking of the Neumann boundary data. The second one, on the other hand, is regarded as a modification of the well-known Kohn-Vogelius objective functional minimization approach, while the third proposed shape problem is a totally different form of optimization formulation which consists of a new boundary cost functional. Regarding the latter, it was pointed out that the cost function was actually derived from an observation that the inequality $\| \cdot \|_{L^2(\Sigma)} \leq C \| \cdot \|_{H^{\frac{1}{2}+\varepsilon}(\Omega)}$, $\Sigma \subset \partial\Omega$, holds true for some constant $C > 0$, for any $\varepsilon > 0$, due to trace theorem. Following the ideas developed in [71], combined with several of the tools established in [19–21, 68], the customary problem of proving the existence of optimal shape solution to the proposed shape problems was addressed.

In Chapter 2, the shape differentiability of the cost functionals associated with the proposed shape optimization formulations were proved. In the case L^2 tracking cost functional of the Neumann data, the shape gradient expression was derived in a rigorous manner through a minimax formulation. Its boundary integral expression was then computed under $C^{2,1}$ regularity of the domain. Meanwhile, the corresponding shape gradient and shape Hessian of the other two functionals were characterized

using the chain rule approach. Their second-order shape derivatives were then expressed in terms of appropriate adjoint variables, removing the dependence of the shape Hessian with respect to the shape derivatives of the states (and adjoint states). Moreover, the necessary optimality conditions corresponding to each of the three formulations were also exhibited. Furthermore, by analyzing the shape Hessian expression at the optimal domain, the algebraic ill-posedness of the last two shape optimization problems under consideration were proved. More specifically, it was shown that the energy space of each of the shape Hessians is the Sobolev space $H^1(\Sigma^*)$ while their respective coercivity at the optimal shape solution only holds in a weaker space.

In Chapter 3, it was demonstrated how the shape gradient and shape Hessian informations can be utilized to design an efficient iterative scheme to solve the minimization problems. Particularly, a boundary variation algorithm using the H^1 gradient (cf. [6, 10, 89]) was first formulated. Then, a second-order method based on the idea first put forward in [7, 9] was also presented. The novelty of the proposed numerical scheme is the utilization of the shape Hessian information at the solution of the Bernoulli problem, instead of using the exact shape Hessian expression, coupled with a novel Newton step-size formula. The feasibility and effective implementation of the proposed gradient-based optimization procedure was then illustrated through various numerical examples.

The numerical results showed that using a mixed Dirichlet-Robin problem, instead of a pure Dirichlet problem, as the state constraint for L^2 tracking cost functional of the Neumann data provides a more accurate approximation of the optimal solution, and better convergence speed and stability of the algorithm. This result was due primarily to the fact that the adjoint state solution associated with the proposed formulation enjoys the same degree of regularity with the state solution as opposed to the case of the classical setting. On the other hand, regarding the second proposed formulation, it was found that, using a Robin problem combined with Tiihonen's condition (2.23), one can actually reduce the number of state constraints appearing on the shape gradient of an energy-gap cost functional such as the Kohn-Vogelius objective functional. As a result, the modified formulation is more attractive compared to that of the classical Kohn-Vogelius formulation, especially in terms of numerical computations because the number of PDE systems to be solved in order to evaluate the corresponding shape Hessian of the cost function is reduced. The results obtained from the numerical experiments revealed that the proposed formulation and the classical Kohn-Vogelius approach are comparable in terms of mean over-all computing time. The classical setting, however, requires less number of iterations to complete the optimization process than the proposed method. This fact, on the other hand, means that the proposed formulation actually demands less computing time per iteration to finish the iterative procedure used (as expected since we only need the solution of (1.7) to evaluate the gradient) in the study. Finally, it was found that the third formulation consisting of the new boundary cost functional called the Dirichlet-data-gap cost functional is more efficient in comparison with the classical Dirichlet-data-tracking cost functional minimization approach (i.e., faster in terms on number of iterations), with comparable computational time.

What can be done in the future?

The investigations carried out in this research work leave space for further investigations towards several directions.

In the last proposed formulation, we introduced a new boundary functional which was derived through the application of trace theorem in connection with the well-known energy-gap objective functional. In [48–51], the authors applied the notion of boundary integral equations (see, e.g., [102]) and used the concept of boundary element methods to numerically solve some of the classical formulations of the exterior Bernoulli problem. It is therefore of interest to examine the efficiency of the third proposed problem and investigate its advantages/disadvantages over the energy-gap type cost functional minimization approach when the boundary element method is employed as a numerical scheme. In this respect, a numerical investigation of the proposed problem in three-dimensional case would also be an interesting prospect to explore.

We recall that the energy-gap objective functional J_{KV} was first used by Kohn and Vogelius in [82] in the context of inverse problems, hence the name Kohn-Vogelius cost functional. For this reason, it would be interesting to utilize the objective functional J_3 as a criterion for shape identification problems such as in the inverse geometry heat conduction problem studied in [96], thereby providing a novel approach for solving such an inverse problem in the context of shape optimization. Moreover, our original shape optimization techniques can obviously also be adopted to treat numerical solutions to the so-called quadrature surface free boundary problems as well as to free surface problems involving Stokes and Navier-Stokes equations. The challenge in this respect is of course the application of second-order methods as a numerical scheme for solving these free surface problems. We emphasize that the complexity of results obtained from second-order shape calculus makes the numerical analysis more involved and challenging. Besides, shape Hessian of cost functionals also allows one to examine the stability of critical shapes and such stability result in the case of free surface problems has not been much given attention in previous studies, making the topic for investigation more interesting especially from theoretical point of view.



A.1 Embedding Theorems

Let us first mention that, in order to give meaning to Sobolev spaces, the notion of weak derivative has to be defined first.

Definition A.1.1. We say that $g \in L^p(\Omega)$ is the γ th weak derivative of $f \in L^p(\Omega)$, where $\gamma = (\gamma_1, \gamma_2, \dots, \gamma_n) \in [\mathbb{N}]^n$ with $|\gamma| = \sum_{i=1}^d \gamma_i$ if

$$\int_{\Omega} g \varphi \, dx = (-1)^{|\gamma|} \int_{\Omega} f D\gamma \varphi, \quad \forall \varphi \in C_0^\infty(\Omega).$$

Accordingly, the Sobolev spaces $W^{m,p}(\Omega)$ and $W^{s,p}(\Omega)$ are respectively defined as follows:

$$W^{m,p}(\Omega) := \left\{ \varphi \in L^p(\Omega) : D_\gamma \varphi \in L^p(\Omega) \, \forall \gamma \in [\mathbb{N}]^n \text{ with } |\gamma| \leq m \right\} \quad (1 \leq k \leq \infty, 1 \leq p \leq \infty);$$

$$W^{s,p}(\Omega) := \left\{ \varphi \in W^{\lfloor s \rfloor, p}(\Omega) : \sup_{|\gamma| = \lfloor s \rfloor} |\partial_\gamma \varphi|_{W^{r,p}(\Omega)} < \infty \right\} \quad (r := s - \lfloor s \rfloor \in (0, 1), s > 0).$$

For two Banach spaces \mathcal{B}_0 and \mathcal{B}_1 , we say that \mathcal{B}_1 is continuously embedded into \mathcal{B}_0 , denoted by $\mathcal{B}_1 \hookrightarrow \mathcal{B}_0$, if for any $\varphi \in \mathcal{B}_1$, it is also in \mathcal{B}_0 and the embedding map is continuous, i.e., for all $\varphi \in \mathcal{B}_1$,

$$\|\varphi\|_{\mathcal{B}_0} \lesssim \|\varphi\|_{\mathcal{B}_1}.$$

Let us now quote some important results about Sobolev embedding theorems for Sobolev spaces.

Theorem A.1.1 (Sobolev embedding theorem). Let $\Omega \subset \mathbb{R}^d$ be an open and bounded with Lipschitz boundary. Moreover, let two integers $m_1 \geq 0$, $m_2 \geq 0$, as well as $0 \leq p_1 < \infty$ and $0 \leq p_2 < \infty$ be given. Then, we have the following.

- (i) If $m_1 - d/p_1 \geq m_2 - d/p_2$ and $m_1 \geq m_2$, then there exists a continuous embedding

$$\iota : W^{m_1, p_1}(\Omega) \rightarrow W^{m_2, p_2}(\Omega).$$

More precisely, for any $\varphi \in W^{m_1, p_1}(\Omega)$, there exists a constant $C > 0$ depending on d , Ω , m_1 , m_2 , p_1 , and p_2 such that

$$\|\varphi\|_{W^{m_2, p_2}(\Omega)} \leq C \|\varphi\|_{W^{m_1, p_1}(\Omega)}.$$

In this case, we write $W^{m_1, p_1}(\Omega) \hookrightarrow W^{m_2, p_2}(\Omega)$.

- (ii) If $m_1 - d/p_1 > m_2 - d/p_2$ and $m_1 > m_2$, then there exists a continuous and compact embedding

$$\iota : W^{m_1, p_1}(\Omega) \rightarrow W^{m_2, p_2}(\Omega).$$

In this case, we have $W^{m_1, p_1}(\Omega) \hookrightarrow\hookrightarrow W^{m_2, p_2}(\Omega)$, or $W^{m_1, p_1}(\Omega) \subset\subset W^{m_2, p_2}(\Omega)$.

Under certain conditions, the Sobolev spaces embed into Hölder spaces as is stated in the following.

Theorem A.1.2. Let $\Omega \subset \mathbb{R}^d$ be an open and bounded with Lipschitz boundary. Moreover, let $m \geq 0$ as well as $0 \leq p < \infty$, an integer $k \geq 0$ and $0 \leq \mu \leq 1$ be given. Then, it holds that if $m - d/p = k + \mu$ and $0 < \mu < 1$, then there exists a continuous embedding

$$\iota : W^{m, p}(\Omega) \rightarrow C^{k, \mu}(\overline{\Omega}).$$

More precisely, for any $\varphi \in W^{m, p}(\Omega)$, there exists a constant $C > 0$ depending on d , Ω , m , p , α , and k such that

$$\|\varphi\|_{W^{m, p}(\Omega)} \leq C \|\varphi\|_{C^{k, \mu}(\overline{\Omega})}.$$

A.2 Gâteaux Semiderivatives

Here, we briefly review some elements of semi-derivatives and derivatives in topological vector spaces. We quote that there are two basic notions of differentiability for functions $f : \mathcal{E} \rightarrow \mathcal{F}$ between Banach spaces \mathcal{E} and \mathcal{F} (see, e.g., [16]).

Definition A.2.1. A function f is said to be Gâteaux semi-differentiable at x_0 if there exists a bounded linear operator $T_{x_0} \in \mathcal{B}(\mathcal{E}, \mathcal{F})$ such that for all $v \in \mathcal{E}$

$$\lim_{\varepsilon \searrow 0} \frac{f(x_0 + \varepsilon v) - f(x_0)}{\varepsilon} = T_{x_0} v.$$

The operator T_{x_0} is called the Gâteaux derivative of f at x_0 .

If for some fixed v the limits

$$\delta_v f(x_0) := \left. \frac{d}{d\varepsilon} \right|_{\varepsilon=0} f(x_0 + \varepsilon v) = \lim_{\varepsilon \searrow 0} \frac{f(x_0 + \varepsilon v) - f(x_0)}{\varepsilon}$$

exists, we say f has a directional derivative at x_0 in the direction v . Hence f is Gâteaux differentiable at x_0 if and only if all the directional derivatives $\delta_v f(x_0)$ (in [43], the Gâteaux semi-derivative at a point x_0 in the direction v is denoted by $df(x_0; v)$) exist and form a bounded linear operator $Df(x_0) : v \mapsto \delta_v f(x_0)$.

If the limit, in the sense of the Gâteaux derivative, exists *uniformly* in v on the unit sphere of \mathcal{E} , we say f is *Fréchet differentiable* at x_0 and T_{x_0} is the Fréchet derivative of f at x_0 . Equivalently, if we set $y = \varepsilon v$ then $\varepsilon \rightarrow 0^+$ if and only if $y \rightarrow 0$. Thus f is Fréchet differentiable at x_0 if for all y ,

$$f(x_0 + y) - f(x_0) - T_{x_0} y = o(\|y\|_{\mathcal{E}})$$

and we call $T_{x_0} = Df(x_0)$ the derivative of f at x_0 .

Note that the two notions of differentiability differ from how the limit is taken. In the Fréchet case, the limit only depends on the norm of y .

Theorem A.2.1. If a function $f : \mathcal{E} \rightarrow \mathcal{F}$ is defined in the neighborhood of x_0 and has a Fréchet derivative at x_0 , then f is continuous there.

We have the following implications.

$$\text{Fréchet derivative} \implies \text{Gâteaux derivative} \implies \text{Partial derivatives exist!}$$

In the Euclidean space, the Fréchet derivative (or *total differential*) coincides with the notion of *Hadamard derivative*. For further review of differentiation in topological vector spaces, we refer the readers to [43, Section 9.2].

BIBLIOGRAPHY

- [1] A. B. ABDA, F. BOUCHON, G. PEICHL, M. SAYEH, AND R. TOUZANI, *A Dirichlet-Neumann cost functional approach for the Bernoulli problem*, J. Eng. Math., 81 (2013), pp. 157–176.
14, 17, 32, 58, 80, 126
- [2] A. ACKER, *An extremal problem involving current flow through distributed resistance*, SIAM J. Math. Appl., 12 (1981), pp. 169–172.
12
- [3] A. ACKER AND R. MEYER, *A free boundary problem for the p -Laplacian: uniqueness, convexity, and successive approximation of solutions*, Electron. J. Differential Equations, 20 (1995), pp. 1–20.
13
- [4] R. A. ADAMS AND J. J. F. FOURNIER, *Sobolev Spaces*, vol. 140 of Pure and Applied Mathematics, Academic Press, Amsterdam, 2003.
5, 9
- [5] A. ALT AND L. A. CAFFARELLI, *Existence and regularity for a minimum problem with free boundary*, J. Reine. Angew. Math., 325 (1981), pp. 105–144.
12, 13
- [6] H. AZEGAMI, *A solution to domain optimization problems*, Trans. Jpn. Soc. Mech. Eng., Ser. A., 60 (1994), pp. 1479–1486.
81, 140
- [7] ———, *Shape Optimization Problems*, Morikita Publishing Co., Ltd., Tokyo, 2016.
85, 140
- [8] ———, *Solution of shape optimization problem and its application to product design*, in Mathematical Analysis of Continuum Mechanics and Industrial Applications, H. Itou, M. Kimura, V. Chalupický, K. Ohtsuka, D. Tagami, and A. Takada, eds., vol. 26 of Mathematics for Industry, Singapore, 2016, Springer, pp. 83–98.
80

- [9] ———, *Second derivatives of cost functions and H^1 Newton method in shape optimization problems*, in *Mathematical Analysis of Continuum Mechanics and Industrial Applications II*, P. van Meurs, M. Kimura, and H. Notsu, eds., vol. 30 of *Mathematics for Industry*, Singapore, 2017, Springer, pp. 61–72.
62, 85, 140
- [10] H. AZEGAMI, S. KAIZU, M. SHIMODA, AND E. KATAMINE, *Irregularity of shape optimization problems and an improvement technique*, in *Computer Aided Optimization Design of Structures, Structural Optimization*, S. Hernandez and C. A. Brebbia, eds., vol. V, Southampton, 1997, Computational Mechanics Publications, pp. 309–326.
81, 82, 140
- [11] H. AZEGAMI, M. SHIMODA, E. KATAMINE, AND Z. C. WU, *A domain optimization technique for elliptic boundary value problems*, in *Computer Aided Optimization Design of Structures, Structural Optimization*, S. Hernandez, M. El-Sayed, and C. A. Brebbia, eds., vol. IV, Southampton, 1995, Computational Mechanics Publications, pp. 51–58.
- [12] H. AZEGAMI AND Z. Q. WU, *Domain optimization analysis in linear elastic problems: approach using traction method*, *SME Int. J., Ser. A.*, 39 (1996), pp. 272–278.
81
- [13] J. B. BACANI, *Methods of shape optimization in free boundary problems*, PhD thesis, Karl-Franzens-Universität-Graz, Graz, Austria, 2013.
14, 32, 51, 55, 70
- [14] J. B. BACANI AND G. PEICHL, *On the first-order shape derivative of the Kohn-Vogelius cost functional of the Bernoulli problem*, *Abstr. Appl. Anal.*, 2013 (2013).
15, 17, 36, 45, 58, 70
- [15] J. B. BACANI AND G. H. PEICHL, *Solving the exterior Bernoulli problem using the shape derivative approach*, in *Mathematics and Computing 2013*, R. Mohapatra, D. Giri, P. Saxena, and P. Srivastava, eds., vol. 91 of *Mathematics & Statistics*, New Delhi, 2014, Springer, pp. 251–269.
14, 32
- [16] Y. BENYAMINI AND J. LINDENSTRAUSS, *Geometric Integration Theory*, vol. 48 of *Colloq. Publ.*, American Mathematical Society, Providence, RI, 2000.
144
- [17] A. BEURLING, *On free-boundary problems for the Laplace equation*, *Sem. on analytic functions*, (1957), pp. 248–263.
12, 13

-
- [18] F. BOUCHON, S. CLAIN, M. SAYEH, AND R. TOUZANI, *Numerical solution of the free boundary Bernoulli problem using a level set formulation*, *Comput. Method Appl. Mech. Eng.*, 194 (2005), pp. 3934–3948.
80
- [19] A. BOULKHEMAIR AND A. CHAKIB, *On the uniform Poincaré inequality*, *Comm. Partial Differential Equations*, 32 (2007), pp. 1439–1447.
25, 26, 139
- [20] A. BOULKHEMAIR, A. NACHAOUI, AND A. CHAKIB, *Uniform trace theorem and application to shape optimization*, *Appl. Comput. Math.*, 7 (2008), pp. 192–205.
27, 28
- [21] ———, *A shape optimization approach for a class of free boundary problems of Bernoulli type*, *Appl. Math.*, 58 (2013), pp. 205–221.
22, 25, 26, 27, 32, 139
- [22] S. BOYD AND L. VANDENBERGHE, *Convex Optimization*, Cambridge University Press, Cambridge, 2004.
88
- [23] D. BUCUR AND G. BUTTAZZO, *Variational Methods in Shape Optimization Problems*, vol. 65 of *Progr. Nonlinear Differential Equations Appl.*, Birkhäuser-Verlag, Basel, 2005.
2
- [24] T. BÜHLER AND D. A. SALAMON, *Functional Analysis*, vol. 191 of *Graduate Studies in Mathematics*, AMS, Providence, Rhode Island, 2018.
18
- [25] L. A. CAFFARELLI AND S. A. SALSA, *Lebesgue spaces of differentiable functions and distributions*, *Partial Differential Equations: Proc. Symp. Pure Math.*, 4 (1961), pp. 33–49.
11
- [26] ———, *Geometric Approach to Free Boundary Problems*, American Mathematical Society, Providence, RI, USA, 2005.
12
- [27] P. CARDALIAGUET AND R. TAHRAOUI, *Some uniqueness results for the Bernoulli interior free-boundary problems in convex domains*, *Electron. J. Differ. Equ.*, 102 (2002), pp. 1–16.
13
- [28] T. CAZENAVE, *Courant lecture notes*, in *Semi-linear Schrödinger equations*, vol. 10, Courant Institute of Mathematical Science, New York, 2003.
30

- [29] J. CÉA, *Conception optimale ou identification de formes: calcul rapide de la dérivée directionnelle de la fonction coût*, Modélisation mathématique et analyse numérique, 20 (1986), pp. 371–402.
4, 34
- [30] D. CHENAIS, *On the existence of a solution in a domain identification problem*, J. Math. Anal. Appl., 52 (1975), pp. 189–219.
10, 23, 26
- [31] P. CIARLET, *Mathematical Elasticity I*, Elsevier Science Publishers B.V., Amsterdam, The Netherlands, 1988.
9
- [32] F. CLARKE, *Functional Analysis, Calculus of Variations and Optimal Control*, vol. 264 of Graduate Studies in Mathematics, Springer-Verlag, London, 2013.
18
- [33] R. CORREA AND A. SEEGER, *Directional derivative of a mimimax function*, Nonlinear Anal., 9 (1985), pp. 13–22.
4, 45, 48, 50
- [34] J. CRANK, *Free and Moving Boundary Problems*, Oxford University Press, Clarendon, Oxford, 1984.
12
- [35] M. DAMBRINE, *On variations of the shape Hessian and sufficient conditions for the stability of critical shapes*, Rev. R. Acad. Cienc. Exactas Fis. Nat. Ser. A. Mat., 96 (2002), pp. 95–121.
74, 78
- [36] M. DAMBRINE AND M. PIERRE, *About stability of equilibrium shapes*, Model Math. Anal. Numer., 34 (2000), pp. 811–834.
74, 78
- [37] M. C. DELFOUR, *Shape Hessian by the velocity method: a Lagrangian approach*, Lect. Notes. Cont. Inf. Sci, 147 (1990).
35
- [38] M. C. DELFOUR AND J.-P. ZOLÉSIO, *Shape sensitivity analysis by min-max differentiability*, SIAM J. Control Optim., 26 (1988), pp. 834–862.
4, 45, 49
- [39] ———, *Shape sensitivity analysis via a penalization method*, Ann. Mat. Pura Appl., 151 (1988), pp. 179–212.
5

-
- [40] ———, *Anatomy of the shape Hessian*, *Annali di Matematica Pura ed Applicata*, 159 (1991), pp. 315–339.
42
- [41] ———, *Velocity method and Langrangian formulation for the computation of the shape hessian*, *SIAM J. Control & Optim.*, 29 (1991), pp. 1414–1442.
35
- [42] ———, *Structure of shape derivatives for nonsmooth domains*, *J. Funct. Anal.*, 104 (1992), pp. 1–33.
35
- [43] ———, *Shapes and Geometries: Metrics, Analysis, Differential Calculus, and Optimization*, vol. 22 of *Adv. Des. Control*, SIAM, Philadelphia, 2nd ed., 2011.
1, 2, 3, 5, 7, 9, 34, 36, 38, 39, 40, 42, 47, 48, 51, 53, 59, 60, 67, 86, 145
- [44] I. EKELAND AND R. TEMAM, *Convex Analysis and Variational Problems*, North-Holland Publishing Co., Amsterdam. Translated from the French, *Studies in Mathematics and its Applications*, Vol. 1., 1976.
45, 46
- [45] K. EPPLER, *Boundary integral representations of second derivatives in shape optimization*, *Discuss. Math. Differ. Incl. Control. Optim.*, 20 (2000), pp. 487–516.
60, 78
- [46] ———, *Second derivatives and sufficient optimality conditions for shape functionals*, *Control Cybernet.*, 29 (2000), pp. 485–512.
78
- [47] K. EPPLER AND H. HARBRECHT, *A regularized Newton method in electrical impedance tomography using shape hessian information*, *Control Cybernet.*, 34 (2005), pp. 203–225.
62, 76, 85
- [48] ———, *Efficient treatment of stationary free boundary problems*, *Appl. Numer. Math.*, 56 (2006), pp. 1326–1339.
14, 130, 141
- [49] ———, *Tracking Neumann data for stationary free boundary problems*, *SIAM J. Control Optim.*, 48 (2009), pp. 2901–2916.
14, 32, 74, 76
- [50] ———, *Tracking the Dirichlet data in L^2 is an ill-posed problem*, *J. Optim. Theory Appl.*, 145 (2010), pp. 17–35.
14, 64, 75, 77

- [51] ———, *On a Kohn-Vogelius like formulation of free boundary problems*, *Comput. Optim. App.*, 52 (2012), pp. 69–85.
14, 17, 32, 58, 74, 76, 77, 141
- [52] ———, *Shape optimization for free boundary problems – analysis and numerics*, in *Constrained Optimization and Optimal Control for Partial Differential Equations*, G. Leugering, S. Engell, A. Griewank, M. Hinze, R. Rannacher, V. Schulz, M. Ulbrich, and S. Ulbrich, eds., vol. 160 of *International Series of Numerical Mathematics*, Basel, 2012, Springer, pp. 277–288.
14, 77
- [53] K. EPPLER, H. HARBRECHT, AND R. SCHNEIDER, *On convergence in elliptic shape optimization*, *SIAM J. Control Optim.*, 46 (200), pp. 61–83.
12, 77
- [54] A. FASANO, *Some free boundary problems with industrial applications*, in *Shape Optimization and Free Boundaries*, G. Leugering, S. Engell, A. Griewank, M. Hinze, R. Rannacher, V. Schulz, M. Ulbrich, and S. Ulbrich, eds., vol. 380 of *NATO ASI Series (C: Mathematical and Physical Sciences)*, Dordrecht, 1992, Springer, pp. 113–142.
12
- [55] M. FLUCHER, *An asymptotic formula for the minimal capacity among sets of equal area*, *Calc. Var. Partial Differential Equations*, 1 (1993), pp. 71–86.
12
- [56] ———, *Variational Problems with Concentration*, vol. 36 of *Progress in Nonlinear Differential Equations and Their Applications*, Birkhäuser, Basel, 1999.
12
- [57] M. FLUCHER AND M. RUMPF, *Bernoulli’s free-boundary problem, qualitative theory and numerical approximation*, *J. Reine. Angew. Math.*, 486 (1997), pp. 165–204.
12, 13, 80
- [58] A. FRIEDMAN, *Free boundary problems in science and technology*, *Not. AMS*, 47 (2000), pp. 854–861.
12
- [59] K. O. FRIEDRICHS, *Über ein minimumproblem für potentialströmungen mit freiem rand*, *Math. Ann.*, 109 (1934), pp. 60–82.
12
- [60] D. GILBARG AND N. S. TRUDINGER, *Elliptic Partial Differential Equations of Second Order*, Springer-Verlag, Berlin, Heidelberg, 1988.
52, 81

- [61] R. GLOWINSKI AND J.-P. ZOLÉSIO, eds., *Free and Moving Boundaries: Analysis, Simulation, and Control*, vol. 252 of Lecture Notes in Pure and Applied Mathematics, Chapman & Hall CRC, Boca Raton, 2007.
3
- [62] P. GRISVARD, *Elliptic Problems in Nonsmooth Domains*, Pitman Publishing, Marshfield, Massachusetts, 1985.
21
- [63] J. HADAMARD, *Mémoire sur le problème d'analyse relatif à l'équilibre des plaques élastiques encastrées*, Mém. Sav. Étrang., 33 (1907), pp. in "Euvres de Jacques Hadamard," 515–641, Editions du C.N.R.S., Paris, 1968.
3, 34
- [64] H. HADDAR AND R. KRESS, *A conformal mapping algorithm for the Bernoulli free boundary value problem*, Math. Meth. Appl. Sci., 39 (2016), pp. 2477–2487.
80
- [65] H. HARBRECHT AND G. MITROU, *Improved trial methods for a class of generalized Bernoulli problems*, Math. Anal. Appl., 420 (2014), pp. 174–179.
80
- [66] ———, *Stabilization of the trial method for the Bernoulli problem in case of prescribed Dirichlet data*, Math. Meth. Appl. Sci., 38 (2015), pp. 2850–2863.
80
- [67] J. HASLINGER, K. ITO, T. KOZUBEK, K. KUNISHI, AND G. H. PEICHL, *On the shape derivative for problems of Bernoulli type*, Interfaces Free Bound., 11 (2009), pp. 317–330.
14, 16, 49, 52, 54, 80
- [68] J. HASLINGER, T. KOZUBEK, K. KUNISCH, AND G. PEICHL, *An embedding domain approach for a class of 2-d shape optimization problems: Mathematical analysis*, J. Math. Anal. Appl., 209 (2004), pp. 665–685.
15, 22, 32, 139
- [69] ———, *Fictitious domain methods in shape optimization with applications in free-boundary problems*, in Numerical Mathematics and Advanced Applications, M. Feistauer, V. Dolejší, P. Knobloch, and K. Najzar, eds., Berlin, Heidelberg, 2004, Springer-Verlag, pp. 56–65.
15
- [70] J. HASLINGER, T. KOZUBEK, K. KUNISHI, AND G. H. PEICHL, *Shape optimization and fictitious domain approach for solving free-boundary value problems of Bernoulli type*, Comput. Optim. Appl., 26 (2003), pp. 231–251.

15, 80

- [71] J. HASLINGER AND R. A. E. MÄKINEN, *Introduction to Shape Optimization: Theory, Approximation, and Computation*, SIAM, Philadelphia, 2003.
18, 19, 21, 32, 87, 139
- [72] F. HECHT, *New development in FreeFem++*, J. Numer. Math., 20 (2012), pp. 251–265.
83, 89
- [73] A. HENROT AND M. PIERRE, *Shape Variation and Optimization: A Geometrical Analysis*, vol. 28 of Tracts in Mathematics, European Mathematical Society, Zürich, 2018.
1, 23, 29, 39, 81
- [74] A. HENROT AND H. SHAHGHOLIAN, *Convexity of free boundaries with Bernoulli type boundary condition*, Nonlinear Anal. Theory Methods Appl., 28 (1997), pp. 815–823.
13
- [75] ———, *Existence of classical solution to a free boundary problem for the p -Laplace operator: II the interior convex case*, Indiana Univ. Math. J., 49 (2000), pp. 311–323.
13
- [76] ———, *Existence of classical solutions to a free boundary problem for the p -Laplace operator, I: the exterior convex case*, J. Reine Angew. Math., 521 (2000), pp. 85–97.
13
- [77] F. HETTLICH AND W. RUNDELL, *A second degree method for nonlinear inverse problems*, SIAM J. Numer. Anal., 37 (2000), pp. 587–620.
87
- [78] K. ITO, K. KUNISCH, AND G. PEICHL, *Variational approach to shape derivative for a class of Bernoulli problem*, J. Math. Anal. Appl., 314 (2006), pp. 126–149.
14, 64, 70, 71, 80, 82
- [79] ———, *Variational approach to shape derivatives*, ESAIM Control Optim. Calc. Var., 14 (2008), pp. 517–539.
4, 49, 80
- [80] K. KÄRKKÄINEN, *Shape Sensitivity Analysis for Numerical Solution of Free Boundary Problems*, PhD thesis, University of Jyväskylä, Jyväskylä, Finland, 2005.
15
- [81] T. KASHIWABARA, C. M. COLCIAGO, L. DEDÈ, AND A. QUARTERONI, *Well-posedness, regularity, and convergence analysis of the finite element approximation of a generalized Robin boundary value problem*, SIAM J. Numer. Anal., 53 (2015), pp. 105–126.

- 45, 53
- [82] R. KOHN AND M. VOGELIUS, *Determining conductivity by boundary measurements*, Commun. Pure Appl. Math., 37 (1984), pp. 289–298.
14, 141
- [83] ———, *On Trefftz' integral equation for the Bernoulli free boundary value problem*, Numer. Math., 136 (2017), pp. 503–522.
80, 101, 119, 128
- [84] C. M. KUSTER, P. A. GREMAUD, AND R. TOUZANI, *Fast numerical methods for Bernoulli free boundary problems*, SIAM J. Sci. Comput., 29 (2007), pp. 622–634.
80
- [85] A. A. LACEY AND M. SHILLOR, *Electrochemical and electro-discharge machining with a threshold current*, IMA J. Numer. Anal., 39 (1987), pp. 121–142.
12
- [86] J. MÁLEK, J. NEČAS, M. ROKYTA, AND M. RØUŽIČKA, *Weak and Measure-valued Solutions to Evolutionary PDEs*, Chapman & Hall, London, 1996.
18
- [87] W. MCLEAN, *Strongly Elliptic Systems and Boundary Integral Equations*, Cambridge University Press, Cambridge, UK, 2000.
11, 18
- [88] D. MEDKOVÁ, *The Laplace Equation: Boundary Value Problems on Bounded and Unbounded Lipschitz Domains*, Springer, Berlin, 2018.
21, 45
- [89] J. W. NEUBERGER, *Sobolev Gradients and Differential Equations*, Springer-Verlag, Berlin, 1997.
81, 140
- [90] J. NEČAS, *Direct methods in the theory of elliptic equations*, Springer Monographs in Mathematics, Springer-Verlag, Berlin, Heidelberg, 2012.
18, 26
- [91] J. NOCEDAL AND S. J. WRIGHT, *Numerical Optimization*, Springer Series in Operations Research and Financial Engineering, Springer-Verlag, New York, 2nd ed., 2006.
87
- [92] A. NOVRUZI AND M. PIERRE, *Structure of shape derivatives*, J. Evol. Equ., 2 (2002), pp. 365–382.
60

- [93] A. NOVRUZI AND J. -R. ROCHE, *Newton's method in shape optimisation: a three-dimensional case*, BIT Numer. Math., 40 (2000), pp. 102–120.
80, 87
- [94] O. PANTZ, *Sensibilité de l'équation de la chaleur aux sauts de conductivité*, C. R. Math. Acad. Sci. Paris, 341 (2005), pp. 333–337.
4
- [95] L. PICK, A. KUFNER, O. JOHN, AND S. FUČÍK, *Function Spaces*, vol. 1 of De Gruyter series in nonlinear analysis and application, Walter de Gruyter GmbH, Berlin, 2 ed., 2012.
5, 7, 9
- [96] J. F. T. RABAGO AND H. AZEGAMI, *Shape optimization approach to defect-shape identification with convective boundary condition via partial boundary measurement*, Japan J. Indust. Appl. Math., 31 (2018), pp. 131–176.
141
- [97] ———, *An improved shape optimization formulation of the Bernoulli problem by tracking the Neumann data*, J. Eng. Math., 117 (2019), pp. 1–29.
xviii, 82, 83, 115
- [98] ———, *A new energy-gap cost functional cost functional approach for the exterior Bernoulli free boundary problem*, Evol. Equ. Control Theory, 8 (2019), pp. 785–824.
xviii, 25, 74, 76, 78, 85
- [99] ———, *A second-order shape optimization algorithm for solving the exterior Bernoulli free boundary problem using a new boundary cost functional*, Comput. Opti. Appl., (2020).
xvii, 25
- [100] J. F. T. RABAGO AND J. B. BACANI, *Shape optimization approach to the Bernoulli problem: a Lagrangian formulation*, IAENG Int. J. Appl. Math., 47 (2017), pp. 417–424.
14, 32, 80
- [101] ———, *Shape optimization approach for solving the Bernoulli problem by tracking the neumann data: a lagrangian formulation*, Commun. Pur. Appl. Anal., 17 (2018), pp. 2683–2702.
14, 32, 80
- [102] S. A. SAUTER AND C. SCHWAB, *Boundary Element Methods*, Springer-Verlag, Berlin, Heidelberg, 2011.
5, 10, 11, 18, 58, 141
- [103] E. SHARGORODSKY AND J. F. TOLAND, *Bernoulli free-boundary problems*, vol. 196 of Mem. Amer. Math. Soc., American Mathematical Society, Providence, RI, 2009.
12

-
- [104] J. SIMON, *Differentiation with respect to the domain in boundary value*, Numer. Funct. Anal. Optim., 2 (1980), pp. 649–687.
34
- [105] ———, *Second variation for domain optimization problems*, in Control and Estimation of Distributed Parameter Systems, F. Kappel, K. Kunisch, and W. Schappacher, eds., vol. 91 of International Series of Numerical Mathematics, Basel, 1989, Birkhäuser, pp. 361–378.
80, 87
- [106] J. SOKOŁOWSKI AND J.-P. ZOLÉSIO, *Introduction to Shape Optimization: Shape Sensitivity Analysis*, Springer Series in Computational Mathematics, Springer-Verlag, Berlin, Heidelberg, 1992.
1, 2, 3, 38, 39, 40, 41, 42, 59, 60
- [107] E. STEIN, *Singular Integrals and Differentiability Properties of Functions*, vol. 30 of Princeton Mathematical Series, Princeton University Press, Princeton, NJ, 1970.
11
- [108] K. STURM, *On shape optimization with non-linear partial differential equations*, PhD thesis, Technische Universität Berlin, Berlin, 2016.
5
- [109] T. TIIHONEN, *Shape optimization and trial methods for free boundary problems*, RAIRO Modél. Math. Anal. Numér., 31 (1997), pp. 805–825.
14, 16, 17, 55, 56, 77, 80, 85
- [110] J. I. TOIVANEN, J. HASLINGER, AND R. A. E. MÄKINEN, *Shape optimization of systems governed by Bernoulli free boundary problems*, Comput. Methods Appl. Mech. Eng., 197 (2008), pp. 3803–3815.
12
- [111] E. TREFFTZ, *Über die kontraktion kreisförmiger flüssigkeitsstrahlen*, Z. Math. Phys., 64 (1916), pp. 34–61.
80
- [112] H. WHITNEY, *Geometric Integration Theory*, Princeton University Press, Princeton, New Jersey, 1957.
11
- [113] J.-P. ZOLÉSIO, *Sur la localisation d'un domaine*, PhD thesis, Université de Nice, Nice, France, 1973.
3

BIBLIOGRAPHY

- [114] —, *Identification de domaines par déformations*, PhD thesis, Université de Nice, Nice, France, 1979.
34, 42